

AD-A173 979

ADVANCED JOINING OF AEROSPACE METALLIC MATERIALS (H)
ADVISORY GROUP FOR AEROSPACE RESEARCH AND DEVELOPMENT
NEUILLY-SUR-SEINE (FRANCE) J GOLBAR ET AL. JUL 86

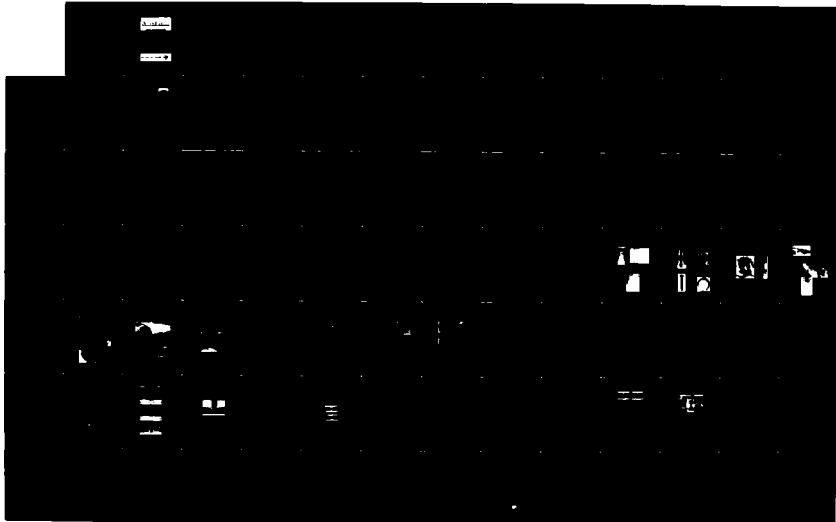
1/3

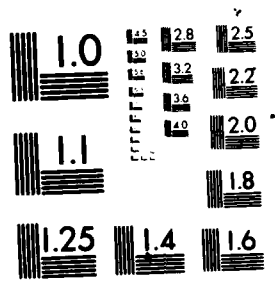
UNCLASSIFIED

ACARD-CP-398

F/C 13/8

NL





MICROCOPY RESOLUTION TEST CHART
NATIONAL BUREAU OF STANDARDS-1963-A

AD-A173 979

2

AGARD-CP-398

AGARD-CP-398

AGARD

ADVISORY GROUP FOR AEROSPACE RESEARCH & DEVELOPMENT

7 RUE ANCELLE 92200 NEUILLY SUR SEINE FRANCE

AGARD CONFERENCE PROCEEDINGS No. 398

Advanced Joining of Aerospace Metallic Materials

This document has been approved
for publication and sale, its
content is unclassified.

NOV 3 1986

010 FILE COPY

NORTH ATLANTIC TREATY ORGANIZATION



DISTRIBUTION AND AVAILABILITY
ON BACK COVER

AGARD-CP-398

NORTH ATLANTIC TREATY ORGANIZATION
ADVISORY GROUP FOR AEROSPACE RESEARCH AND DEVELOPMENT
(ORGANISATION DU TRAITE DE L'ATLANTIQUE NORD)

AGARD Conference Proceedings No. 398
**ADVANCED JOINING OF
AEROSPACE METALLIC MATERIALS**

Papers presented at the 61st Meeting of the Structures and Materials Panel of AGARD
in Oberammergau, Germany, 11–13 September 1985.

THE MISSION OF AGARD

The mission of AGARD is to bring together the leading personalities of the NATO nations in the fields of science and technology relating to aerospace for the following purposes:

- Exchanging of scientific and technical information;
- Continuously stimulating advances in the aerospace sciences relevant to strengthening the common defence posture;
- Improving the co-operation among member nations in aerospace research and development;
- Providing scientific and technical advice and assistance to the Military Committee in the field of aerospace research and development (with particular regard to its military application);
- Rendering scientific and technical assistance, as requested, to other NATO bodies and to member nations in connection with research and development problems in the aerospace field;
- Providing assistance to member nations for the purpose of increasing their scientific and technical potential;
- Recommending effective ways for the member nations to use their research and development capabilities for the common benefit of the NATO community.

The highest authority within AGARD is the National Delegates Board consisting of officially appointed senior representatives from each member nation. The mission of AGARD is carried out through the Panels which are composed of experts appointed by the National Delegates, the Consultant and Exchange Programme and the Aerospace Applications Studies Programme. The results of AGARD work are reported to the member nations and the NATO Authorities through the AGARD series of publications of which this is one.

Participation in AGARD activities is by invitation only and is normally limited to citizens of the NATO nations.



The content of this publication has been reproduced directly from material supplied by AGARD or the authors.

ACQUISITION POINT	
NAME	
ADDRESS	
CITY	
STATE	
ZIP	
PHONE	
TELETYPE	
FAX	
EMAIL	
DATE	
INITIALS	

Published July 1986
Copyright © AGARD 1986
All Rights Reserved

ISBN 92-835-0397-X

Printed by Specialised Printing Services Limited
40 Chigwell Lane, Loughton, Essex IG10 3TZ

PREFACE

During the early 1970s the Materials Group of the Structures and Materials Panel began to address the general subject of advanced fabrication processes. The Panel Members realized that the high cost of ownership of aircraft and space structures was of major concern to operators, and they also realized that both the initial procurement costs as well as subsequent maintenance costs were substantially affected by the manufacturing technology employed at the various stages. These early discussions led to the first SMP Specialists' Meeting in this area, and it dealt with Advanced Fabrication Techniques in Powder Metallurgy and their Economic Implications. The meeting was held in Ottawa in Spring 1976 and was one of the most popular meetings in the history of the Panel, attracting very close to 150 participants. This meeting resulted in Conference Proceedings, CP-200.

Encouraged by the community response to this initiative, the Subcommittee on Advanced Fabrication Processes continued its work. In Fall 1978 a second Specialists' Meeting was held, in which *machining, surface treatments and processes*, and both the fundamental and production aspects of net shape processing were considered. This again was a very successful meeting with about one hundred participants from nearly all of the NATO countries in attendance. This meeting led to the publication of Conference Proceedings CP-256.

In Fall 1979 a third Specialists' Meeting was held, this time in Cologne, West Germany, and it dealt with Ceramics for Turbine Applications. This meeting dealt with ceramics in a comprehensive manner, including papers on component design considerations, properties and performance, microstructures and defects, and inspection. But it also addressed problems as well as opportunities in fabrication, and therefore it also made a significant contribution to this continuing series on advanced fabrication processes.

During 1980—1982 the Panel started once again to consider appropriate follow-on activities in advanced fabrication. In 1983 a Working Group was created to prepare a handbook on Advanced Casting Technology, and at about the same time the decision was made to proceed with a further Specialists' Meeting, this time dealing with Advanced Joining of Aerospace Metallic Materials. In arriving at this decision the Panel was influenced by the fact that joining technology has advanced significantly over the past 10—15 years. These developments have often been driven by demands for lower cost fabrication methods and higher performance in equipment in fields other than aerospace. Not only have many new processes or process modifications evolved but automated joining has developed rapidly to meet high production levels and quality requirements in industries such as the automobile industry. However there are very few applications which demand the same stringent requirements on quality control and structural integrity as aerospace. At the same time many aerospace materials have emerged, such as superplastically formed aluminium and titanium alloys, and high stiffness aluminium-lithium alloys, all of which will present both new opportunities and new problems to design engineers and fabrication specialists.

This Specialists' Meeting on Advanced Joining of Aerospace Metallic Materials had four objectives. Firstly it was intended to provide a state-of-the-art review of advanced joining techniques currently available to the manufacturers of aerospace equipment. Secondly, it was intended to identify newly emerging joining techniques that could be used by airframe and engine operators to extend the useful lives of their equipment, and hence reduce operating costs. Thirdly, it was hoped that any outstanding problems, requiring further attention by research and development, could be identified and hence provide direction for those engaged in such activities. And finally, in all of the above, the Panel hoped to be able to take advantage of work performed for other sectors of the engineering industry.

In total about seventy people have participated in this meeting, and papers of a very high quality have been presented. They deal with the fundamental aspects of joining as well as the practical and economic aspects. The Subcommittee on Advanced Joining will meet in Spring 1986 to consider the results of this meeting and to consider the need for further work in the area of joining or the broader field of advanced fabrication.

On behalf of the Structures and Materials Panel, I would like to thank all authors, recorders, Session Chairmen, and participants for their valuable contributions. Their efforts have been largely responsible for making the meeting such a success. I would like to thank Mr John Lee, a former Panel Member and Chairman of the Subcommittee on Advanced Joining, who steered the ship so effectively during the early stages of planning.

W. Wallace
Chairman, Subcommittee on Advanced
Joining of Aerospace Metallic Materials
October 1985

CONTENTS

	Page
PREFACE	iii
	Reference
<u>SESSION I - OVERVIEWS</u>	
RECORDER'S REPORT by P.Adam	R1
COMPUTATIONAL WELD MECHANICS by J.Goldak, B.Patel, M.Bibby and J.Moore	1
ETUDE DE LA SOUDABILITE PAR FAISCEAU D'ELECTRONS DE SUPERALLIAGES PAR ANALYSE MORPHOLOGIQUE DES ZONES FONDUES par F.Pierquin et J.Lesgourges	2
THE APPLICATION OF DIFFUSION BONDING AND LASER WELDING IN THE FABRICATION OF AEROSPACE STRUCTURES by S.B.Dunkerton and C.J.Dawes	3
ECONOMICAL MANUFACTURING AND INSPECTION OF THE ELECTRON BEAM-WELDED "TORNADO WING BOX" by J.Berggreen	4
Paper 5 withdrawn	
THE WELDING OF ALUMINIUM ALLOYS - A NEW TECHNOLOGY IN SPACE APPLICATION by P.Marchese and G.Banino	6
<u>SESSION II - DIFFUSION BONDING</u>	
RECORDER'S REPORT by M.Dufour	R2
DIFFUSION BONDING IN THE MANUFACTURE OF AIRCRAFT STRUCTURE by D.Stephen and S.J.Swadling	7
DIFFUSION BONDING OF Al-ALLOYS IN THE SOLID STATE by P.G.Partridge, J.Harvey and D.V.Dunford	8
BONDING OF SUPERALLOYS BY DIFFUSION WELDING AND DIFFUSION BRAZING by P.Adam and L.Steinhauser	9
APPLICATION DU SOUDAGE PAR DIFFUSION ASSOCIE AU FORMAGE SUPERPLASTIQUE (SPF/DB) A LA REALISATION DE STRUCTURES EN TOLES MINCES DE TA6V par M.Boire et P.Jolys	10
<u>SESSION III - INSPECTION METHODS, FLAWS AND NEW PROCESSES</u>	
RECORDER'S REPORT by P.R.Wedden	R3
ULTRASONIC TESTING TECHNIQUES FOR DIFFUSION-BONDED TITANIUM COMPONENTS by G.Toher and S.Elze	11
WELD QUALITY MONITOR AND CONTROL SYSTEM by F.Kearney, D.White and W.Ricci	12
NDT OF ELECTRON BEAM WELDED JOINTS (MICRO-FOCUS AND REAL-TIME X-RAY) by R.G.Taylor	13

	Reference
THERMOELASTIC TESTING OF STRATIFIED MATERIALS by P.Cielo and M.Dufour	14
INFLUENCE OF WELDING FLAWS ON THE FATIGUE STRENGTH OF ELECTRON BEAM WELDMENTS IN Ti Al6 V4 by W.Schütz and W.Oberparleiter	15
A REAL TIME VISION SYSTEM FOR ROBOTIC ARC WELDING by M.Dufour, P.Cielo and F.Nadeau	16
INERTIA WELDING OF NITRALLOY "N" AND 18 NICKEL MARAGING 250 GRADE STEELS FOR UTILIZATION IN THE MAIN ROTOR DRIVE SHAFT FOR THE AH-64 MILITARY HELICOPTER PROGRAM by A.G.Hirko and L.L.Soffa	17
<u>SESSION IV – REPAIR TECHNIQUES</u>	
RECORDER'S REPORT by M.Yanishevsky	R4
Paper 18 withdrawn	
WELDING OF ALUMINIUM CASTINGS by J.Leupp, A.Maitland and K.Schellenberg	19
THE APPLICATION OF THE "RBD" PROCESS TO THE DEPOSITION OF ANTI-WEAR ALLOYS by J.Lesgourges	20
EVALUATION OF THE DDH AND WELD REPAIRED F100 TURBINE VANES UNDER SIMULATED SERVICE CONDITIONS by A.J.A.Mom, N.M.Madhava, G.A.Kool and M.Dean	21
REPAIR TECHNIQUES FOR GAS TURBINE COMPONENTS by J.Liburdi and P.Lowden	22

**RECORDER'S REPORT
SESSION I — OVERVIEWS**

by
Dr P. Adam
MTU München GmbH
Abt GWF
Dachauerstrasse 665
8000 München 50
Federal Republic of Germany

Paper 1 on *Computational Weld Mechanics* represents an outstanding analysis of the complex problem consisting of computation of the properties of welds. Although there is no doubt about the high degree of complexity, it is necessary to have the analysis in order to show up where advances have to be pushed further. Forecasting the stresses and distortions would be a very large advance for fusion welding application.

The question remains when the computed forecast would be more useful than the conventional methods of measuring, metallography, x-ray stress analysis and process control.

From experience of computing the friction welding process of superalloys the largest problem is certainly to supply material physical data like c_p , α , or λ for high temperatures. These data are normally not existent because measuring is difficult, but they are of most important interest for weld computation.

Paper 2 describes the relationship between EB-welding parameters and the geometry of the weld pool for superalloys like Inconel 718. Marking with foreign metals reveals exactly how the flow of liquid was. Weld pool geometry is related to cracking occurrence.

The refined analysis identifies the welding parameter ranges with and without macrocracking.

To the Recorder's knowledge Inconel 718 must be welded slowly ($< 4 \text{ mm/s}$) in order to avoid microcracking, which is a particular property of Inconel 718 and Waspaloy. This effect was investigated in detail during the COST 50 European action on superalloy development.

Paper 3 described practical details of diffusion — (also in combination with SPF = Superplastic forming) and Laserbeam-welding of several alloys but mainly Titanium and Aluminium. Parameters and principle knowledge were discussed and basic results reported.

Paper 4 described the manufacturing of the Titanium wing box of the Tornado by EB-welding and subsequent stress relieve by heat treatment. A self-evidencing paper.

Paper 5 was withdrawn.

Paper 6 is a special paper on manufacturing high quality Aluminium parts for spacelab by TIG. It is useful for other Al-structure parts and contains welding details.

Conclusions from the Recorder:

Titanium can readily be welded by TIG-, EB- and diffusion welding even in complex geometry for safety aircraft structures.

Its application range is increasing.

There is great interest in the increasing use of Superplastic Forming (SPF) in combination with diffusion bonding for complex Titanium structures.

Aluminium structures seem to be more difficult to weld, but TIG-, EB- and diffusion welding/bonding are increasing. The laser can sometimes replace EB or TIG, depending on light adsorption.

In general, many most useful details for practical application were reported.

R1-2

Discussion:

The discussion focused on Aluminium welding and computational weld mechanics while the other contributions present well acceptable integral presentations of *individual solutions* for welding tasks. The discussions on computational weld mechanics concentrated on how to achieve applicable computed results in a time and cost-effective way.

The author has a very optimistic approach towards economic applicability. Any problem of welding presented for computational treatment can be analysed first for the ratio of results required to cost. Material and design data have to be furnished from data banks or the applicant. The level of computed result accuracy, tolerance and quantity in relation to cost remains a matter of individual situations. It is recommended to contact Dr Goldak for individual problems.

COMPUTATIONAL WELD MECHANICS

John Goldak⁽¹⁾, Balvantrai Patel⁽²⁾, Malcolm Bibby⁽¹⁾
James Moore⁽¹⁾

June 1985

(1) Department of Mechanical and Aeronautical Engineering
Carleton University, Ottawa, Canada, K1S 5B6

(2) Engineering Mechanics Research Inc.
Troy, Michigan, U.S.A.

ABSTRACT

The goal of this paper is to present an overview of the aims and methods of computational weld mechanics. In particular, relevant literature and recent developments in the authors' laboratory are described. The presentation emphasizes an exposition of the computational principles and the application of computational weld mechanics to practise. In fact, the primary aim of the work is to transfer this technology from the research specialists who are developing it to the engineers who must apply it in the design and production of welded structures.

The numerical methods, algorithms, software and computer hardware needed for computing the temperature, displacement, strain and stress fields associated with the welding process are described. While computer methods are widely applied in the engineering community, thermal strain-stress transients are rarely calculated in welding because of the complexity of the problem. *Finite element analysis (FEA)* together with the equations of continuum mechanics and irreversible thermodynamics forms the basis for a successful analysis of welding processes. The special problems encountered when FEA is used for weld analysis are discussed in detail.

Particular attention is focussed on transient temperature field computations. Modelling heat sources, non-linear thermal properties, the heats of fusion and transformation, and workpiece geometry and boundary conditions are discussed in some detail. Predicting relevant properties (strength, hardness, etc.) of weld joints from computed temperatures is included. In addition, thermo-elasto-plastic analysis for calculating residual strain, stresses and workpiece deformation is described. Measured thermal and distortion changes are compared to computed values as a means of verifying the accuracy of the computational methods. Finally, the computing environment (hardware and software) for computational weld mechanics is discussed at some length.

1. INTRODUCTION

Welding as a fabrication technique presents a number of difficult problems to the design and manufacturing community. Nowhere is this more evident than in the aerospace industry with its emphasis on performance and reliability and yet where materials are seldom selected for their weldability. Traditional welding procedures have been based largely on experience, materials science and extensive testing. Yet the material response defines only one half of the problem. This paper focusses on methods and models for computing the thermal cycle and associated elasto-plastic stress-strain transients. It presumes that the capability to accurately predict temperatures, stresses, and strains in welds is needed to understand and solve efficiently welding problems such as hot cracking, reheat cracking, distortion and residual stress.

Developments in calculating the thermal cycle and elastoplastic stress-strain cycle have been slow because of the inherent complexity of the geometry, boundary conditions and the nonlinearity of material properties and in welding. However, the explosive growth in computer performance combined with equally rapid developments in numerical methods and geometric modelling have enabled computational weld mechanics to reach the stage where it can solve an increasing number of problems that interest industry.

In its narrowest sense computational weld mechanics is concerned with the analysis of temperatures, displacements, strains and stresses in welds and welded structures (Fig. 1). In its broadest context, it is an important element of computer-aided design (CAD) and computer-aided manufacturing (CAM). Computer modelling, in general, provides the capability of storing vast amounts of data; of organizing and storing relations between data in databases or knowledgebases; and of using these data to compute or predict the behavior of products, processes or systems in the real world. On the one hand, it can be viewed as a set of analytical tools for determining the mechanical response of a workpiece to a given welding procedure. On the other hand, it can be viewed as a design tool for predicting the quality of a weld and the deformation (distortion) of a workpiece and to optimize the welding parameters, alloy composition, and geometry (Fig. 2).

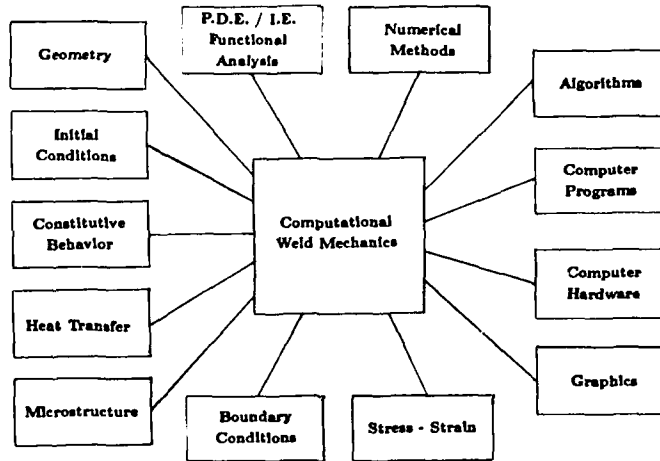


Figure 1. Computational weld mechanics draws on the disciplines shown above to compute the temperature, microstructure, stress and strain in welds. (PDE/IE — stands for partial differential equations / integral equations)

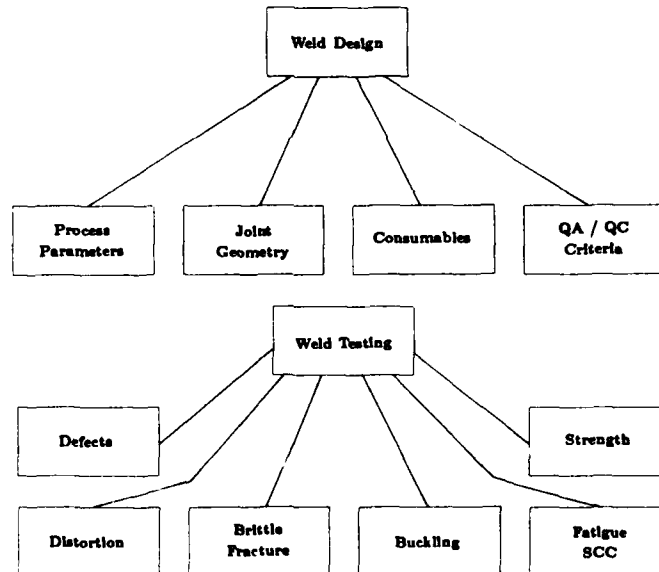


Figure 2. The important issues in design and testing of welds are shown schematically. (QA/QC is quality assurance, quality control and SCC is stress corrosion cracking.)

What if models can be examined to provide insight that could never be achieved by experiment. For example, it is well known that workpiece distortion caused by welding austenitic stainless steel is some three times greater than that caused by welding carbon steel. By analyzing models in which each property is varied separately, the sensitivity of the distortion to the property can be computed. This would provide the knowledge needed to understand the greater distortion in austenitic steel. Of course, this is not possible experimentally.

Although the ability to perform such analyses is important, the real justification for computational weld mechanics is that it is becoming cheaper, faster and more accurate to perform computer simulations than to do laboratory experiments. Taken to the extreme, all relevant decisions would be based on computer simulations. Since nuclear testing in the atmosphere has been banned, this has actually occurred in nuclear weapons design, a field at least as complex as welding. Experiments

are rarely justified in the the design and construction of buildings. However, it is unlikely that computational weld mechanics will eliminate all experiments in welding. Indeed, it is likely to increase the demand for accurate constitutive data, particularly at high temperatures, strain rate sensitivity and to include the effects of changes in microstructure. Nor will it eliminate the need for experiments that simulate or prototype processes or products. However, it will dramatically reduce the number and cost of such experiments and greatly enhance the accuracy and significance of the data obtained for each experiment. In the automotive industry, CAE (computer - aided engineering) is said to have reduced the number of prototypes required from a dozen to one or two.

Since this paper is focussed on computer methods, it is necessary at the outset to clearly fix the relationships of such models to experimental investigation (Fig. 3). Experiments tend to fall into two broad categories. Some are based on clearly understood theory where a strong attempt is made to exclude extraneous factors. Measuring Young's modulus or thermal conductivity of a particular alloy fall into this category. On the other hand, when experiments deal with complex phenomena that do not have a clearly understood theory, a strong attempt is made to include any factor that may be relevant. Developing a narrow gap welding process is an example of this second category.

At the present time, a narrow gap welding process is too complex to model with a computer; i.e., our knowledge of the process is inadequate. The interaction between the shielding gas and weld metal, physics of the arc and weld pool are only three examples of phenomena that are too complex to predict accurately by computer modelling with our current knowledge. Therefore, such processes must first be characterized by experiment before specific aspects, such as the heat transfer and thermal stress and strain, can be modelled by computer analysis.

Certain phenomena can be modelled accurately such as heat transfer outside of the liquid pool. Rapid progress is being made in computing thermal strain and stress. It is now possible to simulate the weld joint by incorporating not only base metal properties but heat-affected zone and weld metal stress-strain data as well. In addition, the interaction between these zones is a major consideration. An encouraging start has been made on the fluid mechanics of the liquid pool [1]. As theory develops, more phenomena will be understood sufficiently to create more complete models for computer analysis.

The objective of this paper is to present an exposition of the fundamental principles of weld mechanics as lucidly and completely as possible. It is addressed not to mathematicians or mechanics for whom an extensive literature exists, but to engineers in design and manufacturing who must apply the theory. Although the presentation is not mathematically rigorous, every effort is made to respect rigorous mathematics. If after reading this paper, decision makers are able to grasp clearly the *basic principles*, terminology, and gain a feel for which issues are easy and which are difficult, the authors' goal will have been achieved.

The reader seeking additional historical background is referred to Okerblom [2], Vinokurov [3], Gray, Spence and North, [4], Tall [5], and Masubuchi [6]. Of these, only Masubuchi considers computer analysis and he emphasizes results rather than explaining the methods for actually performing analyses. Ueda [7] has recently published an excellent review of modern computational weld mechanics.

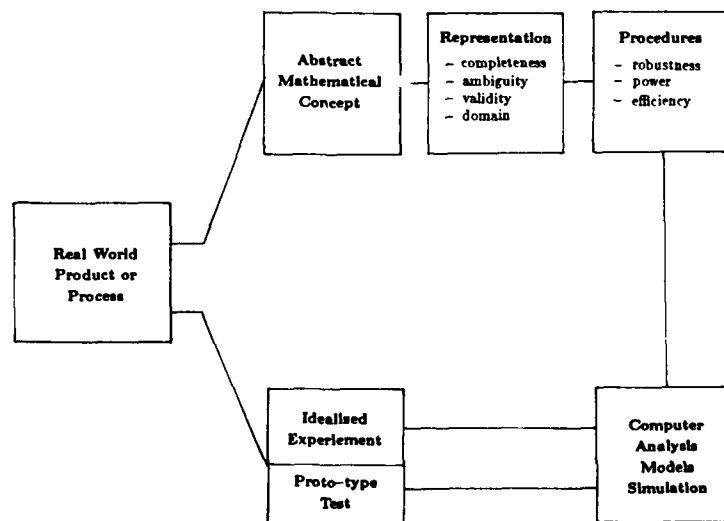


Figure 3. The relationships between the real world, experiments, mathematical abstraction and computer models are shown schematically.

2. HEAT TRANSFER THEORY

In heat transfer theory, we are concerned with energy and ignore stress, strain and displacement. The principal phenomena are shown in Fig. 4. The maturity of numerical methods in heat transfer theory is illustrated by the fact that all these effects except fluid mechanics, two phase regions, and moving interfaces are analyzed in the authors' program and these are under development.

2.1 The Heat Equation

The temperature, $T(x,y,z,t)$, as a function of spatial coordinates (x,y,z) and time, t , satisfies the following parabolic differential equation, the heat equation, at every point in the domain, Ω :

$$\frac{\partial}{\partial x} k_x \frac{\partial T}{\partial x} + \frac{\partial}{\partial y} k_y \frac{\partial T}{\partial y} + \frac{\partial}{\partial z} k_z \frac{\partial T}{\partial z} + Q = c \frac{\partial T}{\partial t} \quad (1)$$

$Q(x,y,z,t)$ = source or sink rate of heat in Ω (W/m^3)

k = thermal conductivity (W/mC)

c = volumetric specific heat (J/m^3)

If k or c are functions of T , equation (1) is nonlinear.

On the boundary of Ω either the essential or natural boundary conditions must be satisfied. The essential boundary condition can be defined as:

$$T(x,y,z,t) = T_1(x,y,z,t) \text{ on the boundary } S_1; \text{ i.e. } (x,y,z) \in S_1 : t > 0 \quad (2)$$

The natural boundary condition can be defined as:

$$k_n \frac{\partial T}{\partial n} + q + h(T - T_o) + \sigma \epsilon (T^4 - T_o^4) = 0 \quad (3)$$

on the boundary S_2 ; i.e. $(x,y,z) \in S_2 : t > 0$.

k_n = thermal conductivity normal to the surface (W/mC)

$q(x,y,z,t)$ = a prescribed flux (W/m^2)

h = heat transfer coefficient for convection (W/m^2C)

σ = Stefan-Boltzmann constant (W/m^2C^4)

ϵ = emissivity

T_o = the ambient temperature for convection and/or radiation (C).

If radiation is included or if the convective heat transfer coefficient is temperature dependent this boundary condition is nonlinear.

In addition, the initial condition must be specified for $(x,y,z) \in \Omega$:

$$T(x,y,z,0) = T_0(x,y,z) \quad (4)$$

If the partial differential equation (1), the boundary conditions (2) and (3), and the initial condition (4) are consistent, the problem is well posed and a unique solution exists.

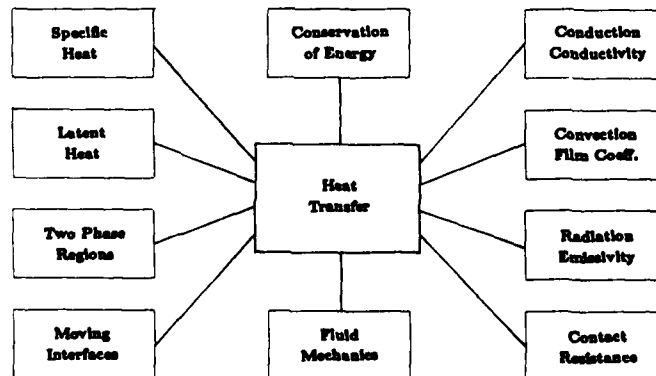


Figure 4. The important phenomena that should be captured in models for heat transfer analysis are shown above.

2.2 Finite Element Formulation for Transient Heat Flow

Of the three strong candidate numerical methods; finite difference, boundary element, and finite element analysis, the authors have chosen the finite element method for its capability for nonlinear analysis and dealing with complex geometry. In addition, it is most compatible with modern CAD/CAM systems. For thermal analysis alone, a strong argument can be made in favour of finite difference methods. However, for thermoelastic analysis the argument is stronger for finite element analysis. The boundary element method is not well developed for nonlinear analysis. Briefly, these considerations led to the choice of FEA as the most effective numerical method for developing a complete analysis capability for computer modelling or simulation of welds.

The finite element method (FEM) imposes a piece-wise polynomial approximation of the temperature field within each element :

$$T(x, y, z, t) \approx \sum_{i=1}^{n_{nodes}} N_i(x, y, z) T_i(t) \quad (5)$$

where N_i are basis functions dependent only on the type of element and its size and shape. Physically $T_i(t)$ are the nodal values of the temperature at time t . Mathematically they are undetermined coefficients. If the basis functions were orthogonalized, they would be generalized Fourier coefficients. The analyst specifies the basis functions N_i by creating a mesh which in turn determines the type and position of each element.

The temperature gradient at any point (x, y, z, t) can be computed directly from eq. (5):

$$\left[\frac{\partial T}{\partial x}, \frac{\partial T}{\partial y}, \frac{\partial T}{\partial z} \right] = \left[\frac{\partial N_i}{\partial x} T_i, \frac{\partial N_i}{\partial y} T_i, \frac{\partial N_i}{\partial z} T_i \right] \quad (6)$$

where $\sum N_i(x, y, z) T_i(t)$ is abbreviated to $N_i T_i$.

The next question is how to evaluate T_i ? Galerkin's FEM is among the most convenient and general of the methods available for this purpose. If eq (5) is substituted into eq (1), a residual or error term must be added. If this was not true eq (5) would be the exact solution. Indeed when eq (5) is the exact solution, the error in the FEM is zero.

Galerkin's FEM requires:

$$\int_{\Omega} \epsilon N_i \, d\Omega = 0 \quad (7)$$

Mathematically ϵ is the residual from eq (1); N_i in eq (7) is a test function and the N_i terms in eq (5) are the trial functions. Since there are i nodes, eq (7) creates a set of i ordinary differential equations which are integrated to form a set of algebraic equations:

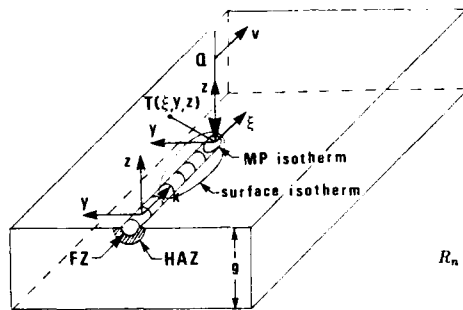
$$[K][T] = [R] \quad (8)$$

These are solved for the nodal temperatures T_i . Usually some form of Newton-Raphson method together with a Gaussian elimination and back substitution would be employed.

2.3 Models for Welding Heat Sources

Rykalin's review [8] summarized current knowledge of heat sources for welds. The basic facts are that weld heat sources produce high heat fluxes which range from 10^4 to $2 \times 10^4 \text{ KJ/mm}^2$ for arc sources to 10^8 KJ/mm^2 for focussed electron and laser beams. The flux is highest at the centre and in most cases experimental measurements suggest a Gaussian distribution. Gas velocities and current densities in the plasma are high. The surface of the weld pool is depressed. In plasma, laser and electron beam welds, the depression often penetrates the plate to form a keyhole. The molten zone is stirred intensively. A rigorous analysis of the heat source for solving the magnetohydrodynamics of the arc and the fluid mechanics of the molten zone is some years away. Ushio and Matsuda [9] have attempted to model the plasma physics of the arc. The model proposed by Oreper, Eager and Szekeley [1] for stirring in electroslag welds is a notable advance. Lawson and Kerr [10] studied stirring and mixing effects in gas tungsten inert gas (GTIG) welds. Friedman [11] studied the depression of the weld pool surface and its effect on heat transfer. While studies such these are important steps toward developing rigorous models for heat sources, current weld analyses assume simpler models that do not explicitly incorporate stirring in the weld pool or the digging of the arc to depress the weld pool surface.

The analyst's knowledge of the heat source can be summarized as follows. The values of the welding parameters — current, voltage, and speed are known. The geometry of the weldment and the material properties are known. The fusion zone (FZ) and heat-affected-zone (HAZ) boundaries represent known isotherms that can be measured from a micrograph of a weld cross-section. Thermocouples can be placed in the HAZ or plunged into the molten zone to record the thermal cycle at a number of points. Of course, these data are not known exactly but only within experimental error. The analyst requires a heat source model that accurately predicts the temperature field, $T(x, y, z, t)$, in the weldment.



$$T(\xi, \eta, \zeta) = T_0 + \frac{\dot{Q}}{2\pi k} \exp\left(-\frac{v\xi}{2\lambda}\right) \left\{ \sum_{n=-\infty}^{\infty} \frac{1}{R_n} \exp\left(-\frac{vR_n}{2\lambda}\right) \right\}$$

$$R_n = \sqrt{\xi^2 + \eta^2 + (z \pm 2ng)^2} \quad \xi = x - vt$$

Figure 5. An idealized point source moving along the surface of a workpiece used for computing the transient temperature fields, $T(x, y, z, t)$, with the classical closed form analytical solutions of Rosenthal/Rykalin [8,12]. T_0 is the ambient temperature (C), t is time (s), \dot{Q} is the heat input rate (W); where $\dot{Q} = \eta VI$, V is voltage, I is current and η is the process efficiency; k is thermal conductivity (W/mC), λ is thermal diffusivity (m^2/s), v is the welding speed (m/s); (x, y, z) is a point in a fixed axes system and (ξ, η, ζ) is a point in an axes system that moves with the heat source, n is an integer, MP is the melting point temperature which in turn is used to define the fusion zone (FZ) boundary, and HAZ is the heat-affected zone.

Rosenthal [12] and Rykalin [8] proposed point, line and plane models that are particularly convenient for classical closed form analysis (Fig. 5). Myers et al [13] reviewed this subject in depth. Closed form solutions suffer from several weaknesses. The geometry is usually highly idealized into forms such as infinite plates or bars. The thermal properties and boundary conditions are usually set equal to a constant value. Convection and radiation are usually ignored. The point, line and plane sources idealize a heat source which in reality is distributed. These solutions are most accurate far from the heat source. At the source, the error in temperature is large — usually infinite! Near the heat source the accuracy can be improved by matching the theoretical solution to experimental data. This is usually done by choosing a fictitious thermal conductivity value.

With numerical methods, these deficiencies have been corrected and more realistic models that are just as rigorous mathematically have been developed. Temperature dependent thermal conductivity and heat capacity can be taken into account (Figs. 6 and 7 for low carbon steels). In addition, temperature dependent convection and radiation coefficients can be applied to the boundaries. Contact thermal resistance between the plate and the jigging can be incorporated. Perhaps the most important factor is to distribute the heat rather than assume point or line sources.

One of the earliest models due to Westby [14] assumed that the weld energy was distributed throughout the molten zone with a constant power density. A similar heat source configuration was used Paley [15]. Experimental evidence shows clearly that the energy is not uniformly distributed. Pavelic [16] distributed the energy in a circular disc with a Gaussian flux distribution on the surface of the workpiece. This is realistic for preheating situations in which there is no melting but ignores the digging effect of the welding arc in distributing the energy. Kou [17] also used both Gaussian and constant flux distributions in a circular disc on the surface of the weld. Argyris, Szimrat and Willan [18] prescribed the temperature in the molten zone. However, it is not clear which of the following methods they used. The temperature of the molten pool was set equal to the melting temperature; the temperature of the FZ/HAZ boundary was set equal to the melting temperature; or a temperature distribution was assumed for the molten zone that was a maximum at the centre and decayed to the

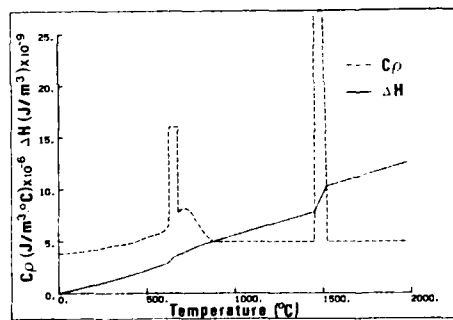


Figure 6. The volumetric heat capacity, latent heats of fusion and transformation, and the enthalpy - temperature relationship for a carbon steel (AISI 1020) used in the FEA program are plotted.

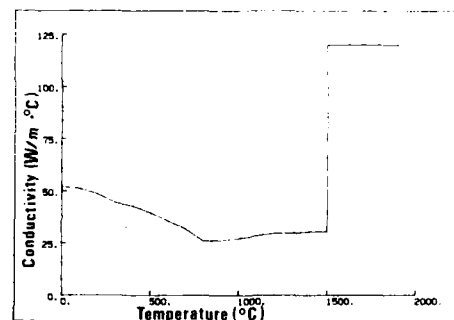


Figure 7. The thermal conductivity - temperature relationship used in the FEA program. Note that a high conductivity in the molten region is used to simulate heat transfer by stirring.

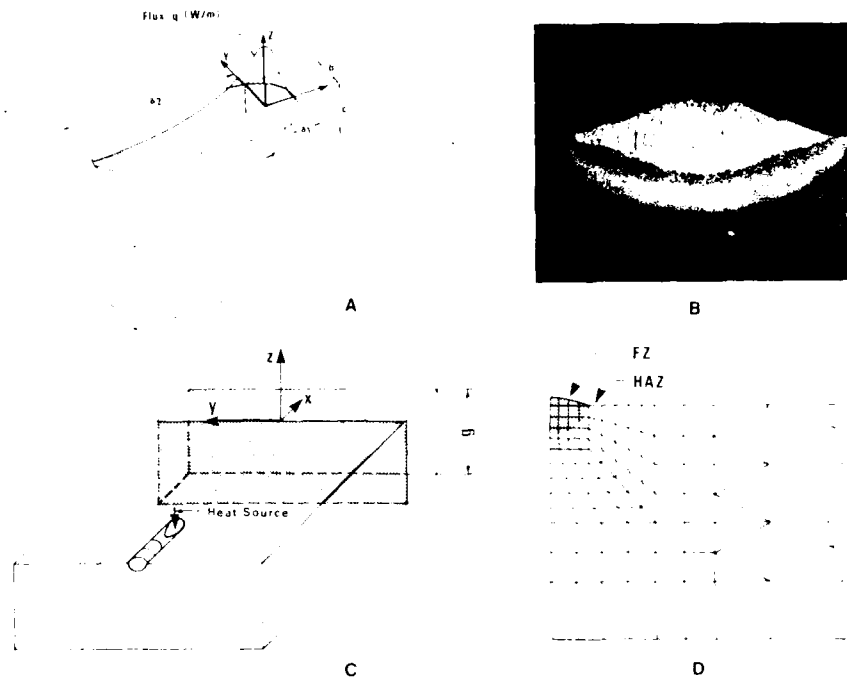


Figure 8. FEA weld analysis: (A) double ellipsoid heat source model, (B) cross section of an SMAW weld bead on a thick plate of low carbon steel ($V = 30$ volts, $I = 265$ amps, $r = 3.8$ mm, $g = 38$ mm, $T = 20.5^\circ\text{C}$), (C) reference plane concept, and (D) mesh used for the analysis.

melting temperature at the FZ boundary. The latter is the most realistic and preferable mathematically. The first two options introduce discontinuities in the temperature field which are unrealistic and mathematically undesirable. Since the temperature distribution in the molten zone is not constant except in the steady state, these models do not permit the analysis of transients during weld start, stop, run on or run off situations where the size and shape of the molten pool must change.

The most realistic models developed to date are due to Goldak et al [19]. In these models arbitrary functions are used to define the distribution of flux on the surface of the weld and the power density throughout the volume of the weld. For arc welds, a double elliptical disc with a Gaussian distribution of flux on the surface of the weld, together with one double ellipsoid function with a Gaussian distribution of power density to model the direct impingement of the arc and a second double ellipsoid with Gaussian distribution to model the energy distributed by stirring the molten metal has given the most accurate temperature fields computed to date (Fig. 8). In cases where the fusion zone differs from the ellipsoidal shape, other models should be used for the flux and power density distribution. For example, in welds with a cross section shaped as shown in Fig. 9, four ellipsoid quadrants can be superimposed to more accurately model such welds. For deep penetration electron and laser beam welds, a conical distribution of power density which has a Gaussian distribution radially and a

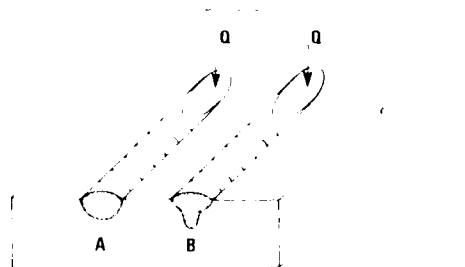


Figure 9. Cross sectional weld shape of the fusion zone where: (A) a double ellipsoid is used to approximate the heat source, (B) compound double ellipsoids must be superimposed to capture a "hot top" nail head configuration.

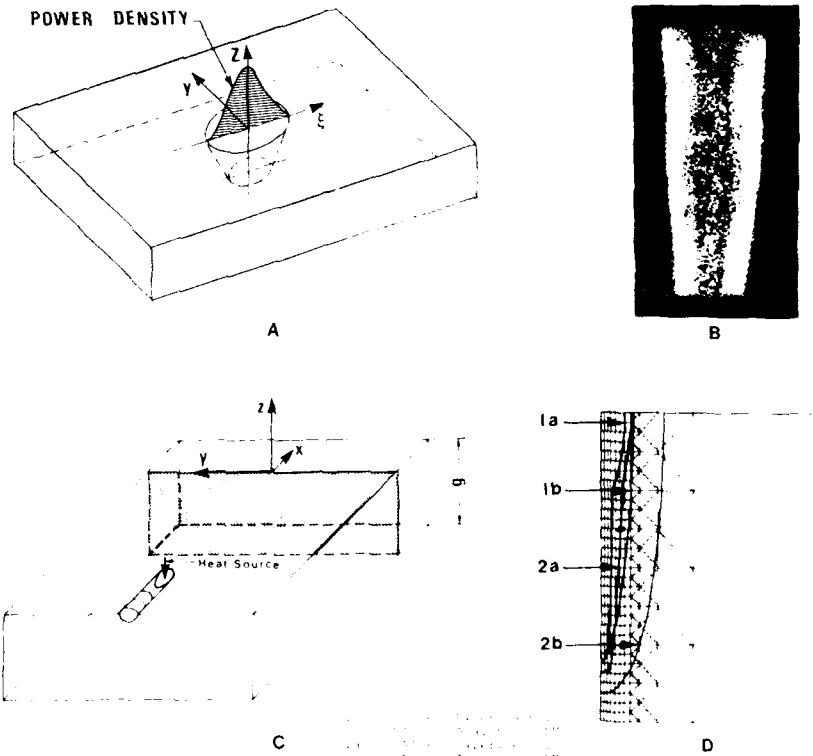


Figure 10. A conical weld heat source used for analyzing deep penetration electron beam or laser welds. (A) conical source, (B) typical electron beam weld, (C) cross-sectional kinematic model with reference plane, (D) computed and measured FZ and HAZ boundaries. ($V = 70\text{ kV}$, $I = 40\text{ mA}$, $v = 4.23\text{ mm/s}$, $g = 12.7\text{ mm}$, $T_c = 21^\circ\text{C}$).

linear distribution axially has yielded the most accurate results (Fig. 10). The analyst must specify these parameters, at least the parameters such as weld current, voltage, speed, arc efficiency, and the size and position of the heat source, ellipsoid, and/or cones. In some cases the weld pool size and shape can be estimated from cross-sectional metallographic data, or from surface ripple markings. If such data are not available, the method for estimating the weld pool dimensions is suggested by Christensen²⁰ for arc welds and by Bibby et al.²¹ for deep penetration electron beam or laser welds should be used.

The size and shape of the heat source model is fixed by the ellipsoid parameters defined in Fig. 8. Good agreement between actual and computed weld pool size is obtained if the size selected is about 10% smaller than the actual weld pool size. If the ellipsoid semi axes are too long, the peak temperature is too low and the fusion zone too small. The authors' experience is that accurate results are obtained when the computed weld pool dimensions are slightly larger than the ellipsoid dimensions. This is easily achieved in a few iterations. Chakravarti, Goldak and Rao²² have studied the sensitivity of the temperature field to the ellipsoid parameters.

On the one hand these distribution functions can be criticized as 'fudge' factors. On the other hand, they do enable accurate temperature fields to be computed. Chosen wisely, varying any parameter changes the computed temperature field. It can be argued that they are needed to model the many complex effects that are quantitatively known, such as electrode angle, arc length, joint design, and shielding gas composition²³. Since they allow the analyst to accurately compute the temperature field in weldments, they are to be preferred until better models are developed.

2.4 Kinematic Models for Heat Transfer in Welds

Having selected a model for the heat source, the analyst has the option of assuming that the heat flows only in cross-sectional planes, only in the plane of the plate, only in a radial direction or is free to flow in all three dimensions (Fig. 11). Such assumptions are analogous to those applied to the displacement field in beams, plates and shells in structural analysis. Since the assumptions restrict the orientation of the thermal gradient, it is suggested they be called kinematic

models. Of course, these kinematic models are quite distinct from the heat source models described in the previous section. In choosing a kinematic model, the analyst must balance accuracy against cost. In all cases, reality is three dimensional but the cost of analysis is the highest. Constraining heat flow to the plane of the plate can achieve useful accuracy for thin plates, particularly with deep penetration plasma, electron and laser beam welds. Assuming heat flows only in the cross-sectional plane can provide a useful and economical approximation for many welding situations. In particular, the results from a low cost cross-sectional analysis can be helpful in designing an efficient 3D mesh. These three models are discussed in detail below.

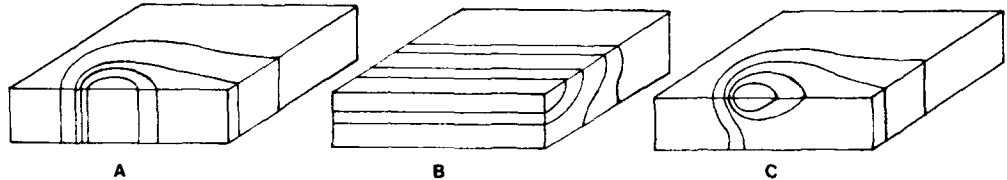


Figure 11. (A) in plane, (B) cross sectional models and (C) 3D models imply temperature fields of the forms shown above.

2.4.1 Two Dimensional Cross-Sectional Model

A schematic diagram of the cross-sectional model is shown in Fig. 8.19. A reference plane is positioned perpendicular to the weld direction at an arbitrary position x . The heat input rate, $\dot{Q} = \eta VI$, where V and I are the welding voltage and current respectively, and η is the efficiency of the heat source, together with the ellipsoid dimensions define the distribution of power density in the heat source. The heat source moves at constant speed. The FEA model is a slice of arbitrary thickness which is discretized into a mesh. At any instant of time, the power density is computed on the intersection of the reference plane and the ellipsoidal heat source. This power density is then applied throughout the thickness of the FEA slice (Fig. 12a). As the heat sources moves across the reference plane, the temperature in the slice increases and then decreases as shown in Fig. 12b and 12c. The form of the weld pool can be mapped as shown in Fig. 12d.

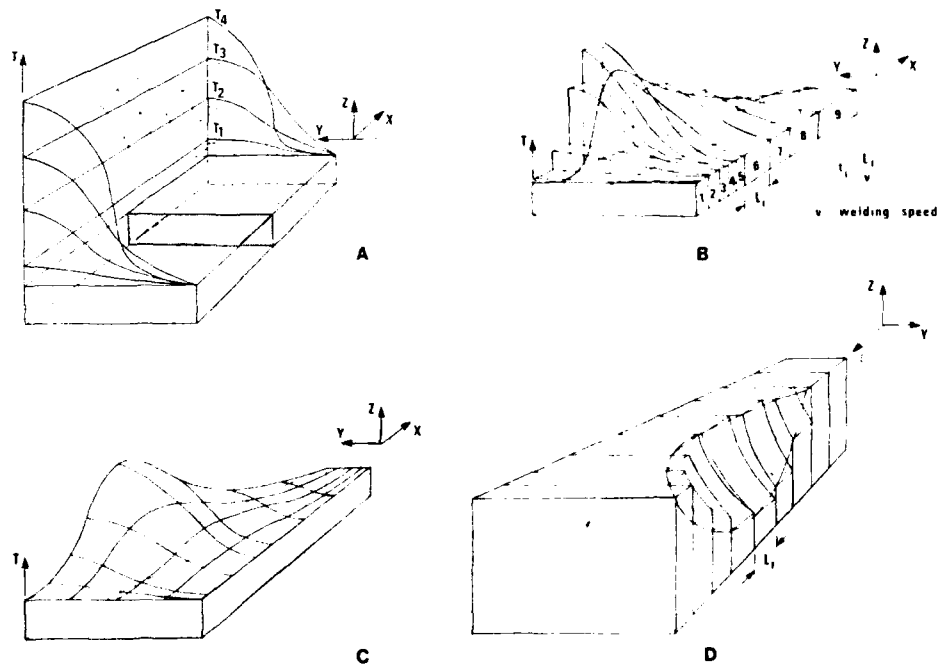


Figure 12. (A) For the cross-sectional model, the temperature distribution on the top of the plate is shown at several instants in time, (B) another way of plotting the temperature distributions on a series of slices to show time dependence, (C) the surface in (B) has been "smoothed" to resemble a steady-state solution: note no heat is allowed to flow in the z direction by the cross-sectional model, (D) approximate 3D steady state FZ boundary obtained from the cross-sectional model.

If it is assumed that $\partial T / \partial x = 0$ (see Figs 5 and 8) then every line parallel to x is an isotherm. Physically this is a reasonable approximation for a strip heat source such as a sheet electron, laser beam or a strip electrode in resistance welding. Even with wire electrode welds where the isotherms approximate distorted ellipsoids and the lines of constant x are clearly not isotherms, this model often predicts the thermal history of points with surprising accuracy for points sufficiently far from the heat source (Fig. 13). The reason is that when isotherms are sufficiently elliptical most of the heat flows perpendicular to the major axis of the ellipse. In fact, a one dimensional model that assumes $\partial T / \partial x = 0$ and $\partial T / \partial z = 0$ often predicts the thermal history of a weld with considerable accuracy for points sufficiently far from the heat source. The accuracy of the cross-sectional model increases as the welding speed increases, the thermal diffusivity decreases, and locations farther from the heat source are considered. As these conditions are relaxed, the error in the model grows as the gradient $\partial T / \partial x$ increases and more heat flows in the x direction. Andersson²⁴ attempted to assess this effect by comparing the analytic solutions for a one and two dimensional heat flow problem. He argued that the results gave a qualitative estimate of the error that should be expected in the cross-sectional approximation to three dimensional reality. The authors have determined the error directly by comparing results from 3D, in plane and cross sectional models.

It has been shown that the cross-sectional model is quite accurate for high speed production welds in steel¹⁹, and useful but subject to significant errors in high speed aluminium welds²⁵. However, in low speed aluminium welds²⁵ or deep penetration electron beam (EB) welds²⁶ the predicted FZ shapes are grossly in error (Fig. 10). At lower temperatures and greater distances from the heat source the model may still be considered acceptable. However, it cannot be used to analyze run on or run off effects.

Conceptually, this model is rather subtle. For the double ellipsoidal heat source model, the power density distribution is calculated on the intersection of the reference plane and the heat source. This power density distribution is then assumed to apply to a cross sectional slice in which the heat flow is analyzed. The reference plane and the slice are different mathematical entities and should be clearly distinguished.

The cross-sectional analysis can be related to a 3D steady state analysis by mapping the cross sectional temperatures, $T(x, y, t)$, onto a 3D steady state field, $T(x, y, \xi)$, where $\xi = x_0 - vt$, x_0 is the location of the arc at time zero and v is the arc speed in the direction x (Fig. 5 and 12). This clearly illustrates the distinction between the reference plane and the cross sectional slice. Thus the cross-sectional analysis is equivalent to a 3D steady state analysis in which heat flow is constrained to the reference plane; i.e., $\partial T / \partial x = 0$. Clearly, coding a 3D FEM formulation for 3D steady state nonlinear heat transfer is expected to be both more accurate and computationally more efficient than the cross sectional model. The reasons are that the heat flow need not be constrained to the reference plane and a 3D steady state problem is expected to require less computing than the 2D transient problem. However, the coding is non trivial and the resulting equation set, $K T = b$, is asymmetric. When it is coded, the authors expect it will make the cross-sectional model obsolete. Neither the cross-sectional nor 3D steady state analysis shed any light on transient effects, such as weld starts or stops. Both are only applicable to infinite prismatic geometries; i.e., geometries that could be extruded. The arc must move in the axial direction only. To deal with transient effects, an in plane or 3D transient analysis is necessary. For these reasons, the authors have focussed their attention on the 3D transient formulation and neglected the 3D steady state analysis.

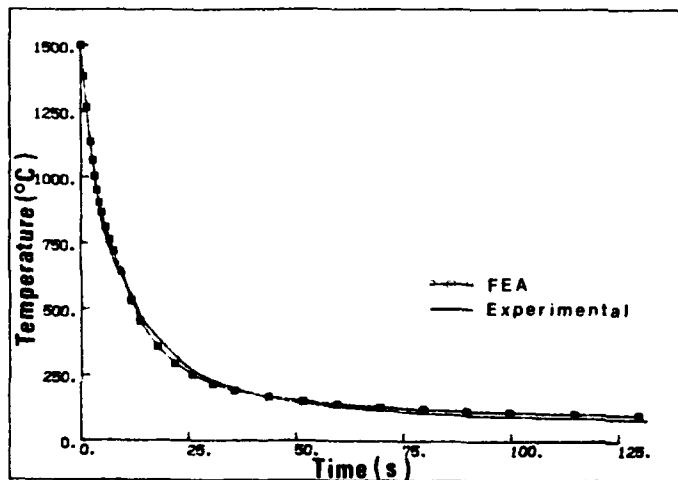


Figure 13. Centreline ($y = 0$, Figure 5) cooling curves: (A) experimental bead-on-plate weld (see Figure 8), $V = 30$ volts, $I = 265$ amps, $v = 3.81$ mm/s, g (thickness) = 38 mm, $T_0 = 20.5$ C (B) FEA computed: ellipsoid parameters (see Figure 8) $a_1 = 9$ mm, $a_2 = 16$ mm, $b = 6$ mm, $c = 6$ mm, thermal properties see Figures 6 and 7, combined radiation - convection surface heat transfer equation $h = 0.00241 \epsilon T^{1.61}$ W/m²C (Vinokurov¹³), arc efficiency $\eta = 0.8$ (shielded metal arc process).

2.4.2 Two Dimensional In-plane Model

If it is assumed that $\partial T/\partial z = 0$ for a weld moving in the x direction, where z is the through thickness direction, a two dimensional in-plane model results (Fig. 14). This model is accurate for full penetration EB welds in vacuo where every line parallel to z is an isotherm (Fig. 14B). The error in the model grows as $\partial T/\partial z$ grows and more heat flows in the z direction. In most arc welds this model does not predict the FZ shape or size accurately. However, in some sense it projects or averages the three dimensional FZ onto the $x - y$ plane and provides an estimate of the FZ size and shape. In sufficiently thin sheets or plates it does provide useful data for points at some distance from the weld pool (Fig. 15). It permits variations in the geometry of the $x - y$ plane such as that found in the Houldcroft test specimen to be analyzed accurately and economically. More importantly the significant problem of weld starts and stops, of which repair welds and run-on and run-off welds are examples, can be analyzed (Fig. 14).

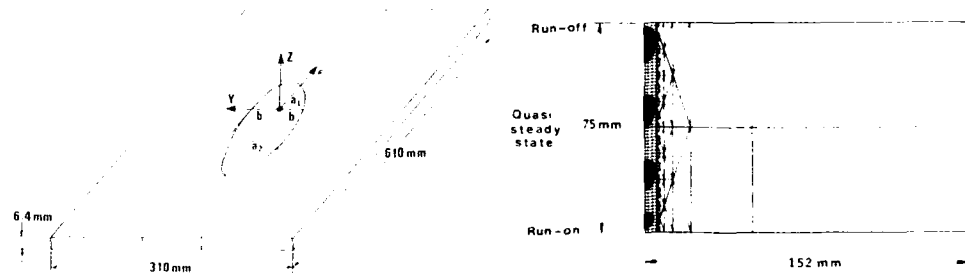


Figure 14. In-plane FEA of a thin plate ($t = 6.4 \text{ mm}$) aluminum (Al 7003) weld showing how the weld pool expands from run-on size to the quasi-stationary state and expands again at run-off; welding process: gas metal arc weld (GMAW): $V = 23.5 \text{ volts}$, $I = 285 \text{ amps}$, $v = 21.5 \text{ mm/s}$, $T_0 = 20.5 \text{ C}$; ellipsoid parameters $a_1 = 3 \text{ mm}$, $a_2 = 9 \text{ mm}$, $b = 3 \text{ mm}$; thermal properties: temperature sensitive thermal conductivity and heat capacity taken from the data of Touloukian [36], emissivity $\epsilon = 0.2$ [87], and convection coefficient $h = 12 \text{ W/m}^2\text{C}$ [24].

2.4.3 Three Dimensional Model

A full three dimensional model with a sufficiently fine mesh can model the heat flow as accurately as errors in the material properties, geometry, heat input, convection and radiation parameters permit. By repeating the analysis with various estimates of the data, error bounds for the computed temperatures can be estimated. The reason that three dimensional analyses have not been standard procedure for the thermal analysis of welds is simply that costs have not been affordable. Chapman [27] clearly documented the trend that computing hardware costs fall tenfold and the efficiency of numerical methods increases tenfold for a hundredfold fall in computing costs every seven years. The authors have demonstrated that a three dimensional analysis of a weld is now possible (Fig. 15). It is quite likely that 3D analysis will become standard practise by 1990.

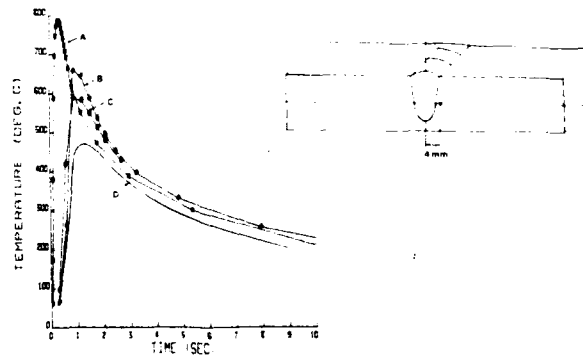


Figure 15. FEA analysis of an aluminum weld: (A) cross sectional model, (B) in plane model, (C) full three-dimensional model, (D) experimentally measured time-temperature curve at 4 mm, mid-plane position; GMAW process: $V = 23.5 \text{ volts}$, $I = 285 \text{ amps}$, welding speed $v = 21.5 \text{ mm/s}$, $T_0 = 21 \text{ C}$; thermal conductivity taken from Touloukian [36], emissivity $\epsilon = 0.2$ [87], convection coefficient $h = 12 \text{ W/m}^2\text{C}$ [24]; cross-sectional and three-dimensional ellipsoid parameters: $a_1 = 3 \text{ mm}$, $a_2 = 9 \text{ mm}$, $b = 3 \text{ mm}$, $c = 4 \text{ mm}$; inplane ellipse parameters $a_1 = 3 \text{ mm}$, $a_2 = 9 \text{ mm}$, $b = 3 \text{ mm}$.

The cost can be minimized by utilizing three dimensional elements near the heat source where three dimensional effects occur and a two dimensional in-plane approximation in regions farther from the heat source (Fig. 16). The transition from the three to two dimensional model must be performed properly. This is easily accomplished by applying sectorial symmetry to the transition nodes '28'.

In the two dimensional region the through thickness temperature gradient due to convection or radiation is ignored of course. A cross-sectional analysis can be used to estimate the error and even more importantly identify the region requiring a three dimensional mesh.

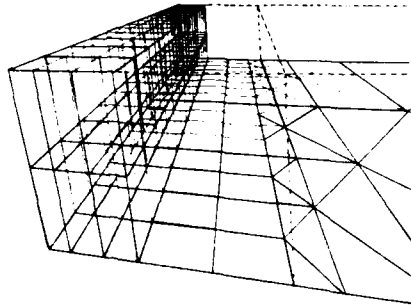


Figure 16. A representation of a three dimensional mesh graded to a two dimensional mesh where the through thickness heat flow becomes small. The dashed lines represent the physical dimensions of the work-piece represented by the 2D mesh.

2.4.4 Spatial Discretization Requirements

How fine must the finite element mesh be? How should the mesh be graded to achieve the desired accuracy while minimizing the cost in both mesh preparation and computing? It is cheap to prepare a very fine mesh that gives accurate results but this would produce very high computing costs. It is more difficult to prepare a carefully graded mesh to achieve the desired accuracy with low computing costs. How to prepare meshes that satisfy both criteria is a question that will not receive a definitive answer for some years. The work of Kela, Voelcker, and Goldak '29 and Sheperd and Law '30 on fully automatic mesh generation lead this field.

However, some guidelines can be offered. The mesh must be sufficiently fine to model the heat source with adequate accuracy. Specifically the Gaussian ellipsoidal model requires approximately four quadratic elements along each axis to capture the inflexion of the Gaussian distribution. In Fig. 17, a Gaussian distribution is approximated with 4, 8 and 30 quadratic elements across the function. Four elements provide a crude approximation and eight elements increase the accuracy considerably. With cubic elements, only two elements along an axis of the ellipsoid may be acceptable. Certainly one quartic element is much more accurate than two quadratic elements.

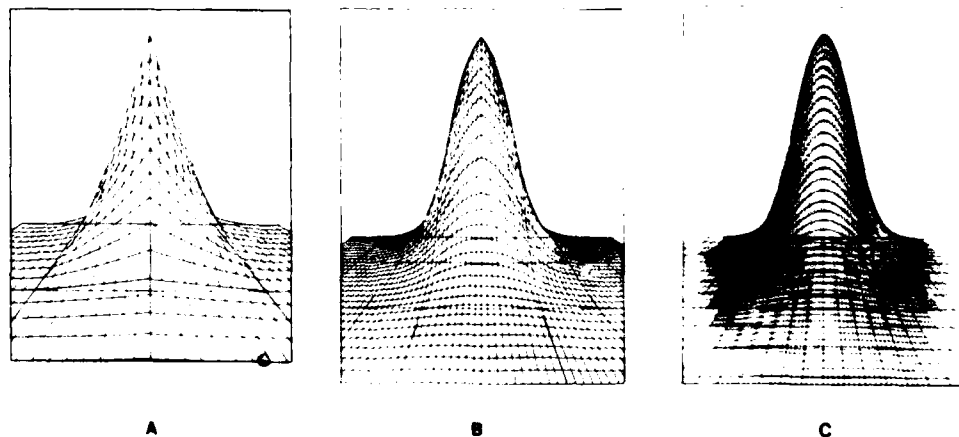


Figure 17. A pictorial representation of the double ellipsoid energy input distribution (cross sectional) using: (A) two elements, (B) four elements, (C) many elements along the y axis (Figure 5). Note four elements representing the double ellipsoid along any axis is considered sufficient.

2.4.5 Time Discretization Requirements

The use of two point integration in the time domain [31] implies linear interpolation. How long can the time steps be before the error becomes unacceptable? Fig. 18 shows that approximately ten to twenty time steps are needed for the ellipsoidal heat source to cross the reference plane in the cross-sectional model. In the in-plane and three dimensional models, the heat source may move approximately one half of a weld pool length in one time step.

It is important for the analyst to recognize the effect of interaction between the integration scheme; explicit ($\theta = 0$), Crank-Nicholson ($\theta = 0.5$), Galerkin ($\theta = 2/3$), and implicit ($\theta = 1.0$), and any prescribed thermal loads, fluxes or power densities. The prescribed thermal loads, fluxes, and power densities are all converted to an equivalent nodal thermal load specified at the beginning of each time step and another at the end of each time step. The time integration scheme linearly interpolates these to the θ point. Several examples are shown in Fig. 18. Any convective or radiative loads are computed at the θ temperature and added to the applied thermal load. This load can be considered to be applied for the full time increment.

Hughes [32] proved that the conductivity and capacitance matrices must be computed at the θ temperature in a nonlinear FEM analysis. Donea [33] showed that $\theta = 2/3$ is more accurate than $\theta = 0.5$ when high frequency components are present in the loads even though the respective convergence rates are linear and quadratic. The work of Pammer [34] should be consulted for a criterion for determining element size to accurately analyze rapid transients in surface temperatures.

2.4.6 Non-Linear Material Properties

The basic reference on high temperature heat transfer by Rohsenow [35] deals with measurement techniques in detail. References [36,37] summarize much of the published high temperature data. Notwithstanding the above, the greatest limitation to computational weld mechanics is obtaining accurate temperature dependent material properties and models to predict properties as a function of history; i.e., temperature, time, strain, etc. In general, properties depend on chemical composition, microstructure, and dislocation density. Therefore they are dependent on the thermal history primarily through microstructural effects such as precipitation, transformations, annealing, recovery, etc. They are dependent on plastic strain history primarily through the density distribution of dislocations and vacancies. The analyst who fails to find the property data required must either have the data measured or use some estimate. The sensitivity of the results to the data can be checked by repeating the analysis with lower limit, best, and upper limit estimates of the data. However, if the analysis involves several properties, many analyses would be required to test all combinations. In this situation the analyst should consult an expert on the statistical design of experiments.

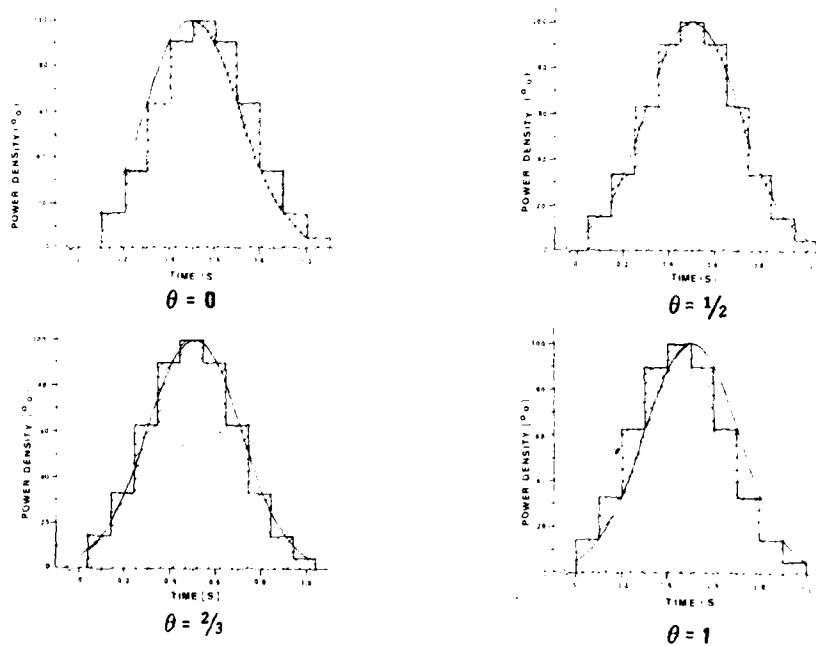


Figure 18. Variation of power density as a function of time as the heat source passes the reference plane in a cross-sectional FEA. The Gaussian energy distribution of a conical heat source as shown in Figure 10 is represented in this diagram. It is clear that 10 to 20 time steps are required to integrate the distribution adequately.

2.4.7 Thermal Conductivity

Most thermal analyses of welds over the past forty years have assumed that the thermal properties were constant. In fact Rosenthal's analysis cannot be extended to include nonlinear properties because the final transformation he applies is only valid for a linear equation. The thermal conductivity and volumetric specific heat of a 0.23 % C steel are plotted as a function of temperature in Fig. 6 and 7 [37]. The temperature dependence is clearly substantial. An example of the error caused by assuming a temperature independent thermal conductivity and specific heat is shown in Fig. 19. The values of constant thermal conductivity and specific heat chosen are those often recommended by advocates of Rosenthal's analytic solution. The error is clearly significant. Actually the value of the thermal conductivity is frequently chosen to obtain the best agreement with welding experiments. For steels, the value of 25 W/m C is usually proposed for 3D heat flow and the value of 41 W/m C for 2D heat flow [38]. Clearly these fictitious thermal conductivities are more correctly called undetermined coefficients that are used to match the equation to experimental data. Since the error in the flux for a given temperature gradient is directly proportional to the error in the thermal conductivity, it is desirable to use the best available data.

The cost of incorporating temperature dependent thermal conductivity in FEM codes is trivial and it should be used whenever the data is available. However, caution is necessary whenever the thermal properties are history dependent in addition to temperature dependent. The investigation of Farnia and Beck [39] is an important contribution in this area. They have shown that the thermal conductivity of aluminum 2024-T351 depends on the volume of precipitates. It appears that their methodology can be applied to other materials and other properties. As it now stands the primary limitation is that it only applies to plates in the solution treated condition and deals only with precipitation. Nevertheless, this is a significant advance.

2.4.8 Heat Capacity and Latent Heats

The heat capacity, $c_p(T)$, and enthalpy, $H(T)$ are related by:

$$H(T) = \int_{T_0}^T c_p(T) dT \quad (9)$$

The temperature dependence of the heat capacity is usually incorporated into a FEM program by evaluating the capacitance matrix at the θ temperature [40]. This value of the heat capacity then applies for the entire duration of the time increment. In cases where the heat capacity varies rapidly as in ferrite near 700 C (Fig. 6), this can cause a significant error in a large time step. An alternative method uses an average value computed from the enthalpy, H , $c_p = (H_2 - H_1) / (T_2 - T_1)$ where the subscripts indicate that the enthalpy has been evaluated at the beginning and end of the time step. When $(T_2 - T_1) \rightarrow 0$, care must be taken to avoid this technique and simply use the temperature dependent value of $c_p(T)$. Of course, small time steps should be considered to achieve the desired accuracy.

Transformations, such as melting and the ferrite-austenite transformation in steel are more difficult to analyze rigorously. The transformation surface; e.g. the liquid-solid boundary has a discontinuity in the thermal gradient which moves. During melting the latent heat is absorbed. During freezing the latent heat is released. Since this latent heat in steel is $2.1 \times 10^9 \text{ J/m}^3$ and the specific heat is $4.5 \times 10^6 \text{ J/m}^3\text{C}$, the transformation absorbs as much heat as a temperature change of 470 C. Solid-solid transformations have less effect on the temperature field but because they can affect the cooling rate substantially during transformation (Fig. 20), the microstructure can be altered significantly.

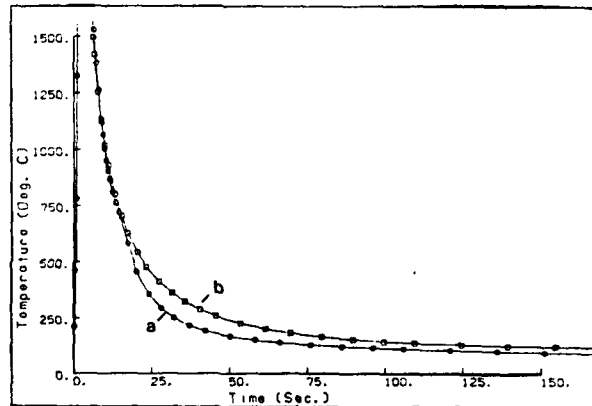


Figure 19. Effect of thermal properties on the FEA computed weld cooling curve of a steel weld: (A) variable thermal properties (Figures 6 and 7), (B) constant thermal properties $k = 25 \text{ W/mC}$, $C_p = 6 \times 10^6 \text{ J/m}^3\text{C}$. Weld parameters described in Figures 8 and 13.

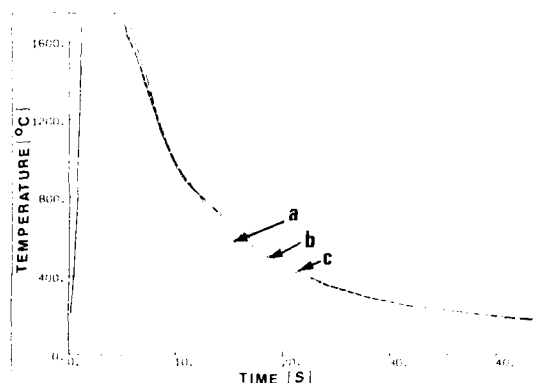


Figure 20. The time temperature centerline thermal history for a steel weld (see Figure 8 for welding conditions) -- without latent heats of fusion and transformation (curve a); with latent heat of fusion included (curve b); and with both latent heat of fusion and transformation included (curve c). Note the substantial effect due to the latent heats of transformation.

The simplest method of including the latent heat is to compute the specific heat from the enthalpy as discussed above. A better way is contained in the presentation of Rolphe and Bathe [41]. Whenever a nodal temperature crosses a transformation temperature, this is noted together with whether it is cooling or heating. A volume or mass is associated with each node and the corresponding heat of transformation, J , is computed. If a node transforms, the temperature is reset to the transformation temperature and the heat subtracted from the heat of transformation until it is reduced to zero. At that time the node is set free. In all other respects, it is a standard FEM analysis. The algorithm is simple, relatively easy to code, and efficient.

The most accurate method of dealing with latent heats of transformation have been developed by Blanchard and Fremont for analyzing frozen soils where the latent heat is the dominant effect and accuracy is critical [42]. However, this algorithm, which can compute two phase regions or mushy zones, is more complex.

2.4.9 Precipitation and Solution Effects

Although the effect of precipitates on mechanical properties is well understood and documented, relatively little data exists for the effect of precipitates on thermal properties. The thermal conductivity in 2024-T351 is a function of the volume of precipitates. In aluminum 2024 alloys, the thermal conductivity is lowest when the copper is in solid solution and highest when the copper is in the precipitate particles. Arajc and Beck [43] have presented equations for computing the thermal conductivity of aluminum 2024-T351 during a thermal cycle. They proposed the following equations:

$$k(T, t) = k_0(T) + k_m(T) \cdot \frac{\eta(T, t)}{\eta(T)} \quad (10)$$

where

$$\eta_m(T) = 8.68 \times 10^{-2} + 3.59 \times 10^{-3}T \quad (11)$$

$$k_m(T) = 148.2 + 0.115T \quad (12)$$

$$k_0(T) = 73.2 + 0.3725T \quad (13)$$

$$\frac{\partial \eta(T, t)}{\partial t} = \frac{1}{r(T)} [\eta_m(T) - \eta(T, t)] \quad \text{if } \eta_m(T) > \eta(T, t) \quad (14)$$

$$r(T) = \exp(-31.93 + 15.7 \frac{1000}{T + 273}) \quad (15)$$

It is a straight forward matter to incorporate these data and behavior into a FEA program to predict the volume fraction of precipitate and the precipitation dependent thermal conductivity. There is a clear need to extend this method to begin with any microstructure and to account for the solution or coarsening of precipitates.

Ashby and Easterling [44,45] predicted austenite grain growth in the HAZ of Nb and V microalloyed steels due to the dissolution of NbC and VC. Ion and Easterling [45] have extended this work to TiC precipitates. Here the austenite grain growth in the HAZ was due to Ostwald ripening of TiC. Both papers predicted only the final austenite grain size. Although their model does not predict the grain size or volume fractions of precipitate as a function of time and temperature, it is an important step towards this goal. At this point in time this work has not yet been extended to thermal properties. However, predicting microstructural changes that occur is an important first step and it is not difficult to imagine that algorithms for computing thermal conductivity similar to the Arajc/Beck approach will appear in the future.

2.4.10 Convection and Radiation

Given the heat transfer coefficient, h , convective heat transfer is easily included in the FEM analysis. Newton's equation for cooling, which may be taken as the definition of the heat transfer coefficient is $q = h(T - T_{amb})$. The value of h must be measured experimentally or taken from handbooks which are based on experiment. Based on experimental data, Vinokurov suggests the following equation for welding hot rolled steel plates [3]. This equation includes both radiation and convection effects:

$$h = 24.1 \times 10^{-4} \epsilon T^{1.61} \quad (W/m^2 C) \quad (16)$$

Convection and radiation have little effect near the heat source where temperature gradients are steep and heat flow is conduction dominated. Far from the heat source, heat flow can be convection dominated if the workpiece and jiggling are not so large that the temperature rise in the workpiece is negligible.

In radiative heat transfer the emissivity must be measured experimentally. In exceptional situations, it may be desirable to take into account view factors. The analysis of an electron beam cavity is an example. If a laser beam interacts with its plume, a participating media should be considered. Neither view factors nor participating media are considered in this paper.

2.4.11 Errors in the Computed and Measured Temperature Fields

Sufficient data now exists to state that temperatures, $T(x, y, z, t)$, can be computed accurately by FEA for welds in steels (Fig. 13). However, more research is needed to establish appropriate models and their accuracy for welds in aluminum alloys where precipitation effects are significant. For example, it is not clear whether the computed or measured temperatures, shown in Fig. 15, are more accurate. In a discussion of errors in $T(x, y, z, t)$, three distinct welds should be recognized. First, the weld described by the experimental data; the weld computed by FEA; and the real weld. Both the experimental data and the FEA results are in error. The issue is to determine the sources of the error. In the FEA the uncertainty in the efficiency of the gas metal arc welding (GMAW) process is high. In the analysis shown in Figs. 14 and 15 it was taken as 65 %. The temperatures were measured with thermocouples pressed into a hole. An error of 0.5 mm in positioning the thermocouple would have caused an error of 25 C in peak temperature in this particular situation. Weld data must be measured more accurately and more research done on computer models in order to accurately compute the temperatures in welding aluminum.

2.4.12 Difficult Issues

The difficult issues in welding heat transfer research that are currently being attacked and show some promise of being solved include moving boundaries with two phase regions. The work of Blanchard and Fremont [42] is particularly significant in this regard. The work of Oreper [1] on stirring in weld pools leads to the possibility of analyzing weld processes more accurately. Computing the position of the free surface of the weld pool has not been attempted. Mass transfer problems such as the welding of dissimilar metals or cladding stainless steel on structural steel involves the change of composition of regions which welders call dilution. Very little is known about numerical modelling this problem. In addition, predicting microstructures from the thermal history of a weld is a problem requiring considerable attention. The work of Coon [46] is a particularly promising solution to this difficult problem.

Most of these difficult issues require the simultaneous solution of more than one differential equation. This is an area of intense interest in finite element analysis research and progress is expected to be rapid.

3. MECHANICS — Displacement, Strain and Stress

The following is an attempt to explain the basic concepts of material behavior that give rise to displacements, strains and stresses. In a general way, there are three theories of elastic behavior - elasticity, hyperelasticity and hypoelasticity. A fundamental assumption of elasticity theory is that a natural state exists that is in thermodynamic equilibrium. If a body is cut into tiny cubes which are separated, the stress and strain in each cube should be zero. If the cubes are reassembled in their original position and shape, the original stress and strain values should be obtained no matter how the cubes were chosen or the order in which they were assembled.

The fundamental assumption of hyperelasticity is that the strain energy density is an analytic function of strain and temperature. In simple terms, hyperelasticity assumes reversible thermodynamics. Hyperelasticity is most successful in the analysis of substances like rubber.

Hypoelasticity assumes irreversible thermodynamics. In particular, the stress and strain at any instant of time may depend on the previous stress - strain values; i.e., the history. This is often referred to as rate theory. Since the stress and strain in a welded structure obviously depends on the welding procedure, stress relief, etc., only hypoelasticity is capable of analyzing welds. From this point onward, the term elastic will be used to mean hypoelastic in this presentation.

3.1 Viscoelasticity

Materials behave elastically only for sufficiently small strains. For larger strains new phenomena appear. In some cases they can be characterized by the simple models shown in Fig. 21a.

The essential feature of all of these viscoelastic models is that if a unit load is applied, the displacement or strain varies with time as shown in Fig. 21b. When the load is removed, the displacement varies as shown in Fig. 21c. Note that for sufficiently long times, the displacement becomes constant; i.e., an asymptotic solution exists that does not depend on time.

3.2 Viscoplasticity and Plasticity

The simple models shown in Fig. 22 illustrate the characteristic behaviour of plasticity and viscoplasticity. Specifically, the models behave elastically until the critical load (stress) on the slider is attained. In plasticity, the slider is a simple constraint that prevents the stress from exceeding the critical stress. Note that there is no time dependent behaviour explicitly incorporated into the plasticity model. However, the spring constant (Young's Modulus) and critical slider load (yield strength) could be dependent on time due to a variation in temperature with time.

Viscoplasticity allows stresses to exceed the yield strength by incorporating a dash pot in which the velocity (strain rate) is proportional to the over stress; i.e., the distance the stress is from the yield strength. The proportionality factor is called the fluidity which is the reciprocal of the viscosity.

The question is which models are best for the analysis of welds? Only plasticity and viscoplasticity capture the yield point behaviour of metals. Argyris [47] has argued that the two formulations are equivalent if performed properly. However, neither exhibits secondary creep. Therefore, it appears that ultimately constitutive models must be developed that incorporate viscoelasticity with plasticity or viscoplasticity. However, Zener's [49] view of a spectrum a viscoelastic phenomena is nearer the truth. Each phenomena, such as the movement of vacancies, dislocations, grain boundaries, etc., is characterized by a set of parameters which include a time constant. Developing algorithms for such models would enable microstructural models to be incorporated into computational weld mechanics. While this is the direction in which research is moving, it will be sometime before it is achieved. In plasticity, the time constant can be considered to be zero. In viscoplasticity, the time constant is simply part of a numerical technique to solve the associated equations and usually is not intended to capture creep-like behavior.

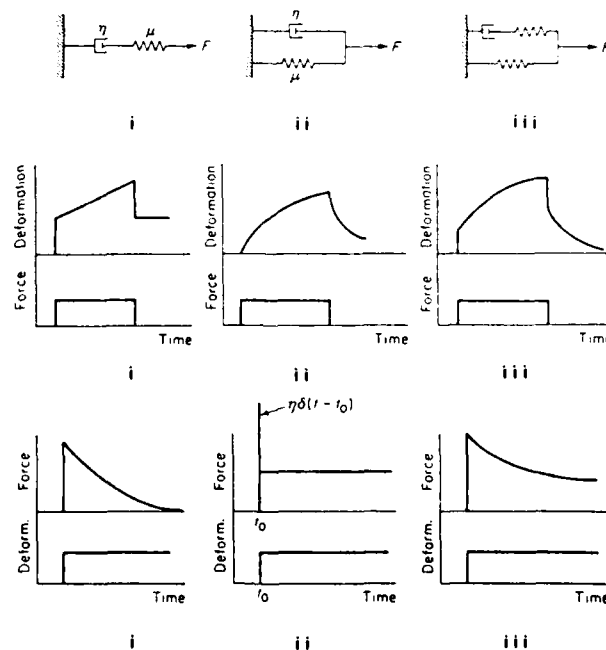


Figure 21. (A) Models of linear viscoelasticity: (i) Maxwell, (ii) Voigt, (iii) standard linear solid. (B) Creep function of: (i) Maxwell, (ii) Voigt, (iii) standard linear solid. A negative phase is superimposed at the time of unloading. (C) Relaxation function, of (i) Maxwell, (ii) Voigt, (iii) standard linear solid.

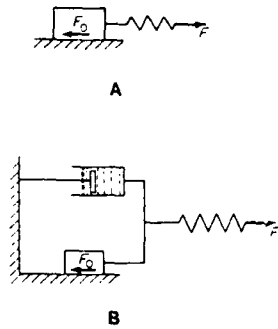


Figure 22. (A) Prandtl body corresponds to elastic plus plastic flow. (B) An example of a viscoplastic model.

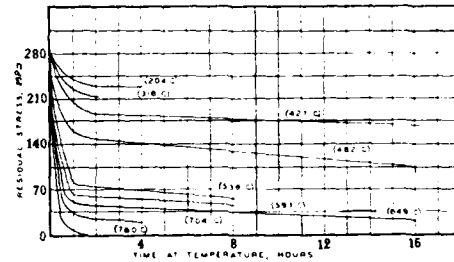


Figure 23. Influence of temperature and time on relieving stress. This steel contained 0.21% carbon and 1.44% manganese. The tensile properties were: 500 MPa UTS, 250 MPa proportional limit, 36% elongation, and 73% reduction of area. Stress is relieved a small amount at 205 C, and is completely removed after some time at 760 C. Stress is reduced first by the recovery phenomenon, and then by permanent yielding. The latter is caused first by the reduction of yield strength at elevated temperature, and second by creep under the prolonged loading at elevated temperature.

In the authors' opinion, viscoelastic effects are usually secondary in weld mechanics. Fig. 23 shows stress versus time for stress relieving at various temperatures. The sharp initial drop in stress, due to the temperature dependent yield strength, is captured by plasticity and viscoplasticity models. The slow decline in stress at longer times, which is due to secondary creep, would be modelled best by viscoelasticity. In this example, the time at temperature is longer than in most welding situations. Since the error in the plasticity model is small even in this case, the authors argue that a plasticity or viscoplasticity theory should be used to analyze most weld mechanics problems. As expertise develops, viscoelasticity should be added along the lines discussed above. This is referred to as unified creep plasticity models. Krieg [48] has shown that several of these models have the same basic form. In all of these models experimental measurements of the parameters is slow and expensive and the resulting equations are stiff which leads to numerical problems in implementing them in finite element or other numerical codes.

3.3 Thermo-Elasto-Plasticity Theory

In each time increment, Δt , at each point in the material the temperature increment, ΔT , is first computed. Then the total strain increment, $d\epsilon_{ij}^{Tot}$, is predicted. It is decomposed into an elastic strain increment, $d\epsilon_{ij}^{Elast}$, a thermal strain increment, $d\epsilon_{ij}^{Therm}$, and a plastic strain increment, $d\epsilon_{ij}^{Plas}$. Next, the associated stress increment, $d\sigma_{ij}$, must be predicted. If plastic deformation occurs, the plastic strain increment, $d\epsilon_{ij}^{Plas}$, must be predicted. The stress increment must satisfy the yield criterion. This is called the consistency condition. It is not always recognized that in triaxial stress states, individual stress components such as σ_{xx} can be far greater than the uniaxial yield stress without causing plastic deformation. The obvious example is that no matter how great the hydrostatic pressure is, no plastic strain will occur in metals.

In accordance with most experimental data, we assume metals obey the von Mises yield criteria. It states that attainable stress states are constrained to lie within a cylinder in stress space or, equivalently, a sphere in deviatoric stress space. Strain hardening that changes the radius of the sphere while holding its centre fixed is called isotropic hardening. Strain hardening that maintains the radius fixed but moves the centre of the sphere is called kinematic hardening. Zeigler [50] showed the centre must move in the direction normal to the yield function evaluated at the location of the stress state on the yield surface. Isotropic - kinematic hardening permits both the position of the centre and the radius to change with strain hardening.

In addition to strain hardening, the yield function is a function of temperature. Usually the radius decreases at higher temperatures. However, metallurgical phenomena such as precipitation hardening can cause hardening as the temperature is increased. In passing through a phase change such as the austenite - ferrite transformation in steel, the yield strength may be very low. Therefore the yield strength vs. temperature data shown in Fig. 24 should be considered only a first approximation in most situations. Experimental measurements of the yield strength for the temperature and strain history of the problem would always be preferred.

The plastic strain increment can be computed in four ways; the exact, radial return, secant, and tangential predictor - radial corrector algorithms [51,52]. Currently the radial return algorithm is recommended because it becomes exact for both very large and very small strain increments and it is computationally efficient. For large increments the exact method, which requires roughly twice the computational effort, may be more efficient. The basic step in all of these methods is to project the plastic component of the trial strain increment onto the normal to the yield surface.

Temperature dependent effects due to the rate of change in Young's modulus, Poisson's ratio and the coefficient of thermal expansion with temperature should be considered. Most formulations ignore these terms which can be significant. One must distinguish carefully between the instantaneous coefficient of thermal expansion, $\hat{\alpha}$, usually used in thermodynamic theory and α the coefficient of thermal expansion reported in most books on high temperature properties. These are defined as:

$$\hat{\alpha} = \frac{1}{L} \frac{\partial L}{\partial T} \quad \alpha = \frac{1}{T - T^r} \int_{T^r}^T \hat{\alpha} dT \quad (17)$$

where T^r is the reference temperature.

Details of thermo-elastic-plasticity theory are given by one of the authors, Patel [53]. The formulation is tested by analyzing a uniaxial tensile test with varying temperature and cyclic loading. This simple test problem exercises many aspects of the phenomena.

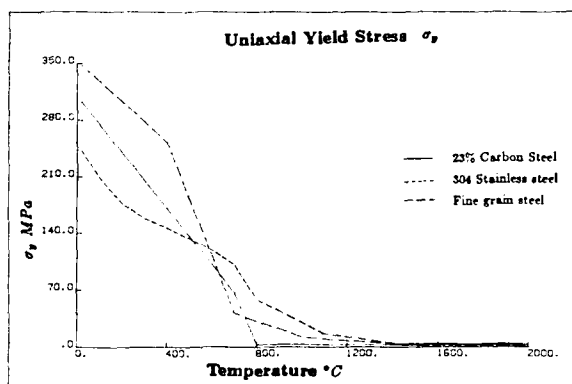


Figure 24. Temperature dependence of uniaxial yield stress for a low carbon steel (0.23 w/o), stainless (AISI 304) and microalloy fine grained steel.

3.4 Uncoupling Heat Transfer From Stress-Strain Analysis

The first point to recognize is that if the work due to plastic deformation in a fusion welding process is converted to heat, the change in the temperature field would be negligible. This would not be true in a processes such as rolling or extrusion where the temperature changes due to plastic work can be hundreds of degrees [47]. Then the heat transfer analysis and stress - strain analysis are strongly coupled. In effect they must be performed simultaneously because the temperature depends on the strain and the strain depends on the temperature. The problem is somewhat simpler in welding because the temperature does not depend on strain. The heat transfer analysis can be performed first, and then a stress-strain analysis can be performed.

3.5 Kinematic Models for Stress or Strain

3.5.1 Plane Strain Assumption

Most thermal stress analyses of welds performed to date have assumed plane strain conditions in order to reduce the complexity of the theory or the computational cost. The experiments of Chihoski [54 - 56] and the FEA of Patel [53] clearly show that the assumption of plane strain is not valid. Hence the question is how serious is the error in a plane strain model. The answer depends upon which data are of interest. In edge welds in rectangular bars, the error in camber is small. However, near the molten pool, the error in assuming plane strain conditions appears to be large [53]. Therefore, it is probable that the plane strain assumption must be rejected and a full 3D stress - strain analysis performed in order to analyze the formation of hot cracking and other defects that occur at high temperatures. In any case, the plane strain assumptions could only be valid for prismatic geometries; i.e., sections that can be imagined as having been extruded, and in which the weld is in the direction of extrusion. At best, the plane strain model could analyze only a small fraction of industrial welds. However, plane strain analysis has been valuable because it has facilitated research in weld mechanics which would have been delayed had 3D analysis been required.

3.5.2 Axisymmetry

Axisymmetry assumes that no parameters depend upon the angle, θ , in cylindrical coordinates, (r, z, θ) . Therefore the weld heat source should resemble a ring burner. In most welds this is obviously not appropriate. However, Marcal and Hibbitt [58] used it to analyze welds but achieved relatively poor accuracy.

4. THERMO-ELASTO-PLASTIC ANALYSIS OF WELDS

The thermal strain and stress caused by a change in the temperature field is complex. Consider a unit cube that undergoes a change in temperature ΔT . If the cube is unrestrained, the strain is $\epsilon_{ij} = \alpha \Delta T$ and the stress is $\sigma_{ij} = 0$. If the cube is fully restrained such that $\epsilon_{ij} = 0$, then the stress is $\sigma_{ij} = D\epsilon_{ij} = D\alpha\Delta T\delta_{ij}$.

If the cube is free to expand on the top and bottom faces but the four vertical faces are held fixed, the situation is more complex. If the stress exceeds the yield stress, plastic deformation will occur. In the above examples, the temperature is constant at any instant of time. In real welds, the temperature gradients are severe in some areas; parts of the weld are heating and expanding while other parts are cooling and contracting. Although it would be nice to explain this with simple intuitive examples such as those above; the complexity is such that it is best to simply state the fundamentals of the necessary theory and utilize computer programs to compute the stress and strain. The fundamental equations are:

1. A change in temperature, ΔT , causes a volumetric strain $\alpha\Delta T$.
2. At each point, the strain increment can be defined as

$$d\epsilon_{ij}^{Tot} = d\epsilon_{ij}^{Elast} + d\epsilon_{ij}^{Plas} + d\epsilon_{ij}^{Therm} \quad (18)$$

$$d\epsilon_{ij}^{Therm} = \alpha\Delta T\delta_{ij} \quad (19)$$

$$d\epsilon_{ij}^{Elast} = D_{ijkl}^{-1}d\sigma_{kl} \quad (20)$$

$$d\epsilon_{ij}^{Plas} = \lambda \frac{\partial F}{\partial \sigma_{ij}} \quad (21)$$

where λ is a nonnegative scalar.

3. The material is assumed to obey the isotropic - kinematic hardening hypothesis and the hardening parameters are assumed known.
4. The Young's modulus and Poisson's ratio are assumed to be temperature dependent.

4.1 The Liquid Pool

As the melting point is approached, Young's modulus and the yield strength approach zero. Since a small force will then produce large displacements, the stress analysis will fail at some temperature. To be precise, the governing mathematical equation changes from the equation of motion to the Navier-Stokes equation. The analysis must make this change or fail. Methods for analyzing the behavior of fluid in tanks and reservoir - dam earthquake response are well established. However, in these methods the Young's modulus of the solid does not approach zero gradually at the liquid - solid interface. It is large in the solid and zero in the liquid and the appropriate mathematical equations are applied in the liquid and solid regions.

In welding the technique usually adopted is simply to set temperatures that are above some cut-off temperature to the cutoff temperature. Patel [53] used a cut-off of 1200 C, Ueda [59] discarded all of the temperature - time curve except the cooling part of the thermal cycle below 800C. This technique appears to be adequate for predicting residual stress and strain. Clearly it would not be appropriate for a detailed analysis of hot cracking due to strain around the liquid pool.

4.2 Strain Hardening Effects

Ideally, the effective stress - effective strain data should be measured by performing a uniaxial tension - compression test with the temperature and strain rate history predicted by the FEA. Such a test would also incorporate microstructure effects accurately. The best strategy would be to perform a FEA with the best available stress - strain - temperature - strain rate data and then use the results of the FEA to run uniaxial tension - compression tests under the nearly identical conditions. This could be done for one point in each of the important zones in a weld; i.e., FZ, coarse grained HAZ, etc. Unfortunately, very little data on high temperature stress strain curves are available. Until better data are available, it will limit the accuracy of FEA analysis of welds.

4.3 Phase Transformations

Most analyses have ignored the effect of phase transformations on strain hardening. In carbon steel (AISI 1020), Patel [53] reset the effective plastic strain to zero at 700 C and 1200 C, to correspond to the austenite-ferrite transformation and the cutoff temperature, and reset the yield criterion to the origin. This can be viewed as removing most of the effects associated with reverse loading. However, a point in the HAZ that reaches a maximum temperature of 650 C would undergo reversed loading. For such points β , the fraction of isotropic hardening, and $1 - \beta$, the fraction of kinematic hardening, would be important. This is expected to be most significant in multipass welds. In austenitic stainless steel (AISI 304) welds Patel [53] found best agreement with experiments by using $\beta = 0.2$ and resetting the strain hardening at 1100 C. This is consistent with the metallurgy of 304L stainless steel. Here HAZ points with peak temperatures less than the cutoff temperature will undergo reversed loading. This is why kinematic hardening is more important in 304 stainless steel welds than in carbon steel welds.

The weld simulation tests of Jones and Alberry [60] are in this spirit. They heated specimens of 2CrMo, 9CrMo and AISI 316 steels to a peak temperature of 1320 C. They then held the length fixed and measured the uniaxial stress as the specimen cooled. The time - temperature cooling curve simulated that of the coarse grained HAZ of a weld. They also measured the strain, the transformation kinetics and the high temperature yield strength. This is a paper that deserves to be read carefully for its experimental techniques and results. However, the hypothesis for stress hardening and strain is not based on rigorous continuum mechanics. The more rigorous method for analyzing temperature dependent uniaxial tensile tests is given by Allen [61] and Patel [53].

In particular, Jones and Alberry observed directly that during an austenite - bainite transformation the stress falls to zero. During an austenite - martensite transformation, the stress becomes compressive. In part, this is because the volume change to martensite is greater.

The ferrite - austenite transformation in steel has a volume decrease of 1.16% at 910 C. Greenwood and Johnson [62] showed that in a tensile test with a small uniaxial stress, σ_{ij} , the plastic strain, ϵ_{ij} , in one cycle of heating and cooling through the transformation is:

$$\epsilon_{ij} = \frac{4\sigma_{ij}}{3E} \frac{dV}{V} \quad (22)$$

$$\epsilon_{ij} = 0.93 \times 10^{-13} \sigma_{ij} \quad (23)$$

where E is the Young's modulus and V is the volume. In a sense, the yield strength drops to zero during the transformation until the strain due to the transformation volume change is accommodated. At higher stress levels the plastic strain is greater.

It is hypothesized by the authors that the following numerical strategy would be desirable. The freezing index method of [42] should be used to specify the fraction ferrite transformed. Then this fraction of the volume change should be applied as an initial strain. The normal constitutive equations of each phase should be applied. Until the research is actually done, this remains a hypothesis.

Currently, most analysts ignore this effect entirely. Andersson [24] varied the coefficient of thermal expansion to accommodate the volume change. However, this misses the essential feature that a volumetric strain between two phases of different yield strength steers the plastic deformation into the weaker phase. Patel's [53] approach of setting the strain hardening to zero at the transformation assumes that a new phase is created with a low dislocation density. This is believed to be valid and important but is an entirely separate issue from the transformation strain.

4.4 Residual Stress Computations in Singlepass Welds

Ueda [57] was the first to compute the residual stress in a weld using FEA. The next attempt to compute the residual stress due to welding with FEA was made by Hibbitt and Marcal [58]. Their expertise in FEA is demonstrated by the fact that MARC, developed by Marcal and Hibbitt, and ABACUS, developed by Hibbitt, are the most highly regarded commercial programs for nonlinear FEA.

They recognized the need to compute the temperature field accurately. They emphasized the need to incorporate latent heats and to use a variable other than temperature to capture the discontinuity in the temperature gradient at the FZ boundary. This anticipates Blanchard and Fremont's [42] replacement of the temperature field with the freezing index. Their careful modelling of the addition of filler metal to the weld has not been repeated to date. However, their distribution of heat in the weld was primitive. Their assumption of axisymmetry for a 75mm diameter circular head on-disc weld is certainly suspect but the magnitude of the error has yet to be determined. From their data, the initial temperature would be 427 °C at the end of the weld. Since they did not compare the computed and experimentally measured temperatures, it is difficult to assess the accuracy of their computed temperature field.

Their stress analysis appears to have used an elastic perfectly plastic stress strain curve with temperature dependent yield point. Rates of properties appear to have been neglected. The paper does not present sufficient detail to reconstruct their theory in detail. It is possible that their assumption of axisymmetry could be the most serious source of error. The general pattern of the computed stresses did agree with experiment but the absolute values were often wrong by 500%. The other unusual feature of this paper was the use of high strength steel - HY80 and HY 130 150 where phase transformation affects can be substantial. The poor results of this analysis by eminently qualified experts in nonlinear FEM probably discouraged others from entering the field. It illustrates the danger of attempting too much too soon.

Following Hibbitt and Marcal [58], Andersson [24] was the next to attempt a rigorous FEM analysis of residual stresses. In this study of a single pass weld in HSLA steel plate, the best available temperature dependent data was used. Temperatures were computed by FEA with a 2D cross-sectional model. He used an enthalpy method to deal with latent heat effects. The arc was modelled as a constant surface flux. The stress analysis appears to be based on the correct thermo-elasto-plastic equations for hypoelasticity, with a von Mises yield criteria and isotropic hardening. Seventy load increments were used under plane strain. The agreement with experiment was excellent for the transverse stress but the error in the longitudinal stress was significant, particularly on the lower side of the plate. Andersson discussed the possibility that the error was due to assuming plane strain conditions or isotropic hardening. Although the paper is not entirely clear on this point, it appears a cut off temperature of 1250 C was applied to avoid the difficulties associated with a stress analysis of the liquid pool and the surrounding low strength material. He does not mention resetting the strain hardening at 800 C or 1250 C. Patel [53] found this to be an important source of error.

4.5 Residual Stress Computations in Multipass Welds

The work of Rybicki [64], who analyzed a thirty pass weld and Ueda [59] who analyzed a twenty pass weld are the most important papers on multipass welds reported to date. Rybicki et al [64] computed the residual stresses created by multipass girth welds in pipe. They analyzed AISI 304 steel pipes of 100 mm (4 in.) and 250mm (10 in) nominal diameter with four wall thickness - schedules 10, 40, 80 and 160. Temperatures were computed with Rosenthal's solution for a point source in an infinite solid - not an infinite plate. As many as 28 other point sources were then superimposed to force an insulated boundary condition on the pipe wall. The elastic-plastic problem was represented as a series of incrementally linear problems. Hence, the stress was computed in incremental steps but no iterations were used to maintain equilibrium or to improve the incremental values. It appears that the only temperature dependent properties used were the coefficient of thermal expansion and the slope of the stress-strain curve which was incorporated as an artificial Young's modulus. If the stress decreased in an increment, the next increment used the real temperature dependent Young's modulus to cope with unloading.

In computing the residual stress for 7 and 30 pass girth welds, Rybicki and Stonesifer [64] addressed a number of issues. They applied the thermal loads in two steps - a heating step to peak temperature at the centroid of each element and a cooling step. The temperature cutoff was 1150 C. If a weld was assumed symmetric, then off centre weld beads were assumed to be performed as symmetric pairs. In the seven pass weld, they considered both cases and noted a small difference. The 30 pass weld was analyzed in nine layers. The temperature field for the passes involved in each layer were applied separately. Then the peak temperature attained at each point; i.e., the envelope of peak temperatures, was used as the thermal load to compute the stresses. They reported that an attempt to group the 30 passes into 3 layers did not yield useful results.

Ueda has contributed a great deal to computational weld mechanics since 1971 [57]. His analysis of a multipass narrow gap weld [63] concluded that considerable accuracy could be obtained while reducing CPU costs by a factor as high as 4 by considering only every fourth pass. Indeed, the residual stress near the last pass can be computed analyzing the last pass alone. However, by computing the stress for every second pass, and using a coarse mesh, Ueda reduced CPU costs by a factor eight.

Rybicki [64] used an envelope of the combined temperature field for all the passes that were grouped into a layer. Ueda used the temperature field only from the pass being analyzed and totally neglected the temperature field due to missed passes. Since both authors were able to obtain useful solutions to difficult problems with limited resources, these approaches were worthwhile and represent a significant advance in computational weld mechanics. Their work demonstrates that rather crude models which are computationally cheap can yield useful data. However, the longer term goal must be to develop the capability to analyze welds rigorously.

4.6 Time Steps

Most FEA analysis performed to date have used the same mesh and the same time steps for both the heat transfer and the stress analysis because the programming is simpler. Andersson [24] changed the 6 noded triangles used for the heat transfer analysis into 3 noded triangles for the stress analysis. The stability and accuracy characteristics of the heat transfer and stress - strain analysis have fundamental differences. Therefore, it is not surprising that computational efficiency can be improved by using different time steps in the two analyses. In broad terms, the stress analysis requires shorter time steps during heating and permits longer time steps during the cooling phase. Implementing such a strategy requires that temperature-time data be interpolated or mapped onto the time stations in the stress-strain analysis. Patel mapped a 2D heat transfer analysis to a 3D stress-strain analysis. [65] summarizes recent developments in FEA by E. Hughes, Winget and Belytschko that allow different elements in an analysis to have different time steps provided all time steps are integer multiples of the shortest time step. In the analysis of large industrial problems, this promises to reduce computing cost substantially.

5. VERIFICATION METHODS (Mechanics)

Under very restrictive assumptions, it is sometimes possible to prove that a program is correct. However, there is general acceptance that it is not feasible to prove that a large complex program will always produce the correct answer just as it is not feasible to prove that an aeroplane will not fail. In both cases, methods have been developed to minimize the risk of failure but not to eliminate it entirely. In computational mechanics the basic method involves several stages. The FORTRAN compiler detects errors in syntax. When these have been corrected, the analyst then tests the simplest possible problems that exercise the theory including all types of initial and boundary conditions. The exact answers to these problems should be easy to compute by hand and usually they require only one element. The uniaxial tensile test is a good test problem. Care should be taken not to use unit values of thickness, specific heat, etc., because $a = b + c$ and $a = c$ are not distinct when $b = 1$. When such tests are performed, it is more likely that the correct input format has been used and that the output data is properly understood. The next series of test problems should attack slightly more difficult problems such as the stress in a thick cylinder or cantilever beam. They usually use a small number of elements. In this case the FEA solution is likely not exact which gives the user a better appreciation of the FEA approximation to the exact solution, how fine a mesh is required and what type of elements are most efficient.

The development of a verification procedure is an important element of computational weld mechanics. It requires care, knowledge, time and money. Since it is an excellent mechanism for evaluating the progress and quality of a project, the wise manager will stress its importance. The reader is referred to Patel [53] for an additional details.

The testing of thermo-elasto-plastic codes has received little attention in the literature which reflects its immaturity. The most rigorous tests are given by Patel [53]. His verification program started with a simple uniaxial tensile test in which complexity was increased in steps by adding reversed loading, thermal loading, temperature dependent material properties, and rate dependent material properties. In all cases the FEA results should converge to the exact result. Patel's next test was a thick cylinder under internal pressure. A thermal load due to a temperature gradient was added later.

The final test was an infinite strip with a transverse temperature gradient. Fig. 25 compared the closed form solution to his FEA solution. This result was important because it increased confidence in the program and it demonstrated that the rate dependence of the constitutive properties was significant. Neglecting rate dependence would have resulted in an error in strain of 50 %. In the available literature only Patel [53] and Argyris, Szimant and Willan [18] have included this effect in a weld analysis. However, neither ran the analysis with and without rate dependent properties to determine its effect on an actual weld analysis. Most papers consider only temperature dependence; i.e. the modulus of elasticity $E(T)$, and ignore terms with dE/dT . More experiments and FEA is needed to clarify the effect.

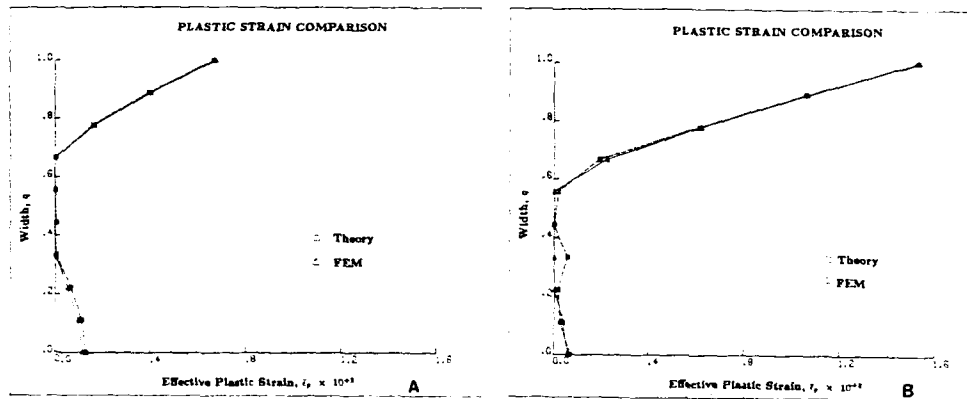


Figure 25. (A) Elasto-plastic analysis of thin strip with isothermal material properties — comparison of plastic strain (ϵ^p) distribution. (B) Elasto-plastic analysis of thin strip, nonisothermal material properties — comparison of plastic strain (ϵ^p) distribution.

6. COMPUTING CAMBER IN EDGE WELDED BARS — An Example

Distortion or residual strain increases the cost of fabricating welded structures and may detract from their performance or appearance. Some views on current industrial practise can be found in reference [66]. Here, a summary of Patel's [53] analysis of the distortion of edge welded steel bars is presented to demonstrate the potential of computational weld mechanics. Patel chose to analyze an edge weld on rectangular bars of a carbon steel (AISI 1020) and a stainless steel (AISI 304L). The problem is of particular interest since welders have long recognized that austenitic stainless steel workpieces distort about three times as much as welded carbon steel workpieces if all other factors are held constant. However, the reason for this difference has not been explained. If his computed camber agreed with the camber measured by Hogan [67] this would support his analysis methods.

The geometry and welding parameters are shown in Fig. 26. Patel first computed the transient temperature field using the cross sectional model shown in Fig. 2. The results shown in Fig. 27 demonstrate that the HAZ defined by the 500 C isotherm is much larger in the 304L bar. This strongly suggests that stainless steel will distort more than carbon steel. It is not obvious that the HAZ of stainless steel should be larger than that of carbon steel until such computations are actually carried out.

Patel's next step was to analyze the transient strain using the mesh shown in Fig. 28. Here the transient temperature field is a boundary condition that must be transformed from the original 2D cross sectional heat transfer analysis to the 3D stress analysis. Furthermore the stress analysis used different time steps. This capability of mapping data from one mesh to another will become increasingly important in coping with the complexity of industrial welding problems.

This 3D mesh is somewhat less constrained than a plane strain analysis. The assumption is that the ends of the slice are fixed which does not allow the bar to bend freely during the weld. However, the temperature varies in the longitudinal

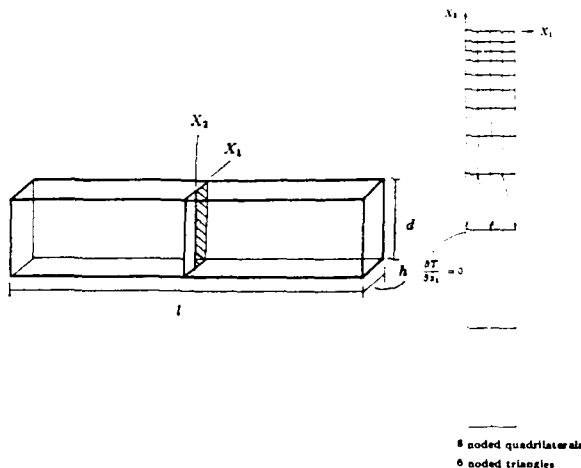


Figure 26. Geometry, finite element mesh and boundary conditions for transient cross-sectional heat transfer analysis. ($d = 50\text{ mm}$, $h = 12.7\text{ mm}$, $l = 1000\text{ mm}$, $Q = 0.4\text{ kJ/mm}$)

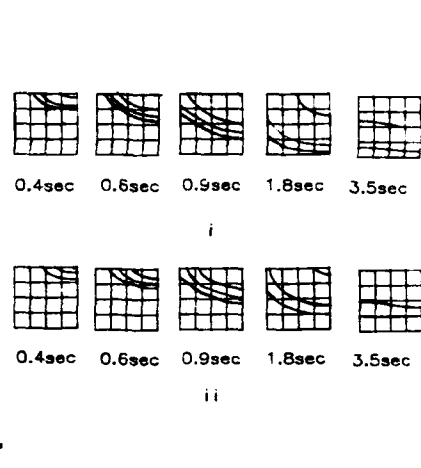


Figure 27. Transient isotherms (i.e. 1500, 800 and 500 °C) generated for (i) a AISI 304 stainless steel and (ii) a AISI 1020 carbon steel. ($d = 50\text{ mm}$, $h = 12.7\text{ mm}$, $l = 1000\text{ mm}$, $Q = 0.4\text{ kJ/mm}$)

direction and some of the nodes are free to move this direction. Neither is true for a plane strain model. If the plane strain assumptions were valid, the stress components σ_{33} , σ_{31} , σ_{32} and their corresponding strain components would be zero. In fact, Patel found them to be of yield point magnitude at certain times during the weld. This is in agreement with the experiments of Chafoski [36].

To compute the camber, Patel performed a third analysis in which the σ_{11} , σ_{22} , σ_{12} stress components were projected onto the (x_2, x_3) plane of the mesh shown in Fig. 29. This was analyzed in plane stress with the ends of the bars simply supported. The resulting camber shows remarkable agreement with Hogan's experimental data Fig. 30.

These results do not explain why austenitic stainless steel welds distort three times as much as carbon steel welds. Is it due to differences in the thermal conductivity or specific heat or is it due to differences in the stress-strain curves? However, by repeating Patel's analysis with different values of these parameters, this question could now be answered.

The computing time for the 3D analysis was roughly 5 hours on an Apollo DN 660 for each bar. Supercomputers might run it 20 to 100 times faster. The computing cost is of the order of a few hundred dollars per bar which is comparable to the cost of the experiment. Software now under test promises to analyze much larger 3D meshes at even lower costs.

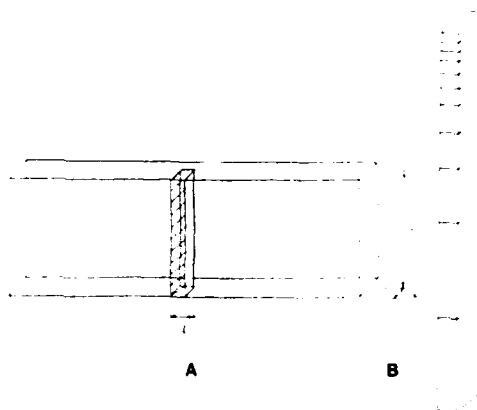


Figure 28. (A) Geometry of bar slice for 3-D stress analysis, (B) finite element mesh for 3-D bar slice for stress analysis.

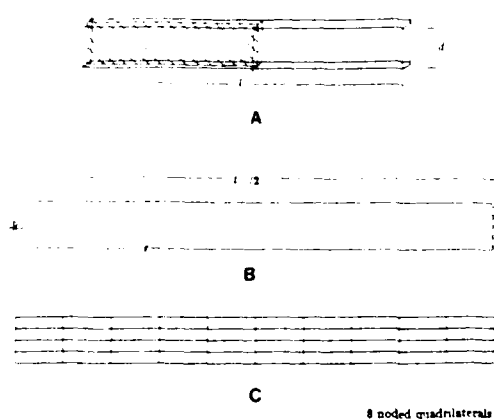


Figure 29. Geometry, boundary conditions and finite element mesh for 2-D plane stress analysis of camber: i.e. beam deflection. ($d = 50\text{ mm}$, $h = 12.7\text{ mm}$, $l = 1000\text{ mm}$, $Q = 0.4\text{ kJ/mm}$)

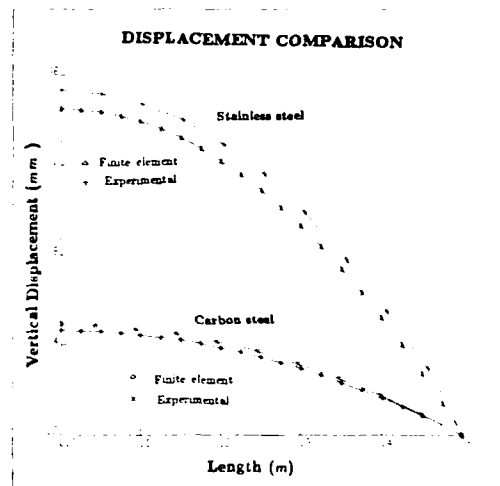


Figure 30. Comparison between finite element and experimental results for vertical deflection of edge welded steel bars; edge weld = 0.4 kJ/mm , bar dimension $12.7 \times 50 \times 1000 \text{ mm}$.

7. CHIHOSKI'S THEORY AND EXPERIMENTS

Chihoski sought a theory to explain why welds cracked under certain conditions but not others (54-56). Basically, he imagined that the weld was divided into longitudinal strips and into transverse strips. He then computed the thermal expansion and contraction in each of these strips due to the temperature field of edge and butt welds in 2024-T6 aluminum for welding speeds of 2.5, 5.5 and 8.5 mm/s.

He concluded that a small intense biaxial compression stress field exists near the weld pool. Ahead of the compression field there may be a gap or a tensile stress field. Behind the compression field a tensile field or a crack can appear. The startling aspect of Chihoski's theory was that by varying the welding procedure, the position of this compressive field could be controlled. For example, by placing it in the solidification region, hot cracking could be suppressed.

To support his theory, Chihoski developed a Moiré fringing technique to measure displacements during edge and butt welds. Today this technique is one of the most powerful means of assessing FEA of stress and strain in welds. (Also see Johnson (68) for more on Moiré fringing methods for measuring strain in welds.)

Chihoski used his theory to understand and solve a number of common problems: cracks and microcracks, forward gapping, upset and part distortion, sudden changes in current demand, and unexpected responses to welding gaps. He considered the position and pressure of hold down fingers, the influence of localized heating or cooling, and the effects of gaps. He argued that these parameters could be optimized to obtain crack free welds.

The authors consider Chihoski's papers to be among the most important in computational mechanics because he combined experience in production welds with an insight into weld mechanics to conceive a theory that rationalized his observations and predicted solutions to his problems. The fact that his theory was not based on rigorous continuum mechanics is unimportant. It was probably as complex as could be managed at the time. The important issue is that it provided a framework for rationalizing stress and strain in welds. He was not able to predict stresses accurately nor was he able to apply it to complex geometries. The FEA techniques described in this review clearly overcomes these limitations and provides the opportunity to computerize, test and extend Chihoski's vision.

8. THE COMPUTING ENVIRONMENT

8.1 Trends in Computer Hardware

The price, performance, and functionality of computers is improving at a rate of 35% per year. Since labour, energy, space and most supplies are inflating at rates of roughly 5% per year, computational methods are expected to continue to displace experimental methods. With falling computer costs, more engineers are turning from service bureaus to their own work stations and personal computers. Swanson Analysis (69) reports that a version of their ANSYS program runs on an IBM PC AT 4 to 10 times slower than on an empty VAX 11-780. However, the size of problems that can be run on the PC is limited. The next generation of PC is not expected to have this limitation. The power of a computer is often measured

by its speed in performing certain tests such as multiplying two matrices or running a specific set of problems. The size of a computer is usually measured by its memory size. Supercomputers have memories as large as 16 Mwords. Personal computers usually have 64 or 512 Kbytes of memory. In addition to the size of the memory, the size of the addressable memory is important. This ranges from 32K words in an IBM PC to 16 Mwords or more in professional workstations and mainframes. The functionality of a computer is measured by the richness and value of features such as virtual memory, networking, editors, etc. Its operating system should hide as many details as possible with minimum constraint on the user.

The clock cycle time in the fastest computers is roughly only ten times as fast as relatively cheap computers because they are all limited by the speed of transistors. To achieve greater throughput, computer architects turn to multiprocessing or parallel processing. The falling costs of designing and building computers has encouraged this trend. The greatest gains are obtained from parallel processing when the computer architecture is designed for specific algorithms. Computers for CAT scanning, the IRIS for graphics, and the FPS 164 for structural analysis are examples.

At least as important as these cost trends, is the change in the nature of computing from an electronic slide rule towards a totally integrated work environment for the individual and an integrated management system for the organization. Graphics, documentation software and laser printers, spread sheets and databases, are among the growing list of software tools and peripherals that make up a computer environment. From this viewpoint, the computer is rapidly evolving a capability to mirror the real world it is used to analyze. The greatest contribution of computing may well be that it rewards the search for entities and processes that are fundamental in both the natural and the artificial world.

The goal of artificial intelligence (AI) is to computerize those tasks such as designing, planning, scheduling and chess playing, that are not based on simple natural laws such as the conservation of mass, energy and momentum. The USAF calls this command, control, communications and intelligence or C^3I . AI has had its greatest success in expert systems that mimic an expert in a narrow field of knowledge. Certainly, expert systems can and will be developed to assist welding engineers in selecting processes and procedures, where such decisions are based on judgement and not mathematical analysis. Extending this to broader fields is the current challenge. It will require new methods and new computers such as the Japanese "hunch cruncher". Computational weld mechanics will be increasingly integrated into such systems.

8.2 Computational Geometry

Geometry is one of the pillars upon which computational weld mechanics is built. For decades engineers have used drawings to specify designs. Drawings are a complex ambiguous language that is inappropriate for computerization. In computer aided drafting, the computer stores the lines and symbols from the drawing, but does not understand them and cannot interpret them. With wire frame models that store vertices and edges, the computer has some understanding of the geometry and can rotate an object or at least its wire frame representation. However, the ambiguity of wire frames prevents the program from computing values such as the volume of an object.

Modern computational geometry has developed representations and operations that overcome these difficulties (Fig. 31). The best known of these is solids modelling which was developed to provide a mathematically complete representation of the geometry of an object [70]. A solids modeller can answer any geometric question such as, "What is the centre of mass, volume, and moments of inertia". The high quality graphics images they provide are of great value. There is no doubt that computational weld mechanics must utilize solids modelling to deal with geometric issues.

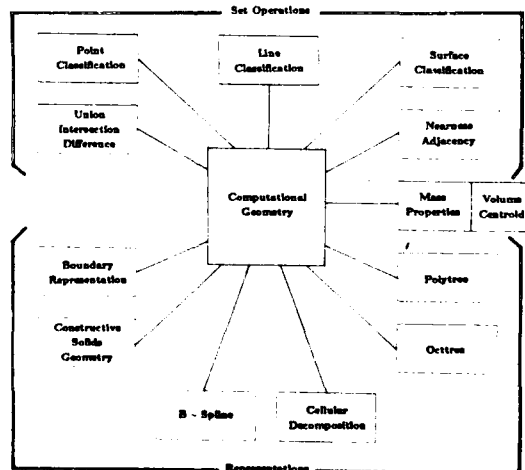


Figure 31. The representations and set operations that have been developed for computational geometry are shown above.

8.3 Better Algorithms

It can be argued that the gains in computational weld mechanics to be made by developing better algorithms are more important than the gains in computer hardware. The weakness of this argument is that these algorithms will shortly be transferred to silicon; i.e., hardware. The strength of the argument is that the algorithm must come first. Moreover, people in computational weld mechanics are much more likely to develop algorithms than computer hardware.

8.3.1 Mesh Generation

To perform a heat transfer or stress analysis a mesh must be generated. The most popular commercial mesh generators are Patran G, Ansys, Femgen and Supertab. Their fundamental limitations are that the mesh is difficult to change during an analysis; the mesh design requires expert judgement and it is labour intensive.

A new class of mesh generators are being developed by Kela, Voelcker and Goldak [29] and Sheperd and Law [30] that do not depend on expert judgement. They are fully automatic. Since 90 % of the time and cost of a FEM analysis of a complex structure currently is absorbed by pre and post processing, progress in mesh generation is a critical factor that is pacing the development of computational weld mechanics.

The automatic mesh generators open the possibility of changing the mesh at any, even every, time step. This is particularly important in welding where a fine mesh is needed near the molten pool and a coarse mesh far from the molten pool could decrease costs and improve performance by several orders of magnitude.

The arbitrary Euler-Lagrange method [71] would allow a fine mesh that moves with the arc. The mesh far from the arc would be stationary. The mesh in between would move with a velocity that is interpolated.

The above examples illustrate the rapid improvements expected in mesh generation methods that will reduce the cost of FEA of welds and permit real welding situations to be analyzed routinely.

8.3.2 New Forms of Elements

In 3D analysis, brick elements are preferred because they tend to be more accurate and easier to use and interpret than tetrahedral elements. However, it has been difficult to grade a mesh with small brick elements near the welding arc to capture the rapid changes in temperature and large brick elements far from the arc where the temperature varies slowly. To solve this problem, McDill, Goldak and Bibby [72] developed a special brick element for graded 3D meshes.

The advantages of this element are demonstrated by analyzing the problem shown in Fig.32. Using a Gaussian solver, the computational cost varies as n^7 and memory requirements vary as n^5 for the uniform mesh. In comparison the cost and the memory requirements vary as $\log_2 n$ for the graded mesh. It is expected that even for problems of a modest size, a personal computer with McDill's graded elements would outperform a supercomputer with a uniform mesh. The larger the problem the greater the advantage of the graded mesh. This clearly illustrates that the gains from better algorithms can easily outpace the gains from better computers.

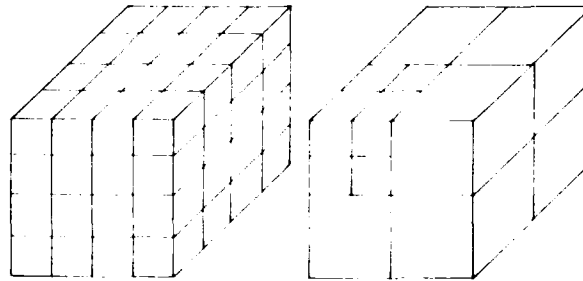


Figure 32. (A) A uniform mesh $n = 4$ and (B) McDill's grading scheme for a cube of $n = 4$. The number of elements is equal to n^3 and $7 \log_2 n + 1$. The computational cost varies as n^7 and $\log_2 n$. (Where: n is the number of elements along an edge in a uniform mesh and, m is the number of recursive subdivisions of the upper left hand cube. Note: the size of the element in the upper is the same when $n = 2^m$.)

8.4 Equation Solvers

Current commercial FEM packages spend up to 90% of the computing time solving a set of linear equations, $Kx = b$, [73] using a Gaussian elimination method. New computer architectures, such as Floating Point Systems' FPS-164 MAX use parallel processing to solve this equation set so quickly that it requires as little as 10% of the CPU time. However, no currently conceived computer could cope with memory requirements for solving large problems in this way. For example, an implicit in-core solution of the Navier Stokes equations for a cube discretized into $128 \times 128 \times 128$ eight-noded brick

elements would require 10^{11} 64 bit words of memory with current commercial FEM codes. This is 10000 times more memory than the largest computers have today.

To address this problem, incomplete Choleski conjugate gradient (ICCG) solvers have been developed for fluids problems by Glowinski, [74] and by Jennings and Ajiz [75] for structural problems. Although the experience to date does not permit a definitive statement, the evidence suggests these solvers require less CPU time and less memory for large problems. Hughes [76, 77] has developed an iterative method that promises to solve the memory problem and reduces the CPU costs. With his method, the global equations $[K]\{x\} = b$ are never assembled. The solution proceeds almost entirely at the element level. More research is needed to confirm the performance, robustness and limitations but the potential of the approach is obvious.

8.5 Spatial Integration Schemes

Since FEM is primarily an exercise in numerical integration, it is not surprising that better integration schemes are being sought. Numerical integration schemes replace an integral by a summation: e.g. $\int_1^1 f(x)dx = \sum_1^n w_i f(x_i)$. The choice of the number of sampling points, n , the weights, w_i , and the location of the sampling points, x_i , characterize the integration scheme. If $f(x)$ is a polynomial of degree $2n - 1$, it can be integrated exactly with n sampling or integration points as shown by Gauss. In two dimensions, the stiffness matrix of the popular 4 noded rectangular element can be integrated exactly with four integration points. If only one integration point is used, the integration is approximate and spurious nodes may appear that corrupt the solution. Belytschko [78] discovered a way to remove these spurious modes and thus reduce the integration costs by almost a factor of four.

8.6 Time Integration Schemes

In transient heat transfer analysis, the FEM program must integrate a set of ordinary differential equations in time:

$$C\dot{T} + KT + F = 0 \quad (24)$$

where T is temperature, C is a capacitance matrix, K is a conductance matrix, and F is a load vector. Current commercial FEM programs use two point integration schemes that are either explicit or implicit. Explicit schemes use primarily element level operations. The cost per time step is small but time steps must be short — less than $l^2/2\alpha$ where l is the shortest distance between nodes and α is the thermal diffusivity. Thus, the element with the smallest critical time, $l^2/2\alpha$, controls the time step. Implicit schemes solve a global set of equations $Kx = b$ which is expensive but can take larger time steps — roughly ten times larger. Provided the load does not vary too rapidly, the longer time steps can be more efficient.

A recent development in integration schemes allows those elements with short critical time steps to be integrated implicitly with longer time steps and those elements with longer critical time steps to be integrated explicitly [79]. This can reduce computing costs dramatically.

The generalization of this concept to use different time steps in different elements is called subcycling [78]. McDill is applying this to welds to achieve dramatic gains. The mesh shown in Fig.33 is created by recursively subdividing the square m times. The number of elements is $1 + 3m$; the smallest element has edge length $L/2^m$; and critical time step $2^{2m} \alpha L^2$. If each element is integrated only with its critical time step, the number of element time steps $3(2^m - 1)$ or $O(2^m)$. If all elements are integrated with the smallest critical time step as is current commercial practice, the number of element time steps is:

$$(1 + 3m)2^{2m}\alpha/L^2 \quad \text{or} \quad O(m2^{2m}) \quad (25)$$

If $m = 9$, subcycling can reduce the CPU cost from 10^6 to 10^3 . Here again, the power of better algorithms to dramatically reduce computing costs is illustrated.

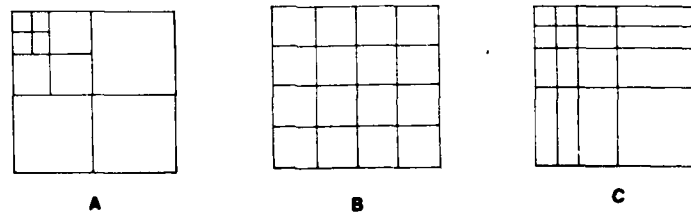


Figure 33. The mesh in (A) is obtained by recursively subdividing the square in the upper left hand corner. This can be significantly more efficient than the regular mesh shown in (B) or the grading strategy used in (C) for point like loads at the upper left hand corner.

9. RELATION TO CIMS

Weld mechanics must be knitted into computer aided design and fabrication analysis that creates a computer integrated manufacturing system (CIMS). This is discussed at length in reference [80]. Given the capability of analyzing a design or process, numerical optimization techniques can be applied to optimize it in terms of design goals such as minimizing weight, cost or time subject to requirements such as bearing certain loads over certain spans. This will lead to more efficient, higher performance products. However, the prerequisite for optimization is the capability of accurately analyzing welds. The methodology for numerical optimization of design problems is presented by Esping [81] and Vanderplaats [82].

10. CONCLUSIONS

This paper argues that the capability exists to accurately compute the temperature, strain and stress in welds and welded structures. The costs which now are often less than the costs of experiment, will fall by more than a factor of 1000 in the next seven years and in large problems by a much larger factor. Thus, we conclude that computational weld mechanics will become the driving force advancing welding technology.

Chihoski's [54] recommendation still says it best: *A changed set of conditions often changes the weld quality too subtly to be seen, except in large quantities, and there are too many possible changes to try. Hit or miss changes in the perfect lab (the production shop) are often not permitted. It would seem then to be of great use to the welding industry to develop and evolve computer programs that rigorously portray the stress and strain arrangements for different weld conditions. This route may be the only path from the current state of technology to the ideal in scientific promise, where a manufacturer who chooses an alloy and thickness and weld conditions can find out the value of each of the other weld conditions that minimizes his production problems.*

This paper has argued that Chihoski's vision is rapidly becoming reality and will soon be part of normal operating practise in the welding industry.

ACKNOWLEDGEMENTS

The financial support of NSERC 4601 (M. Bibby), NSERC A2922 (J. Goldak), and AMCA International are gratefully acknowledged. Over the years, the encouragement and advice from friends in industry, particularly D. Reynolds, L. Malik of AMCA and B. Altshuller of Alcan, has been important. Finally, Professors Bibby and Goldak wish to acknowledge the contribution of several graduate students. B. Patel [53] developed the code for thermo-elasto-plastic analysis and analyzed the camber in edge welded bars. L. Beresford [83] developed the code for 3-D transient heat transfer analysis. A. Chakravarti [84] developed the code for 2-D transient heat transfer analysis, developed the double ellipsoid model for weld heat sources and analyzed the cross-sectional model. R. House [25] performed the first in-plane and 3-D heat transfer analysis of welds. J. Adam [26] did the conical heat source model for electron beam welds. Moore [85] meticulously compared Rosenthal's solution with FEM models. Y.L. Wan [86] and S. Hogan [67] measured the camber of edge welded bars.

11. REFERENCES

- [1] G.M. Oreper, T.W. Eager and J. Szekeley, "Convection in Arc Weld Pools", Welding Research Supplement, Nov. 1983, p. 307-312.
- [2] N. O. Okerblom, "The Calculation of Deformations of Welded Metal Structures", Mashgiz Publications, Moscow, 1955, Translated by Her Majesty's Stationery Office, London, 1978.
- [3] V.A. Vinokurov, "Welding Stresses and Distortions", The British Library, Lending Division, Translated from Russian into English by J.E. Baker, 1977, pp. 118-119.
- [4] T.G.F. Gray, J. Spence and T.H. North, "Welding Processes and their Influence on Design", Rational Welding Design, London Newnes-Butterworths, 1975, p. 44-61.
- [5] L. Tall, "Residual Stresses in Welded Plates, A Theoretical Study", Welding Research Supplement, January 1964, p. 10-24.
- [6] K. Masubuchi, "Analysis of Welded Structures", Pergamon Press, 1980.
- [7] Y. Ueda and H. Murakawa, "Applications of Computer and Numerical Analysis Techniques in Welding Research", Transactions of JWRI, 1984, vol. 13, No. 2, p. 337-346.
- [8] R.R. Rykalin, "Energy Sources for Welding", Welding in the World, 1974, Vol. 12, No. 9/10, p. 227-248, (Houdrement Lecture, International Institute of Welding, London, 1974, p. 1-23).
- [9] M. Ushio and F. Matsuda, "Mathematical Modelling of Flow Field and Heat Transfer of Welding Arc", Fourth International Symposium of the Japanese Welding Society, Osaka, paper 4JWS-I 4, November 1982.

- [10] S. Lawson and H. Kerr, "Fluid Motion in GTA Weld Pools - Parts 1 and 2", Welding Research International, 1976, vol. 6, No. 5,6
- [11] E. Friedman, "Analysis of Weld Puddle Distortion" Welding Journal Research Supp., 1978, p. 161s-166s.
- [12] D. Rosenthal, "The Theory of Moving Sources of Heat and Its Application to Metal Treatments", Trans ASME, 1946, vol. 68, p. 849-865.
- [13] P.S. Myers, O.A. Uyehara and G.L. Borman, "Fundamentals of Heat Flow in Welding", Welding Research Council Bulletin, No. 123, New York, 1967.
- [14] O. Westby, "Temperature Distribution in the Workpiece by Welding", Department of Metallurgy and Metals Working, The Technical University, Trondheim, Norway, 1968.
- [15] Z. Paley and P.D. Hibbert, "Computation of Temperatures in Actual Weld Designs", Welding Journal Research Supplement, 1975, vol. 54, p. 385s-392s.
- [16] V. Pavelic, R. Tanbakuchi, O.A. Uyehara and P.S. Myers, "Experimental and Computed Temperature Histories in Gas Tungsten-Arc Welding Thin Plates", Welding Journal Research Supplement, 1969, vol. 48, p. 295s-305s.
- [17] S. Kou, "Welding, Glazing and Heat Treatment - A Dimensional Analysis of Heat Flow", AIME Metallurgical Trans. A, 1982, vol. 13A, p. 363-371.
- [18] J.H. Argyris, J. Szimmat and K.J. Willan, "Computational Aspects of Welding Stress Analysis", Computer Methods in Applied Mechanics and Engineering, 1982, vol. 33, p. 635-666.
- [19] J.A. Goldak, A. Chakravarti and M.J. Bibby, "A New Finite Element Model for Welding Heat Sources", Trans. AIME., 1984, vol. 15B, p. 299-305.
- [20] N. Christensen, L. de.V. Davies and K. Gjermundsen, "Distribution of Temperatures in Arc Welding", British Welding Journal, 1965, vol. 12, p. 54-75.
- [21] M.J. Bibby, G.Y. Shing and J.A. Goldak, "A model for Predicting the Fusion and Heat-Affected Zone Sizes of Deep Penetration Welds", CIM Metallurgical Quarterly, 1985, Vol. 24, No. 2, (in press)
- [22] A.P.Chakravarti, J. Goldak, and A.S. Rao, "Thermal Analysis of Welds", International Conference on Numerical Methods in Thermal Problems, Swansea, UK, July, 1985
- [23] J.F. Key, H.B. Smartt, J.W. Chan and M.E. McIlwain, "Process Parameter Effects on the Arc Physics and Heat Flow in GTAW", p. 179-199.
- [24] B.A.B. Andersson, " ", Journal of Engineering Materials and Technology, Trans. ASME, 1978, vol. 100, p. 356-362.
- [25] R. House, "Analysis of an Aluminum MIG Weld", Internal report, Carleton University, Ottawa, Canada, April, 1984.
- [26] J. W. Adams, "Development and Verification of a Conical Weld Source for Finite Element Analysis of Electron Beam Welds", Internal report, Carleton University, Ottawa, Canada, April, 1984.
- [27] D.R. Chapman, "Computational Aerodynamics - Development and Outlook", AIAA Journal, 1969, vol. 17, No. 12, p. 1293-1313.
- [28] B.M. Irons and S. Ahmad, "Techniques for Finite Elements", Ellis Horwood, 1980.
- [29] A. Kela, H. Voelcker and J.A. Goldak, "Automatic Generation of Finite-Element Meshes from CSG Representations of Solids", International Conference on Accuracy Estimates and Adaptive Refinements in Finite Element Computations (ARFEC), Sponsored by the International Association of Computational Mechanics, Lisbon, Portugal, June 19-20, 1984.
- [30] M.S. Sheperd and K. H. Law, "The Modified-Quadtree Mesh Generator and Efficient Adaptive Analysis", International Conference on Accuracy Estimates and Adaptive Refinements in Finite Element Computations (ARFEC), Sponsored by the International Association of Computational Mechanics, Lisbon, Portugal, June 19-20, 1984.
- [31] O.C. Zienkiewicz, "The Finite Element Method", McGraw Hill Book Company, 3rd edition, 1977.
- [32] T.J.R. Hughes, "Unconditionally Stable Algorithms For Heat Conduction", Computer Methods in Applied Mechanics and Engineering, 1977, vol. 10, p. 135-139.
- [33] J. Donnea, "On the Accuracy of Finite Element Solutions to the Transient Conduction Equation", International Journal for Numerical Methods in Engineering, 1974, vol. 8, p. 103-110.
- [34] Z. Pammer, "A Mesh Refinement Method for Transient Heat Conduction Problems Solved by Finite Elements", International Journal for Numerical Methods in Engineering, 1983, vol. 15, p. 495-505.
- [35] W.M. Rohsenow and J.P. Hartnet, "Handbook of Heat Transfer", McGraw Hill, 1973
- [36] Y.S. Touloukian, Powell, Ho and Klemens, "Thermal Conductivity: Metallic Elements of Alloys", New York, 1970, Vol. 1.
- [37] The British Iron and Steel Research Association, "Physical Constants of Some Commercial Steels at Elevated Temperatures", London, Butterworths Scientific Publications, 1953.
- [38] N. Yurioka, S. Ohsita and H. Tamehiro, "Study of Carbon Equivalents to Assess Cold Cracking tendency and Hardness

- in *Steel Welding* ", The Specialist Symposium on Pipeline Welding in the 80's, Melbourne, Australia, March 18/81.
- [39] K. Farnia and J.V. Beck, "Numerical Solution of Transient Heat Conduction Equation for Heat Treatable Alloys Whose Thermal Properties Change With Time and Temperature ", Journal of Heat Transfer, Trans. ASME, vol. 99, p. 471-478.
- [40] G. Comini, S. del Guidice, R.L. Lewis and O.C. Zienkiewicz, "Finite Element Solution of Nonlinear Heat Conduction with Special Reference to Phase Changes ", IJNME, 1974, vol. 8, pp. 613-624.
- [41] W.D. Rolphe III and K.J. Bathe, "An Efficient Algorithm For Analysis of Nonlinear Heat Transfer With Phase Changes ", IJNME, 1982, vol. 18, pp. 119-134.
- [42] D. Blanchard and M. Fremont, "The Stefan Problem, Computing Without the Free Boundary ", IJNME, 1984, vol. 20, p. 757-771.
- [43] S. Al-Araji and J.V. Beck, "Heating Time and Heating Temperature Dependence of Thermal Conductivity of As-Received Aluminum Alloy 2024-T351 ", Journal of Heat Transfer, Trans. ASME, 1975, p. 148-149.
- [44] M.F. Ashby and K.E. Easterling, "A First Report on on Diagrams for Grain Growth in Welds ", Acta Met. 30, 1982, p. 1969-1978.
- [45] J.C. Ion and K.E. Easterling, "Grain Growth During Welding ", The Third Scandinavian Symposium in Materials Science, 20-21 June, 1983, The University of Oulu, Finland, Metal Abstracts 8407-72-0526.
- [46] L. Coon, "Computer Simulation of Welding ", B.A.Sc. Thesis, University of Windsor, Windsor, Canada, May 1985.
- [47] J.H. Argyris, J. St. Doltsinis, P.M. Pimenta and H. Wustenberg, "Thermomechanical response of Solids at High Strains - Natural Approach ", Computer Methods in Applied Mechanics and Engineering, 1982, vol. 32, p. 3-57.
- [48] R.D. Krieg, "Numerical Integration of Some New Unified Plasticity-Creep Formulations ", Proceedings of 4th SMIRT Conference, San Francisco, California, Paper No. M6/4, 1977
- [49] C. Zener, "Elasticity and Anelasticity of Metals ", University of Chicago Press, Chicago, 1948.
- [50] H. Zeigler, "A Modification of Prager's Hardening Rule ", Quarterly Applied Mathematics, 1959, pp. 55-65.
- [51] R.D. Krieg and D.B. Krieg, "Accuracies of Numerical Solution Methods for the Elastic-Perfectly Plastic Model ", Journal of Pressure Vessel Technology, November 1977, p. 510-515.
- [52] P.J. Yoder and R.G. Whirley, "On the Numerical Implementation of Elastoplastic Models ". Journal of Applied Mechanics, Trans. ASME, 1984, p. 1-6.
- [53] B. Patel, " Thermo-Elasto-Plastic Finite Element Analysis of Deformations and Residual Stresses due to Welds ". Ph.D Thesis, Carleton University, Ottawa, Canada, Jan., 1985
- [54] R.A. Chihoski, "Understanding Weld Cracking in Aluminum Sheet ", Welding Journal, January 1972. p. 24-30.
- [55] R.A. Chihoski, "The Character of Stress Fields Around A Weld Arc Moving on Aluminum Sheet ", Welding Journal, January 1979, p. 9s-18s.
- [56] R.A. Chihoski, "Expansion and Stress Around Aluminum Weld Puddles ", Welding Journal, September 1979, p. 263s-275s.
- [57] Y. Ueda and T. Yamakawa, "Analysis of Thermal Elastic-Plastic Stress and Strain During Welding by Finite Element Method ", Trans. Japan Welding Society, 1971, vol 2, No. 2, p. 90-100.
- [58] H. D. Hibbitt and P. V. Marcal, "A Numerical, Thermo Mechanical Model for the Welding and Subsequent Loading of a Fabricated Structure ", Computers and Structures, 1973, vol. 3, p. 1145-1174.
- [59] Y. Ueda and K. Nakacho, " Theory of Thermal Elastic-Plastic Analysis With a More General Workhardening Rule ". Transactions of JWRI, Welding Research Institute of Osaka University, 1980, vol. 9, No. 1, p. 107-114.
- [60] W.K.C. Jones and P.J. Alberry, "A Model for Stress Accumulation in Steels during Welding ", Edited by R.W. Nichols, Residual Stresses in Welds by Welded Construction and Their Effects, London, U.K., Nov. 1978, p. 15-17.
- [61] D.H. Allen, "Computational Aspects of the Nonisothermal Classical Plasticity ", Computers and Structures, 1982, vol. 15, p. 589-599.
- [62] G.W. Greenwood and R.H. Johnson, "The Deformation of Metals under Small Stresses during Phase Transformations ", Proceedings Royal Society, A283 (1394), January, 1965, p. 403-422.
- [63] Y. Ueda, E. Takahashi, K. Fukuda, K. Sakamoto and K. Nakacho, "Multipass Welding Stresses in Very Thick Plates and Their Reduction from Stress Relief Annealing ", Transactions of JWRI, 1976, vol. 5, No. 2, p. 79-89.
- [64] E.F. Rybicki and R.B. Stonesifer, "Computation of Residual Stresses Due to Multipass Welds in Piping Systems ", ASME Journal of Pressure Vessel Technology, 1979, vol. 101, p. 149-154.
- [65] T. Belytschko and T.J.R. Hughes, "Computational Methods for Transient Analysis ", North-Holland Publishing Co., 1983.
- [66] American Society for Metals, "Control of Distortion and Residual Stress in Weldments ", Edited by Z.P. Saperstein Proceedings of an International Conference, 16-17 Nov. 1976, Chicago, Illinois, published by ASM, Metals Park, Ohio.

Nov. 1977.

- [67] S. Hogan, "Structural Deflections of Carbon and Stainless Steel Sections due to Weldings", Internal Report, Carleton University, Ottawa, Canada, March 1979.
- [68] L. Johnson, "Formation of Plastic Strains During Welding of Aluminum Alloys", Welding Research Supplement, July 1973, p. 298s-305s.
- [69] "Introducing ANSYS-PC/Linear", ANSYS News, Second Issue, 1985, pp. 1.
- [70] A.A.G. Requicha and H.B. Voelcker, "Solids Modelling: Current Status and Research Directions", IEEE Computer Graphics and Applications, 1983, vol. 3, No. 7, p. 25-37.
- [71] J. Donnea, "Arbitrary Lagrangian - Eulerian Finite Element Methods", Computational Methods for Transient Analysis, Vol. 1, North-Holland publishing Co., Edited by T. Belyschko and T.J.R. Hughes, 1983, p. 473-516.
- [72] M. McDill, J.A. Goldak and M.J. Bibby, To be Published.
- [73] J.A. Swanson, G.R. Cameron and J.C. Haberland, "Adapting the Ansys Finite-Element Program to an Attached Processor", IEEE Computer Journal, 1983, vol. 16, No. 6, p.85-91.
- [74] R. Glowinski, B. Mantel, J. Periaux, P. Perrier and O. Pironneau, "On an Efficient New Preconditioned Conjugate Gradient Method. Application to the In-core Solution of the Navier-Stokes Equations Via Non-linear Least-Square and Finite Element Methods", Finite Elements in Fluids, Vol. 4, 1982, p. 365-401
- [75] M.A. Ajiz and A. Jennings, "A Robust Incomplete Choleski-Conjugate Gradient Algorithm", International Journal for Numerical Methods in Engineering, 1984, vol. 20, p. 949-966.
- [76] T.J.R. Hughes, I. Levit and J. Winget, "An Element-by-Element Solution Algorithm for Problems of Structural and Solid Mechanics", Computer Methods in Applied Mechanics and Engineering, 1983, vol. 36, p. 241-254.
- [77] T.J.R. Hughes, J. Winget, I. Levit, and T.E. Tezduyar, "New Alternating Direction Procedures in Finite Element Analysis Based Upon EBE Approximate Factorizations", ASME Proc. of Synp. on Recent Developments in Nonlinear Stress and Solid Mechanics, June 1983
- [78] T. Belyschko, "An Overview of Semidiscretization and Time Integration Procedures", Computational Methods for Transient Analysis, Vol. 1, North-Holland, Edited by T. Belyschko and T.J.R. Hughes, 1983.
- [79] W.K. Liu "Mixed Time Integration Methods for Transient Thermal Analysis of Structures", NASA Contractor Report 172209, Sept. 1983, p. 1-55.
- 80. J.A. Goldak, "From Know How to Know What", Davidson-Dunton Lecture, Carleton University, Ottawa, Canada, K1S 5B6, Nov. 1984.
- 81. B.J.D. Esping, "A CAD Approach to the Minimum Weight Design Problem", Report No. 83-14, ISSN 0280-4646, Royal Institute of Technology, Department of Aeronautical Structures and Materials, S-100 44 Stockholm, Sweden, 1983.
- 82. G. N. Vanderplaats, "Numerical Optimization Techniques for Engineering Design: with Applications", McGraw-Hill, 1984.
- 83. L. Beresford, "Three-dimensional Transient Heat Flow in Solids", Carleton University, Ottawa, Canada, K1S 5B6, M. Eng. Thesis, 1983.
- 84. A.P. Chakravarti, "Modelling Welds and Heat Sources with the Finite Element Method", Carleton University, Ottawa, Canada, K1S 5B6, M. Eng. Thesis, 1982.
- 85. J.E. Moore, "A Comparison of the Calculation Schemes for Computing Weld Cooling", Carleton University, Ottawa, Canada, K1S 5B6, M. Eng. Thesis, 1985.
- 86. Y.L. Wan, "Camber in Welded Mild Steel Sections", Carleton University, Ottawa, Canada, K1S 5B6, M. Eng. Thesis, 1979.
- 87. McAdams, W.H., "Heat Transmission", McGraw Hill Book Company, New York, 3rd edition, 1954.

ETUDE DE LA SOUDABILITE PAR FAISCEAU
D'ELECTRONS DE SUPERALLIAGES PAR ANALYSE MORPHOLOGIQUE
DES ZONES FONDUES

F. PIERQUIN J. LESGOURGUES
LABORATOIRE ASSEMBLAGE METALLURGIQUE
DIRECTION TECHNIQUE
SNECMA

2, Bd Victor
75724 PARIS CEDEX 15

RESUME

Le soudage par faisceau d'électrons, caractérisé par une forte énergie spécifique, permet le soudage à des vitesses élevées. Les zones fondues et les zones thermiquement affectées obtenues sont étroites et les cycles thermiques correspondant brefs, il en résulte des contraintes élevées au niveau des soudures. Ainsi le soudage des superalliages à haute résistance, présentant des capacités de déformation limitées, peut poser des problèmes de fissuration à chaud.

La forme du bain fondu est logiquement reconnue comme un facteur important sur l'apparition et la nature des défauts : fissures verticales, horizontales, longitudinales, de doigts de gants,...

Pour repousser la limite d'utilisation du procédé, une technique permettant d'étudier la morphologie des bains liquides et d'établir une corrélation avec la nature des défauts rencontrés a été développée. Le procédé, fondé sur une pollution du bain à un instant donné du soudage permet de révéler, par des examens micrographiques, la forme du front de solidification sans interférence sur le processus.

L'INCO 718 en assez forte épaisseur, configuration correctement maîtrisée sur le plan de la soudabilité, est traité dans ce texte à titre d'exemple.

SUMMARY

Characterized by a high specific energy, electron beam allows a high welding velocity. The melted zones and heat affected zones are narrow and the thermal cycles involved are short, and, therefore, the weld joints are submitted to high stresses. Thus, welding of high strength superalloys raises hot cracking problems, due to their low ductility.

The configuration of the melted pond is logically recognized as an important factor on the generation of defects and on their type : vertical cracks, horizontal cracks, axial cracks, spike cracks, etc...

To extend the applications of the process, a technique was developed to investigate the melted pond morphology and establish a correlation with the type of defects observed. The process, based on the pollution of the melted pond at a given time during welding, reveals ; though micrographic examination, the solidification front configuration.

1. INTRODUCTION

Le développement de matériaux toujours plus résistants à des températures élevées est un des buts de la métallurgie dans le domaine des turbomachines. Malheureusement, mais fort logiquement, les progrès réalisés sur les alliages s'accompagnent d'une difficulté croissante dans l'application des techniques d'assemblage métallurgiques.

Le soudage par faisceau d'électrons, couramment employé dans l'industrie aéronautique pour assembler des ensembles fixes ou des pièces tournantes fortement sollicitées, n'échappe pas à cette loi. Par exemple, le soudage des superalliages de fonderie et métallurgie des poudres peut poser des problèmes de fissuration à chaud.

Cependant des résultats satisfaisants ont été obtenus par une détermination empirique des paramètres opératoires. La forme du bain de fusion étant logiquement reconnue comme un facteur important dans l'initiation des défauts, il est apparu nécessaire d'étudier plus scientifiquement ce facteur pour maîtriser le soudage de certains de ces alliages.

Des techniques d'examen existent déjà (!). Toutefois leur mise en oeuvre est peu accessible. Un procédé a été développé à la SNECMA pour répondre à ce besoin.

Le propos de cette présentation est de décrire la technique d'examen mise au point. L'alliage 718 a été retenu pour en illustrer le développement, cette configuration étant parfaitement maîtrisée sur le plan de la soudabilité.

2. LES DEFANTS DE ZONE FONDUE

Dans une soudure réalisée par faisceau d'électrons, les anomalies suivantes peuvent être rencontrées :

- défauts d'aspect visuel et/ou géométrique,
- fissuration de zone affectée,
- fissures, cavités et soufflures de zone fondue.

Les défauts de la dernière catégorie sont en général les plus critiques et difficiles à éliminer. Ils peuvent se classer et se définir de la façon suivante :

- a) Les fissures horizontales dans le sens longitudinal de la soudure (figure 1), se forment lors du refroidissement vers la mi-épaisseur de la pièce, sont imputables aux facteurs suivants (2) (3) (4) :
 - l'épaisseur soudée,
 - la nature et le niveau de résistance de l'alliage,
 - la forme du bain de fusion.
- b) Les fissures verticales dans le sens longitudinal de la soudure (figure 2), résultent de la déchirure du métal, sous l'effet des contraintes de retrait, dans un plan correspondant physiquement au plan de convergence des dendrites lieu privilégié des ségrégations, impuretés et microretassures.
- c) Les retassures verticales dans le sens longitudinal de la soudure (figure 3), résultent d'un manque de liquide en fin de la solidification de poches qui se trouvent parfois emprisonnées au cours de soudage. Ces retassures sont,

dans la plupart des cas, fines et souvent assimilées à des fissures. C'est en procédant à un examen fractographique que l'on peut les distinguer. Il a été constaté (2) (5) que les retassures se forment dans des élargissements du cordon et que leur formation peut être périodique.

- d) Les soufflures (porosity), sont de petites bulles gazeuses piégés lors de la solidification de la zone fondue. Leur diamètre varie de quelques centièmes de millimètre à plusieurs millimètres dans les cas extrêmes (figure 5). Leur présence peut être due au rejet de gaz dissous lors de la solidification du liquide ou aux vapeurs dégagées par la décomposition des corps exogènes.
- e) Les cavités (cavity) (figure 4), sont le propre du soudage des fortes épaisseurs. Elles constituent la difficulté majeure du soudage par FE pour les aciers au-delà de 50 mm (6) (7). Leur formation est associée à des élargissements de la zone fondue. Elles se localisent généralement au niveau ou le faisceau présente la plus forte densité électronique (volume focal) (3) (8).
- f) Les défauts de doigts de gant sont des pointes de pénétration du faisceau électronique rencontrées systématiquement en fond de cordon, lors de soudage à jet non débouchant. Les pointes de pénétration donnent au fond de cordon un aspect en dent de scie, ce qui n'est pas un défaut en soi. Par contre, elles constituent des sites où apparaissent fréquemment des défauts tels que cavités, fissures, gouttes froides, dès que l'épaisseur soudée dépasse 3 mm, quel que soit la nature de l'alliage (figure 6). Des études ont été effectuées (1) (8) pour comprendre les mécanismes de la formation des doigts de gant et des défauts qui y sont associés. Toutes mettent en évidence le rôle déterminant des perturbations dans l'écoulement et les mouvements du bain liquide.

3. PROBLEME PARTICULIER DES ALLIAGES BASE Ni OU Co RESISTANT A CHAUD

L'expérience a montré (10) (11) que les défauts les plus à craindre lors du soudage des superalliages en régime débouchant permanent étaient les fissures transversales et les fissures verticales de zone fondue.

Ces défauts présentent dans leurs mécanismes de formation, un point commun qui est la forme particulière du front de solidification ; caractérisée par des ventres ou renflements locaux.

Pour maîtriser le soudage de ces alliages il convient d'étudier les bains liquides en relation avec les paramètres opératoires afin d'éviter les formes favorables à l'initiation des défauts. Toute méthode d'examen doit, pour être valide, permettre une appréciation tridimensionnelle de la surface isotherme du front de solidification.

4. METHODE D'OBSERVATION DES FRONTS DE SOLIDIFICATION

Les techniques d'examen en dynamique étant très difficiles à mettre en oeuvre il a été choisi de s'orienter vers des observations à postériori.

La technique la plus simple consiste à observer macrographiquement la soudure selon des plans verticaux longitudinaux et verticaux transversaux (figure 7).

Les observations réalisées après une attaque chimique appropriée révèlent des rides périodiques qui semblent matérialiser le front de solidification au cours de sa progression (figure 8).

Une étude plus approfondie de cet "effet mémoire" a révélé que :

- il n'existait pas de différences de composition chimique entre une ride et un intervalle,
- les rides étaient des zones caractérisées par des tailles de dendrites plus fortes et d'orientation légèrement différentes.

Il semble que ces rides soient dues à des pulsations de la vitesse d'écoulement et de solidification du liquide.

Cette technique particulièrement simple et fidèle présente cependant des inconvénients :

- les attaques chimiques ou électrochimiques sont difficiles à mettre au point et à mener pour obtenir des résultats exploitables sur tous les alliages,
- il est arrivé que l'on ne puisse pas mettre en évidence de fronts dans certains cordons, contrairement à toute logique (10 à 20 % des cas selon les alliages),
- la précision dans le positionnement du plan d'examen et la qualité de l'usinage effectué conditionnent quelquefois la validité de l'observation.

Néanmoins, elle conserve tout son intérêt pour l'étude des terminaisons de soudure et la résolution de problèmes ponctuels.

A titre d'exemple la figure 9 montre la *visualisation longitudinale obtenue lors d'une étude sur les terminaisons de l'alliage 718.*

Pour améliorer la fiabilité des observations macrographiques, il a paru intéressant de modifier la composition chimique à un instant donné pour créer un contraste entre le bain pollué et le métal déjà solidifié.

La frontière entre les deux zones correspond à la forme du front de solidification à l'instant précédant la pollution.

Sur l'alliage 718, les essais de mise au point de la technique ont montré que :

- la meilleure solution consiste à intercaler un feuillard métallique entre deux demi-éprouvettes (figure 10),
- l'aluminium et le cuivre sont les métaux les plus efficaces pour polluer la zone fondue et obtenir ensuite un contraste net à l'attaque micrographique,
- un seul feuillard en A5, d'épaisseur 0,2 mm, est suffisant pour donner après attaque chimique un contraste correct.

La figure 11 donne un exemple de pollution réalisée sur l'alliage 718 avec un feuillard en aluminium.

Cette technique s'est révélée très fiable et a été appliquée également à d'autres alliages moyennant une détermination spécifique de l'élément polluant.

L'utilisation de cette méthode d'examen a permis de tirer les enseignements suivants :

- a) Les deux plans d'examen P_1 et P_2 (figure 7) suffisent pour évaluer le volume et les mouvements du liquide.
- b) Une information rapide et qualitative peut-être obtenue par l'examen d'un seul essai par jeu de paramètres éprouvé.
- c) Une information plus complète implique la réalisation de plusieurs essais par jeu de paramètres et un dépouillement statistique des résultats.

5. ENSEIGNEMENTS CONSECUTIFS A L'APPLICATION DE LA TECHNIQUE SUR L'ALLIAGE 718

L'alliage 718 (NC19 Fe Nb) est d'un emploi courant dans l'industrie des turbomachines. En version forgé il est utilisé pour la fabrication de rotor de compresseur. La soudabilité par faisceau d'électrons est bien maîtrisée jusqu'à environ 12 mm d'épaisseur. Néanmoins cet alliage est susceptible de présenter des défauts de type fissuration de zone fondue pour certains réglages.

Les problèmes de fissuration de la zone affectée associés à la grosseur de grain ne sont pas abordés dans ce texte.

Un plan d'expérimentation exhaustif a été réalisé sur l'alliage 718 en épaisseur moyenne pour étudier :

- les relations entre les principaux paramètres de soudage (focalisation, intensité, vitesse) et la forme des bains de fusion,
- les relations entre la forme des bains de fusion et la présence de défauts,
- la dynamique du bain de fusion.

Les niveaux des paramètres ont été fixés de façon à cerner le domaine de soudage où les cordons sont pénétrés :

- position du point de focalisation théorique couvrant une plage étendue correspondant à plusieurs fois l'épaisseur soudée.
- intensité : de 120 à 180 mA,
- vitesse de soudage : entre 1 et 2 m. min⁻¹.

La tension d'accélération a été maintenue constante à 55 KV.

Au total plus de 220 essais ont été réalisés.

Les paragraphes suivants présentent la synthèse des observations effectuées.

5.1. Relation entre paramètres et forme du bain

L'analyse des macrographiques relatives à chaque essai permet de diviser la zone fondue en trois régions distinctes qui répondent différemment aux variations des paramètres (figure 11) :

- une zone supérieure ou trainée liquide endroit,
- une zone médiane pouvant présenter des ventres,
- et une zone inférieure correspondant à la trainée liquide envers.

L'influence de la variation des paramètres sur la morphologie de ces trois régions ressort de la façon suivante :

a) Trainée endroit

La trainée de liquide endroit est essentiellement dépendante du paramètre position du point de focalisation du faisceau électronique.

Le volume maximum est obtenu pour des positions du point de focalisation éloignées de la surface supérieure de la pièce.

La trainée minimale est obtenue pour des valeurs proches de la surface supérieure.

b) Zone médiane

Cette zone est également principalement influencée par la position du point de focalisation qui entraîne, ou non, la formation de ventres. Ces derniers sont les plus marqués pour une focalisation du faisceau légèrement au-dessus de la surface supérieure de la pièce. Ils deviennent très faibles pour une focalisation située à environ 2 ou 3 fois l'épaisseur soudée par rapport à la surface supérieure de l'éprouvette.

c) Trainée envers

L'importance de cette zone est influencée par les trois paramètres principaux. Intensité, focalisation et vitesse de soudage.

Un accroissement de l'intensité provoque une augmentation du volume de la trainée envers, inversement, un accroissement de la vitesse de soudage en provoque une diminution. La trainée envers est systématiquement minimale pour des positions du point de focalisation situées entre la surface et la mi-épaisseur de l'éprouvette.

Du point de vue comportement d'ensemble, l'expansion des trainées endroit et envers s'effectue au détriment de la partie médiane.

Deux profils types caractéristiques sont donnés avec les réglages correspondants par les figures 12 et 13.

5.2. Relations entre la forme des bains et la présence des défauts

Les défauts observés dans le plan expérimental sont des fissures verticales. Leur formation est associée à la présence de ventres plus, ou moins prononcés dans la partie médiane. Quoique leur formation ne soit pas systématique, il semble que des fissures puissent apparaître lorsque la profondeur du ventre dépasse 1 mm.

L'apparition de ces défauts peut s'expliquer de la façon suivante :

Le plan médian est le plan de convergence des dendrites en fin de solidification, il est le siège d'un enrichissement en impuretés et microretassures. Deux cas peuvent être dissociés :

a) Bain de fusion sans renflement ou ventre de la partie médiane (figure 15)

La fin de solidification a lieu pratiquement simultanément sur toute la hauteur de cette zone, d'où une répartition homogène des impuretés et autres défauts de compacité.

b) Bain de fusion présentant un renflement de la partie médiane (figure 16)

La fin de solidification se produit au milieu du renflement. Les impuretés et défauts de compacité se trouvent concentrés dans un petit volume environ à mi-hauteur de la soudure à un niveau où les contraintes engendrées par le retrait au refroidissement sont les plus intenses.

Des fissures peuvent alors s'initier à cet endroit puis se propager dans le plan médian de la soudure.

De toute évidence la seconde configuration apparaît plus néfaste.

5.3. Enseignements sur la dynamique de bains de fusion

A l'usage il s'est révélé que la méthode de pollution permettait également de visualiser les différents courants existant au sein du métal liquide. La dilution de l'insert n'est pas homogène dans l'épaisseur de l'éprouvette et varie en fonction des lignes d'écoulement du liquide. L'attaque chimique ultérieure les révèle en créant un contraste visible entre les zones polluées différemment.

Les enseignements tirés de l'ensemble des observations montrent :

- a) Les trainées endroit et envers du bain de fusion sont formées par deux grands courants liquides indépendants et réguliers (voir figure 1). Ceux-ci sont particulièrement visibles pour les valeurs de focalisation extrêmes produisant des bains de fusion volumineux.
- b) L'écoulement du liquide en fin des trainées est souvent turbulent.
- c) Les fronts de solidification droits sont précédés par des zones fortement agitées, délimitées par les écoulements des trainées liquides supérieures et inférieures (figure 14). Ce volume liquide est soumis à une forte agitation, on y observe des tourbillons que l'on peut associer aux ventres des fronts de solidification.
- d) Les cordons non pénétrés avec des ventres dans leurs parties inférieures présentent deux courants liquides distincts (figure 15) :
 - un écoulement principal formant la trainée liquide endroit,
 - un écoulement tourbillonnaire au niveau du ventre du front de solidification.

A partir de ces enseignements un modèle expliquant le comportement du bain de fusion a été établi :

Les écoulements liquides correspondant aux trainées endroit et envers du bain de fusion délimitent avec le front de solidification un volume où le liquide est soumis à une violente agitation. L'action cumulée de l'homogénéisation de la température du liquide, du fait de l'agitation et du phénomène de cavitation, retarde localement la solidification du métal et forme dans le front un ventre dont la profondeur fluctue, l'écoulement tourbillonnaire qui le crée étant de nature instable.

Ce modèle illustré par les figures 12, 13 et 14 reflète le soudage par faisceau d'électrons à jet débouchant en faibles épaisseurs.

6. CONCLUSION

Le but de cette présentation était de décrire une technique d'observation du bain de fusion en soudage par faisceau d'électrons.

La méthode de pollution de la zone fondue qui a été mise au point pour visualiser les fronts de solidification s'est montrée à l'usage fidèle et simple à mettre en oeuvre.

appliquée à l'alliage 718 elle a permis de définir :

- les relations entre paramètres de soudage et la forme des bains de fusion,
- les relations entre forme des bains de fusion et les défauts observés.

La présence des ventres dans la partie médiane du bain a été confirmée comme néfaste et favorise la formation de défauts tels les fissures verticales dans le cas de l'alliage 718.

En outre les enseignements concernant la dynamique des bains de fusion ont permis de mieux appréhender le comportement des bains lors du soudage à jet débouchant en faible épaisseur.

BIBLIOGRAPHIE

1. Y. AHATA, E. ABE, M. FUSISAWA
A study on dynamic behaviors of electron beam welding (report 1). The observation by a fluoroscopic method
Transaction of JWRI 5 n° 1 1976 p. 1 à 9

2. V.P. MOROCHKO, Yu PANOV, A.N. SOKOLOV
Improving the resistance of high - temperature alloys to hot cracking during electron beam welding
Automatic welding 8 1979 p. 37 à 39

3. S. TOMOHIKO, K. HISANAO, O. HIANORI
Effet des paramètres de soudage et prévention des défauts en soudage par faisceau d'électrons à grande pénétration sur tôles fortes d'acier
Le soudage dans le monde 1979 N° 7/8 17 p. 197 à 207

4. V.P. MOROCHKO, B.F. YAKUSIN, A.M. VERIGIN
The selection of energy parameters of electron beam welding aimed at reducing the formation of hot cracks in the weld zone of creep resisting alloys
Automatic welding 8 1979 p. 4 à 7

5. B de SIVRY, B. SUDREAU, C. BONNET
Soudage par faisceau d'électrons de canalisations posées en mer profonde
Soudage et Technique connexes 2 1981 p. 5 à 17

6. H. KITA, Y. KAHATSU, T. NAKAZAKI, Y. AKATSO
Application du soudage FE à grande puissance au soudage en forte épaisseur
Le soudage dans le monde 19 1981 p. 80 à 90

7. Y. ARATA, K. TERAJ, H. NAGAI, S. SHIMIZU
Fundamental studies on electron beam welding of heat resistant superalloys for nuclear plants (report II)
Transaction of JWRI 6 n°1 1977 p. 70 à 79

8. Y. ARATA, K. TERAJ, S. MATSUDA
Studies on characteristics of weld defect and its prevention in electron beam welding (report II)
(some metallurgical features of weld porosities)
Documentation I.I.W. IV 147 1974 p. 69 à 78

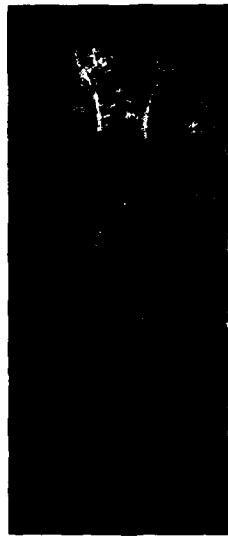
9. Y. ARATA, E. ABE, E. NABEGATA, W. FUJISAWA
Dynamic welding phenomenon during EB welding
Publication du CEA 2nd CISFFE 1978 p. 13 à 27

10. COST MTU D15
Welding of PM superalloys
Cost 50 D15 1979

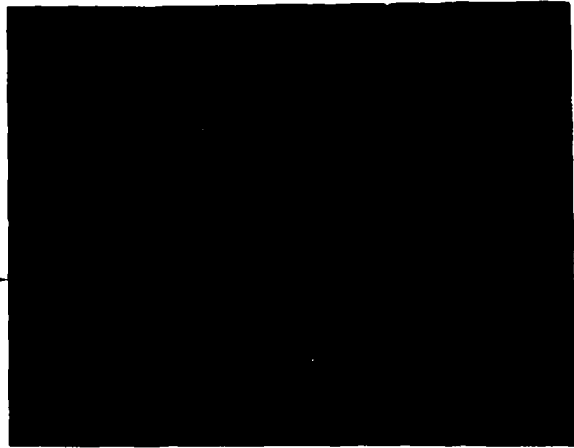
11. TURBOMECA
Soudage FE du Ni 17 CDAT
STPA MA n° 81 L.T. 4



Figure 1 : FISSURE HORIZONTALE DE ZONE FONDUE



x 8,5



x 50

Figure 2 : FISSURE VERTICALE DE ZONE FONDUE



x 50

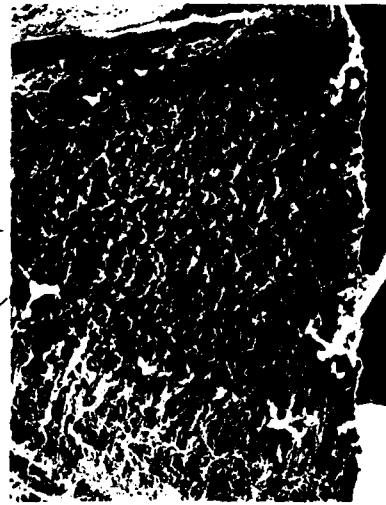


Figure 3 : RETASSURE VERTICALE DE ZONE FONDUE



X 5

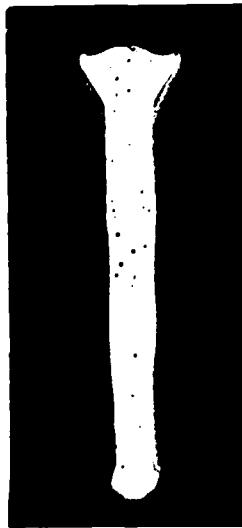
FRACTOGRAPHIE D'UNE
RETASSURE



X 20

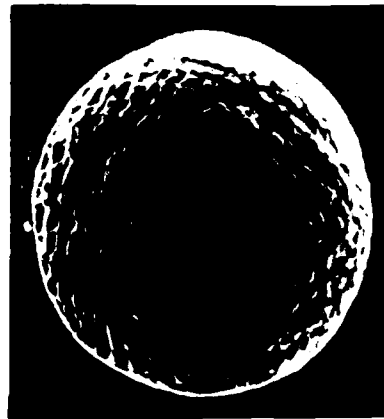
ASPECT
DENDRITIQUE

Figure 4 : SOUFFLURE DE ZONE FONDUE



X 85

DETAIL D'UNE SOUFFLURE



X 1000



Figure 5 : CAVITE DE ZONE FONDUE

COUPE LONGITUDINALE



X 5

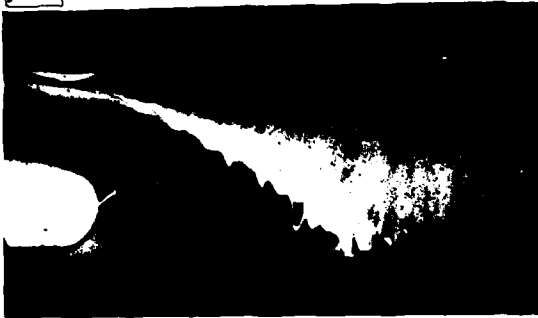
COUPE TRANSVERSALE



X 5

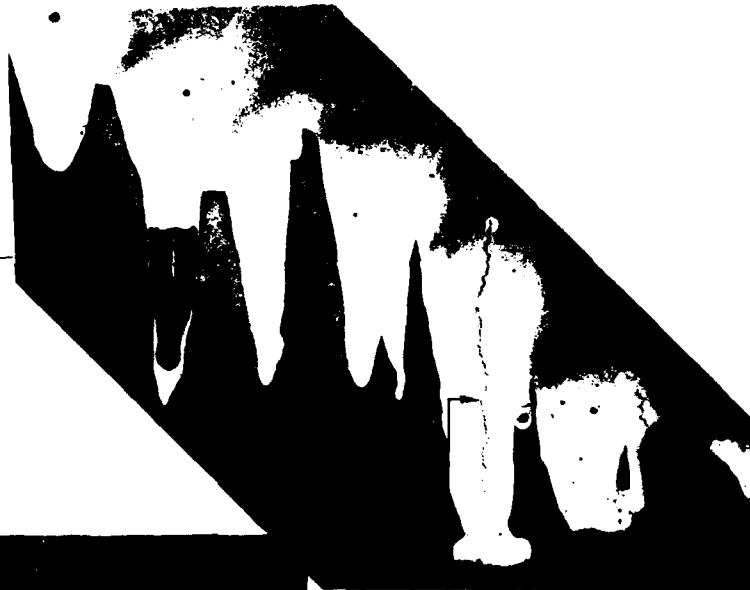
CAVITE

Figure 6 : DEFAUTS DE DOIGTS DE GANT



Terminaison d'un cordon
(régime transitoire)

x5

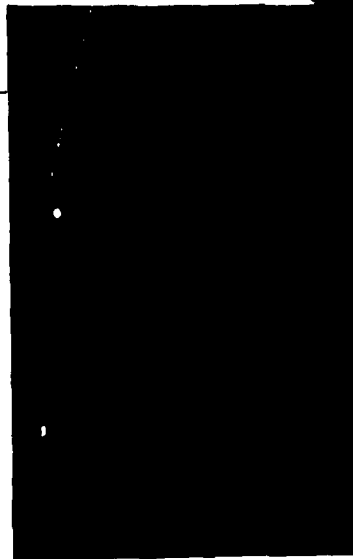


Cavité

x30

Surface de non cohésion
"goutte froide"

Fissure de
doigts de gant



x100



Figure 7 : DESCRIPTION D'UN BAIN DE FUSION

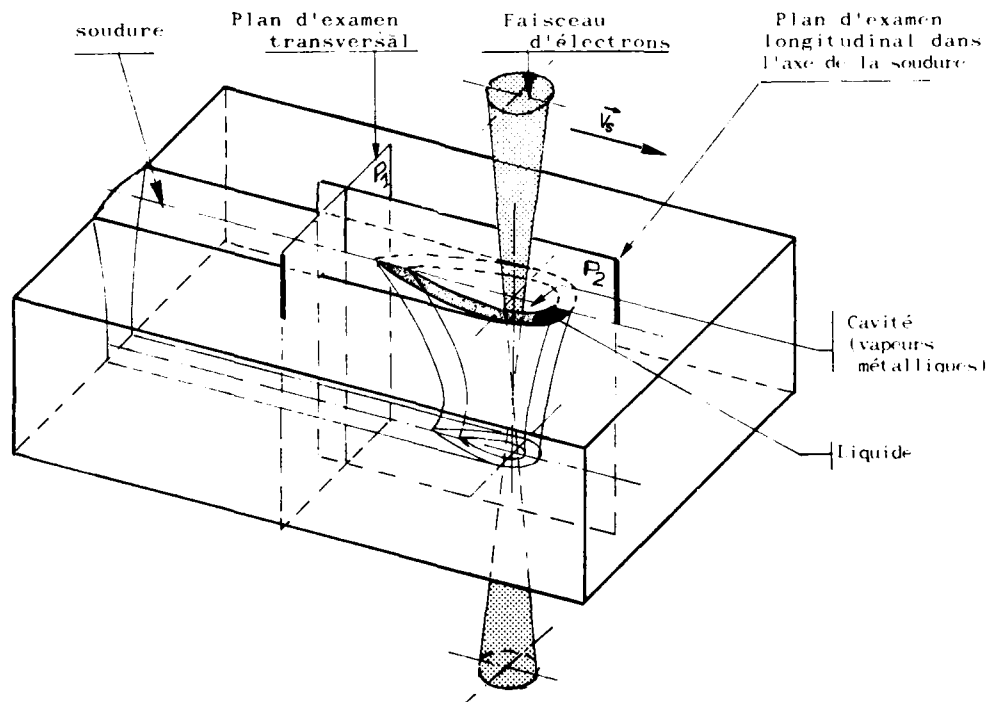
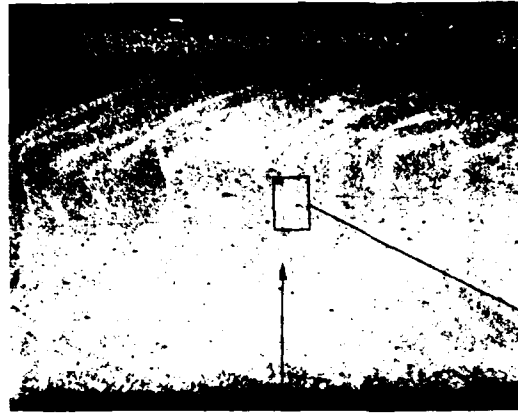


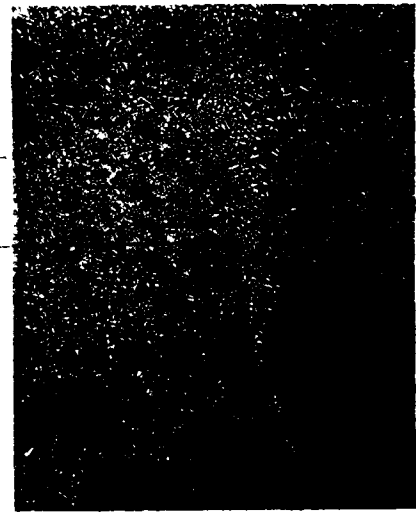


Figure 8 : EFFET MEMOIRE D'UNE ZONE FONDUE
(examen des rides de solidification)

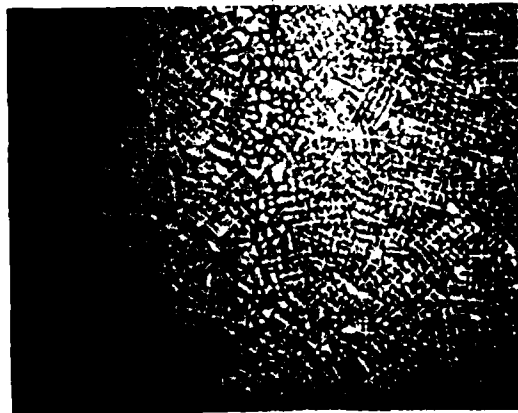


x7

Rides de
solidification



x320

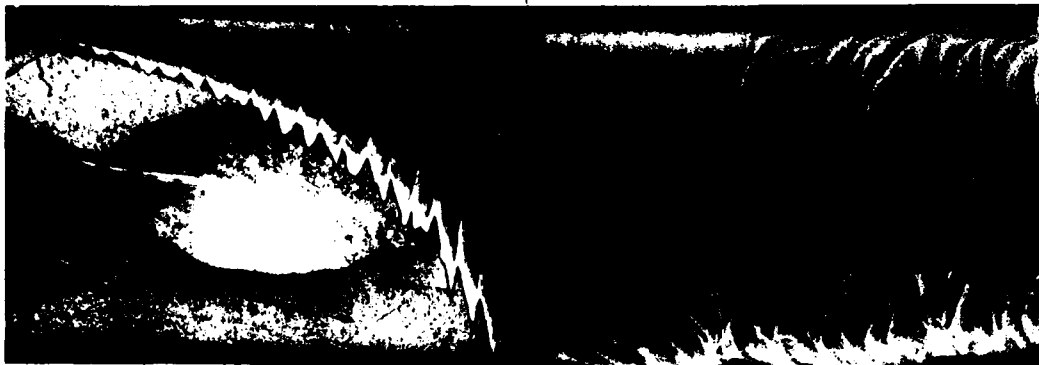


x800



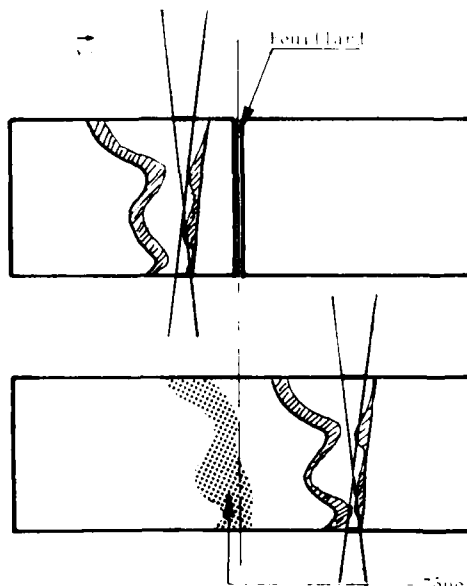
Figure 9 : EFFET MEMOIRE DANS LA TERMINAISON
D'UNE SOUDURE

RIDE DE SOLIDIFICATION



x 6

Figure 10 : PRINCIPE DE LA METHODE DE POLLUTION
DU BAIN DE FUSION



zone polluée



Figure 11 : PARTAGE D'UN BAIN DE FUSION

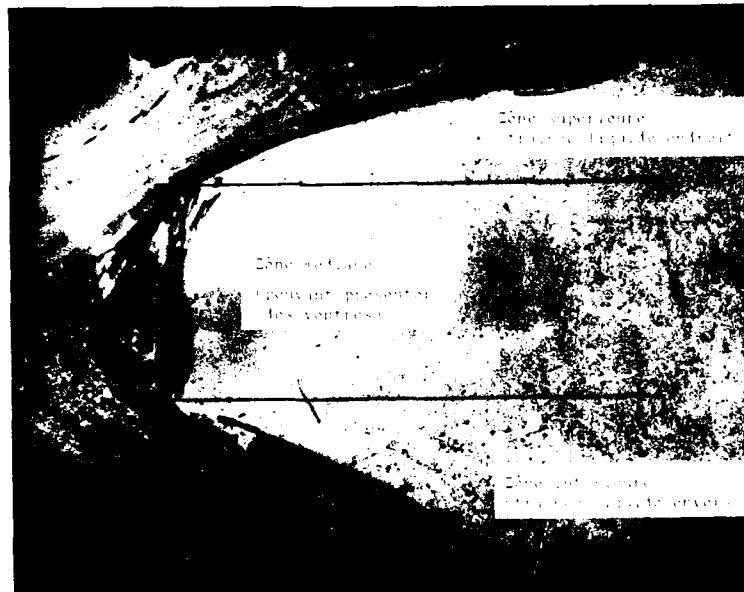




Figure 12 : PROFIL TYPE DE FRONT DE SOLIDIFICATION
SANS VENTRE DANS LA PARTIE MEDIANE



X 5

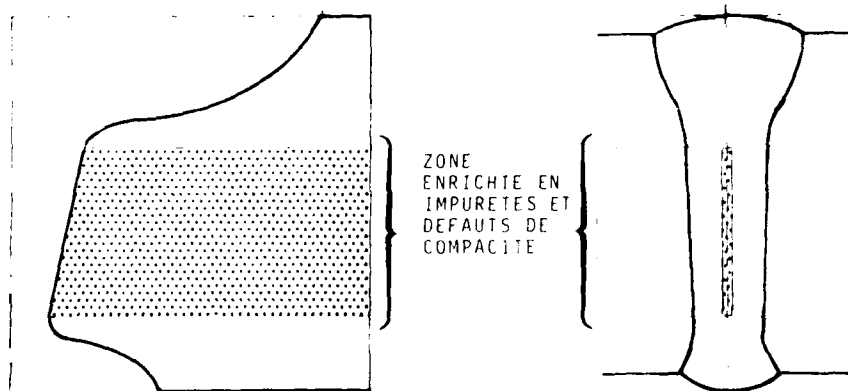




Figure 13 : PROFIL TYPE DE BAIN DE FUSION AVEC VENTRE DANS LA PARTIE MESSAGE

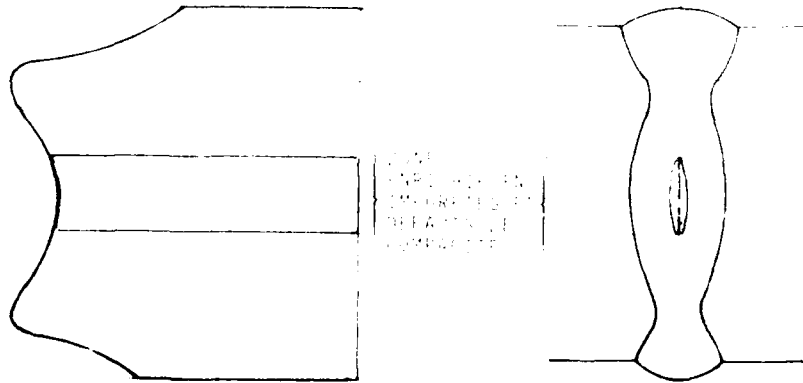
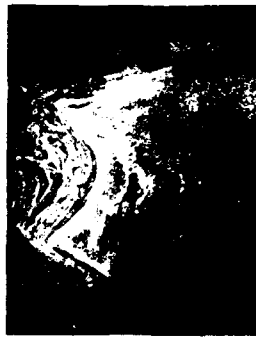




Figure 14 : PHÉNOMÈNE DE CAVITATION DU LIQUIDE
AU NIVEAU DES FRONTS DE SOLIDIFICATION
(cas de ventres importants)



schématisation de l'écoulement du liquide

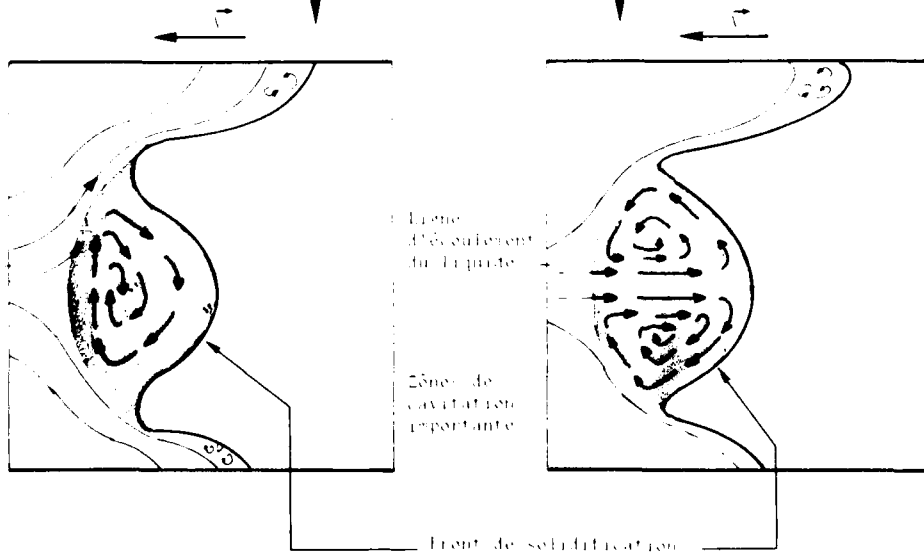




Figure 15 : ECOULEMENT DU LIQUIDE DANS LE CAS D'UN CORDON
NON CENTRE PRESENTANT UN VENTRE

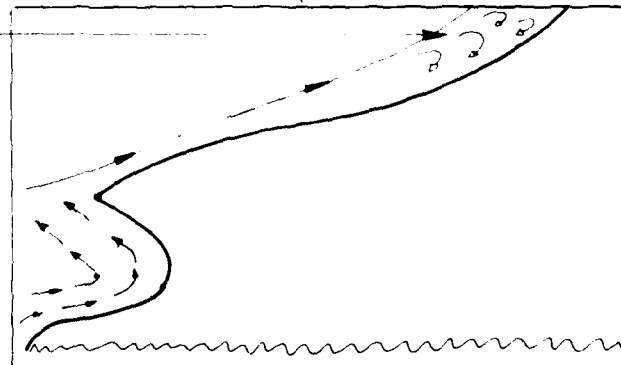


Schématisation de l'écoulement

Turbulence en fin
de traînée liquide

traînée liquide

Ventre



THE APPLICATION OF DIFFUSION BONDING AND LASER WELDING
IN THE FABRICATION OF AEROSPACE STRUCTURES

By: S.B. Dunkerton
Senior Research Engineer: Solid Phase Welding Group
and C.J. Dawes
Principle Research Engineer: Laser Section
THE WELDING INSTITUTE
Abington Hall
Abington
Cambridge
CB1 6AL
England

SUMMARY

A review is given of work undertaken in both diffusion bonding and laser welding which is relevant to the aerospace industry. The wide use of superplastic forming/diffusion bonding of titanium alloys is mentioned with reference to particular applications. This is extended to include the newly developed superplastic aluminium alloys and data are presented on the diffusion bonding of conventional aluminium materials.

The laser welding of aluminium, steel, nickel alloys and titanium alloys is covered with detail given on mechanical properties such as tensile and fatigue. The weld quality is shown to be tolerant to changes in process parameters by means of weldability lobes while dimensional tolerances such as beam/joint alignment and component fit-up can be critical. Finally, the development of laser beam spinning is mentioned with data on the increased tolerance to joint mismatch.

INTRODUCTION

Welding is relatively little used in the aerospace industry compared to other major industries. However, the development, over the last 20 years, of welding methods which have less detrimental effect on material properties and shape than more conventional arc welding has led to a gradual increase in the use of welding. The two processes considered here, diffusion bonding and laser welding are capable of joining a wide range of materials of interest in aerospace fabrications and offer significant advantages over conventional fusion welding. Of particular importance is the ability to join the more difficult aerospace alloys with minimal component distortion and high reproducibility of joint quality.

The aerospace industry is the main user of diffusion bonding in the world today. The technique relies on diffusion controlled mechanisms to form a metallurgical bond between contacting surfaces, with minimum macroscopic deformation. Where feasible, solid state bonding is used when microyielding, creep, dissolution of contaminants/oxides and diffusion form the bonding mechanisms. However, certain metals and metal combinations benefit from the introduction of a dissimilar metal interlayer to form a liquid phase diffusion bond. In this case, the interlayer material reacts with the parent metal to form a eutectic composition which melts at the bonding temperature. The time to form the melt is generally very short, but the bonding time can be extended either at the eutectic temperature or below, to diffuse away the dissimilar elements and hence raise the remelt temperature.

Where diffusion bonding has proved most successful is in the joining of titanium alloys. These materials are readily bonded in the solid state with no special preparation of the surfaces. By combining the diffusion bonding of titanium with superplastic forming, significant advances have been made in aerospace technology. Further material developments have introduced aluminium alloys into the superplastic field, by a range of thermo-mechanical processing techniques. Of future importance to aerospace will be the joining of these new superplastic aluminium alloys, particularly if the superplastic forming/diffusion bonding (SPF/DB) technique developed for titanium can be adapted for aluminium. This paper will discuss briefly the SPF/DB process for titanium and review some recent work undertaken at The Welding Institute on the diffusion bonding of aluminium alloys.

Laser welding is a fusion technique which operates with a keyhole mechanism to form a deep penetration weld. The depth of penetration achieved by laser welding is less than that possible with electron beam welding, but the process has the advantage of being able to operate in any desired atmosphere. Also, the laser has great potential flexibility for use in industry since the beam can be transmitted substantial distances which provides the opportunity for multi-station working.

Laser welding of aerospace materials has been investigated at The Welding Institute where it is recognised that aluminium alloys pose certain problems while steels, nickel alloys and titanium are generally weldable. Weldability lobes have been established for a range of materials in both butt and T-joint configurations. These have demonstrated the laser weld to be tolerant to changes in the main process parameters. However, beam/joint alignment and component fit up are important because of the inherent narrowness of the laser beam and the resultant weld.

Techniques to reduce the criticality of these features have been developed, one of which is laser beam spinning. By causing the beam to move in a circular trajectory, the process can become much more tolerant without detriment to the weld quality.

DIFFUSION BONDING

The ability to join metals in the solid state opens up many opportunities for the diffusion bonding process in the aerospace industries. One advantage is the joining of dissimilar metal combinations which are difficult or impossible to weld by normal fusion welding processes. Typically, titanium to stainless steel and aluminium to titanium have been joined by diffusion bonding. The process may also be applicable to metal and ceramic joints and the joining of the new metal composites, which could be of great benefit to aerospace. These latter materials/material combinations have yet to be fully examined.

Diffusion bonding is also capable of joining large surface areas independently of bonding time, and it is this feature coupled with the ease of bonding of titanium alloys that has resulted in the wide use of the process in aerospace applications.

Superplastic Forming/Diffusion Bonding

The main area of application for diffusion bonding has been in the joining of superplastic titanium either prior to superplastic forming or combined with it in one unique operation: superplastic forming/diffusion bonding or SPF/DB. The development of the technique has introduced large weight and cost savings by the production of complex, internally strengthened components with fewer parts, fewer fasteners and less material waste. Typically, wing sections, doors, frame members and sandwich panels are manufactured in titanium alloy using the SPF/DB process.

Superplasticity is the capability of a material to develop unusually high tensile elongation with a reduced tendency to necking. This stretching capacity is utilised to form various components from a single sheet of material, but when combined with diffusion bonding can be expanded to include double and multiple sheets from which complex honeycombe or net-section components can be produced. This is demonstrated schematically in Fig. 1, with a simple arrangement involving two sheets. In this example, selected areas are diffusion bonded prior to forming and then gas pressure is applied to the sheets causing them to stretch outwards. This forming continues until the sheets contact the die or neighbouring sheets at which point diffusion bonding again occurs between mating titanium sheets. The titanium bonds very readily to itself without any special preparation of the surfaces. Therefore, to prevent bonding in those areas where a joint is not required, a stop-off material is applied. This can be yttria, boron nitride, alumina or graphite to name a few, although the first two are most commonly used.

The SPF/DB process for titanium has been widely used in aerospace since its development in the mid 1970's. One example of the possible improvements is shown by the door panel of an aircraft fuselage, Fig. 2 (1). The conventional fabrication consisted of 16 parts held together by 500 fasteners which was then replaced by a 2 sheet assembly, integrally stiffened, produced by simultaneous superplastic forming/diffusion bonding. The technology for titanium is now well proven, and research has covered the main diffusion bonding aspects of surface finish and cleanliness, bonding conditions and stop-off materials. However, developments in the SPF/DB process does not stop there. Within recent years, new materials have come on the market which could be of even greater benefit to the aerospace industry. One main group of materials is the new superplastic aluminium alloys to which it is hoped the SPF/DB process can be transferred. Touching briefly on the superplastic forming of these alloys, a great deal of research is currently underway examining straining rates, percentage deformation, back pressures, post-SPF HIPping and their effect on cavitation (2). The latter occurs during the forming of the aluminium alloys and can obviously affect the post formed properties. Despite this, the alloys have already found use as formed components for non-structural aerospace applications. Typical examples include door skins and air intakes for the W30 helicopters, bomb rack fairings for the F18, air filter frame and plenum for the DC10 together with various ejector seat components and covers (3). The aluminium alloys are also being considered for structural applications because of developments in higher strength superplastic aluminium alloys and procedures to reduce cavitation.

Aluminium Bonding

To follow the success of the superplastic titanium alloys, it is necessary to develop procedures for diffusion bonding the aluminium alloys. This is not straightforward, as all aluminium alloys are characterised by a tenacious and very stable oxide layer which inhibits the diffusion bonding process. The three basic techniques which have been investigated for bonding conventional aluminium alloys are: 1) solid state bonding without an interlayer 2) solid state bonding with an interlayer and 3) liquid phase bonding (4). Previous published data were very meagre and therefore The Welding Institute set up a detailed development programme to examine the above techniques using initially pure aluminium and two conventional aluminium alloys: aluminium 4.5% magnesium (5083) and aluminium 4.3% copper (2014A). Having established basic procedures, it is hoped the principles can be adapted for other aluminium alloys.

The work was undertaken on 22mm diameter bar, and with the heat treatable aluminium copper alloy in the solution treated and naturally aged condition. Joint assessment

consisted of metallurgical examination and tensile testing.

For all three alloys it was possible to produce high strength joints by the direct, solid state bonding approach but the results exhibited so much scatter that the technique was impractical. Bonding again in the solid state but via a silver interlayer also gave some success. For example, pure aluminium bonded at 550°C and 2N/mm² for 60 mins with a 0.025mm silver foil interlayer, failed in the parent metal at an ultimate strength of 85N/mm². However, the work in this area was limited, and reproducibility of weld quality was not checked.

The third bonding route involving a liquid phase gave the most promising results. The main emphasis of the work was on pure aluminium and the aluminium-magnesium alloy. Interlayer materials of copper, brass and silver were examined, initially in foil form. It was determined by a series of bonding trials that copper foils gave the best results. By adopting a double thermal cycle technique of 520°C followed by 560°C (2N/mm²), pure aluminium was bonded, via copper, with high strength and good reproducibility. Six bonds were produced at the same condition and all gave failure in the parent metal with strengths ranging between 70 and 80N/mm². Single thermal cycles only were attempted for the aluminium alloy when tensile strengths of 210-225N/mm² were achieved (i.e. nominally 60% of the parent).

Further development introduced the use of vapour deposited coatings for the interlayer material. This gave similarly good joints when using the double thermal cycle on pure aluminium, but it was also found that single thermal cycles were just as effective in creating a strong joint. A typical cross section is shown in Fig. 3, where diffusion of the interlayer can be seen up the grain boundaries of the parent aluminium. No attempt was made in this example to completely diffuse away the interlayer material.

Further work with the aluminium magnesium alloy also proved encouraging. One aspect of importance was that by using thin coatings of 0.2µm, the bonding times could be reduced to 10 mins and still give high strength joints. A short production run gave joints with tensile strengths of 60-80% of that of the parent metal. Slight deterioration of joint strength occurred at 5 and 1 mins bonding times, Table 1. Another factor recognised was the condition of the deposited coating. Storage of plated specimens beyond 24 hours, prior to bonding could lead to deterioration of the bond quality. After four days storage the joint strength could drop by 10%.

This provides a very brief review of work undertaken at The Welding Institute on conventional aluminium materials. The success achieved with the liquid phase bonding route suggests that this principle should be examined further for the superplastic aluminium alloys of interest to the aerospace industries. With continued development, it is hoped that the SPF/DB process can eventually be implemented in an industrial environment for joining the new aluminium alloys.

LASER WELDING

The Welding Institute (TWI) has been active in the study of CO₂ laser welding of aerospace materials since the early seventies. The early work covered feasibility studies on plain butt joints for comparison with butt joints made by other welding techniques. Aluminium, nickel, steel and titanium alloys were examined. Subsequently other joint configurations, mechanical properties, welding parameter data and process tolerances have been established. Aspects of this work are presented here.

Materials

Aluminium and its alloys have proven to be very difficult to CO₂ laser weld in the continuous wave mode. This is because this group of alloys does not readily absorb the 10.6µm wave length of the CO₂ laser, unless special absorption coatings are used (this also applies to most similar high conductivity materials). Nevertheless, it has been found that the joint configuration influences absorption. For example the butt joint, when welded with filler wire, with a preset parallel gap between the weld faces and the flared T joint, Fig. 4, tend to absorb the laser beam better than the autogenously welded close fitting butt joint. This is because the angle of beam incident in the latter joint reflects the beam away from the joint instead of in the direction of welding, as occurs with the former joints. Apart from the beam absorption problem, many of the aerospace aluminium alloys, especially the machineable grades, suffer from solidification cracking and porosity when welded. For some alloys laser welding with a filler wire addition (eg type 4043), to modify the weld metal, can reduce or overcome these problems. It is clear, however, that much more research is necessary before high quality laser welds in aluminium alloys can be made in production. This objective is currently being pursued.

Nickel alloy C263, alloy steel Jethete M152, high strength low alloy steel and titanium alloy Ti-6Al-4V have been examined in various material thicknesses up to 10mm. Generally these materials can be easily laser welded. The welds are usually neat in appearance and have low distortion when compared to their arc welded counterparts. Their fusion zone width and grain growth can usually be controlled according to the laser power and welding speed used. To illustrate this Fig 5 shows macro sections, taken transverse to the direction of welding, of three welds, in 4mm thick Ti-6Al-4V alloy, which have been welded at a power of 5kW and welding speeds of 1, 3 and 5 m/min. It can be seen that the weld width has decreased almost inversely proportional to the increase in welding speed for this material.

Joint Configurations

A wide range of joint configurations, Fig. 6, can be laser welded and it includes several which are difficult or impossible to achieve by arc welding without the addition of a filler wire e.g., flared T and T butt joint. A section through a T butt joint, in 3.2mm thick nickel alloy C263, made by a single pass laser weld is shown in Fig. 7. This joint configuration alone has numerous potential applications, such as attaching internal and external flanges and longitudinal fins to jet pipes and rocket bodies.

Mechanical Properties

For butt joints in material thickness below 6mm, tensile strength and fatigue testing perhaps provide the most practical information with respect to mechanical properties for gas turbine applications. Generally, sound laser welds (i.e. free from serious undercutting, cracks and voids) in weldable materials have tensile strengths equal to the parent metal and can achieve fatigue properties similar to those achieved by electron beam (EB) and tungsten inert gas (TIG) welding. Results of tensile tests on laser welded butt joints in 1.5mm thick C263 material are given in Table 2. The tests were carried out at room temperature, 700°C, 800°C and 900°C, with two tests at each temperature. With one exception, all the failures took place in the parent material through the gauge mark. The exception failed at the edge of the weld. Results of fatigue tests on the same joint and material are given in Table 3. Fatigue testing was carried out under conditions of axial loading. An alternating load cycle, where $f_{min}/f_{max} = -1$ was used. The testing temperatures were 750°C and 850°C. The average testing frequency was approximately 148 Hz and the tests were conducted up to an endurance limit of 5×10^7 cycles (approx 100 hrs). Table 3 also shows the results of fatigue tests on EB and TIG welds for comparison.

At room temperature the mean fatigue strength for the laser welds was $193N/mm^2$ at 5×10^7 cycles. The equivalent values for the EB and TIG welds were $190N/mm^2$ and $220N/mm^2$ respectively. Thus it can be seen that at room temperature the laser and EB welds give the same strength, but both are marginally weaker than the TIG welds. However, the scatter band results for all three processes fell within the same range though the degree of scatter was least for the electron beam welds.

When considering the 750°C results it is interesting to observe that the 5×10^7 cycle strengths were virtually identical for the three processes. The mean value was $251N/mm^2$. It was also noted the scatter bands were almost identical. Comparison between the 750°C and room temperature values shows that the increase in strength at 750°C for the laser and electron beam welds was approximately 30% but for the TIG welds was only 15%. This arose because the room temperature strength of the TIG welds is higher than that of the laser and electron beam welds.

Charpy testing is generally recommended for establishing weld toughness in materials thicker than 6mm. No work has been conducted on Charpy testing laser welds in aerospace materials at TWI to date. However, experience gained on Charpy tests on laser welds in structural steels, has shown that this test is difficult to conduct on laser welds. This is because the fracture path often deviates out of the narrow fusion zone into the heat affected zone and sometimes even into the parent metal. Consequently the weld metal is not always tested.

Welding Parameter and Process Tolerances

The laser power, welding speed and focus spot size are the most important parameters as they control the weld heat input per unit of weld length (J/mm). Combinations of these parameters determine the weld fusion zone width and penetration depth. For weldable materials the range of welding power and speed combinations is usually quite wide. Reference to Fig. 5 indicates a speed range of 1 to 5m/min when welding 4mm thick titanium alloy at a laser power of 5kW. For a given material and thickness, the power and speed ranges can change according to the joint configuration due to the different absorption characteristics as mentioned earlier. Fig. 8 shows the different weldability lobes for butt and T joints in the same material and thickness.

The size of the focused spot controls the power density of the laser beam at the work. The spot size is dependent upon, and increases with, the f number of the focusing system. The f number is derived by dividing the focal length of the focusing system by the laser beam diameter incident on the system. Generally, numbers between f3 and f8 are used; however, a systematic study has yet to be undertaken. The smaller the f number the faster the maximum welding speed for a given joint. (This is assuming a perfect focusing optic, as transmissive optics with f numbers less than 2.5 suffer lens aberration). Also the fusion zone produced is narrower and therefore alignment of the laser beam will be more critical. With a smaller f number the depth of the focus is less and the tolerance to focus position variation about the workpiece surface will be less. Also access to working areas is more difficult. Therefore, to ensure maximum tolerances it is best to choose the largest f number that will produce the required welding speed and a satisfactory tolerance to laser power variation.

A laser beam focus position set at the workpiece surface is generally quite satisfactory when laser welding. The tolerance to laser beam focus position in relation to the workpiece surface is generally greater for joints where the laser beam is applied at right angles to the work surface. Where the beam is applied at an angle, variation in focus height can cause the focus spot to be displaced to one side of the joint. As

indicated already the focus height tolerance range is dictated by the f number. A typical tolerance value for making butt joints ± 2 mm when using an f7.5 lens system and a 40mm diameter laser beam.

The distance by which the focused laser beam can be displaced to one side of the joint line and still produce a weld zone which encompasses the joint line is very small, because laser welds are inherently narrow. The absolute value is dictated by the fusion zone width produced by the welding conditions used and is usually approximately just under half the width. Further reference to Fig. 5 (a) and (c) shows that at 1m/min the beam could be displaced up to 2mm to one side of the joint line, whereas at 5m/min for the same laser power, the beam could only be displaced approximately 0.25mm. In nickel and steel alloys the increase in weld width in relation to reduction in welding speed is considerably less than for titanium. In fact at practical welding speeds (>1 m/min) conventional laser butt welds in these materials, in 4mm thick plate would have fusion zone widths less than 1.5mm at their narrowest point.

Because laser welds are very narrow the fit up of the workpieces is important if autogenous welds are to be made. When welding sheet metal joints both joint face gaps and surface fitup have to be considered. Gaps at the joint face present the biggest problem since, if they are larger than the laser beam focused spot size the beam will pass straight through the joint. The thicker the material the larger the gap that can be welded, as there is more bulk material for bridging which results from the metal slumping from the sides of the joint. When conducting conventional laser welding trials on butt joints in 2mm low carbon steel, gaps <0.12 mm have been consistently welded, whereas in 4mm material, gaps <0.18 mm have been achieved. The type of joint configuration also has some influence on the gap that can be tolerated, as can be seen from Fig. 9. The figure illustrates typical test specimens used to establish the weld face mismatch of butt and T joints. The macrosections shown are from test welds in 2mm thick materials. The gap distances between the workpiece faces at the positions where the sections were taken are shown in parentheses on the specimen illustrations. From the macrosections it can be seen that the T joint is more tolerant to face gaps than the butt joint. This is because of the availability of extra bulk metal from the T crosspiece and the influence of the laser beam impingement angle (10° from the normal position) which reduces the weld energy that would pass through the joint. As mentioned earlier both laser power and welding speed influence the fusion zone width. Both joints illustrated were welded at 4kW, but the welding speed for the butt joint was slower (2m/min, cf 3.5m/min), hence the wider fusion zone.

Laser welding is quite tolerant to workpiece surface mismatch when making sheet metal joints. Trials on butt joints in 2, 3 and 4mm materials have been very successful with up to 50% surface mismatch. T joints in 2 and 3mm material have been acceptable with up to 40% mismatch. The reduction arose because the laser beam impingement angle caused the incident position of the beam to move marginally away from the joint line owing to the change in surface height. With 4mm material, 50% surface mismatch was achieved as a result of the wider fusion zone encompassing the joint line. Nevertheless it is unlikely that many industrial applications would tolerate welds with 40% surface mismatch.

The Welding Institute's most recent research has examined laser beam spinning, Fig. 10, in a bid to improve the tolerance to beam/joint alignment and gaps at the joint faces. Most laser welds are often narrower than necessary; they are usually less than a quarter of the width of a TIG weld for the same material thickness. Therefore improving tolerances by expanding the fusion zone width by a factor of 2 is a practical approach. Defocusing the laser beam reduces the laser power density and consequently the weld penetration depth, unless extra power is available to compensate (doubling the spot size reduces the power density to a quarter of its original value). Beam spinning maintains the maximum power density, but reduces the welding speed by at least 20%. Trials with laser beam spinning have shown that gaps of 0.25mm (an increase of $\sim 100\%$) between the faces of butt joints in 2mm material can be bridged with less than 15% total undercutting when compared to conventional laser welds see Fig. 11. Furthermore, butt welds have been made between plates with guillotined edges, which were previously impossible without the addition of filler material.

CONCLUDING REMARKS

Advances in welding technology have resulted in the increased use of welding in aerospace with both solid state joining (diffusion bonding) and deep penetration fusion processes (laser welding) having significant advantages for aerospace application. As shown in the present work, further development is required to fully exploit their advantages particularly in the joining of aluminium alloys.

REFERENCES

1. OHSUMI, M. et al. 'A study in the Fabrication Method of Integrated Light Titanium Sheet Metal Structures by Superplastic Forming/Diffusion Bonding' Mitsubishi Heavy Industries Technical Review. Vol. 21, No. 1, 1984, pp. 42-49.
2. International Conference on 'Superplasticity in Aerospace-Aluminium' Cranfield Institute of Technology, England 12-15 July 1985.
3. Superform Metals (Newsletter provided for Farnborough International 1984).

4. CRAWFORD, D.G. 'The Joining of Aluminium and its Alloys to Similar and Dissimilar Materials by Diffusion Bonding - A Review' The Welding Institute Research Report 216/1983.

Table 1. EFFECT OF BONDING TIME ON THE TENSILE STRENGTH OF DIFFUSION BONDS IN 5083 ALUMINIUM MAGNESIUM ALLOY USING A COPPER INTERLAYER

Bonding time, mins	Tensile strength, N/mm ²
60	255
30	240
15	230
10	237
5	181
1	134

Table 2. C263 ALLOY LASER WELDS - TENSILE PROPERTIES

Test Temperature	UTS N/mm ²	Elongation %	Position of failure
Room temperature	923	19	Parent material through gauge mark
	895 (909)	16	As above
	720	-	As above
700°C	729 (725)	-	As above
	610	14	As above
800°C	485 (548)	16	As above
	245	50	Edge of weld
900°C	218 (232)	48	Parent material through gauge mark

Cross head speed 2mm/min Instron machine

Table 3. C263 ALLOY LASER, ELECTRON BEAM AND TIG WELDS - FATIGUE STRENGTH (N/mm²) - ALTERNATING CYCLE, 5 x 10⁷ CYCLES

Test Temperature	Laser	Electron Beam	TIG
Room temperature	$\frac{+167 - 218}{193}$	$\frac{+190}{190}$	$\frac{+204 - 235}{220}$
750°C	$\frac{+237 - 264}{251}$	$\frac{+232 - 270}{251}$	$\frac{+239 - 264}{252}$
850°C	$\frac{+156 - 184}{170}$	$\frac{+154 - 185}{170}$	$\frac{+131 - 170}{151}$

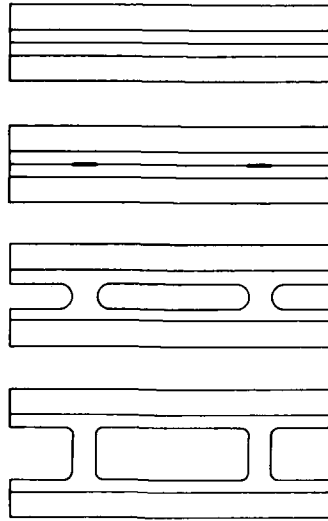


Fig 1 Schematic showing principle of superplastic forming/diffusion bonding

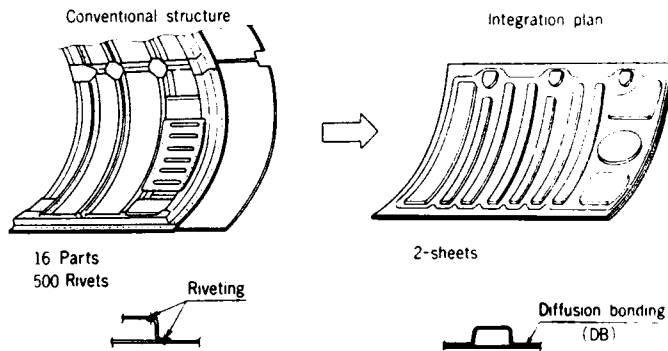
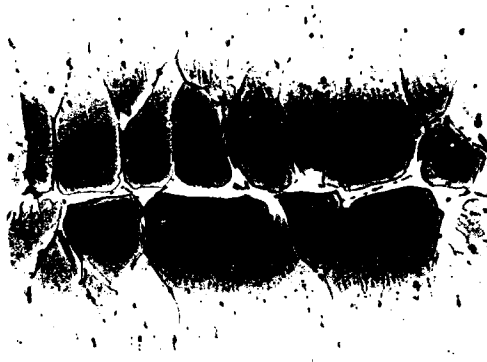


Fig 2. Conventional structure and integrated plan for door panel using SPF/DB (1)



Neg No 51262

Fig. 3. Pure aluminum liquid phase diffusion bond with copper (rod laser, 700 W, 1000°C, 10 min).



Neg No 51263

Fig. 4. Laser welded flared T joint in a 6000 series aluminum alloy, made with the addition of a filler wire.

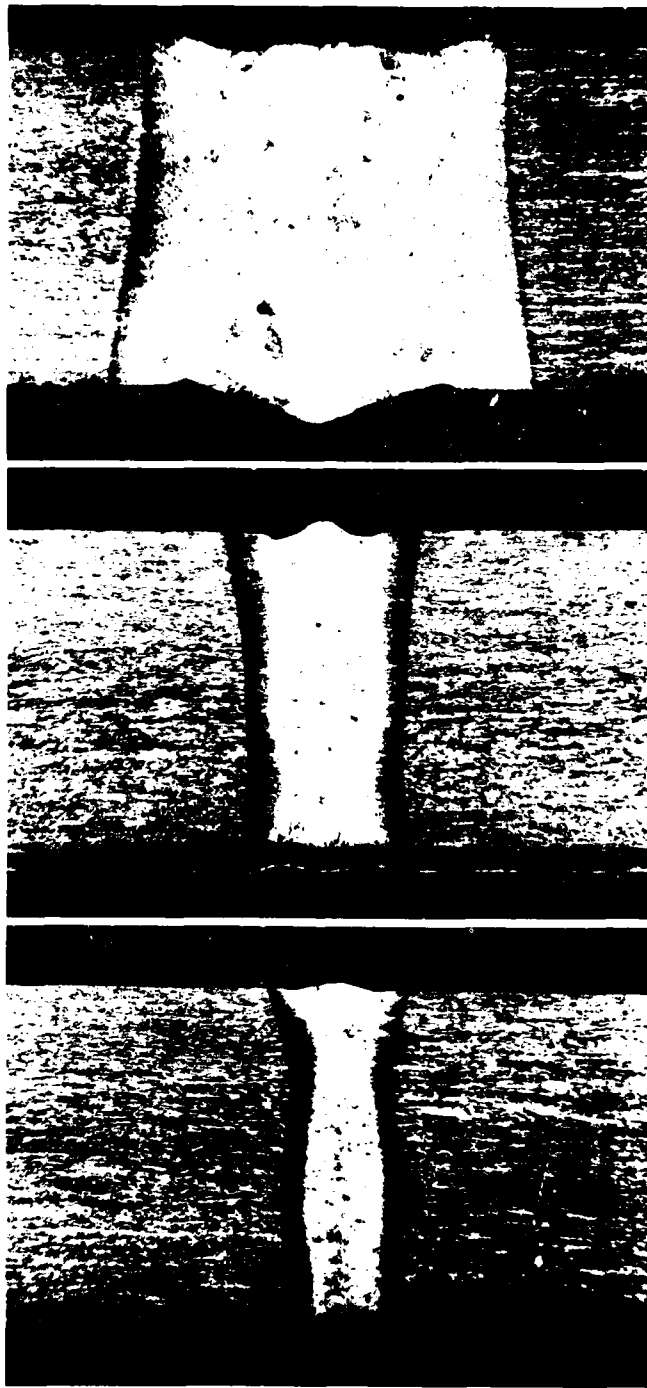


Fig. 5. Macrosections through butt joints in 3mm thick Ti-6Al-4V alloy, welded at 5kW power and speeds of a) 1m/min. Neg. No. OP1351, b) 3m/min. Neg. No. OP1328 and c) 5m/min. Neg. No. OP1326.

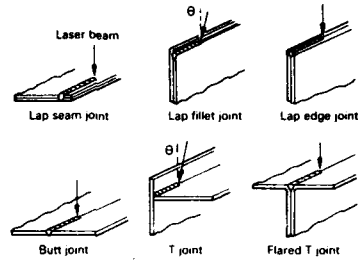
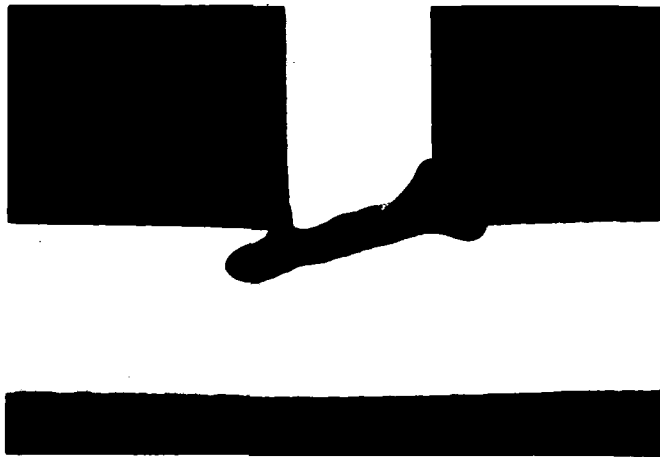


Fig 6. Basic joint configurations which are suitable for laser welding.



Neg No ON2645

Fig 7. Laser welded T joint in 3.2mm thick, C263 nickel alloy. Made at 5kW laser power, 3m/min welding speed and a beam impingement angle of 15° to the horizontal plate.

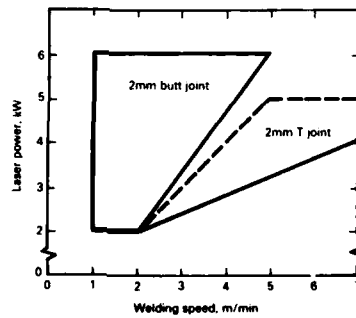


Fig 8. An example of different weldability lobes for butt and T joints in the same material and thickness.

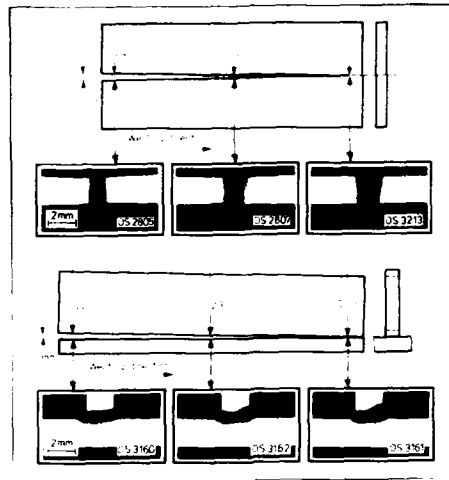


Fig. 9. Typical test for specimens used for establishing weld face mismatch of butt and T-joints. The sections shown are from tests welds in 2mm material.

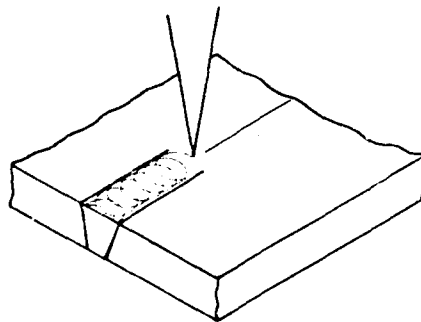


Fig 10. Laser beam spinning trajectory.

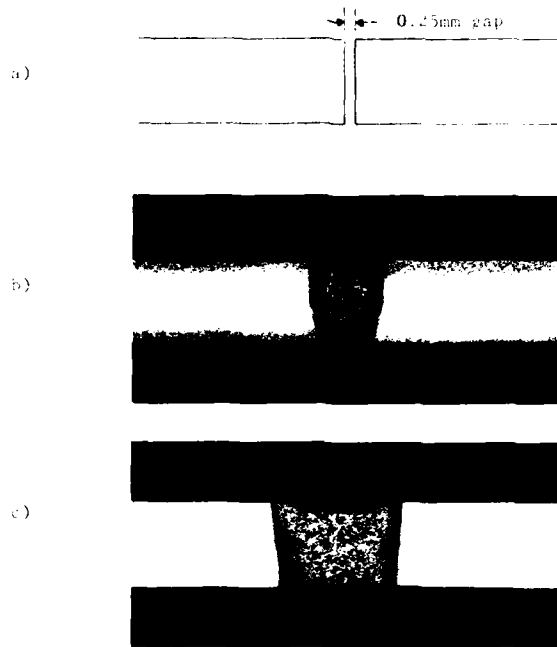


Fig. 11. Sections through conventional and beam spun laser welds: a) butt joint test specimen set up prior to welding, b) conventionally laser welded, Neg No 014743 and c) laser welded with beam spinning, Neg No 014744

ECONOMICAL MANUFACTURING AND INSPECTION OF THE ELECTRON-BEAM-WELDED "TORNADO WING BOX"

Dr. Jurgen Berggreen
Materials and Technologies
Messerschmitt-Bölkow-Blohm GmbH
8900 Augsburg
Germany

SUMMARY

The Tornado wing box is an extensively Electron-Beam-welded titanium 6Al4V-alloy component. The design and the manufacturing steps are described with emphasis on joining and inspection techniques.

As EB-welding requires expensive investments and operations the manufacturing costs have been cut by several means being shown.

The advantages of EB-welding on the material's side and the experience gained with this technique meanwhile allow to use EB-welding for major titanium structures even with thick cross sections as a well-known and established and no longer uneconomic advanced joining method.

INTRODUCTION

The Multi Role Combat Aircraft Tornado being produced in cooperation by Great Britain, Italy and the Federal Republic of Germany has a variable geometry by sweeping the wings.

The highly stressed structural component transferring the wing loads into the fuselage - the wing carry through structure - is the "breast bone" of the Tornado. It is produced together with the center fuselage section at MBB. Due to the component's shape it will be called "wing box" in the following and is shown in figure 1.

WING BOX DESIGN

The main task of the wing box is to pick up the aerodynamic loads from the wings at the wing bearings and to transfer them to the fuselage via shackle bearings. In addition to that the forces from the wing sweeping mechanism have to be taken up. There is only little space in the aircraft for this load transfer so that high force concentrations occur. Although a most weight saving design and an equivalent material has had to be found.

As furthermore the wing box is used as a fuel tank it has to be absolutely tight. The wing box material must not corrode within the fuel medium or it should be protected against corrosion.

The titanium alloy TiAl6V4 has been selected as the component's material. The reason for that is the more favourable combination of the well proven characteristics i.e. high specific strength, high fatigue strength and ductility, good creep resistance at elevated temperatures and good corrosion resistance compared with many steels and especially with the common aluminium alloys (see figure 2).

After all the alloy TiAl6V4 can be used in the annealed condition and without any quenching and the problems involved.

Unlike the aged condition with the annealed condition of TiAl6V4 one cannot achieve a minimum of weight, but the fatigue and crack propagation properties are better controllable especially in the welded state.

The wing box is formed as an open box totally welded. The eight detail parts are integrally stiffened and machined out of plates and die forgings. The cover plate is bolted to the wing box. This allows to machine the welding seams' inner side and to inspect the seams from the inside. Because the quality of the joint is better reproducible, this type is not heavier than a welded but unmachined cover-to-box joint even with respect to the additional weight of the bolts.

For joining the electron beam welding has been selected. Its advantages against conventional fusion welding methods like TIG-welding are manifold. The differences in the performance of the seam and the heat affected zone are obvious from figure 3. The reasons for that are shown in figure 4. Due to less heat input shrinkage and distortion by EB-welding are much less than by conventional TIG-welding.

Furthermore the properties of the EB welded TiAl6V4 in the annealed condition are excellent. In many tests the static strength of the weld was found equal to the parent metal's one; and the dynamic strength is only little less than that of the parent metal; yet for safety reasons the cross section of the area is thickened up by 40 %. The automated EB-welding process ensures a good reproducibility even at a high production rate.

EB-WELDING

The detail parts are machined in a computerized integrated and automated manufacturing system. The lower plates are machined from rolled and creep planed plates; the sidewalls and the facewalls are cut from forgings. For reasons of inspection the welding area is thickened up by 3 mm on each side to be removed later. As no filler wire is used the detail parts' butt has to fit with a maximum gap of 1/10 mm.

The EB-welding of the wing box is performed in vacuum chambers at 10^{-4} hPa and with up to 30 kW being able to weld titanium alloys up to 70 mm thickness in one path. The welding equipments work with nearly 60 kV EB acceleration voltage (see figure 6). Compared with other equipments this voltage is fairly low. But it allows to minimize the insulation and thus the dimension of the welding gun. So the gun can be mounted to a movable gantry and thus positioned to all sides of the work piece by use of relevant tilting devices. The maximum usable welding lengths are shown in figure 7. Welding machines with an acceleration voltage of 150 kV and with a fixed gun therefore have to be dimensioned enough to move the workpiece under the gun. For the wing box this would require a fourfold machine size with correspondingly increased costs and evacuation time.

The narrow welding seam asks for an accurate positioning of the beam to the butt. For that a television camera with monitor and a scanning system for fast and exact alignment of the EB-gun is used. In a fixture the cleaned detail parts are positioned exactly and clamped for welding. At both ends of the seam proper start- and runout-blocks are fixed on to keep the risk of defects involved with the welding's start and stop out of the work piece; these blocks are cut off later. Furthermore an absorption bar is fixed behind the welding seam to catch the remaining energy exceeding the welding root. Then the fixture with the parts is driven into the welding chamber. The chamber is closed and evacuated.

The welding parameters are programmed with data obtained from specifying tests. The gun is positioned with the afore mentioned equipment, camera and scanner. After that the seam is welded and then inspected with the camera by a second path searching for defects visible at the surface. Then the chamber is floated and opened. The welded component is inspected both visually and non-destructively as described later.

An unacceptable seam will be rewelded. Reweldings especially in the TiAl6V4 alloy are possible nearly unlimited times without significant lack of strength properties.

The fully welded wing box is stress relieved in order to reduce any residual stresses by the welding process.

ECONOMY

The electron beam welding is an expensive technique concerning the investment costs and the auxiliary process time. This in general is justified by the technical advantages of the EB-welding. The afore mentioned financial disadvantage can be compensated yet by several means so that EB-welding economywise is competitive with conventional welding methods. With close contacts between engineering and manufacturing the wing box has been designed to minimize the expenditure of EB-welding. So there are only straight seams because it is easier with straight or circular seams than with curved ones to machine them and to fit together the detail parts and to align the gun. The number of seams has been reduced also during the production investment phase. The two kinks in the lower plate of the prototype version have been combined to a single bend. Finally the welding seams have been positioned for good access with the electron beam. To weld the remaining 23 seams with the required production rate the afore mentioned operation sequence would demand for multiple welding machines as only one percent of the machine's utilization time is used for the real welding of a seam. By reducing the idle time we have optimized the process so far that only two welding machines are necessary to accomplish the production rate.

In the smaller chamber the wing box subcomponents are welded whereas in the larger machine the halves are joint to the complete wing box. The small chamber is sized to take up the wing box complete welding with remedial measures in case of any trouble with the large chamber. Both equipments have the same design which optimizes the costs for maintenance, spare parts storage and operation. The pumping time to achieve the vacuum for welding is minimized by a pair of simultaneously working pumping stations in each welding equipment. Yet each pumping station alone is able to evacuate the chamber leading to redundancy in case of break down of a pump. Each chamber is provided with two loading stations enabling to mount the next welding order on the second station whilst the first order is still in operation. The fixtures holding the detail parts for welding are manufactured exactly due to the narrow seam geometry. The fixtures are designed to position and to clamp the parts quickly so minimizing the setting period. Furthermore the fixtures are turnable enabling to turn the components within the chamber by remote control and to weld several seams in one pump-down. Thus it is possible to

produce two halves of a wing box with 16 welding seams all together in only one operation. For the remaining seven welding seams to join the halves to a complete wing box again only one pump-down is required. So there is no need for the repeated evacuation and floating of the chamber for each weld.

By using a modern CNC-control-programming and presetting and controlling the welding parameters are eased and accelerated. The welding current is controlled by a tetrodes' transformer and can be shut down so rapidly in case of any occurring high voltage spark-over that nearly no defect within the workpiece is caused.

The EB-guns are evacuated separately from the chamber. So the metal vapour from the welding puddle is prevented to penetrate into the high voltage area thus largely eliminating the risk of spark-overs.

Finally preventive maintenance helps to avoid welding defects generated by any machine's disorder due to wear or pollution. All these provisions lead to the production time scheme shown in figure 8.

The stress relief heat treatment is performed in a vacuum furnace. Thus the protective coating which is required for treating titanium in an aircirculating oven and which consumes time and costs for applying, especially for removing, is not necessary. In case of repeated stress relieving in an aircirculating oven the repeated removal of the coating and of surface-near layers contaminated with oxygen and nitrogen by abrasive blasting and pickling would lead to loss of thickness. It may be mentioned that the cover plate in the prototype version has been machined out of a bended raw material TiAl6V6Sn2 plate due to the somewhat higher strength in the annealed condition compared to TiAl6V4. Now it is welded together of two plane premachined plates of the TiAl6V4 alloy. This design modification lead to a reduction of the raw material costs and of the machining costs as well because now six parts are premachined in one operation on a six-spindled milling machine.

The material change also enables us to recycle the chips from the cover plate's milling operation within our recycling process qualified for the TiAl6V4-alloy. Also the material change allows to repair defects in the cover plate by a welding operation whereas the TiAl6V6Sn2 alloy could scarcely be repaired due to the poor weldability.

QUALITY ASSURANCE

The quality assurance of EB-welding major structures is triple and related to the welding process, to the welding position and to the welding quality.

To the welding process:

The welding parameters are developed in extensive welding tests, optimized and specified in data-sheets for different applications. According to those the welding equipment is programmed by the operator and checked by both - the responsible welding engineer and the inspector - before starting to weld.

To the welding position:

The advantage of the narrow seam by EB-welding may be a disadvantage if there is a misfit in the assembly of the detail parts or if the beam is deflected. In that case the butts to be welded will be molten unsymmetrically or not totally by the beam. Thus welding defects may occur not visible externally. So a system of witness-lines has proved a success where the lines are scribed on face and root of each welding edge (figure 9). Maintaining a minimum width and counting the number of witness-lines yet visible after welding on both sides of the welding seam are very simple but reliable means to check the position of the seam.

To the welding quality:

For proving the seam quality a combination of ultrasonic test, X-ray test and dye-penetrant test is used. Prior to it the area of the welding seam is machined and smoothed on both sides which are thickened up for this purpose. This is to remove weld leads and undercuts and to set the preconditions for a well defined inspection and for a sure detectability of defects. The ultrasonic inspection which is performed in the immersion technique for sufficient coupling and with focussed beam enables to detect defects equivalent to a 0,2 mm diameter reference hole. A directly linked recorder allows to localize exactly each defect indication and to record it permanently. By X-ray inspection with various directions and parameters defects can be identified additionally. Defects open to the part's surface are detected by dye-penetrant inspection with fluorescent media.

CONCLUSION

Starting from the description of the Tornado wing box as a very complex EB-welded titanium structure means have been shown by which the welding is performed economically and in quality.

The advantages of EB-welding on the material's side and the experience gained with this technique meanwhile allow to use EB-welding for major structures even with thick cross sections as a well-known and established and no longer uneconomic advanced joining method.



Fig. 1 TORNADO Wing Box

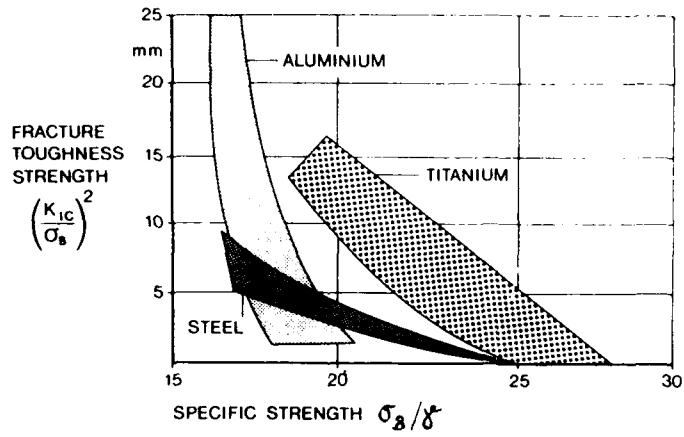


Fig. 2 Comparison of Aerospace Materials

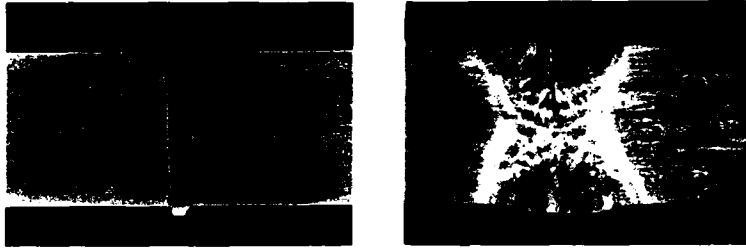


Fig. 3 Etched Cross Sections of Welded 1" thick Plates

	EB WELDING	CONVENTIONAL WELDING
FILLER WIRE	NON	SEVERAL WELD PASSES WITH FILLER WIRE REQUIRED
HEAT AFFECTED ZONE	MINOR	LARGE
SPECIFIC HEAT-INPUT	2,5 kcal/cm	18 kcal/cm
RESIDUAL STRESSES	LOW	HIGH

Fig. 4 Facts about EB- and Conventional TIG-Welding of Titanium

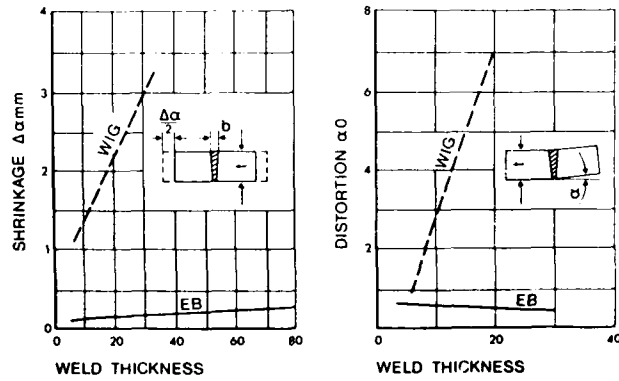


Fig. 5 Influence of the Welding Process to Shrinkage and Distortion

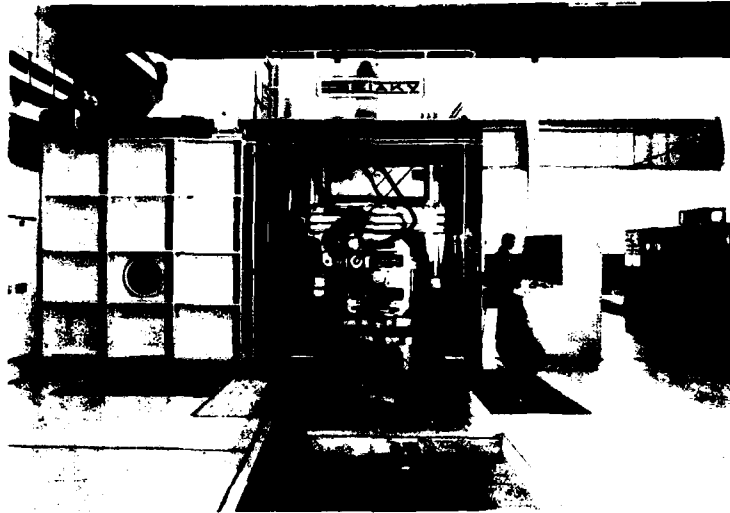


Fig. 6 View to one of the EB-Welding Equipments at MBB Augsburg

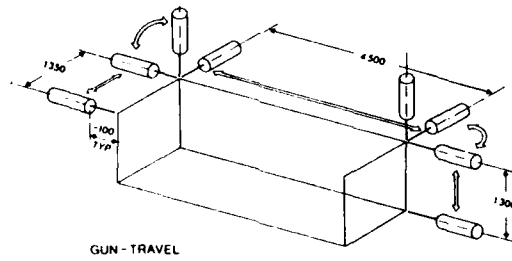


Fig. 7 Maximum Usable Welding Lengths of the Equipment in Fig. 6

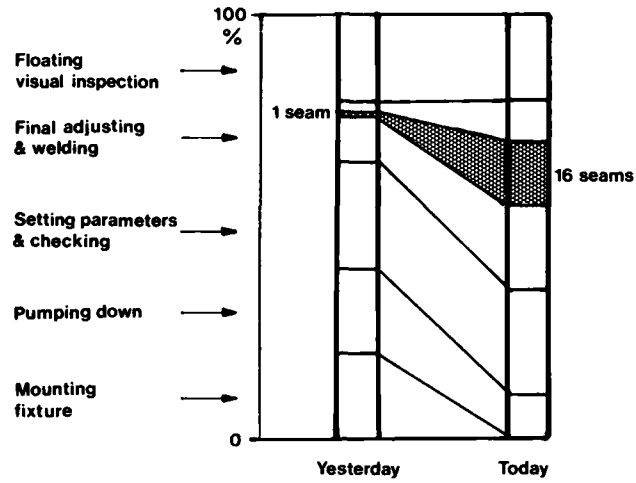


Fig. 8 Production Time Scheme

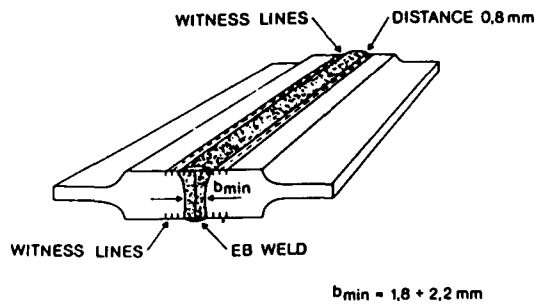


Fig. 9 Quality Assurance by Witness Lines

THE WELDING OF ALUMINIUM ALLOYS
A NEW TECHNOLOGY IN SPACE APPLICATION

Ing. P. MARCHESE, Ing. G. BANINO
AERITALIA, SPACE SYSTEM DIVISION
Corso Marche 41
10146 TORINO - ITALY

SUMMARY

The optimization of the structural weight of the "Spacelab" structure, the first European manned laboratory designed according to "Shuttle" requirements, led to the choice of 2219-T851 aluminium alloy, T.I.G. welded with process completely developed and qualified from Aeritalia as briefly described in this paper.

To demonstrate the high quality and reliability of the welded primary structure, new inspection technique, many different tests on welded joint, and expensive fracture mechanics analysis were applied, and the main assumptions and results here presented.

The main efforts were concentrated to the reduction of number and size of welding defects, improving in one side the welding technique and the other side accepting single defects after fracture mechanics analysis based on sophisticated measurement of their dimensions in the thickness, on the schematization of embedded flaw in tension and bending, and on careful measurement of material properties as here briefly presented.

Possible improvement of T.I.G. application for future space programs (Space Stations) or its substitution with "plasma" welding process are also mentioned.

INTRODUCTION

The Aeritalia is the first company in Europe that has introduced the weld to join primary structural parts of manned spacecrafts, improving remarkably in this last years the technological process and the knowledge in this special field.

This type of joint is a good structural solution to save weight and assembling time, either for pressurized shells to guarantee the structural continuity or for any other item that will never be disassembled, only if the welding process does not degrade too much the material properties in the seam and heat affected zone.

Therefore the welding process of aluminium alloys may introduce a consistent number of defects located in the seam which may strongly reduce the material properties leading the primary structure to a catastrophic failures.

Once selected the weld as structural items connection technique, many effort have to be addressed to improve the welding process reducing the number and the dimensions of the defects, and to apply extensively the fracture mechanics concepts demonstrating that in spite of the defects presence, the "leak before burst" of pressure vessels and the failure in all other structural items are reached only after the life requirements. In the following pages the Aeritalia experience on Spacelab project for what concerns the technological process, the tests, the fracture mechanics analysis of the welded joints are here briefly presented and discussed, with the view to demonstrate the high quality and reliability of the final structure.

WELDING PROCESS DESCRIPTION

The primary structure of spacelab module comprises the cylindrical shells and the conical end closures forming a pressurized compartment where the environment have to be identical in temperature and pressure to an earth laboratory.

The cylindrical shell and the two cones, which the overall dimensions are reported in Figure 1, are both made in aluminium alloy 2219-T851; the cylinder welding longitudinally a curved waffle pattern panels then circumferentially the panels at two forged rolled rings, the cones welding together longitudinally a numerical controlled machined panels, then circumferentially the panels at two forged rings, of different diameter.

The aluminium alloy 2219-T851 (6% Cu, 0.3% Mn, 0.2% Mg) was chosen at the beginning of the program (8) after a trade-off with different other materials for:

- High stress corrosion resistance even after welding
- High fracture toughness properties in all conditions and forms
- Good weldability
- Good machinability
- Minimum reduction of mechanical and fracture mechanics properties after several automatic or manual repairs (more than one fusion).

To guarantee in all the cylinder or cone profile a stress field as uniform as possible, the thickness of the welding zone was increased respect the unwelded skin and chosen equal to 4.0 mm for all the cylinder and 7.0 mm for all the cones (final values after a shaving of the seam) compensating in such a way the reduction of the material properties in the welds and the influence of different other parameters (mismatch, tenting, etc.).

The welding technique so called "Tungsten Inert Gas, direct straight polarity" (T.I.G.), using 2319 as filler wire having 1.6 mm DIA. and "Helium" as inert gas to protect the seam against the atmospheric oxidation, was used for the primary Spacelab module structure (1), (4).

The choice of this process was mainly based on:

- Good protection of the weld pool for atmospheric oxidation;
- High and concentrated heating flux between the tungsten electrode and the aluminium, able to compensate the high material conductivity;
- Reduction of number of fusions with minimum reduction of mechanical properties;
- Regular and uniform penetration of the weld;
- Minimum thermal and structural modification with consequently less internal stresses;
- Minimum influence of the operator skill during welding process.

All the welding process was automatic in a single complete fusion with filler wire, after an initial intermittent manual tack of about 50+60 mm step, apart the circumferential weld in cone made with two passes, the first without filler wire.

The process was always performed in a "clean room" with a controlled temperature between 18+25°C and dust contamination, accepting initially a maximum of 26000 particles (> 10 µ) per cube meter while no specific requirements were established for humidity.

The typical welding parameters for all type of welds and both 4 and 7 mm thickness, defined after many trials and test, including a full scale Development module were:

- Arc voltage : 12 + 17 Volts
- Current : 135 + 220 Amperes
- Wire speed : 1430 + 2700 mm/1'
- Torch speed : 210 + 300 mm/1'
- Helium flow rate : 15 + 25 l/1' (torch side)
- Argon flow rate : 10 l/1' (reverse side)

IMPROVEMENT OF WELDING TECHNIQUE

During the welding of Development and Qualification Units it was experienced that the requirements of humidity, cleaning of the room, cleaning of material edges or filler wire, geometrical relative position of the edges, clamping fixtures position and welding parameters uniformity, were stronger than expected, creating at the beginning a lot of welding defects, that were reduced only after many efforts and experiences acquired on coupons or on the first modules weldement.

Such improvement is schematically showed in Fig. 2 where total number of defects for unit welding length (A), and the number of defects repair because out of specification (B), always for unit welding length, are plotted versus all the different Spacelab Module Units manufactures during all the program.

Briefly the main modifications to reduce as much as possible the density and the size of the welding defects improving joint quality and reliability were:

- To improve surface preparation with more carefull chanfer (1x45°) of sharp edges, complete removal of alodine or any other protective surface of plates and deep vacuum cleaning of the prepared area followed by an inspection at black light.
- To increase the purity of shielding gas "Helium", at more than 99.999%. The presence of minimum quantity of nitrogen and/or humidity in the gas might create pores and non metallic inclusions.
- Protection of the filler wire spool against the umidity and surface oxidation, storing it in sealed containers full of nitrogen at the highest purity.
- Fixtures very stiff to avoid any vibration during the weld process, use of copper clamps to drain the heating, and accuracy in the clamping to not introduce any tenting, mismatch, picking, etc.
- Correct position of the torch respect the surface in circumferential weld and carefull control of the main important welding parameters using recorder.

All these above mentioned efforts were applied in different steps not only to reduce pores, non metallic inclusions, etc. but even to limit geometrical errors as mismatch, tenting, pickins as far as the internal stresses, leading the quality of the final product at very high level.

MATERIAL PROPERTIES AND TESTS ON WELDING

To evaluate the impact of the material degradation after welding and the defect presence in the seam on the structural requirements, a lot of tests on 2219-T851, using flat coupons containing all the parameters considered necessary to satisfy the analytical requirements and to reach the best quality of the joint were performed, involving a qualified personell, test apparatus, large amount of money for a long time. A summary of tests on welded material performed for Spacelab project are here briefly presented:

- mechanical properties as σ_u , σ_y , E, A₅ for many different welding conditions, including automatic and manual repairs to establish the minimum material allowables properties;
- mechanical properties as above in presence of different mismatches, tentings or typical defects to evaluate their impact on the material degradation respect the strength requirements;
- corrosion resistance and sustained load values in presence of high humidity air and laboratory air environment, to protect the structure against corrosion degradation for the required lifetime of 10 years;
- stress intensity factor K_c and crack propagation parameters for each type of thickness to met the requirements of "structural integrity" and "leak before burst";

- fatigue life degradation of specimens with different mismatches and tentings respect the nominal conditions, to demonstrate survival of such type of defect during all the operational life.

Each of above tests was done on sufficient number of specimens to have a correct statistical evaluation of final values, besides preproduction specimens were always made before to weld each type of seam on any module to guarantee the minimum mechanical properties, with chosen welding parameters.

The following table shows the minimum acceptable values obtained from statistical evaluations of all the performed test on welded joint including preproduction samples compared to the design allowable established from the preceding minimum acceptable values reduced from factor different from each type of weld determined on the bases of mismatch, tenting, difficulty to perform the weld, n° of passes, etc.

WELD CONFIGURATION	MINIMUM ACCEPTABLE VALUE (FROM TEST SAMPLES)		DESIGN ALLOWABLE	
	Ultimate (MPa)	Yield (MPa)	Ultimate (MPa)	Yield (MPa)
LONGITUDINAL TENDERS	137	140	137	137
LONGITUDINAL SEAM	137	140	137	137
CIRCUMFERENTIAL TENDERS	137	140	137	137
CIRCUMFERENTIAL ONE FLANGE	175	140	140	137
CIRCUMFERENTIAL ONE SMALL	175	140	140	137
BASE METAL	L	435	437	434
	TB	435	437	434

TAB. 1 - Mechanical properties derived by test for 2219-T851 welded

DEFECT ACCEPTANCE CRITERIA

At the beginning of the Spacelab program, the defect acceptance criteria definition as reported in the Table 2 was mainly based on the Marshall Space Flight Center specification, MSFC-SPEC-504, March 1970 and on American experience in the "Apollo" Program.

As far as it concerns the pores, the mismatch and the tenting, a later on verification by tensile and fatigue test, as just mentioned in the preceding paragraph, was done, including the possibility to enlarge the acceptability beyond the maximum fixed limits in specification.

Most of the actual defects discovered on development qualification and flight units were left in the seam being in line with the minimum acceptable dimensions reported in Table 2.

For all the other defects, the following statements might be applied:

- manual repair if defect is affecting only a limited part of the seam;
- automatic repair if defect is affecting a large zone of the seam;
- to accept the defect as it is after positive results of test reproducing a coupon with identical defect loaded in the same actual condition;
- to accept the defect as it is on the bases of fracture mechanics analysis results;
- to accept the defect under the condition to remove it because appearing on the surface, on the bases of static and fracture mechanics analysis results.

TYPE OF DEFECT	ACCEPTANCE CRITERIA
MISMATCH	0.4 ± 0.9 MM
TENTING	$\alpha \leq 1.30^\circ$
INDIVIDUAL PORE	MAX 2 MM.
NON METALLIC INCLUSION	MAX 2 MM.
UNDERCUT	MAX 0.1 x THICKNESS
ARC STRIKE	NONE ACCEPTABLE
CRACK	NONE ACCEPTABLE
LACK OF PENETRATION	NONE ACCEPTABLE
UNDERFILL	NONE ACCEPTABLE
METALLIC INCLUSION	NONE ACCEPTABLE

TAB. 2 - Defect acceptance criteria for Spacelab project

AIT followed mainly the criteria to repair all the defects out of specification but sometimes, to avoid the risk to introduce with such a technique one or more severe defects than a pore or a nonmetallic inclusion, they were accepted but only on the bases of fracture mechanics analysis positive results (6).

The defect repair criteria and methodology are here briefly summarized, while the tests defining all the mechanical properties of such a technique have been just mentioned in preceding paragraph.

AUTOMATIC REPAIR

NOTE: NORMALLY USED IN CASE OF DIFFUSED DEFECTS.

METHOD A - Automatic rewelding without defect removal.

METHOD B - Automatic rewelding with defect removal.

METHOD C - Automatic rewelding with defect removal and with one manual filling at low current.

METHOD D - Automatic rewelding with defect removal and with one automatic filling at low current.

METHOD A - This method is recommended for repair of weld with lack of penetration.

METHOD B - This method is recommended when the defects grind-out are aligned with the weld seam.

METHOD C - This method is recommended when the defects grind out are not aligned with weld seam.

METHOD D - This method is recommended when a groove on all the seam is required for a complete defect removal.

MANUAL REPAIR

NOTE: NORMALLY USED IN CASE OF LOCAL DEFECTS.

METHOD A - Manual repair with a max defect machine-out depth of 40% of the seam thickness.

METHOD B - Manual repair with a max defect machine-out depth of 80% of the seam thickness.

It is interesting to point out that some welding defects, out of specification, were left on cylinder circumferential weld of Qualification module which was used for "Fatigue and Fracture Mechanics" full scale test, then inspected at the end of the test with same technique preceedingly used, including a destructive inspection with electro-scanning microscope of the most severe defects confirming the not propagation, and the safety of our assumptions and methodologies.

NON DESTRUCTIVE WELDING INSPECTIONS

To verify the welding quality and to minimize the probability of module leak at internal pressure or defect propagation until leak or catastrophic failure under repetitive loads or aggressive environment, all the seams were inspected using:

- Liquid Penetrant both faces after seam shaving, to detect any surface flaw;
- X-ray to detect the hidden cracks or to confirm the presence of surface flaws once revealed by liquid penetrants.

Besides, to accept by fracture mechanics analysis any type of defect, it was necessary non only to measure its length but even the depth and its position in the thickness. For this reason Aeritalia developed a new X-ray inspection technique at two inclinations performed on a films exposed two times under a radiographic source, which displacement is defined in advance.

Two lead wires (or similar like copper), F1 and F2, are applied each side of the object at the same distance from the defect and fitted in a way to be perpendicular to the direction of the source displacement as shown in Fig. 3, then a film 1 is exposed twice moving the source of well known distance from position 1 to position 2. The measurement of the displacements of each lead wire can be plotted in a diagram versus thickness in order to determine the defect position within the weld seam cross section, as shown in Fig. 4.

To minimize reading inaccuracy and to obtain reliable measurements, a second film (film 2 of Fig. 3) has been adopted in Spacelab weld inspections, placed 20 mm from the original film that is normally in contact with the lower weld side, and the displacements versus thickness also plotted.

All the values of defect edge distance from one of the two surfaces measured with the two films method have been compared among them and the extreme boundary assumed.

FRACTURE MECHANICS ANALYSIS

To guarantee the complete fulfillment of "Structural Integrity" and "Leakage Requirement" a Fracture Mechanics analysis (on module primary and secondary structure) has been performed with carefull attention to the cone and cylinder welded areas. The initial standard defects assumed for the analytical life predictions were the same as for the other structural parts:

- $a = 1.5 \text{ mm}$, $2c = 15 \text{ mm}$, $a/2c = 0.1$
- $a = 3.0 \text{ mm}$, $2c = 6.0 \text{ mm}$, $a/2c = 0.5$ } Surface flaw
- $2c = 6.0 \text{ mm}$, for through the thickness crack,

while the material properties as Kc and dc/dN or da/dN were obtained from preceedingly mentioned tests.

The analytical results were largely succesfull, in fact for the most severe loaded areas, the "Leak Before Burst" was demonstrated and the depth propagation of the assumed surface defects through the thickness was reached far beyond the required 200 missions. These results were achieved assuming initial defects dimensions greater than the acceptable welding defects, then the possibility to accept by analysis even some

type defects with dimensions out of specification, as just mentioned in preceeding paragraphs, was investigated.

Firstly an embedded flaw schematization (2), (11), where the welding defect is assumed of elliptical or circular shape was defined taking into account the tension and the bending stress field, then the mentioned special X-ray method was applied to evaluate the defect position in the thickness as depicted in Figure 5, where a and b are the two measure defect dimensions, d is one distance of defect from edge and t are actual thickness.

Using material properties preceedingly measured by test, a Linear Elastic Fracture Mechanics analysis, using "Paris" crack growth formulation, was then performed applying the following statements:

- verification of the "structural integrity" assuming through the thickness cracks with a length equal to 1.2 times the "X-ray" at 90° indication;
- verification of the "leakage" assuming an embedded flaw which dimensions are, in depth and in length, $\Delta = 0.25$ mm each side greater than X-ray inspection indication, as shown in Figure 5, to cover measurement uncertainties and demonstrating that such a flaw become through the thickness crack in more than 200 missions.

Besides, to avoid any chance of corrosion, it was decided to repair or remove any welding defect either lying on one of the skins (surface flaw) or found propagating by analysis until to reach one skin in less than 200 missions.

Before any defect removal but not repaired, the following calculations based on actual gross stresses expected in that area were performed (7):

- residual static strength on remaining thickness taking into account the bending moment due to introduced offset and stress concentration factor K_t for material removal;
- fracture mechanics analysis assuming an initial standard defect in addition to the removed material, to demonstrate the life requirements against the leak on the remaining thickness.

FUTURE APPLICATIONS

Several new manned space projects proposals are appeared during this last year in the European scenario as ARIANE 5, Space Station, Columbus, where the strong reduction in weight and heavier payload transportation capability are required as a main goal to reduce the costs.

Welded primary structures using aluminium alloy 2219 or similar, will be surely chosen, then the welding techniques of aluminium alloys with high reliability and safety will be required either improving TIG technique or developping other processes as the "PLASMA".

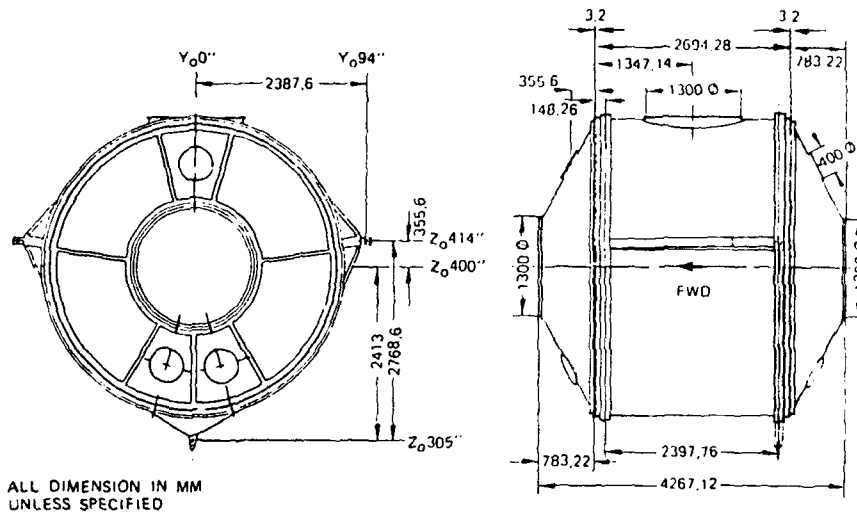
Aeritalia, in these last months, started to plan preliminary activities (bibliography, market investigation of welding facilities, test planning, potential european aluminium supplier) to develop plasma welding technique of 2219 aluminium alloys having thicknesses higher than 3.5+4 mm and to improve TIG welding process on the bases of the past experience, for thinner thicknesses.

In both cases the fracture mechanics analysis will be extensively applied to all the type of welded structures not only for "Leak Before Burst" demonstration and life prediction, but even to enlarge the defect dimensions acceptability respect the present specification.

In the mean the efforts will be addressed to furtherly improve the non destructive inspection techniques applied to large structures, reducing the minium detectable limits and increasing the structural safety of any manned future spacecraft.

REFERENCES

- VARIOUS - Specification on 2219-T851 T.I.G. welding for S/L project, SP-AI-0.00810/5, February 1979.
- SAHA R.C., KOBAYASHI A.S. - Stress intensity factor for an elliptical crack approaching the surface of plate in bending, ASTM-STP-513, 1972, p.p. 3-21.
- FIFTAL C.F. - Fracture mechanics data on 2219-T87 aluminium for the space Shuttle external tank, test report n. 826-2027, Martin Marietta, July 1975.
- MASUBUKI K. - Welding of high-strength aluminium alloys, M.I.T., department of Ocean Engineering, Sept. 1973.
- MASTERS J.N. - Investigation of deep flaws in thin walled tanks, NASA-CR-72606, Jan. 1970.
- BANINO G. - Crack growth evaluation of welding defects, Aeritalia Spacelab doc. RP-AI-0252, Feb. 1979.
- GUCCINI E. - Flight unit defects grind-out evaluation, Aeritalia Spacelab doc. RP-AI-0253, Jan. 1979.
- MARCHESE P., BANINO G. - Fracture mechanics and fatigue criteria in material selection for space applications, AGARD-CP-327, Sept. 1982, p.p. 1-10.
- MARCHESE P., BANINO G. - Fracture mechanics approach applied to spacelab module design, IAF'81, n. 390, Sept. 81.
- LIEBOWITZ H. - Fracture mechanics of aircraft structures, AGARD-AG-176, January 1974.
- ROOK D.P., CARTWRIGHT D.K. - Compendium of stress intensity factors, Her Majesty's Stationery Office, 1974.



ALL DIMENSION IN MM
UNLESS SPECIFIED

FIGURE 1 - SPACELAB MODULE, PHYSICAL DIMENSIONS

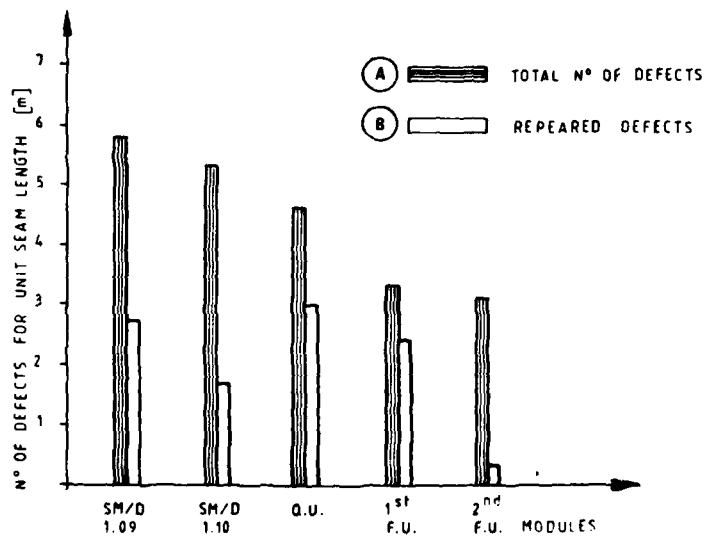


FIGURE 2 - DEFECT DENSITY DISCOVERED AND REPAIRED DURING SPACELAB MODULES MANUFACTURING

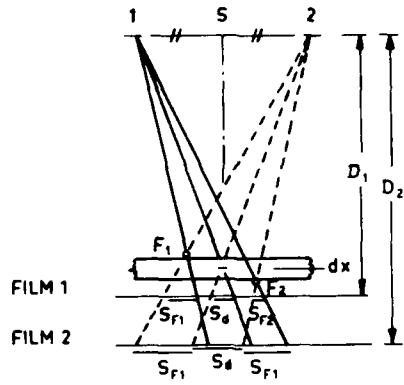


FIGURE 3 - X-RAY AT TWO INCLINATIONS - TWO FILM METHOD

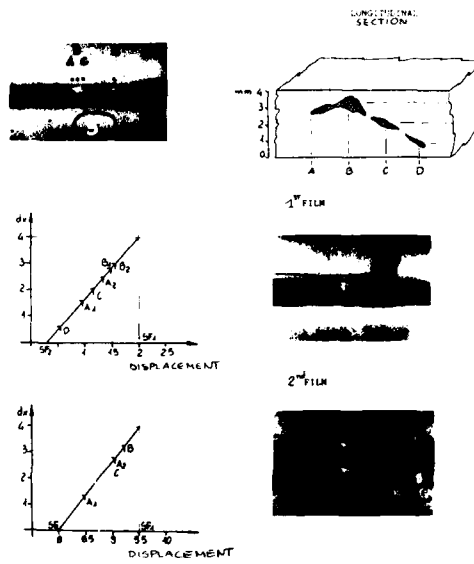


FIGURE 4 - DISPLACEMENT MEASUREMENTS IN X-RAY TWO INCLINATION FILMS

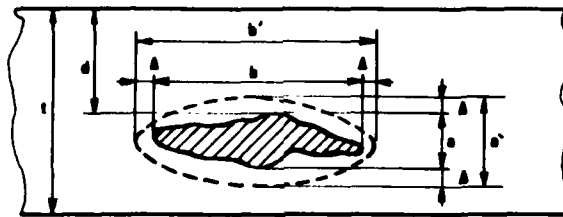


FIGURE 5 - EMBEDDED FLAW SCHEMATIZATION OF WELDING DEFECTS FOR FRACTURE MECHANICS ANALYSIS

RECORDER REPORT ON SESSION II : DIFFUSION BONDING
SPECIALIST MEETING II ON ADVANCED JOINING OF METALLIC MATERIALS

by
MARC DUFOUR

Industrial Material Research Institute (IMRI)
National Research Council Canada (NRCC)
75, de Mortagne
Boucherville (Québec)
Canada J4B 6Y4

Four papers about diffusion bonding (DB) were presented during session II. A fifth paper on DB was also presented at the end of Session I.

Several industrial examples where DB was found particularly useful were presented. Dr. Adam ("Bonding of Superalloys by Diffusion Welding and Diffusion Brazing") has shown us that DB could be advantageously used to repair some important parts (leading and trailing edges in coated vanes). Another example was about the manufacturing of parts that normally requires single crystals. DB allowed the same part to be produced from smaller parts resulting in an improved design which permits fast dimensional changes without coating tool changes.

Authors have demonstrated a high interest for the use of super plastic forming (SPF) techniques combined with DB (called SPF/DB) to improve fabrication processes and the quality of resulting parts. SPF/DB was identified as being already a very powerful technique. There is potential for much more new applications. M. Boire's conference ("Application du soudage par diffusion associé au formage superplastique à la réalisation de structures en tôles minces de TA6V") showed us how economic it could be even if the costs of materials and of specialized tooling are very high, because of the large savings that could be made on man-power. Furthermore the end-results would present better characteristics at least for its weight, as compared to a stainless-steel based design. However, engineering design methods have to be further adapted to these materials. Failure to do so may result in a higher price of the final product, as it would probably not take advantage of those special properties of the material. Mathematical modeling of the forming process has been pointed out by Mr. Boire. A better understanding of the process used with a good mathematical model would allow for better engineering methods and more performant designs.

About the fabrication procedure, Mr. Stephens said that several aspects as the surface preparation and cleaning are very critical. However, by implementing a close process control, high quality products are obtained with a low rejection rate.

An interest was shown for the use of aluminum with SPF/DB. Encouraging results have been obtained by using special alloys, interlayer coating or by bonding, involving a liquid phase. Further work is required in this area to characterize the bonded joint or to convince the industries of its reliability. About future development, it was proposed to investigate the possibility of applying semiconductor fabrication technology for surface etching before bonding.

Finally, even if high quality products rely mainly on good process control, it was determined that NDT techniques are still to be improved in particular for the detection of micro-voids or close-contact disbond, or to overcome the accessibility problem.

There is also an interest for further investigations of the mechanical properties of bonded structures used in a real environment.

Diffusion Bonding in the Manufacture of Aircraft Structure

D. Stephen,
Chief Development Engineer (SPF/DB)
British Aerospace p.l.c.
Civil Aircraft Division,
Filton House,
BRISTOL,
BS99 7AR

S. J. Swadling,
Chief Designer A320,
British Aerospace p.l.c.
Civil Aircraft Division,
Filton House,
BRISTOL,
BS99 7AR

SUMMARY

Over the last twenty years, considerable Aerospace Research and Development effort has been directed to the development of the diffusion bonding (D.B.) process as a means of manufacture of low cost structures. To date the main thrust of these developments have been associated with titanium which has inherent metallurgical characteristics which make this material ideally suited for joining by this technique.

For these titanium alloys which exhibit superplastic (SPF) properties, the combined processes of SPF and DB considerably extend the range of low cost and structurally efficient titanium aerospace components which can be manufactured; even as replacements for conventionally fabricated aluminium alloy components.

Recent developments in the SPF of high strength aluminums and metal matrix composites has stimulated work in the field of DB of aluminium. It is thought that in the longer term this field of DB could have the highest levels of application.

This paper details the range of aerospace structural forms which can and are currently being manufactured using the diffusion bonding process. The process options, bond integrity, and NDT aspects are discussed.

1.0 Introduction

Over the past twenty years, considerable Aerospace research and development effort has been directed towards the development of the metallic diffusion bonding process (DB) as a means of manufacturing primary aerospace structures and components. To date the main thrust of these developments has been associated with titanium alloys which have inherent metallurgical characteristics which make these materials ideally suited to this joining technique. In recent years, however, the development of metal matrix composite materials (MMC) has stimulated work in the field of diffusion bonding of aluminium alloys:- this being an essential process in the manufacture of components from the thin fibre reinforced foil raw product.

Both titanium and aluminium alloys exhibit superplastic properties and hence a further interest in the use of DB has been stimulated by its association with superplastic forming (SPF) as a combined process (SPF/DB) in the manufacture of high quality low cost aerospace components.

This paper reviews the current situation with respect to the use of DB in its own right or in combination with other processes in particular SPF, as a means of manufacturing aerospace structures.

2.0 Diffusion Bonding

DB has been exploited as a method of joining from ancient times but in aerospace manufacture its earliest use was associated with cladding of materials for corrosion protection. This process is generally carried out in cold/high pressure conditions associated with heavy rolling and also involves significant straining/deformation of the materials to be bonded.

By contrast the latest development in the DB process are associated with high temperatures and relatively low pressures with low or negligible strains.

The process of DB is defined in British Standard 499 as

"a joining process where in all of the faces to be bonded are held together by a pressure insufficient to cause readily detectable plastic flow, at a temperature below the melting point of any of the parts, the resulting solid state diffusion, with or without the formation of a liquid phase, causing bonding to occur. Additional heat may or may not be applied."

Two categories of DB are recognised:- these are "solid state" or "liquid phase" and the definition of these is stated as follows:-

"diffusion bonding in which all the reactions occur in the solid state"

and

"diffusion bonding in which solid state inter diffusion between dissimilar materials results in the formation of a liquid phase".

From a practical point of view the primary advantage of liquid phase relative to solid state bonding is the reduced pressures and times associated with liquid phase bonding.

3.0 Theoretical Predictions

The early empirically derived processing conditions for DB, have now been supported by the establishment of a number of theoretical models of the process¹⁻⁶. These models vary in their assumptions but in all cases demonstrate the dominance of surface topography in the determination of the processing conditions required to achieve a bond.

For solid state bonding, the models consider surface diffusional mechanisms for areas of intimate contact, preceded by deformation mechanisms such as power law creep and plastic yielding.

Work has also been done on the modelling of liquid phase bonding when using low melting point interlayer between the bond faces⁵. The primary advantage of the interlayer is its ability to "wet" the bond surfaces and effect "erosion" type mechanisms coupled with rapid transport within the liquid. This model confirms the practical experience of reduced pressures and times to effect a liquid phase bond.

4.0 Process Conditions

The main processing variables associated with DB are:-

- Temperature
- Pressure
- Time

4.1 Temperature

All of the mechanisms associated with DB - diffusion, creep, plastic yielding etc. are assisted by carrying out the DB processing at high temperature.

In a practical situation, it is usual to maintain the temperature of the process constant and uniform and as high as possible subject only to material considerations, such as alloy phase transformation temperatures, and liquid phase temperatures. By maintaining the temperature as high as possible the time to effect a bond is minimised for any given bond pressure and surface condition.

4.2 Pressure

Because of the creep and plastic yield mechanisms, pressure is an important process parameter. Clearly the higher the pressure that can be exerted at a given temperature the lower the time to effect a bond. The level of pressure employed however, is usually a compromise between the economic considerations of time, capital equipment, and tooling material, the latter being a particular consideration for the high temperature conditions associated with titanium DB.

As the "wetting" effect associated with liquid phase DB brings the two joint faces into direct contact without the deformation required in solid state bonding, the pressures associated with liquid phase bonding are reduced.

4.3 Time

Apart from the obvious economic consideration associated with the time to effect a good quality bond, consideration also needs to be given to time dependent metallurgical phenomena such as grain growth in the material being bonded and the consequent reduction in mechanical properties that might result. In a similar vein, in the case of MMC, fibre/matrix interface degradation with loss of mechanical properties needs to be considered in particular at the high bonding temperatures associated with titanium.

In addition, consideration needs to be given to the effect of grain growth on the SPF performance of the base material if the combined SPF/DB process is being used⁷.

In general however, these metallurgical effects are minor and enable processing times of several hours to be accommodated without significant degradation in material properties.

5.0 Material requirements

The essential material requirements for DB relate to conditions of the mating faces to be joined. These are:-

1. Flatness
2. Surface roughness
3. The absence of insoluble substances on or between the faces

Because of the essential requirements of intimate contact between mating faces as a prerequisite for bonding by atomic diffusion, the surfaces to be joined should be as flat and smooth as possible. For practical applications of DB it is usual to specify a roughness equivalent to a ground surface (RA Circa 0.5 μ m). Rougher surfaces can be accommodated however, by appropriate adjustments in the process conditions. Figure 1 shows for reference the surface roughness associated with a range of surface machining operations.

Although bonding times can be reduced by the use of the finest possible finish, this needs to be balanced against the time that would be required to achieve such a finish.

The existence of insoluble substances on or between the surfaces will prevent bonding. These "no bond" areas manifest themselves as voids in the case of entrapment of insoluble gasses such as argon, or alternatively areas of intimate contact in the case of insoluble surface layers such as oxide layers.

The inhibition of bonding by the introduction of insoluble surface layers has a practical significance in the manufacturing process, as it enables selective bonding to be carried out and thus facilitates the manufacture of highly complex structural forms by the combined SPF/DB processes. This important aspect is discussed later in this paper.

6.0 Titanium as a bondable material

Because of its associated superplastic properties the 6% Aluminium 4% Vanadium titanium alloy has become the most widely used and recognised high strength titanium alloy in the manufacture of DB components. DB temperatures for this alloy are usually in the region 930-950 $^{\circ}$ C - this temperature range being conditioned/limited by the phase transformation temperature for this two phase alloy of 985 $^{\circ}$ C.

At temperatures in excess of 800 $^{\circ}$ C. titanium and its alloys become highly reactive and will absorb their own limited oxide layer, thus producing a "self-cleaning" action which is compatible with the DB process requirements. The reactivity of titanium at these temperatures does however require that the material is protected in an inert (argon) atmosphere or alternatively under vacuum. Because of the insolubility of argon in titanium care needs to be taken, however, to ensure that during the bonding sequence the argon is expelled from between the mating faces and does not become entrapped, thus producing large voids in the bonds.

Because of the self-cleaning action associated with titanium alloys, these materials can be used in the bonding process as "as received" materials with the pre-preparation of sheet for example being limited to standard cleaning processes such as degreasing and "pickling" (acid etch). This factor obviously enhances the economic advantages of the use of titanium in low cost component manufacture.

Although solid state DB of titanium is readily achievable, there are practical advantages to be had in the use of liquid phase DB. In particular, the use of an interlayer can significantly reduce the pressures required to effect a bond. Fitzpatrick⁸ reports that the use of a Cu/Ni interlayer, electro plated onto the bond faces, allows bonding pressures to reduce to less than 700 mb.

This contrasts with sheet titanium solid state bonding pressures of 20 to 30 bar which are typical of current component manufacture. Based upon the familiar Wiesert/Stacher relationship presented on Figure 2 the associated times to achieve a bond are 1 to 1.5 hours.

7.0 Aluminium as a Bondable Material

The major obstacle which prevents aluminium alloys as "as received" materials being used for DB, is the existence of a tenacious oxide layer which is insoluble even at DB temperatures. Before aluminium and its alloys can be bonded therefore, it is necessary to either remove this oxide layer by chemical/mechanical cleaning, or to substitute a soluble alternative which will be absorbed by the base material at the DB temperatures - thus behaving in a self cleaning manner akin to that for titanium. The introduction of a substitute layer can also be used as a means of effecting liquid phase bonding with a resultant reduction in bonding pressures and times.

DB of aluminium in the form of cladding has been in use for a considerable number of years. This process involves cold/high pressure rolling and considerable straining of the material, which causes break up of any residual oxide layer.

AD-A173 979

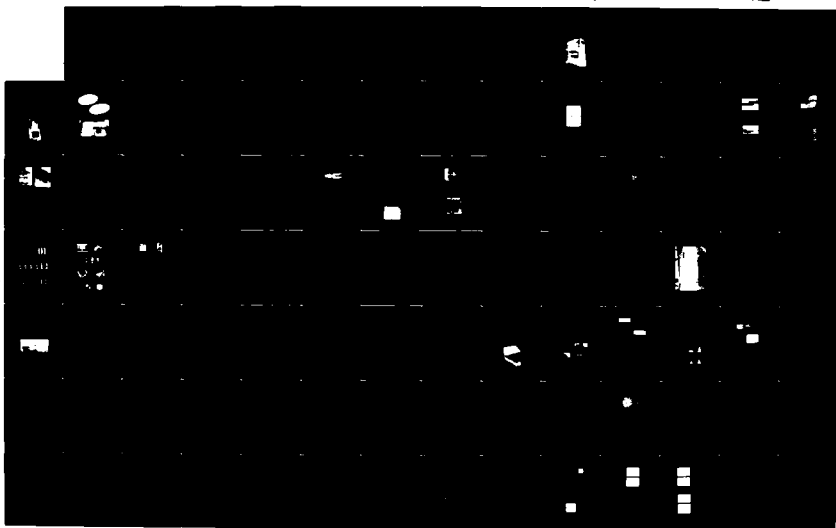
ADVANCED JOINING OF AEROSPACE METALLIC MATERIALS (II)
ADVISORY GROUP FOR AEROSPACE RESEARCH AND DEVELOPMENT
NEUILLY-SUR-SEINE (FRANCE) J GOLDAK ET AL. JUL 86
AGARD-CP-398

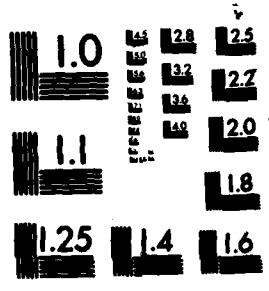
2/3

UNCLASSIFIED

F/G 13/8

NL





MICROCOPY RESOLUTION TEST CHART
NATIONAL BUREAU OF STANDARDS-1963-A

The pretreatment of the aluminium alloy involves chemical/mechanical removal of the oxide layer. Because of the capital equipment involved this bonding technique has not been viewed as a method for component manufacture but recent developments by Texas Instruments in the manufacture of components by their "thermally expanded metal" process could result in cold roll bonding gaining some prominence in future aerospace component manufacture.

For low pressure/high temperature bonding, which is being developed in association with SPF and MMC fabrication, the method of oxide pre-treatment involves either chemical/mechanical cleaning or alternatively the substitution of the oxide layer with a thin absorbable metallic coating of elements such as Cu, Ag etc., the choice of element being subject to the base alloy being bonded.

Coating techniques such as Ion Vapour Deposition (IVD) allow these absorbable coatings to be of minimal thickness and hence their absorption has negligible effect on the base alloy composition and its associated mechanical properties.

Development work carried out by British Aerospace concludes that the oxide layer substitution technique provides higher quality bonds with less variability in bond strength.

DB temperatures for aluminium alloys are in the region of 500° C. but the actual temperature used is subject to the base alloy and the metallic coating employed.

Bonding Pressures for aluminium alloys using the "hot" DB process are relatively low compared with the roll bonding process and times as low as 15 minutes have been achieved.

8.0 Bond strengths

The following table summarises typical strengths of DB joints in titanium and aluminium alloys. These are compared for reference with parent material strengths and typical rivetted and adhesively bonded joint strengths.

Mechanical Properties of DB Joints

<u>Material</u>		<u>Shear Strength</u> <u>MPa</u>
Titanium 6 AL. 4V	Parent	575
	DB	575
Aluminium	Parent	320
	DB	150 - 170 ¹⁰
Rivetted Joint (Typical)		10
Adhesive Bond Joint (Typical)		20 - 40

What is evident from this table is the capability of titanium to achieve parent strength properties and the significant increase in shear strength of titanium and aluminium DB joints relative to current conventional joining techniques.

Baker and Partridge ¹¹ have demonstrated that for good quality bonds in titanium the fatigue performance of DB joints is equal to parent material but that the existence of micro voids in the joint area will degrade the fatigue performance without significantly affecting the static strength. Work by the same authors has demonstrated that even for joints with minimal voiding a significant reduction in impact strength is experienced at a DB joint in titanium.

From a component design point of view, parent material fatigue strengths are usually of academic interest as these properties are usually degraded to take account of stress concentration effects associated with notches and joints. For the case of titanium 6/4 the parent material endurance limit (10⁷ cycles) of 530 MPa would be reduced to 330 MPa for normal design purposes i.e., 38% reduction. Data from the literature and from testing conducted by British Aerospace, suggests that this reduction in parent strength represents a realistic degradation factor to cover practical limits of micro voiding.

9.0 DB Joint Defects

DB joint defects fall into three categories. These are:-

1. Micro voids
2. Large voids
3. Intimate contact disbands

Figure 3 shows a typical micro void in a DB joint - such a defect is only likely to occur as a result of the application of the incorrect processing conditions. This defect can be largely overcome by ensuring that the processing conditions of pressure and or time are chosen to encompass the widest range of surface conditions likely to be encountered in the manufacture of a given component.

The effect of the presence of micro voids has and continues to be studied. Results so far indicate some insensitivity to micro voids in static strength properties but reductions in fatigue, impact and elongation to failure have been demonstrated.

The cause of large voids/disbonds is most likely to be associated with argon gas entrapment when bonding in an argon environment. This defect can be overcome by employing the correct processing technique and in the detail design of the component to ensure progressive venting of the faces to be bonded. Large void areas can also arise due to irregularities in the platens or workpiece when carrying out "massive" DB. In this case, the bond faces have failed to come into contact because the pressures employed are generally insufficient to forge the material into the required shape. The effect of large voids on component integrity is currently being studied - of particular concern is whether such voids, even if deemed to be initially non critical because of their location on a component, will propagate to a critical state in a service environment.

As discussed previously, intimate contact disbonds are associated with non gaseous insoluble layers between mating faces. These insoluble areas can either be present on the faces to be bonded, or arise during manufacture due to inadequate pre-processing or as a result of the ingress of surface contaminants during the DB processing. The prevention of such disbonds is clearly dependant upon good process control. As in the case of large voids, such disbonds may not be critical on a particular component, provided they do not propagate, but unlike large voids the intimate contact in these disbonds makes their extent difficult to ascertain by current NDT techniques.

10.0 N.D.T.

Of the three defect types discussed in the previous section, only the large voids can be readily detected by current N.D.T. techniques such as C-Scan ultrasonics and X-Rays 12,13.

Detection of microvoids can only be accomplished by micrographic examination and in a practical situation this is usually carried out on a sample basis either by cut up of production components or by the examination of areas of the components which are removed during subsequent production operations; control of such defects is however best accommodated by correct processing and process control.

Intimate contact disbonds is a defect which is common to all bonding processes and is therefore not unique to DB. Detection of such defects presents difficulties for all bonding processes and this is currently the subject of a considerable amount of research using technique such as thermography, holography etc. As in the case of microvoids and in common with other bonding processes currently accepted for aircraft production, close control of the processing route is seen as the most practical solution to this particular problem.

11.0 Component manufacture

11.1 Equipment

The process of DB requires a means of maintaining the workpiece at a uniform temperature, together with the means of applying and reacting the loads required to produce intimate contact between the faces to be bonded. The equipment most widely used as a means of providing these conditions is a heated platen press, a typical example of which is shown on Figure 4. Provision of a protective environment in particular when DB'ing titanium is either provided by the addition of a vacuum chamber as an integral part of the press or alternatively as a integral part of the individual component tooling.

11.2 DB Processing

DB in component manufacture is generally categorised into two forms:-

1. "Massive DB"
2. "Thin Sheet DB"

Massive DB involves the joining of machined plate elements and is generally associated with the manufacture of thick section components which would otherwise be machined from solid, or alternatively, from a forged blank. Figure 5.

As a general rule, the bonding pressures associated with "massive" DB are applied by mechanical means and can require the application of loads in more than one direction.

The DB joints in components manufactured by this route are a substitute for parent metal in the conventional equivalent and would in general be subject to high levels of stress in service use; this in turn demands high integrity bonds in the manufacture of these components if good structural efficiency is to be maintained in the DB component.

The need to achieve such high quality bonds coupled with the remoteness of the applied mechanical bonding loads places considerable demands on the accuracy required of both the tooling and the individual plate elements employed in the component manufacture.

By contrast the use of "thin sheet" DB has two practical advantages relative to "massive" DB. These are:-

1. Thin sheet usually has a good surface finish as an "as received" material (R_a Circa 0.5 μ m) and therefore requires limited pre-preparation. (This is particularly true of titanium alloy sheet).
2. Bonding loads can be applied by gas pressurisation which facilitates intimate contact between faces to be bonded and is therefore independent of the platen or workpiece flatness. Figure 6.

When associated with sheets of superplastic quality, conformity between faces to be bonded can be readily achieved by the fact that the material will form to provide intimate contact. In addition, the bonding pressures will remain normal to the surfaces of the sheets irrespective of the shape of the two sheets to be bonded.

11.3 SPF/DB

Since the late sixties, much experimental work has been conducted in the potential use of the combined process of SPF/DB, in particular, using the 6/4 titanium alloy. The structural forms which can be manufactured using these combined processes are universally recognised in terms of the numbers of sheets employed in their manufacture. Figures 7 to 9 illustrate the 2, 3 and 4 sheet forms respectively.

The manufacture of thin sheet SPF/DB components, in particular the two and three sheet forms rely upon selective DB prior to SPF. The achievement of the selective DB is associated with the use of an insoluble surface coating which is applied to the mating surfaces in areas which are not required to be bonded. In the case of the four sheet structure, the core line bonding can be carried out in a similar manner to that for the two and three sheet forms and prior to its enclosure into the skin pack. This structure also has a DB cycle as the completion of forming in the tool.

11.4 MMC

Because of the form in which these materials are produced (thin foil), coupled with the large areas of bond required, DB of MMC either as selective reinforcement in association with SPF/DB or in the manufacture of MMC components, generally uses gas pressure bonding to ensure good quality bonds. The use of these materials is still in the early development stage but the attractive weight saving potential provided by these high specific strength materials suggests that in the longer term this could represent the greatest potential use for DB in future aircraft component manufacture.

12.0 Component Integrity

Component integrity in respect to the use of DB in manufacture is dependent upon the type of structure and the method of manufacture employed in the production of the DB joints.

As discussed previously the types of structure and the high levels of joint loading associated with "massive" DB places considerable demands on the process conditions, tooling integrity and accuracy/finish of the component elements. Because of the low forecast usage of "massive" DB in the manufacture of its products, British Aerospace have carried out only limited development work in this particular DB technique. It is not therefore within the competence of the authors to provide an authoritative comment on the viability of this form of the DB process in the manufacture of high integrity components. By contrast, however, British Aerospace has been involved in the pioneering of the use of thin sheet SPF/DB having patented the two sheet structure as early as July 1972.

In general the DB joints associated with the thin sheet structure forms which are typical of SPF/DB manufacture, replace conventional joining technique such as welding, rivetting, or adhesive bonding. The load transfer demanded by such joints is well within the strength capability of DB joints, as demonstrated in section 8.0, where a comparison is provided between conventional and DB joint strengths.

Testing of practical SPF/DB structure has demonstrated however that the integrity of these thin sheet components is more dependent upon local stress concentrations in the parent material which arise from structural features which are typical and peculiar to this form of construction. Figure 10.

13.0 Economic Advantages

The economic advantages associated with DB and SPF/DB have been well documented and have been substantiated fully by a wide range of full size development/demonstrator projects conducted by most Aerospace Companies throughout the Western World 14 - 17.

The fundamental aspects associated with these economic advantages are:-

1. Simple starting blank forms (particularly significant for titanium)
2. High material utilisation
3. Reduced parts count
4. Process times which are insensitive to size, complexity of structural form, or numbers of components manufactured in one operation
5. In the case of SPF/DB concurrent forming and bonding

It is recognised that the actual savings achieved are a function of the component, its equivalent conventional method of manufacture and the associated material. A highly significant factor in the maximisation of these savings is however a requirement to design for these processes - in particular SPF/DB - rather than slavishly attempting to reproduce the conventional equivalent.

As an example of the significant reduction in parts count which is attainable by SPF/DB; the pressure shell escape hatch illustrated in Figure 11, and which is currently being developed by British Aerospace for 125/800 Aircraft, has a reduction of 76 detail parts and 1,000 fasteners in transforming from aluminium fabrication to titanium SPF/DB. The SPF/DB door will have only 14 details and some 90 fasteners. Allowing for differences in the raw material costs between the two methods of manufacture a 30% cost saving is predicted for the SPF/DB door.

In the case of MMC, the economic consideration is perhaps less relevant than the fact that DB appears at this time to be the only practical method available for exploiting these high specific property materials in component manufacture.

14.0 Weight Advantage

Again the weight saving potential provided by these processes has been well documented and substantiated by full scale component manufacture. These weight savings occur from the ability of SPF/DB in particular, to produce efficient structural forms with the elimination of fasteners and associated joint flanges. A particular example is shown on Figure 12. This shows the titanium SPF/DB wing access panel which has been developed by British Aerospace and is now in full production for fitment to Airbus A310 and A320 aircraft. This particular component achieves a weight saving in excess of 40% of the aluminium alloy equivalent.

15.0 Applicability

Based upon an assessment of civil and military aircraft an estimate of the potential embodiment levels for components using the various DB process routes is seen as follows:

	<u>% of Structure Weight</u>
"Massive" DB	1 - 2
SPF/DB	8 - 10
MMC	20 - 25

The likely areas of application are seen as

"Massive" DB	<ul style="list-style-type: none"> - highly loaded structure (in particular on military aircraft) - wing "carry through" structure - control surface pivots - under carriage supports - flap tracks
SPF/DB	<ul style="list-style-type: none"> - control surfaces - smaller flying surfaces - access panels/doors - engine bay component - hot ducting - engine rotating parts
MMC	<ul style="list-style-type: none"> - reinforcement of SPF/DB applications - wing and flying surface skins and stringers - engine pylons - cabin floor structure

16.0 Status of the technology

Since its early beginnings in the sixties, DB has attracted a considerable R & D interest and funding support, in particular when associated with SPF and MMC. The wide range of applications which have been studied and for which demonstrator programmes have been carried out are well documented in the literature and do not need to be chronicled in this paper. The results of these programmes have broadly confirmed the benefits predicted for these new technologies. As discussed by Weisert in his paper presented to the ASM WESTEC Conference in 1984 early production exploitation of these processes, which is obviously a measure of maturity of a new technology, has suffered from the fortunes of a number of key projects such as Concorde and B1 and as is the case with all new technologies the difficulty of attaining maturity in phase with new project start dates has also been experienced in the evolution of these processes. Nevertheless, production has commenced and in the UK components are now being produced for:

Tornado	- Hot Air Ducts - Figure 13
Airbus A310/A320	- Access Panels - Figure 12
Rolls Royce RB211-535E4	- Fan Blades

The two airframe components identified above used solid state DB whereas the Fan Blade uses liquid phase DB.

Since the commencement of production of the components listed above several hundred components have been produced and are now in service operation.

Further production components are under development within British Aerospace and will be introduced progressively in the next two years on current military and civil aircraft projects. Embodiment of these new processes into future British Aerospace projects is well advanced.

From the literature, it is clear that most of the European Aerospace Industry is involved in the development of these processes and anticipate the early introduction of components on to their existing and new projects.

17.0 Conclusions

DB has come of age in as much as it has now been introduced into the volume production of a number of primary components for airframe and aero engines.

The process is well understood and compares favourably in strength and quality with existing conventional joining techniques. In titanium, parent material strength properties can be readily achieved and hence DB has considerable potential in the efficient, cost effective manufacture of components which demand high strength joints.

Conventional NDT techniques can and are already being successfully applied in the quality control of DB joints. Further R & D in this field is desirable in particular in respect to intimate contact disbands but in the final analysis the key to DB quality is seen as close process control.

Future developments, in the use of DB are likely to be in the manufacture of larger and more complex components produced by the SPF/DB route and in the field of MMC fabrication of airframe and aero engine components.

Long term in service experience is yet to be established but there is every confidence that components manufactured by this route will be in no way inferior to there conventionally manufactured equivalents. The superior fatigue and corrosion resistance of titanium would suggest a likely improvement in "cost of ownership" relative to aluminium.

As a process therefore we anticipate DB growing in significance in future airframes and aero engine component manufacture.

References

1. C. H. Hamilton - Titanium Science & Technology
1973 Vol. 1, 625
Plenum New York
2. G. Garmang, N.E. Paton,
A. S. Agan - Metall. Trans.
6A 1269, 1975
3. B. Derby, E. R. Wallach - Met. Science
16 49-56, 1982
4. A. Hill, E. R. Wallach - Metals Society
DB Conference, London
March 1984
5. B. Derby - Metals Society
DB Conference, London
March 1984
6. J. Pilling, N. Ridley - 5th International Conference on Titanium
Munich 1984
Vol. 2, p 733 of proceedings
7. C. Hammond - AIME Conference, San Diego
Superplastic Forming of Structural Alloys
P 131 of proceedings
8. G. A. Fitzpatrick - Metals Society
DB Conference, London
March 1984
9. Texas Instrument Brochure -
10. J. Harvey, P. G. Partridge,
C. L. Snooke - Metals Society
DB Conference, London
March 1984
11. T. S. Baker, P.G. Partridge - 5th International Conference on Titanium
Munich 1984
Vol. 2, p 861 of proceedings
12. R. Bilgram, S. E. Lize,
W. K. Lemmt, G. Tober - 5th International Conference on Titanium
Munich 1984
Vol. 2, p 955 of proceedings
13. P.M. Onyan - Metals Society
DB Conference, London
March 1984
14. J. R. Williamson - AIME Conference, San Diego
Superplastic Forming of Structural Alloys
p 291 of proceedings
15. E. D. Weisert - 5th International Conference on Titanium
Munich 1984
Vol. 2, p 122 of proceedings
16. W. Beck, P. J. Winkler - 5th International Conference on Titanium
Munich 1984
Vol. 2, p 1229 of proceedings
17. M. Ohsumi, M. Shimizu,
A. Takahashi, T. Tsuzuku - Mitsubishi Heavy Industries Publication
18. E. D. Weisert - Proceedings of A.S.M.WESTEC
1984 Los Angeles

Process	Roughness R_a in μm								
	0.05	0.1	0.2	0.4	0.8	1.6	3.3	6.3	
Lapping	████████████████████								
Polishing		████████████████							
Grinding		████████████████████							
Turning				████████████████████					
Milling					████████████████████				

Fig.1 Typical roughness values obtainable by machining processes

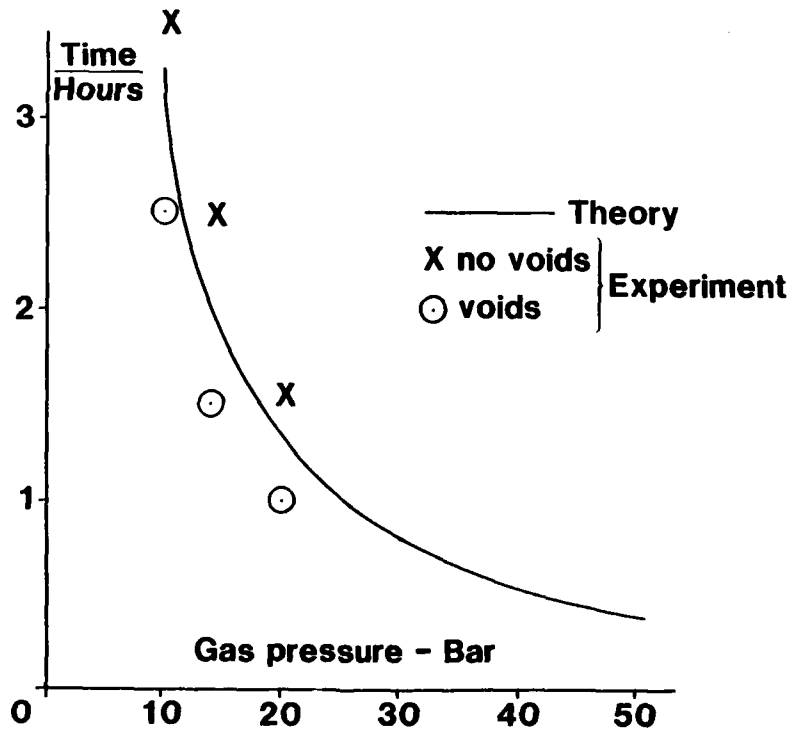


Fig.2 Diffusion bonding. Titanium 6Al-4V 925°C

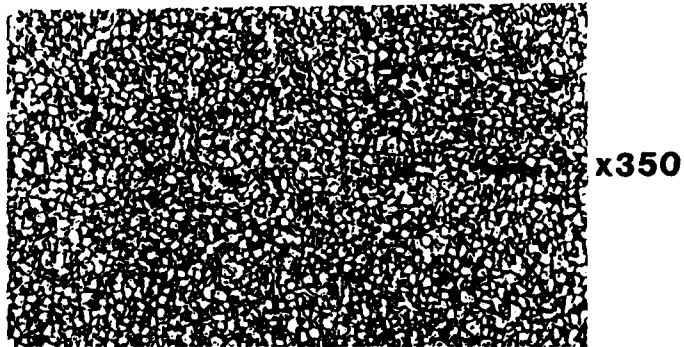


Fig.3 Diffusion bond defects — micro voids

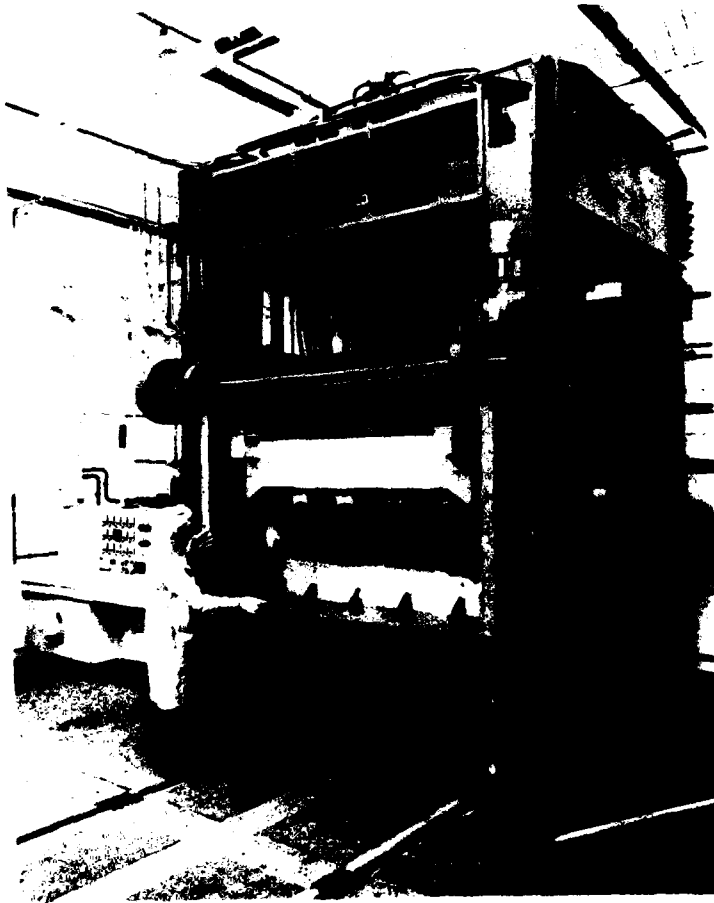


Fig.4 Typical. Heated platen press used for SPF and DB

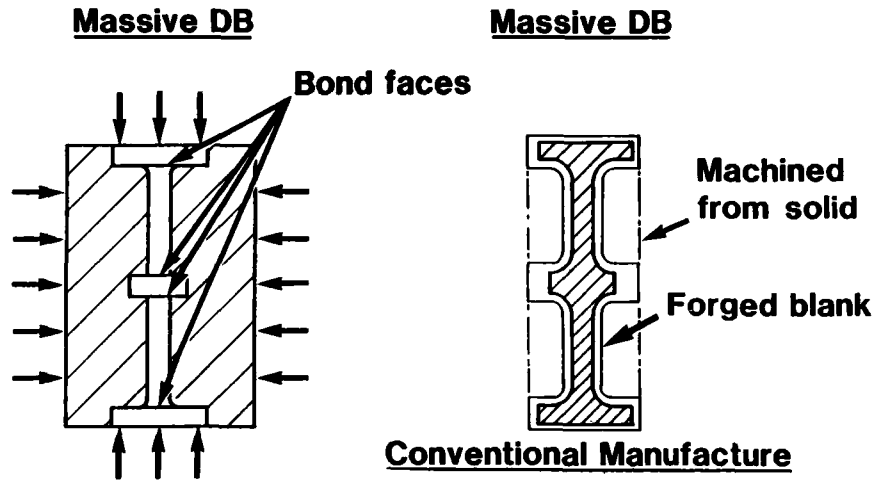


Fig.5 Massive DB bonding

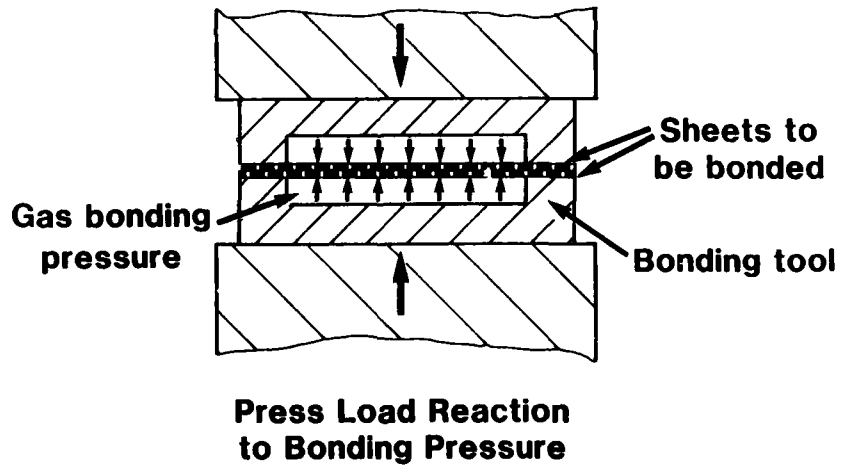


Fig.6 Thin sheet DB-gas pressure bonding

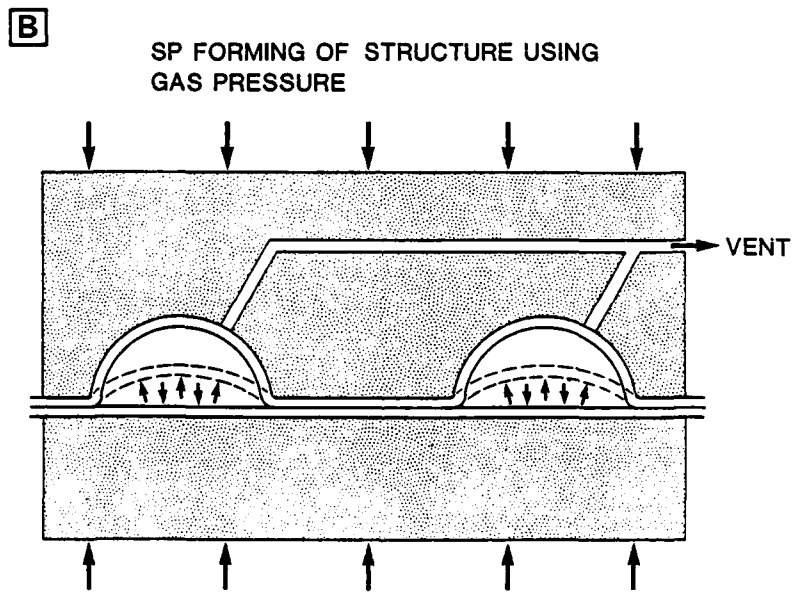
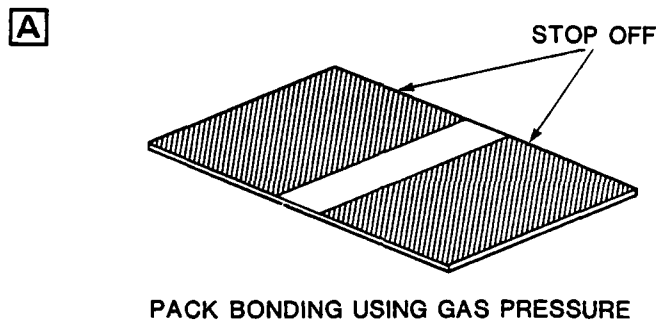
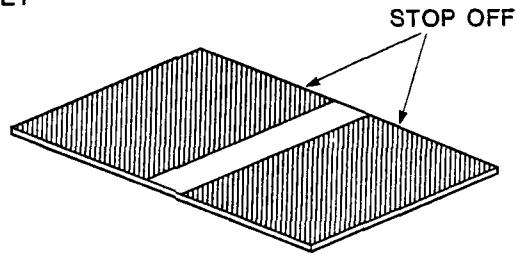
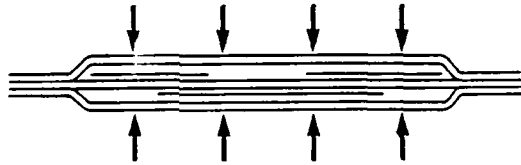


Fig.7 Two sheet SPF/DB

A CORE SHEET



B PACK BONDING



C FORMING

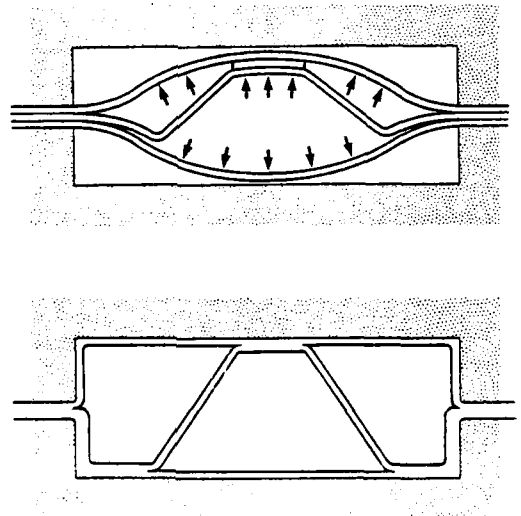
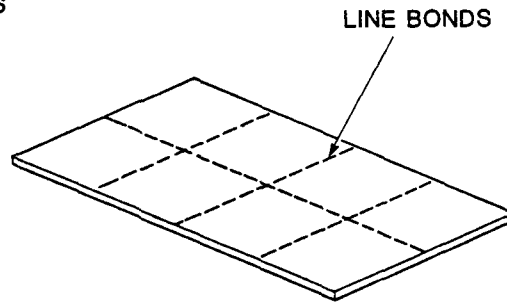


Fig.8 Three sheet SPF/DB

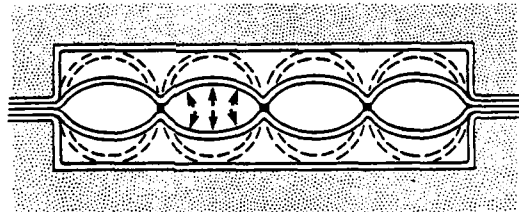
A CORE SHEETS



B PACK BONDING



C FORMING



D BONDING

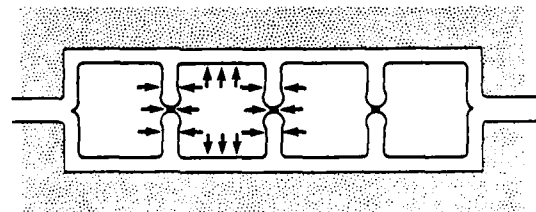


Fig.9 Four sheet SPF/DB

↔ Typical failure locations

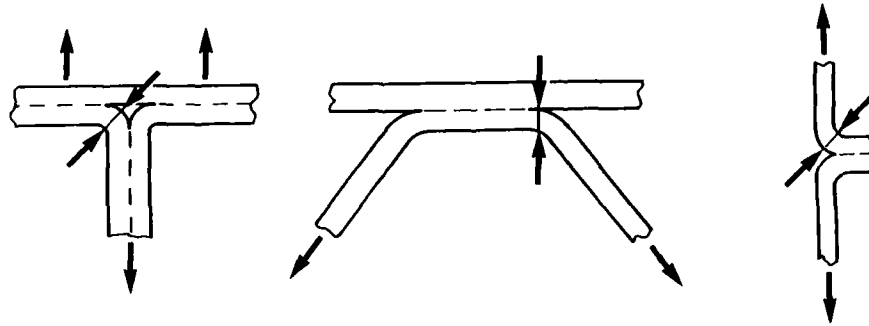


Fig.10 SPF/DB Structural details



Fig.11 125/800 escape hatch — titanium SPF/DB

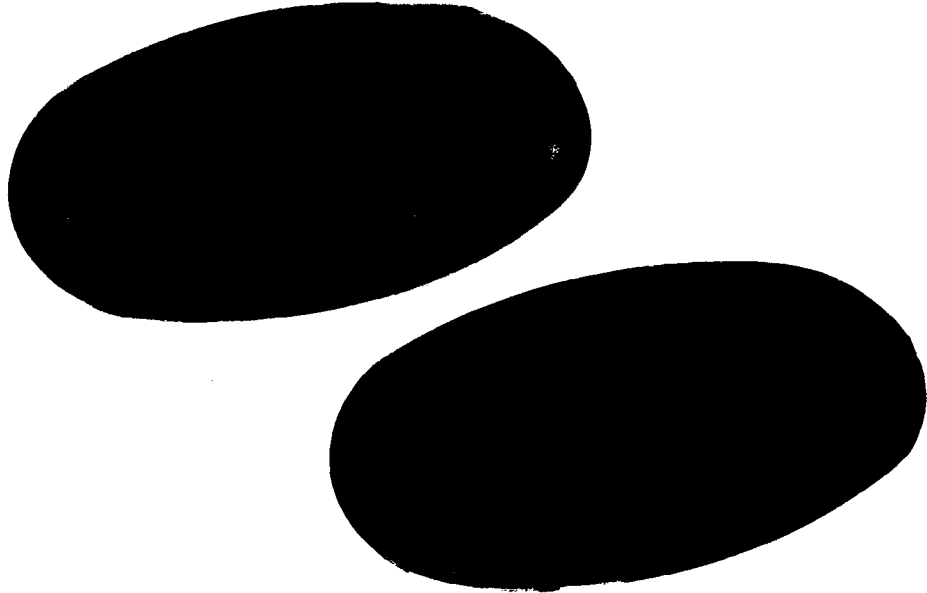


Fig.12 Airbus A310/A320 Wing access panels — titanium SBF/DB

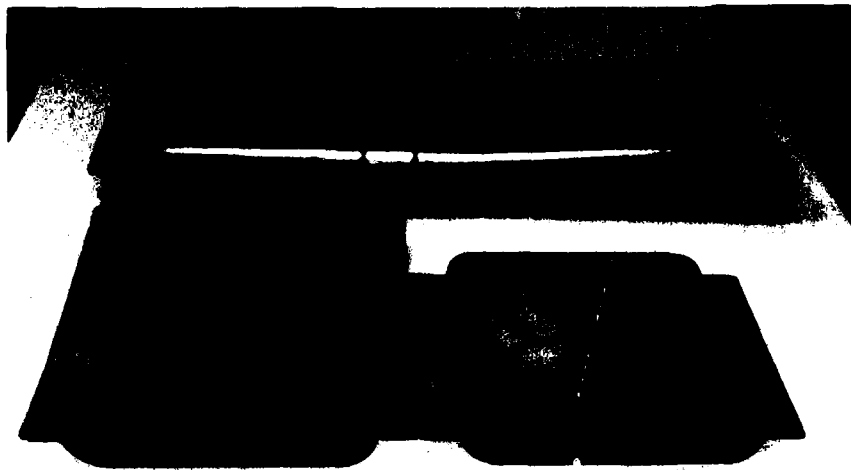


Fig.13 Tornado hot air duct — titanium SBF/DB

DIFFUSION BONDING OF Al-ALLOYS IN THE SOLID STATE

P G Partridge
 J Harvey
 D V Dunford
 Materials and Structures Department
 Royal Aircraft Establishment
 Farnborough
 Hampshire GU14 6TD UK

SUMMARY

Solid state diffusion bonds have been produced between clad Al-alloy sheets in alloys 7010, 2024, SUPRAL 220 and LITAL A. The sheet surface was first ion plated with a 1 μ m layer of silver before bonding at 280°C or 450°C under 130 MPa or 7 MPa pressure. Lap shear strengths were in the range 140 MPa - 180 MPa and peel strengths were more than 40 N/mm. The effects of test piece design, surface finish, clad layer thickness and of oxide films on diffusion bond strengths are described. The results suggest that a combination of thin silver coating and a clad layer should enable any Al-alloy to be diffusion bonded.

1 INTRODUCTION

Substantial cost and weight savings can be achieved for titanium sheet structures by combining superplastic forming with diffusion bonding¹. The weight savings arise from reduced numbers of parts and of mechanical fasteners. Similar savings might also be achieved for Al-alloy sheet structures if a joining process could be found that was compatible with the superplastic forming conditions for the high strength Al-alloys.

The efficient utilisation of advanced Al-alloys produced by rapid solidification processing²⁻⁵ and of Al-metal matrix composites⁶ could also depend on a suitable low temperature joining process, since the properties of the former depend upon a fine grained metastable microstructure which is degraded by temperatures above about 300°C - 350°C^{5,7,8} and the latter often require joining temperatures below conventional brazing temperatures.

Adhesive bonding^{1,3} and weld-bonding^{1,9} are well established techniques but the demand for higher bond strength, improved environmental performance and temperature capability has directed attention to ultrasonic welding⁹, diffusion brazing⁹⁻¹³ and solid state^{9,10,14,15} diffusion bonding (DB). There are several features unique to DB which makes this method particularly suitable for Al-alloys; these are summarised in Table 1.

TABLE 1
 SOME CHARACTERISTICS OF DIFFUSION BONDED JOINTS

1	Parent metal strength may be obtained.
2	Large area joints are possible.
3	Bonding involves minimum distortion and deformation and close dimensional control is possible.
4	No corrosion arises from fillers or fluxes at the joint interface.
5	Thick and thin sections can be joined to each other.
6	Cast, wrought and sintered powder products and dissimilar metals can be joined.
7	Machining costs may be reduced.
8	More efficient design may be possible.
9	May be combined with superplastic forming.

The possibility of obtaining parent metal strength and combining DB with superplastic forming are especially attractive for airframe structures.

Unfortunately Al-alloys are among the most difficult metals to DB, because of the rapid formation of a stable oxide film on bare aluminium surfaces. Most of the Al-bonding work reported has involved high temperatures and large deformations^{10,15}. Less deformation is required if foil interlayers or electroplated coatings are used,^{10,14,15} and still lower pressures and deformation are needed in the presence of a transient liquid phase^{9,10,12}, but these methods often produce brittle intermetallic phases and low bond strengths.

Much improved surface cleaning and thin film coatings are now possible using plant developed for the semiconductor industry¹⁶. In the future such coatings could provide the flexibility and quality control hitherto lacking in the solid state bonding of metals¹⁷. A preliminary investigation has therefore been carried out using argon-ion sputter cleaned and silver-ion plated clad Al-alloy sheet. Silver oxide dissociates above about 200°C and silver exhibits significant solubility in the Al-lattice at the solution temperatures of 480°C - 520°C, as shown in Figure 1. A silver coating was therefore considered ideal for the development of a solid state diffusion bonding model for Al-alloys. This paper describes the bonding and testing techniques used and gives bond strength data for 7010, LITAL A, SUPRAL 220, and 2024 alloys. Some of the factors affecting the bond strength are discussed.

TABLE 2
ALUMINIUM ALLOY COMPOSITION AND HEAT TREATMENT

	Alloy	Composition Wt %										Heat treatment	
		Cu	Mg	Zn	Li	Fe	Zr	Mn	Cr	Ge	Si	Solution heat-treat	Age
1	2024	4.4	1.5	-	-	-	-	0.6	-	-	-	498°C	16 h at 190°C
2	SUPRAL 220	5.9	0.35	0.07	-	0.18	0.4	-	-	0.1	0.12	520°C	16 h at 180°C
3	7010	1.7	2.3	6.0	-	-	0.11	-	-	-	-	480°C	24 h at 120°C and 10 h at 172°C
4	LITAL 'A'	1.2	0.7	-	2.4	-	0.1	-	-	-	-	530°C	5 h at 185°C

2 EXPERIMENTAL TECHNIQUE

The compositions of the alloys bonded are given in Table 2; 2024 and SUPRAL 220 are based upon the Al-Cu system, 7010 on the Al-Zn-Mg system and LITAL A on the Al-Li-Cu system. All the alloys were clad on each surface to a thickness of 40 µm - 60 µm (2024), 100 µm (LITAL A), 120 µm (7010) and 140 µm (SUPRAL 220). Sheet thicknesses were in the range 1.6 mm - 3.5 mm. Lap shear tests on bonds made at 280°C used test pieces made from blanks 30 × 25 mm which were cut, drilled and bonded as shown in Figure 2. The overlap L was $\leq 2t$ (where t is the sheet thickness) to ensure failure by shear in the bond interface¹⁸. After bonding the section A in Figure 2 was used to study the as bonded microstructure and section B was used to monitor the effect of post bonding heat treatment. A modified test piece, described later, was used for joints made at 450°C.

Peel test piece blanks 100 × 18 mm were bonded at one end to a length of ~ 20 mm prior to bending into a shape suitable for peel testing as shown in Figure 3. Shear and peel strengths for all the alloys were obtained for bonds made between surfaces mechanically polished to 1 µm diamond to give a surface finish¹⁹ $R_a = 0.05$ µm (Figure 4a). The effect of surface finish on bond shear strength was determined for the 7010 alloy. Tallysurf traces for typical surfaces are shown in Figure 4. The polished surfaces were sputter cleaned either in a triode (T) or a diode (D) apparatus using argon gas plasma at a pressure of $1-8 \times 10^{-4}$ torr. In the T-apparatus the test piece was stationary and subjected to 1000 V DC whereas in the diode apparatus the test piece was rotated about a vertical axis under an RF voltage. The sputtered aluminium surfaces were silver ion-plated by sputtering either from a planar silver electrode (T-apparatus) or from a magnetron silver source (D-apparatus). The silver coatings produced were about 1 µm thick.

In order to investigate the effect of the major variables on the bond shear strength, jigs were designed¹⁸ for bonding (Figure 5) and testing (Figure 6) the small test pieces in Figure 2. These jigs reduced the scatter in test data by ensuring accurate alignment of the blanks during bonding and minimum bending during shearing. Bonding was carried out either in air or in an apparatus flushed with argon at 280°C in 0.5 hour under 100 MPa - 130 MPa pressure or in vacuum at 450°C in 1 hour under 7 MPa pressure to produce overall reductions in thickness of 5% - 20%.

3 STRUCTURE OF DIFFUSION BONDED JOINTS

3.1 Macrostructure

After bonding a uniform cross-section was obtained across the bond and no macroscopic defects were visible in the bond interface (eg at A in Figure 7a). However the reduced constraint at the ends of the sheets led to greater deformation in one sheet and a non-planar interface near the bond edges normal to the tensile axis. This is illustrated in

Figure 7b, which is a schematic diagram of a typical bond interface; bonding was poor in the non-planar regions at B and notches resembling sharp cracks were often produced at C.

The strength of the lap shear joint was sensitive to bonding method, sheet edge preparation and to sheet overlap. For example the end effects depicted in Figure 7b were accentuated in guillotined sheets compared with edge ground sheets. When the overlap was significantly less than $2t$ the bond interface became inclined to the sheet plane and was subjected to shear during bonding, as shown in Figure 8. Although notch-like contours were developed such bonds could fail at high stresses because the surface films were disrupted by the shear deformation during bonding. This deformation sometimes led to secondary recrystallisation, as shown at A in Figure 8.

At bonding temperatures greater than 300°C the whole bond interface (BAB in Figure 7b) became inclined to the tensile axis even for overlaps $> 2t$; this led to a reduced bond shear component during testing. Test pieces were therefore modified as shown in Figure 7c. The overlap ABCD was about $6t$, but the surfaces were only coated with silver in the central region $BC = 2t$. This ensured that the bond interface remained planar and parallel to the sheet plane and to the tensile axis and the shear properties were then less dependent on the bond plane curvature effects at the sheet ends.

3.2 Microstructure

A mirror-like surface finish was obtained for $1\ \mu\text{m}$ diamond polished surfaces as shown in Figure 4a. A normal section through a 7010 bond made at 280°C is shown in Figure 9a; the two $1\ \mu\text{m}$ silver layers at A were typically flat and free from coarse defects over the whole bond interface.

After solution heat treatment (SHT) at 480°C for 16 hours followed by a cold water quench the silver layer was replaced by small Al grains (at A in Figure 9b). A transmission electron micrograph after SHT is shown in Figure 10a. No continuous films were visible at the original Ag/Ag interface at A, but fine and coarse precipitates were present at the alloy/cladding interfaces (B-B and C-C in Figure 10a). After ageing both the original silver region and the cladding contained a uniform distribution of fine precipitates (Figure 10b); one of the transverse grain boundaries shown at A in Figure 9b is visible at A in Figure 10b.

Electron probe microanalysis across the bonds produced the curves in Figure 11. These show that after SHT (Figure 11b) silver had diffused a distance of $400\ \mu\text{m}$ from the bond line and into the 7010 alloy to reduce the Ag content at the bond interface to about 1%. Other solutes had diffused into the cladding from the alloy to produce a uniform alloy composition across the bond of 4% Zn, 1% Mg, 1% Ag and 0.5% Cu. However a marked depletion of alloying elements remained in the cladding relative to the 7010 alloy.

4 BOND STRENGTH

The shear strength values depended on many factors including coating technique, surface finish, silver and clad layer thickness, test piece design and heat treatment. These variables were not optimised for each alloy in the present experiments.

4.1 Lap shear strength and hardness

In the as bonded state (Figure 9a) shear strengths up to 90 MPa were obtained. The strength increased with time at the SHT temperature of 480°C coinciding with an increase in solute diffusion into the cladding. Maximum strengths of 144 MPa - 182 MPa were obtained after about 15 hours (Figure 12); strengths were greater for $1\ \mu\text{m}$ polished surfaces than for as received sheet surfaces. There was little change between 16 hours and 64 hours. All test pieces in the present programme were therefore SHT for 16 hours.

A substantial increase in the hardness of the alloy and the cladding was obtained after SHT but ageing had little further effect on the hardness of the clad layer (Figure 13). In the cladding the increase in hardness was caused largely by solid solution strengthening by Zn and Mg; the copper content was insufficient for age-hardening.

The load-time curve exhibited by a good bond during a lap shear test is shown in Figure 14a for material in the SHT condition; the rounded peak followed by a reduction in load indicated significant plastic deformation had occurred in the bond region prior to shear fracture. This plasticity was absent in poor bonds (Figure 14b) and these interfaces were subsequently found to have defects or unbonded areas. The plasticity was also less for aged test pieces.

Some shear strength values are shown in Figure 15. As bonded strengths of $80\ \text{MPa} \pm 3\ \text{MPa}$ were obtained for all the alloys and fracture occurred partly in Ag/Ag interfaces and partly in Ag/cladding interfaces. After solution treatment the shear strengths increased to values in the range 95 MPa - 174 MPa. Higher values were usually obtained for test pieces produced in the triode apparatus. The effect of ageing depended on the alloy system and on whether the diode or triode apparatus was used, but strengths up to 150 MPa were obtained for 7010 and SUPRAL 220 test pieces from the triode apparatus. Ageing appeared to have little effect on the LITAL A alloy. Deviations from pure shear loading occurred with overlaps much less than $2t$ when bond interfaces were inclined to the loading axis, as in Figure 8; the fracture stress (load/bond area) was 214 MPa for

this specimen. With overlaps much greater than $2t$ increased bending and peel type fracture occurred. The curve of load versus overlap length eventually reached a plateau analogous to that found for adhesive bonded joints²⁰. These factors together with other variables associated with the diffusion bonding process, make precise comparisons of published data difficult, but the bonds are significantly stronger than the 30 MPa - 40 MPa reported for adhesive bonded Al-alloys²¹.

4.2 90° Peel Strength

Peel test data are known to be very dependent on test piece design and testing technique. However some simple tests were considered necessary to check whether the fracture behaviour of diffusion bonded joints were particularly sensitive to peel stresses. Some preliminary results were therefore obtained using the non-standard but easily produced and tested test pieces shown in Figure 3.

A typical load-time curve for these test pieces is shown in Figure 14c; the load remained almost constant during crack growth. In the SHT condition extensive plastic deformation was associated with crack growth (Figure 16); the deformation extended beyond the clad layer and into the parent alloy. The crack appeared to grow in a series of jumps with large plastic zones developing during the slow crack growth period. These zones are visible at A in Figure 16. A saw-tooth fracture reflected these variations in crack speed.

Peel strengths at room temperature (Figure 17) for 7010, 2024 and SUPRAL 220 alloys in the SHT condition were in the range 42 N/mm - 54 N/mm and after ageing the values were 41 N/mm - 48 N/mm. The values for the Al-alloys are significantly greater than values reported¹ for adhesive bonded Al-alloys (~ 9 MPa). However precise comparisons are not possible because of the different test pieces used. Preliminary work on the above bonded joints suggest that the hot peel strengths would be low.

5 EFFECT OF SURFACE FINISH

7010 Alloy sheets with five different surface finishes were coated, bonded, and tested in shear. Typical Talysurf traces for $1 \mu\text{m}$ diamond polished, as received and 600 grit ground surfaces are shown in Figure 4. The polished surface, had a very low surface roughness and small waviness in both L (longitudinal) and T (transverse) directions. As received sheet had relatively low roughness superimposed on significant waviness with peak to trough of $1 \mu\text{m}$. The ground surfaces had much greater roughness but less waviness.

Data for the 7010 alloy in the SHT condition are plotted in Figure 18. Lapped, chemically polished and ground surfaces produced shear strengths in the range 100 MPa - 130 MPa on a plateau in the curve of shear strength versus surface finish. As the surface became smoother (for as clad and $1 \mu\text{m}$ diamond polished) there was less variation in surface finish with direction in the surface and a significant increase in shear strength was obtained up to a maximum of ~ 180 MPa.

It is interesting to note the effect on the shear strength of orientation of the surface grooves in the ground surfaces. A maximum shear strength was obtained when the grooves in both sheets were parallel to the shear direction and a minimum value was obtained when the grooves in one sheet were normal to the shear direction. Circular grooves produced strengths between these two extremes. Under the bonding conditions used these strength differences reflected the number of interface voids or unbonded regions present after bonding.

Bonded interfaces containing defects (pores or SiC particles) were obtained with the 600 SiC grit ground surface as shown in Figure 19a. The low strength obtained after SHT was attributed to these defects and to the presence of an intermetallic layer (Figure 19b)

6 EFFECT OF CLAD LAYER THICKNESS

To measure the effect of clad layer thickness on bond strength, specimens were lapped to partially remove the clad layer and then polished to $1 \mu\text{m}$ surface finish. Specimens were then silver coated and bonded under identical conditions. The range of clad layer thickness and bond quality obtained is shown in Figure 20. The excellent uniformity and defect free interfaces characteristic of the $1 \mu\text{m}$ polished surface were obtained for all clad layer thicknesses. The shear strength data are plotted in Figure 21. The shear strength was very sensitive to the clad layer thickness, decreasing to less than 9 MPa when the clad layer thickness was about $9 \mu\text{m}$ - $15 \mu\text{m}$ thick on one side and $25 \mu\text{m}$ - $30 \mu\text{m}$ thick on the other side of the silver layer. Specimens bonded without a clad layer failed either during heat treatment or under very low loads during testing.

The microstructure of the bond interface after annealing also depended on the clad layer thickness. In the bonds made between unclad or thin clad layers and after 16 hours at 480°C a continuous intermetallic layer was visible at the bond line (at A in Figure 22) and large particles were visible in the clad/alloy interface as shown at B in Figure 22; the layer and particles were not removed by prolonged annealing. Qualitative analysis of these regions^{22,23} showed the layer to be rich in Ag, O and Cu and the particles to be rich in Ag, Cu, Zn and Mg. Protruberances extending from the layer into the cladding (at C in Figure 22) appeared to be caused by enhanced diffusion along a grain boundary. The low bond shear strengths were attributed to the presence of this brittle intermetallic layer. The changes in microstructure and bond strength with decreasing clad layer

thickness were attributed to the way in which local solute concentrations in the cladding changed with time. This is shown schematically in Figure 23 where it is assumed that the presence of interface 3 does not affect the diffusion of Ag. With thick cladding layers it is believed that, by the time solute atoms from the alloy have diffused through the cladding to the original position of the Ag cladding interface (interface 2), the silver concentration will have been reduced to below a critical concentration at which intermetallics form (Figure 23a). With thin cladding layers, however, the solute atoms arrive sooner at interface 2 where a high concentration of Ag (or Ag itself) may still exist and this leads to the formation of intermetallics. Similarly with thin cladding layers the concentration of Ag at the alloy-cladding interface reaches higher values than with thick cladding and intermetallics also occur at this interface (Figure 23b). In practice diffusion takes place most rapidly down grain boundaries and it is thought that this accounts for the isolated nature of the intermetallic particles in the region of the alloy-cladding interface.

7 EFFECT OF INTERFACE OXIDE FILMS

Oxide films have a marked effect on aluminium solid state bonds¹¹. They inhibit diffusion of silver and prevent grain boundary migration across the bond interface. Increasing bonding temperature and deformation during bonding helps to disrupt the interface oxide. Figure 24 shows an Ag coated Al-surface in contact with an uncoated oxide covered Al-surface after being subjected to the usual bonding procedure. The Ag coating is on the upper sheet alone at A in Figure 24a. Note that after bonding at 450°C the Ag layer is no longer uniform (compare Figure 9a) because significant Ag diffusion has occurred during bonding. This produced a band of Ag-rich precipitates in the cladding at C in Figure 24a adjacent to the Ag layer. No Ag precipitation was apparent in the lower uncoated sheet at D in Figure 24a since Ag could not diffuse across the oxide film at B on the surface of the lower sheet. With increased deformation the oxide film became discontinuous (Figure 24b), silver diffused across the interface and Ag-rich precipitates were visible on both sides of the bond interface at C and B in Figure 24b.

8 DISCUSSION

The results have shown that monolithic aluminium alloy joints can be obtained by solid state diffusion bonding. All the bond strengths given in Figures 15 and 17 were obtained with a total clad layer thickness of 80 μm - 280 μm . Although some solute diffusion into the cladding occurred during heat treatment, the clad region was markedly depleted in alloying elements. However the clad layer played a vital role in the bonding process since it enabled intermetallic phase formation to be avoided by reducing the local concentration of the diffusing solute and it deformed more rapidly during bonding than the parent alloy, thus reducing the bonding time, temperature or pressure.

In spite of the soft clad layer, the maximum shear strength of 150 MPa obtained for the aged 7010 and SUPRAL 220 alloys is about a factor 3 greater than the values quoted

TABLE 3

	Alloy	Condition or temper	Tensile strength (MPa)		Shear strength
			Ultimate	Yield	
Parent metal properties [25]	1060	0	69	28	48
		H18	131	124	76
	5254	0	241	117	152
		H38	331	269	197
6066	0	152	83	97	
	T6	393	359	234	
7010 LITAL A	T7651	528	455	(320)	
	T6	450	375	(270)	
Adhesive bonded joint [21]	L73	-	-	-	~ 40
Diffusion bonded joint	7010	T6	-	-	150
	LITAL A	T6	-	-	100

for adhesive bonded Al-alloys (Table 3). The peel strengths of the 7010, 2024 and SUPRAL 220 alloy bonds were more than 40 N/mm compared with typical values for adhesive bonded Al-alloys of less than 9 N/mm. No peel test data have been found for diffusion bonded Al-alloys, but for comparison Pb - Sn soldered copper joints have peel strengths in the range 14 N/mm - 34 N/mm²⁴. From Table 3 the bulk shear strength of Al-alloys is ~ 60% of the tensile strength which suggests shear strengths of ~ 320 MPa and ~ 270 MPa for 7010 and LITAL A alloys. The maximum shear strengths obtained for the diffusion bonds in these alloys were 150 MPa (7010) and 100 MPa (LITAL A) which correspond to 47% and 37% respectively of the bulk shear properties. Some improvement on these values should be possible by reducing the Ag and clad layer thicknesses and optimising the diffusion annealing stage, provided the conditions for intermetallic and oxide phase

formation are avoided. However the maximum strength will be dictated by the weaker clad layer.

Even with the present bonding method oxide films can cause problems if the combination of time and temperature allows Al to diffuse through the Ag coating to the free surface before bonding or allows sufficient oxygen to dissolve in the Ag and react with Al at the Ag/cladding interface. The presence of intermetallic films in the bond interface of the rough surface (Figure 19) could be caused indirectly by the longer time to make complete surface contact.

The above restrictions, together with the possibility of limited hot peel strengths of the bonded joints, suggests that secondary diffusion bonding during superplastic forming would be difficult. However platen or gas pressure bonding at 280°C - 450°C prior to forming should be possible as indicated in Figure 25. It follows from the above results that any Al-alloy can be bonded by combining a silver coating with a clad surface and in practice this could have the advantage of a single bonding procedure for all Al-alloys.

9 CONCLUSIONS

Solid state diffusion bonding of commercial high strength clad Al-alloy sheet has been demonstrated at 280°C and 450°C. After heat treatment lap shear strengths of 140 MPa - 180 MPa and peel strengths of ~ 40 N/mm were obtained. The combination of Ag coating and clad surface should enable any Al-alloy to be bonded.

REFERENCES

- 1 Advanced Aluminium and Titanium Structures ASME 1981.
- 2 W S Cebulak, Proc. of Inter. Confer. on Rapid Solidification Processing 1978, p.324.
- 3 I F Saka, S L Langenbeck, SAE Tech Paper 831441 1983, p.3.
- 4 F H Froes, J R Pickens, J. Metals, p.14, January 1984.
- 5 R L Bickerdike et al, Microstructures and Tensile Properties of Vapour Deposited Aluminium Alloys, Inter. J. Rapid Solidification 1985 In the press.
- 6 G Metzger, ASM Technical Paper W9-23.2, 1969.
- 7 D M Bowden, P J Meschter, Scripta Met 18, 963, 1984.
- 8 W A Baeslack, Metallography 18, 73, 1985.
- 9 M M Schwartz, Metals Joining Manual, 1979.
- 10 C L Cline, Welding J. Suppl. 45, p.481s, 1966.
- 11 C W Haynes, Metal Progress p. 83, March 1969.
- 12 O E Osintsev, Svar Proiz No 1 p.33, 1972.
- 13 J T Niemann, G W Wille, Welding Res. Suppl. p.285s, 1978.
- 14 I M Barta, Welding Res. Suppl. p.241s, 1964.
- 15 D Hauser, D A Kammer, J H Dedrick, Welding J. Suppl. 46, p.11s, 1967.
- 16 T J Garosshen, T A Stephenson, T P Slavin, J. Metals, p. 55, May 1985.
- 17 M O Ohashi, T Hashimoto, J. Light Metal Welding and Construction, 5, 123, 1977.
- 18 J Harvey, P G Partridge, C L Snooke, J. Mater. Sc. 20, 1009, 1985.
- 19 British Standard, 1134, Pt I, 1972.
- 20 W A Lees, Metals and Materials, p.431, July 1985.
- 21 E W Thrall, Adhesion 4, 1, 1980.
- 22 P G Partridge, J Harvey, A M Lurshay, Mater. Sci. Eng. J. In the press.
- 23 J Harvey, C J Gilmore, P G Partridge, To be published.
- 24 R E Beal, J. Metals, p.63, November 1984.
- 25 Source Book on Selection and Fabrication of Al-alloys, ASM 1978 p.1.

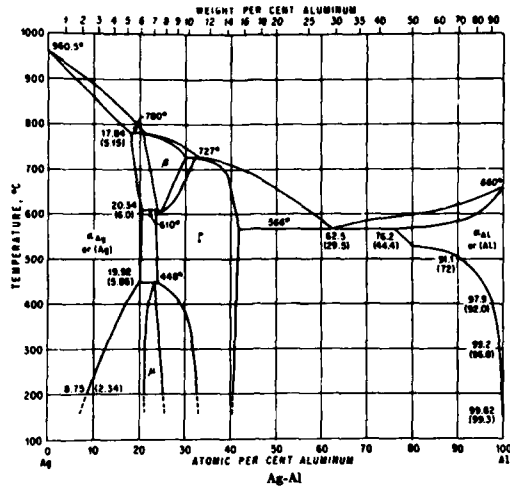
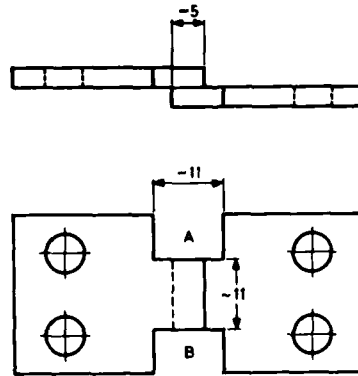


Figure 1 Ag - Al phase diagram.



Dimensions in mm

Figure 2 Lap shear test piece.

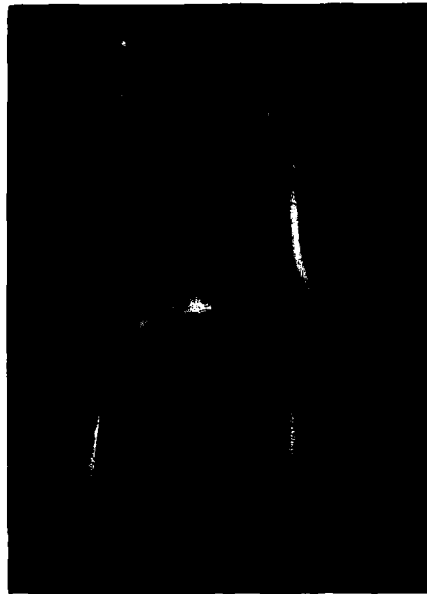
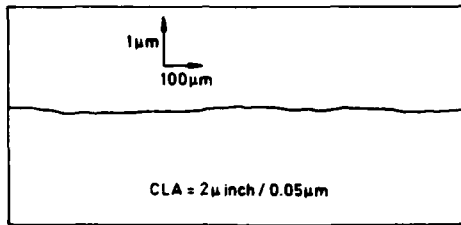
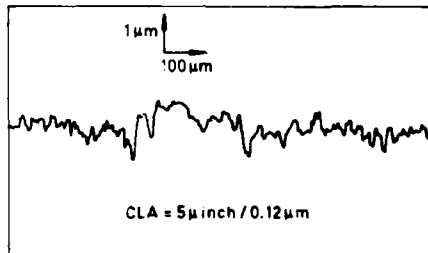


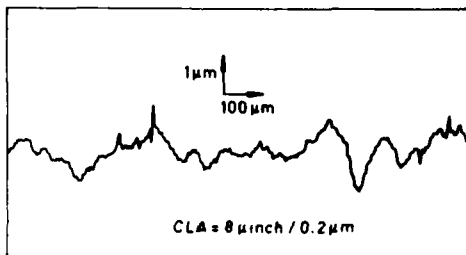
Figure 3 Peel test pieces.



a Talysurf traces for 1 μm diamond polished clad sheet



b Talysurf traces for 600 SiC ground surface of the clad sheet



c Talysurf traces for as received clad sheet

Figure 4 Talysurf traces for the surfaces of clad sheet (a) 1 μm diamond polished (b) 600 SiC grit ground (c) as received.

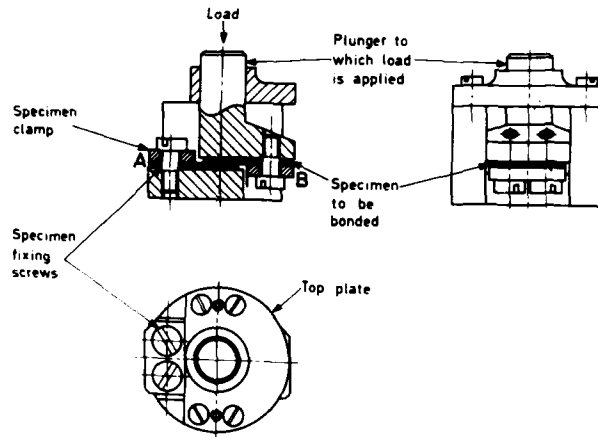


Figure 5 Lap shear test piece bonding jig.

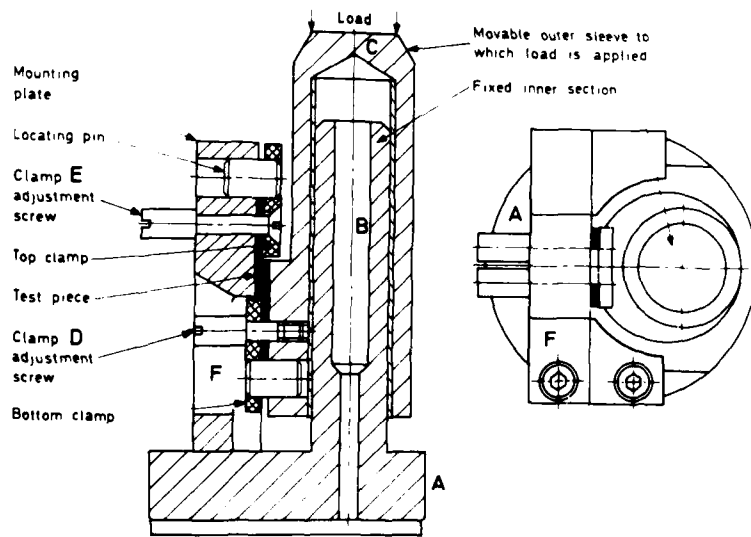


Figure 6 Lap shear test jig.

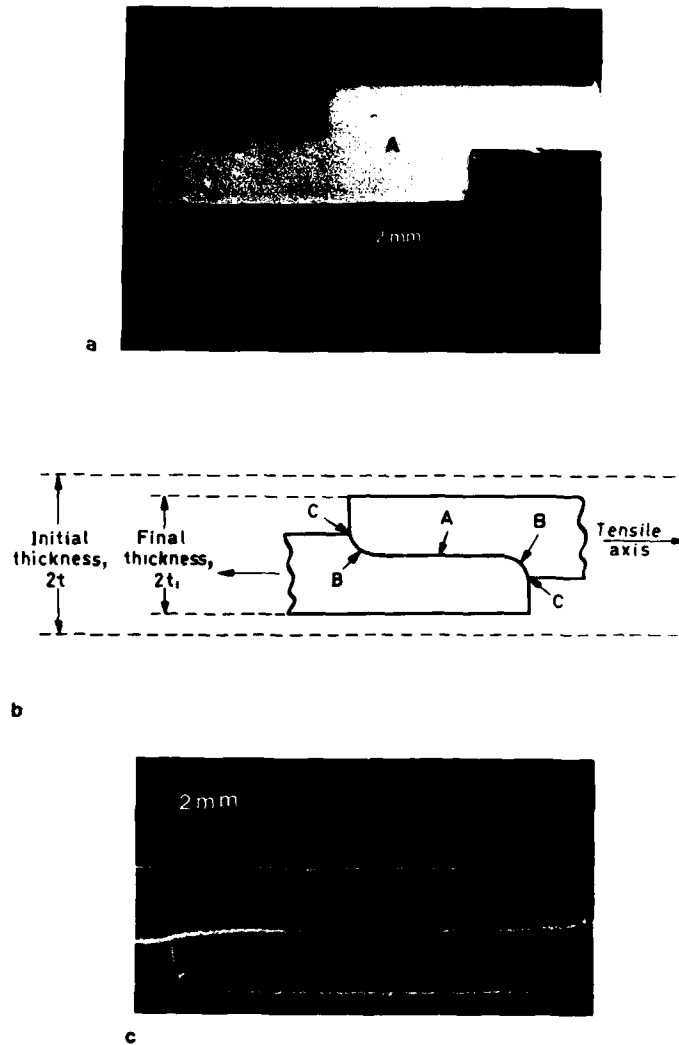


Figure 7 Lap shear test piece joints (a) section through $2t$ overlap joint (b) schematic diagram of bond interface (c) section through $6t$ overlap joint.



Figure 8 Section through lap shear test piece with overlap $< 2t$.

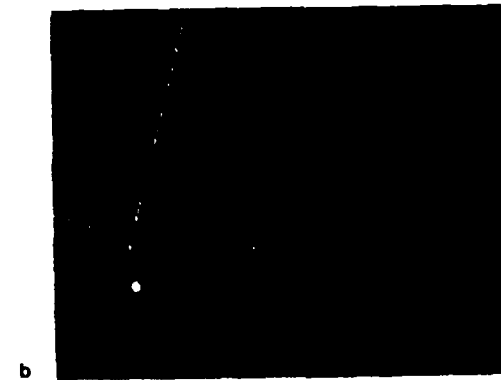
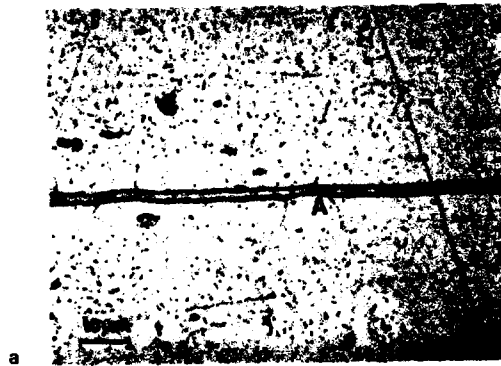


Figure 9 Diffusion bonded joint in 7010 alloy (a) as bonded (b) after solution heat treatment.

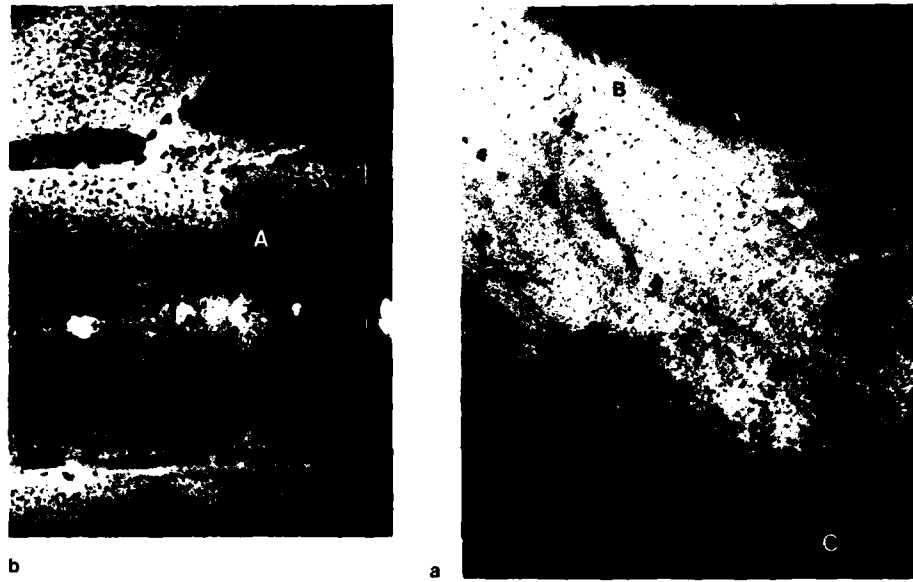
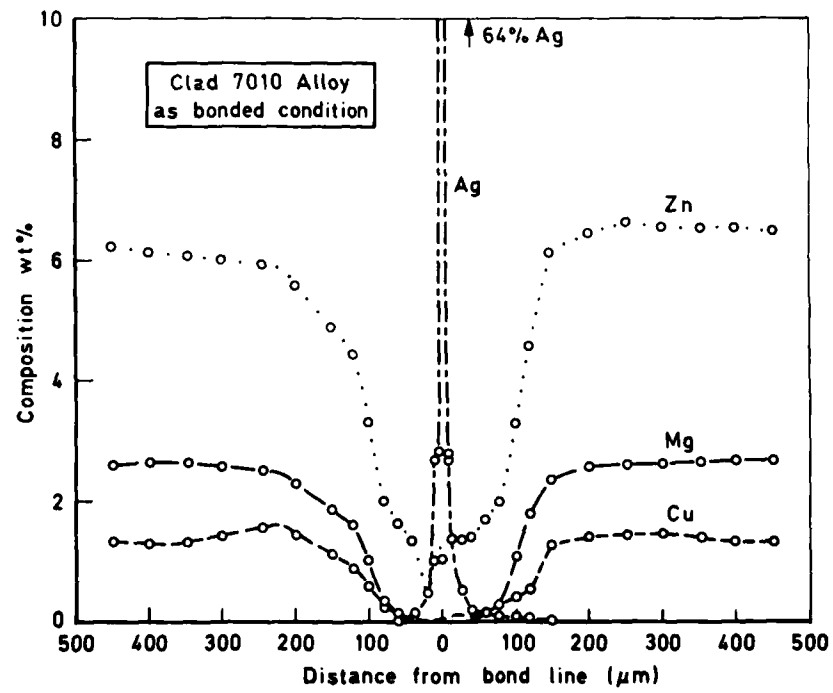


Figure 10 Transmission electron micrographs of sections through diffusion bonded joint in 7010 alloy (a) after solution heat treatment (b) after SHT and ageing.



11a

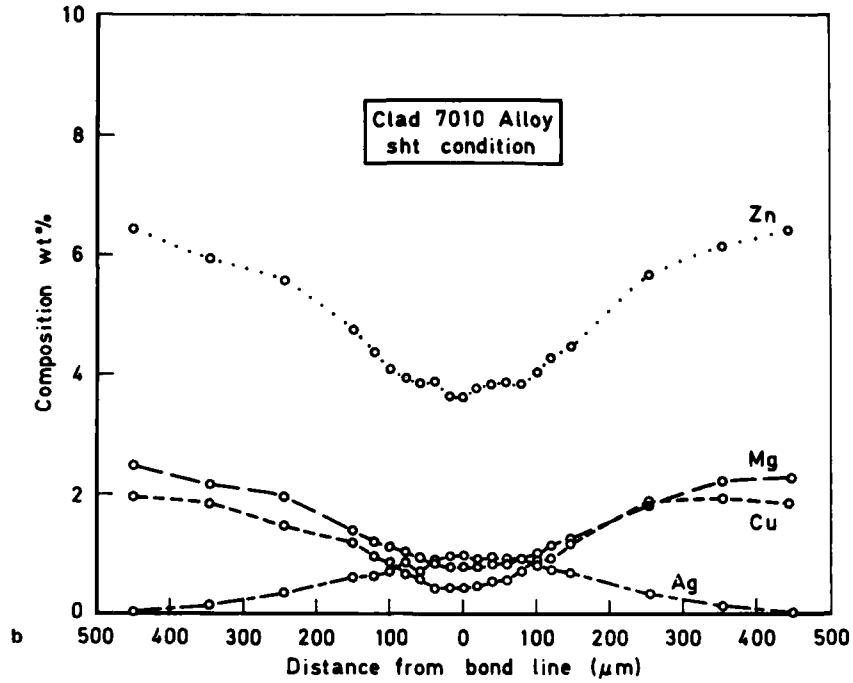


Figure 11 Composition curves across diffusion bonded joint in 7010 alloy. (a) as bonded (b) after solution heat treatment.

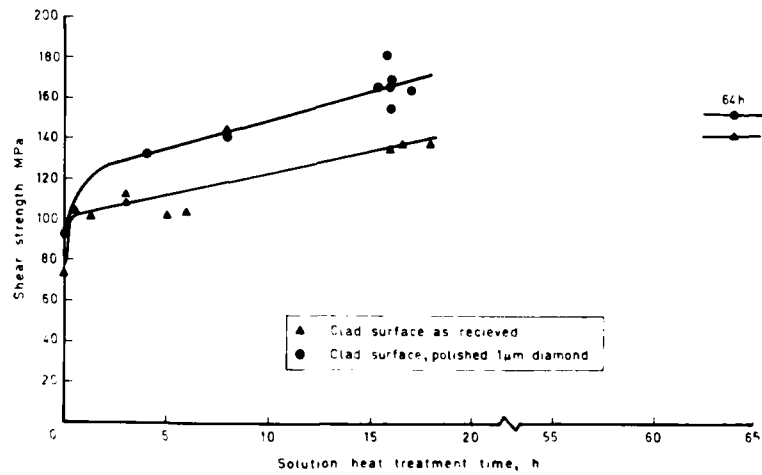


Figure 12 Shear strength versus diffusion heat treatment time at 480°C for 7010 alloy.

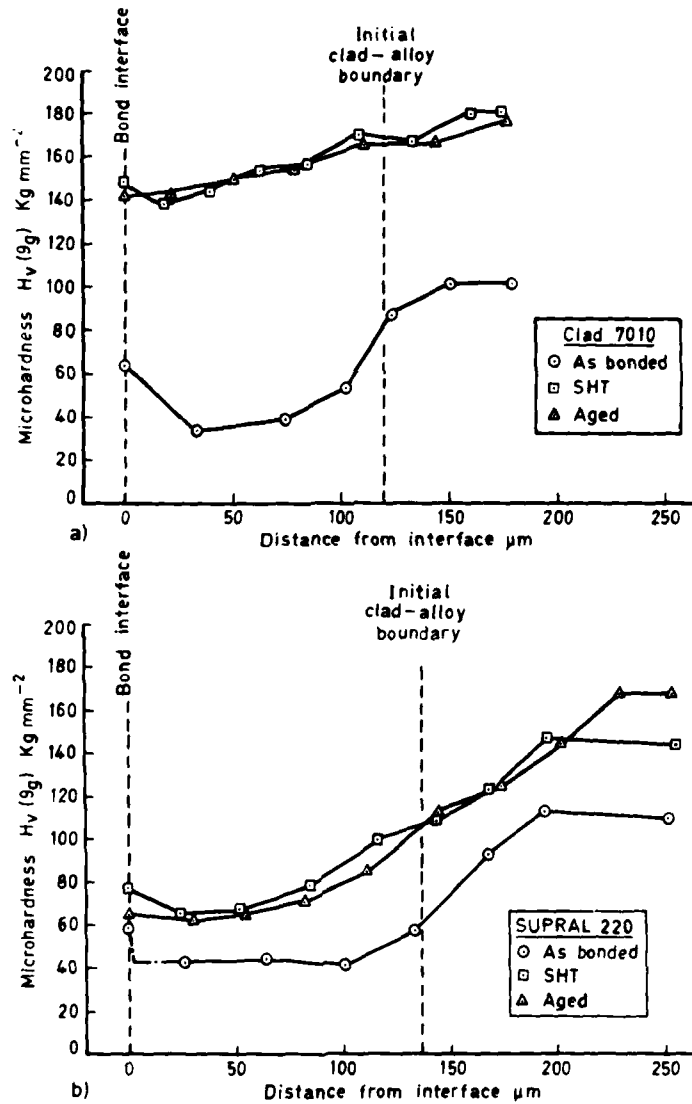


Figure 13 Microhardness versus distance from bond interface (a) 7010 alloy (b) SUPRAL 220 alloy.

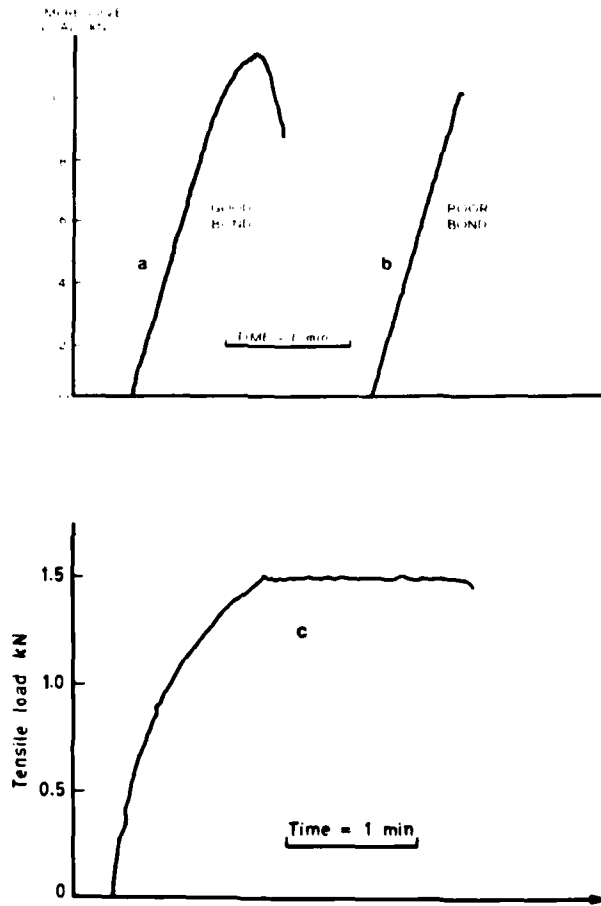


Figure 14 Load versus time curves for lap shear test pieces (a) good bond (b) poor bond and (c) for peel test piece.

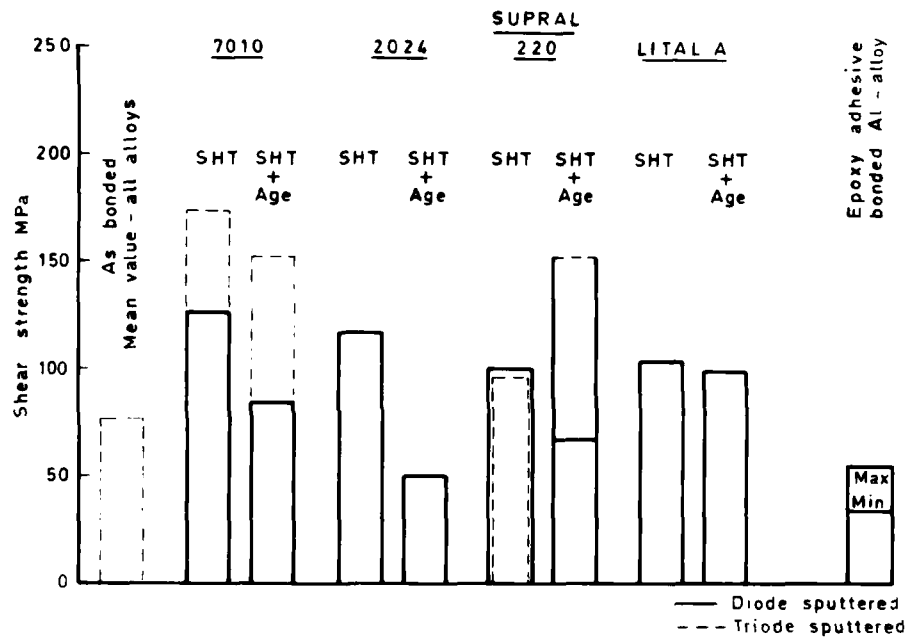


Figure 15 Lap shear strengths of diffusion bonded alloys

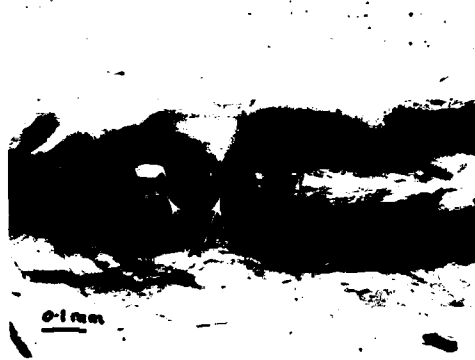


Figure 16 Plastic deformation associated with crack growth in peel test piece. (SUPRAL 220 alloy, SHT condition)

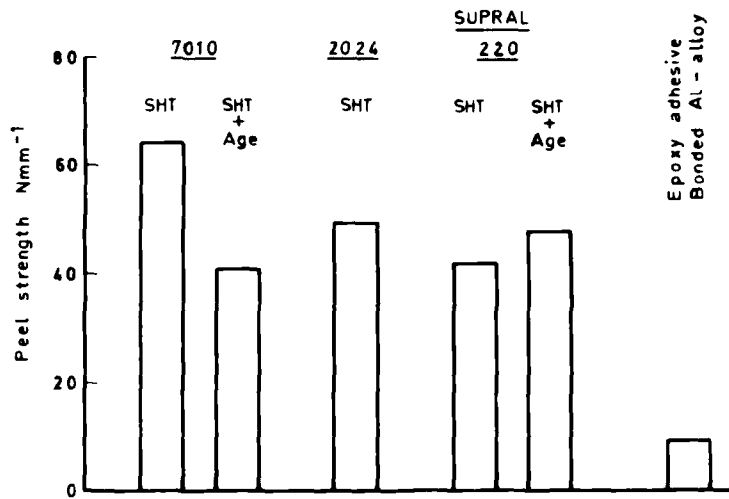


Figure 17 90° Peel strengths of diffusion bonded alloys

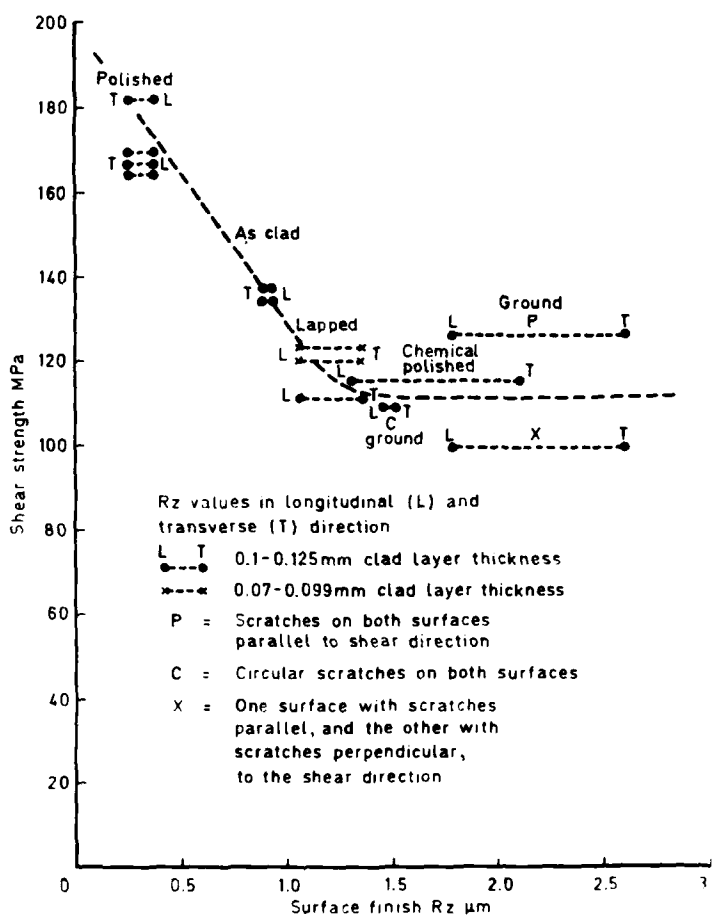


Figure 18 Shear strength versus surface finish R_z for 7010 alloy in SHT condition.

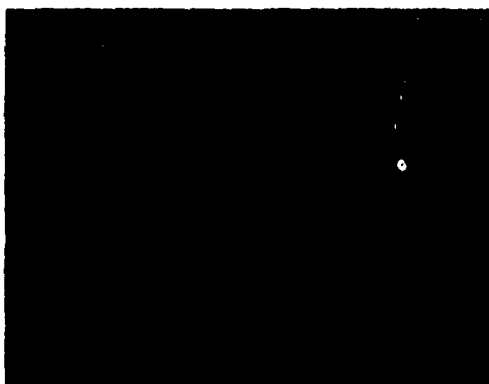
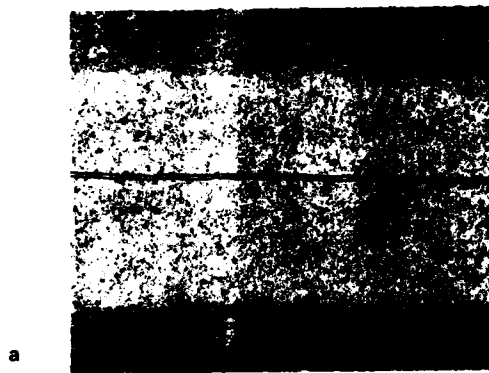
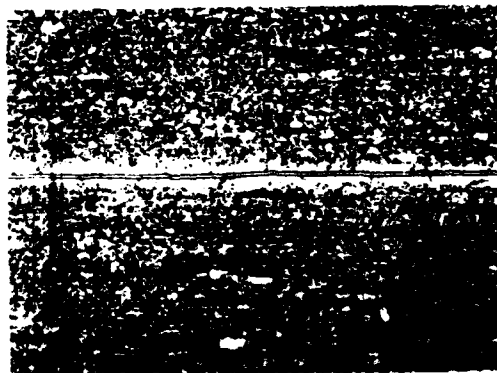




Figure 19 Diffusion bond between ground surfaces in 7010 alloy (see Figure 4c) (a) as bonded (b) after solution heat treatment.



a



b

Figure 20 Diffusion bonded joints in 7010 alloy with clad layer thickness (a) 110 μm (b) 9 μm - 24 μm.

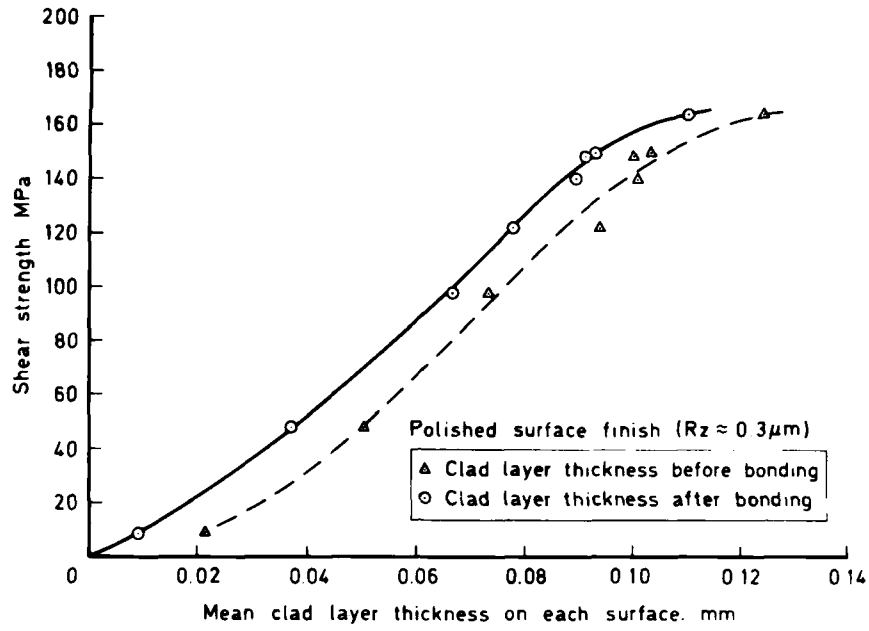
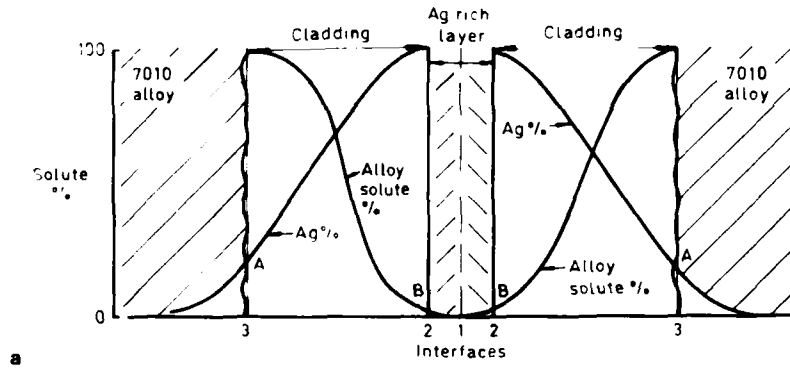


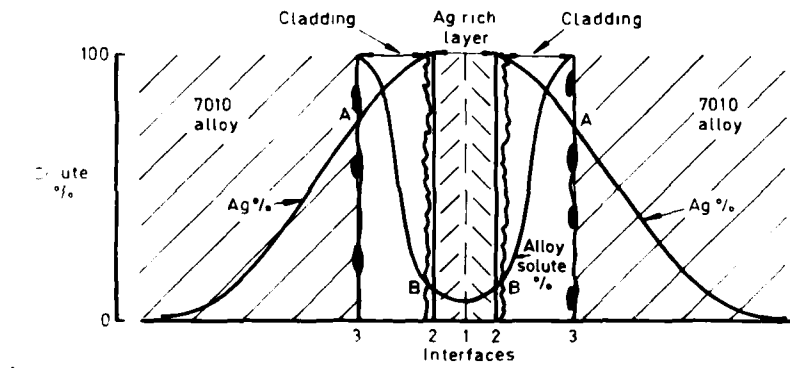
Figure 21 Shear strength versus clad layer thickness for 7010 alloy.



Figure 22 Intermetallic phases in diffusion bonded joint of 7010 alloy with thin clad layers.



a



b

Figure 23 Schematic diagram of solute concentration in diffusion bonded joints (a) thick clad layer (b) thin clad layer.

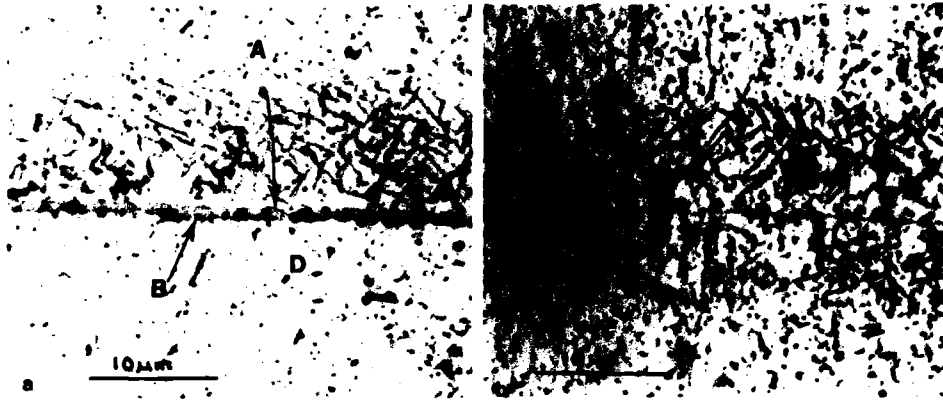


Figure 24 Diffusion bonded joint between Ag coated and uncoated sheets (a) low deformation (b) high deformation.

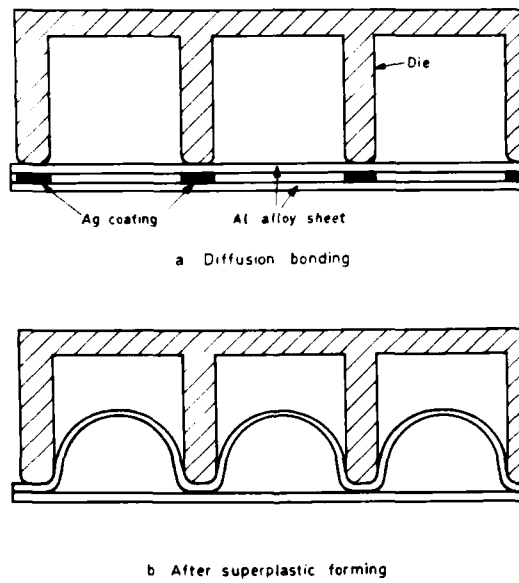


Figure 25 Superplastic forming of diffusion bonded sheet (a) bonding cycle (b) forming cycle.

**BONDING OF SUPERALLOYS BY DIFFUSION WELDING AND
DIFFUSION BRAZING**

by

Dr. P. Adam, Dipl. Ing. L. Steinhauser

MTU-München
Dachauerstr. 665
8000 München 50

SUMMARY

The paper summarizes several developments of diffusion welded and diffusion bonded turbine engine parts out of superalloys, blades, vanes, blisks. The description of results comprises nondestructive testing of parts and mechanical testing of material samples. Results are mainly presented as conclusions on the expense of detailed test results which would require individual parts/material problem presentations.

1 INTRODUCTION

Feasibility studies with accompanying extensive metallurgical investigations and mechanical strength evaluations are the contents of this paper. The poor weldability of superalloys with high strength levels up to non weldability creates the demand for other ways of manufacturing integral parts and for repair. Special interest is coming from the strength and lifetime potential of hybrid parts containing different types of superalloys. Another demand is coming up from cost escalation in casting highly sophisticated cooled blades, in particular single crystal blades.

2 MAIN FEATURES OF SUPERALLOY METALLURGY WITH RESPECT TO BONDING AND WELDING

Without reviewing superalloy metallurgy widely as in /1/ and /2/, it is recommendable for better understanding to repeat the basis characteristics with respect to bonding.

The alloys must be grouped as cast alloys and forged alloys. Cast alloys serve usually above 600 °C, forged below. Cast alloys use to contain such a high percentage of γ' -precipitation phase (> 6 weight % Al+Ti) that crack free welding is only successful in very few special cases. The solutioning of γ' -phases occurs at very high temperatures, depending on the alloy, sometimes close at the melting range. Other strengthening mechanisms are carbide precipitation and solid solution strengthening by means of large atoms like Tungsten and Molybdenum. The high level of creep strength up to very high temperatures reduces the possibility for plastic deformation during fusion welding and makes the cast alloys prone to cracking. Only a few percent plastic elongation to fracture characterizes the material under static loads.

Forged superalloys have lower γ' -contents which dissolve between 900 ° and 1100 °C completely. In the high temperature range exists no more precipitation hardening, only solid solution strengthening and some carbide precipitation. Fusion welding of these alloys is usually successful due to sufficient plasticity. The plastic elongation under static loads is an order of magnitude above cast alloys (10-20 %).

Adapted heat treatments serve to regenerate the precipitation distribution and reasonable strength after welding although the grain structure in the fused zone is basically different to the environment as a as-cast structure.

Fusion and friction welding of standard alloys are described extensively in /1/ /2/ /3/ /4/ /5/ /6/ /7/.

Some new aspects have to be considered with respect to PM-alloys which represent the floating transition between the forged and cast alloys. Their weldability is described in /8/ /9/.

3 DIFFUSION BONDING AND WELDING

Diffusion welding is defined as a process of bonding without any liquid phase. Diffusion bonding is understood to be the transitive process between brazing and diffusion welding. The essential feature of diffusion bonding is the use of an interlayer with lower melting point than the matrix but with a distinct reduction of gap width compared with brazing. Both processes are controlled mainly by diffusion.

Diffusion welding of superalloy parts suffers from the extrem small plasticity and temperature range for plastic flow, especially with cast alloys. But the supply of missing material in the weld gap can be achieved only by plastic flow. An additional difficulty is the passive surface due to the Chromium - and Aluminiumoxides. Furthermore with respect to engine parts, the reliable evacuation of the gap must be accomplished by partial separation of the parts before applying the weld pressure, which is a costly requirement.

In order to compensate the misfit between the parts in an easier way for manufacturing the diffusion bonding offers two ways: Thin layers of braze applied by evaporation or sputtering or thin foils between the parts. The strength of the joint increases with the decrease of gap width. Isothermal solidification after melting the interlayer is aspired to achieve. The principle of isothermal solidification is described in /10/, fig. 1.

3.1 DIFFUSION BONDING OF BLADES WITH ONE BONDING PLANE

Two types of blades had been selected for bonding of two halves. Fig. 2 shows a shrouded version, fig. 3 shows an unshrouded very stiff version with different designs of the cooling passages. The material was IN 100 (C 0,17, Cr 9,5, Mo 3,0, Co 15,0, Ti 5,0, Al 5,0, V 1,0). The purpose of manufacturing these blades was the evaluation of quantitative experience with this technique. Each part was machined from a complete full size blade by grinding and spark erosion of internal cooling passages. After machining the blade halves were selected pairwise by tolerance of the gap contour which had to be within $\pm 0,02$ mm. After cleaning the pairs were either coated with the braze alloy or assembled with a brazing foil between the halves. After assemblance the blades had been diffusion bonded in a high vacuum furnace (/11/ /12/) with advanced properties (operation pressure below 10^{-3} Pa, ultimate pressure 10^{-5} Pa, pumping speed of cryogenic pumps, integrated press). The blades were inspected by fluorescent penetrant inspection, x-rayed and partially checked by metallography.

The blades were tested afterwards tentatively by ultrasonic inspection. Unbonded areas can be detected as long as the geometrical condition of the test volume is favorable. If the outer and inner surface of the blade penetrated by the sound ray are defocussing, the flaw detection becomes a basic problem. Internal material bridges of less than 2 mm width are not testable with commercial equipment. Progress can only be achieved by high specific power, small and focussing transducers which are integrated in automatic scanning equipment with computerized signal analysis.

After NDT of the bonded blades they were tested for component strength twofold: Vibration test (axf) was made (RT) and cyclic hot bending tests (950 °C).

The axf-test was started with 0,6 mHz and with 0,1 mHz increments until fracture with $5 \cdot 10^6$ cycles per level.

The hot bending test was made with hot gas flow around the airfoil ($T_{max} = 990$ °C leading edge), while the root was fixed. The load was alternated between maximum and minimum for 10 s each.

The overall result can be summarized as follows: The RT-axf-test yielded only crack initiation and -growth in the matrix. The bonding plane is not weak enough. The hot bending test, accompanied by partial severe corrosion, produced cracking in the bonding plane at the leading edges but dependant on the corrosion attack. Since the corrosion attack was quite different between bonds with foils and with 8 μ m-coating in favor of the foil bonds, is it recommended to replace the hot bending test by cyclic thermal load tests with internal cooling of the blades. It seems to be the most realistic testing mode with significant bonding behaviour. As an average, the bonded blades performed almost as well as the solid blades. Restrictions must be made with respect to corrosion at the bonding line.

An additional version was used in order to vary the internal shape of radial cooling holes, fig. 4. This version required flat grinding only without a profiled grinding wheel as in the other two cases before. The diffusion bonded blades were used for rig tests for maximum leading edge cooling.

3.2 DIFFUSION BONDING OF BLADES WITH SEVERAL BONDING PLANES

With respect to difficult casting problems it is attractive to use diffusion bonding or diffusion welding of several machined rectangular pieces in one run. The different preforms can be cast without casting cores as solid blocks. Machining of cooling passages is made after casting. The final external shape is made after bonding by grinding, ECM and EDM. Fig. 5, 6, 7 and 8 show different stages of a multiple bonded small blade out of the material IN 100. The bonding material was NiCrB-foil of 50 μ m thickness. The bonding was accomplished by vacuum $< 10^{-3}$ Pa and a pressure of 20 MPa. The reference plane for all machining operations and bonding was kept the same after grinding and stacking of the rectangular pieces.

The two most interesting aspects of this exercise were the cost effectiveness and fast dimensional changes without casting tool changes. The cost analysis yielded an approximately two machining hours increase over a standard cast blade version of the same geometry. This result is important with respect to single crystal blades with increased cast scrap rates due to complex cooling systems. The mechanical and thermal testing of the blades before engine tests is started now.

3.3 DIFFUSION BONDING OF VANES

The fig. 9, 10 show the replacement of leading and trailing edges in cooled vanes. Vane repair is one of the reasons for this kind of development. Additionally repair may be performed with material of better properties than the matrix. The vanes suffer severely from thermal cyclic loads with cracking in the high temperature regions of the leading edge. The spare edges were made from the ODS-alloy YDNiCrAl in order to achieve better LCF-properties at high temperatures than the matrix material PD 16 as cast.

The manufacturing feasibility was proved and the dimensional results excellent. The LCF-testing of these repaired vanes showed cracking in those parts of the bonding with axial direction. Obviously the thermally induced stress at these positions was still too large and must be reduced by shifting the bonding position to lower thermal stresses.

3.4 DIFFUSION WELDING AND BONDING OF BLISCS (INTEGRAL TURBINE ROTORS)

Since EB- and angular friction welding fail to produce safely crack free welds between cast blades or cast rims respectively and the forged or PM disc, the diffusion welding or bonding is one of the most promising solution. The fig. 11 and 12 show two modifications of a hybrid material integral turbine rotor. The blades and the rim are cast IN 100, the disc is PM-Astroloy LC (AP 1). A version made of IN 792 (rim) and PM-Astroloy is currently under investigation.

Before bonding the disc and the rim were ground with very small angular tolerance of the cone surfaces and fitted together. After electrochemical cleaning the bonding and welding was carried out under axial pressure with diameter-enlargement of the rim between 0,1 and 0,4 mm. The diffusion bonding interlayer was 8 μm thick on each side, disc and rim.

The essential property of these bonded integral rotors must be reliability in terms of a given number of LCF-cycles.

Cyclic testing is carried out at room and elevated temperature. The results are correlated with dimensional and process parameters, with penetrant and visual inspection results. Computer x-ray tomography was applied but yielded not yet sufficient resolution for typical defects.

The average of achieved strength is excellent, allowing more than 10^3 s^{-1} operation speed. But still the possibility of undetected lower strength of single bliscs according to poor bonding must be reduced by improved NDT and sophisticated process control. The largest potential is considered to be high resolution ultrasonic testing. Computer tomography will give problems with bonding areas of lower bond strength since they will not have sufficient differences in x-ray absorption.

3.5 DIFFUSION BONDED TEST PIECES FOR NONDESTRUCTIVE TESTING

Since NDT, especially ultrasonic testing, requires always calibration of signals against defined defects, the diffusion welding and bonding with very small amounts of bonding material offers a unique way of defect incorporation in defined depth, material and size. The fig. 13, 14, 15 show examples of bonded test pieces, used for calibration and NDT-development. The test pieces were made from several different superalloys including PM-material. The bonding parameters were the same as for the bonding and welding of parts.

3.6 MECHANICAL TESTING OF MATERIAL SAMPLES

Fig. 16 shows a compilation of materials and testing modes which had been investigated so far with samples. The mechanical strength was investigated mainly in order to improve the bonding process and to gain insight into the strength potential in relation to individual materials. The quantitative results can not be reported here with respect to their large amount. The overall conclusions are:

Process control and NDT, especially US, can be improved as far as necessary to assure a sound bond without unacceptable bonding areas of decreased mechanical strength. The limit of not acceptable is therein defined as above the size of flaws within the base material, for instance casting pores. This statement holds for easily accessible bonding planes, for instance cylindrical samples. Turbine parts may have though geometrical shapes which complicate the NDT-task significantly and require shape related NDT-development.

A sound bond, either diffusion welded or diffusion bonded with liquid interlayers, has base material properties in the majority of material combinations.

LITERATURE

- 1) C.T. Sims, W.C. Hagel, editors, the superalloys 1972, John Wiley & Sons.
- 2) M.M. Schwartz, Metals joining manual by McGraw-Hill, Inc., 1979, ISBN 0-07-055720-9.
- 3) M. Prager, C.S. Shira, Welding of Precipitation-Hardening Nickel-Base Alloys, WRC Bulletin, 128, February 1968.
- 4) P. Adam, Welding of high-strength gas turbine alloys, 1978, Proc. of COST-I-Conf., ISBN 0853348154.
- 5) P. Adam, Schwungradreischweißen von Superlegierungen - Temperaturverlauf und Wulstbildung, Schweißen und Schneiden 31, 1979, 7, S. 279-83.
- 6) P. Adam, Phänomenologischer Ablauf beim Schwungradreischweißen von Superlegierungen, Schweißen und Schneiden 32, 1980, 1, S. 30-33.
- 7) P. Adam, Festigkeit von Schwungradreischweißverbindungen hochwarmfester Legierungen, Schweißen und Schneiden 33, 1981, 3, S. 123-127
- 8) P. Adam, H. Wilhelm, Welding of PM-Superalloys, 1982, Proc. of COST-II-Conf. ISBN 90-277-1468-1.
- 9) P. Adam, H. Wilhelm, Reischweißen von PM-Superlegierungen, DVS-Bericht 77, 1983, S. 52-55.
- 10) Duvall, D.S. Owczarski, W.A., and Paulonis, D.F., "TLP" Bonding: A New Method for Joining Heat Resistant Alloys," Welding Journal, 53 (4), April 1974, Research Suppl, pp. 203-s to 214-s.

- 11) P. Adam, Pilotanlagen zum Diffusionsverbinden und Beschichten von Triebwerksteilen, 1980, 2. BMFT-Statusseminar, S. 575-599, ISBN 3-88585-022-2.
- 12) P. Adam, Aufbau und Erprobung von Pilotanlagen zum Diffusionsverbinden und Beschichten hochlegierter Triebwerksteile, 1983, 3. BMFT-Statusseminar Bd. 2, ISBN 3-88135-131-0.

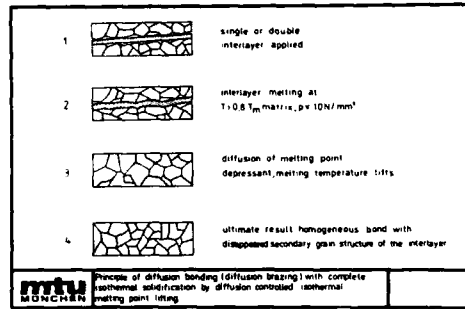


Fig. 1

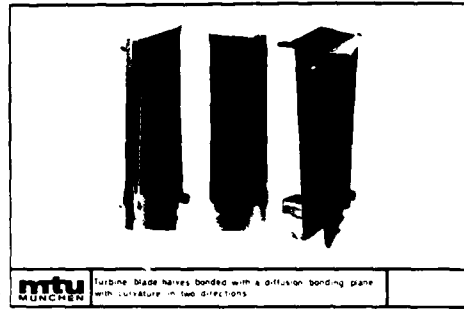


Fig. 2

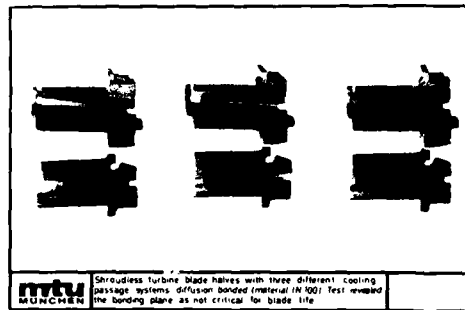


Fig. 3



Fig. 4

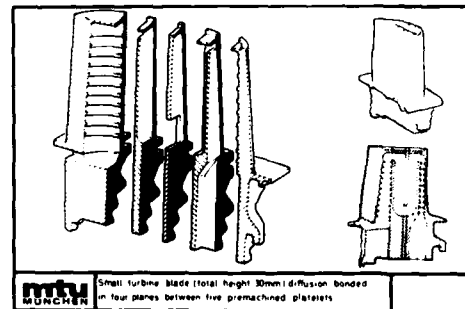


Fig. 5

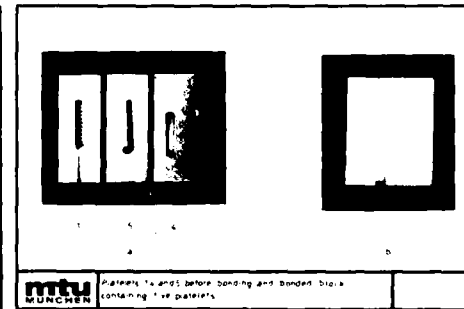
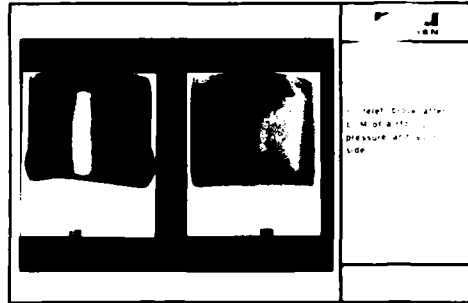


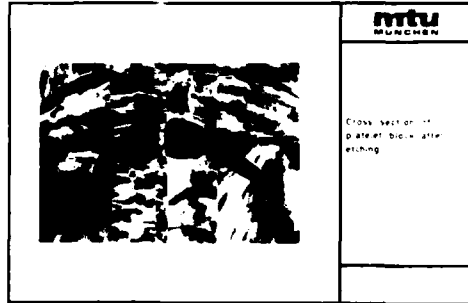
Fig. 6



mtu
MÜNCHEN

Comparison of two different types of airfoil pressure and suction side

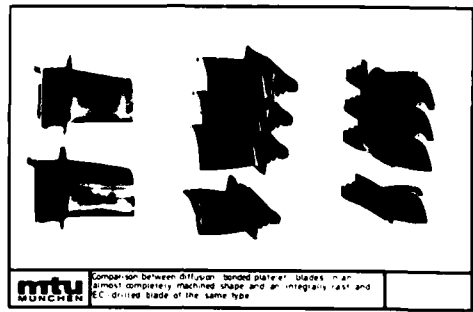
Fig. 7a



mtu
MÜNCHEN

Cross section of plate after etching

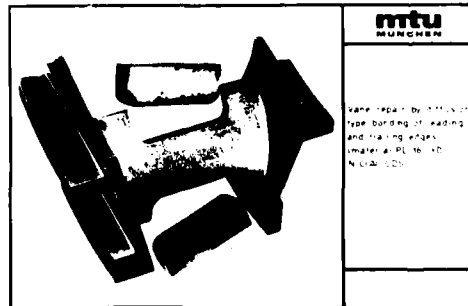
Fig. 7b



mtu
MÜNCHEN

Comparison between diffuser-bonded pattern blades in an almost completely machined shape and an integrally cast and EC-driven blade of the same type

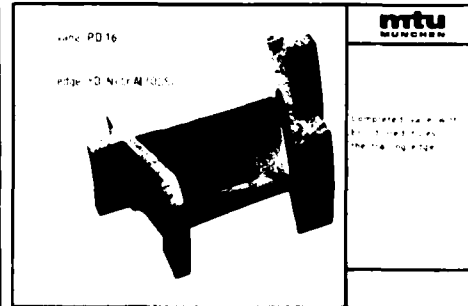
Fig. 8



mtu
MÜNCHEN

Same shape as Fig. 8 but type bonding of leading and trailing edges. Material: PL 16-10 NiCrAlCo

Fig. 9

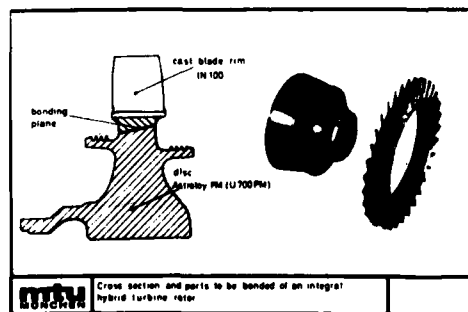


mtu
MÜNCHEN

Line: PD 16
edge: 10 NiCrAlCo

Integrated blade with EC-driven leading edge

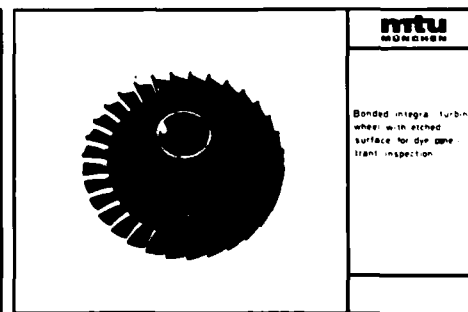
Fig. 10



mtu
MÜNCHEN

Cross section and parts to be bonded of an integral hybrid turbine rotor

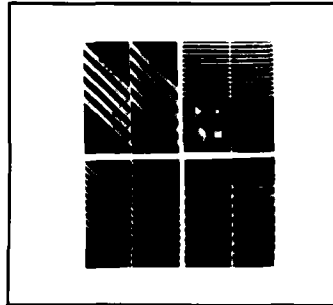
Fig. 11



mtu
MÜNCHEN

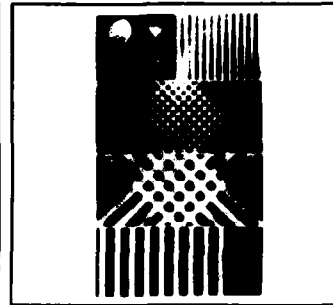
Bonded integral turbine wheel with etched surface for dye penetrant inspection

Fig. 12



mtu
MÜNCHEN

Samples for NDT calibration before diffusion bonding. The patterns 1-4 are detected after bonding by X-ray and ultrasonic devices.

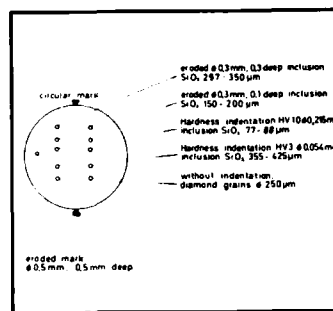


mtu
MÜNCHEN

X-ray inspection after diffusion bonding the four pairs of parts shown in Fig. 13.

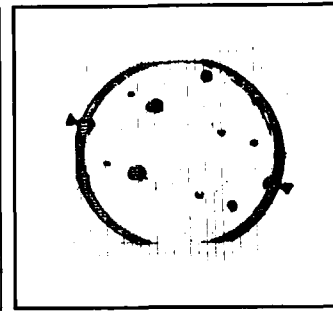
Fig. 13

Fig. 14



mtu
MÜNCHEN

Sample for ultrasonic detection of small size holes and inclusion within the diffusion bonding plane. Material: Astroloy PM / Astroloy PM.



mtu
MÜNCHEN

Scan of the test sample in Fig. 15a. US signals correlate with inclusion site. Below 100 µm inclusions no signal with available equipment.

Fig. 15a

Fig. 15b

Material	type of bonding	NDT*	Destructive type of testing
IN 100/IN 100	Diffusion bonding	FPI US	tensile; hot tensile; creep; hot ε-LCF hot σ-LCF; RT HCF; metallography, fractography
	Diffusion welding	FPI	tensile; hot tensile; creep; metallography
Single crystal IN 100/IN 100	Diffusion bonding	-	metallography
IN 100/Astroloy PM	Diffusion bonding	FPI US	hot tensile; creep; HCF RT; σ-LCF hot; metallography; fractography; SEM
	Diffusion welding	FPI US	tensile; hot tensile; metallography
IN 752/Astroloy PM	Diffusion bonding	FPI US	tensile; hot tensile; creep; HCF RT; σ-LCF hot; fracture toughness; SEM
	Diffusion welding	FPI US	tensile; hot tensile; metallography
MA 6000/MA 6000 (ODS)	Diffusion bonding	-	hot tensile; creep; fracture toughness; RT bending; metallography
	Diffusion welding	-	metallography
MA 956/MA 956 (ODS)	Diffusion bonding	-	RT-bending; metallography
	Diffusion welding	-	metallography
MA 754/MA 754	Diffusion bonding	-	RT-bending; metallography
	Diffusion welding	-	metallography
Single crystal alloys CMSX 2/CMSX 2 CMSX 3/CMSX 3 MSRR 99/ MSRR 99	Diffusion bonding	FPI US	4-point-hot bending 950°C metallography

mtu
MÜNCHEN

* NDT = Nondestructive testing
FPI = Fluorescent penetrant inspection
US = Ultrasonic testing

Fig. 16
Summary of investigations of diffusion bonded and welded test samples

**APPLICATION DU SOUDAGE PAR DIFFUSION ASSOCIE AU FORMAGE SUPERPLASTIQUE (SPF/DB)
A LA REALISATION DE STRUCTURES EN TOLES MINCES DE TA6V**

M. BOIRE et P. JOLYS
Direction Centrale Industrielle
Département Production - Recherches
AEROSPATIALE
12, rue Pasteur
92150 - SURESNES - France

Résumé

Après un bref rappel de l'intérêt de l'alliage de titane TA6V pour la réalisation de structures et des problèmes relatifs à sa mise en oeuvre, on présente l'apport potentiel de la technologie SPF/DB.

Les conditions de mise en oeuvre de cette technologie sont précisées ainsi que leur impact sur certaines propriétés du matériau.

Des exemples de réalisation de structures sont présentés et on se propose, à travers ceux-ci, de dégager un bilan technique et économique.

Enfin, les principaux problèmes à résoudre pour aboutir à la maîtrise industrielle du processus, sont explicités et les développements correspondants proposés.

1. INTRODUCTION

Certains alliages de titane et notamment le TA6V, possèdent des propriétés intéressantes pour la réalisation de certaines structures aéronautiques.

En effet, cet alliage est :

- . résistant, $R > 900$ MPa (état recuit)
- . léger (densité = 4,5)
- . stable vis-à-vis de la corrosion
- . compatible avec les matériaux composites à base de fibres de carbone

Par contre, il présente :

- . un coût matière élevé
- . une mise en oeuvre difficile et onéreuse (usinage, formage à chaud, etc ...).

Les technologies de mise en oeuvre, qui permettent de diminuer l'enlèvement matière et allègent les conditions actuelles de fabrication, méritent donc d'être développées.

Celle, relative au SPF/DB qui associe assemblage et formage dans un même cycle de chauffe, et donc réduit certains usinages (pièces élémentaires, trous pour assemblage, etc ...) offre à cet égard des avantages potentiels importants.

Après avoir rappelé les conditions opératoires attachées à la réalisation du soudage par diffusion et du formage superplastique, on présente des exemples d'application et les moyens utilisés.

A partir de ces applications, on tente de dégager un bilan technico-économique ainsi que les développements à entreprendre, soit pour résoudre les problèmes rencontrés, soit pour élargir le champ d'emploi de cette technologie.

2. SOUDAGE PAR DIFFUSION

2.1 - Définition

Le soudage par diffusion est défini comme "un soudage en phase solide, dans lequel les pièces maintenues en contact sous une pression donnée sont portées à une température définie pendant un temps contrôlé".

Ces conditions opératoires conduisent, par des déformations plastiques locales de la surface, à un contact intime et à une migration des atomes permettant d'obtenir la continuité de la matière. (Voir Fig. 1).

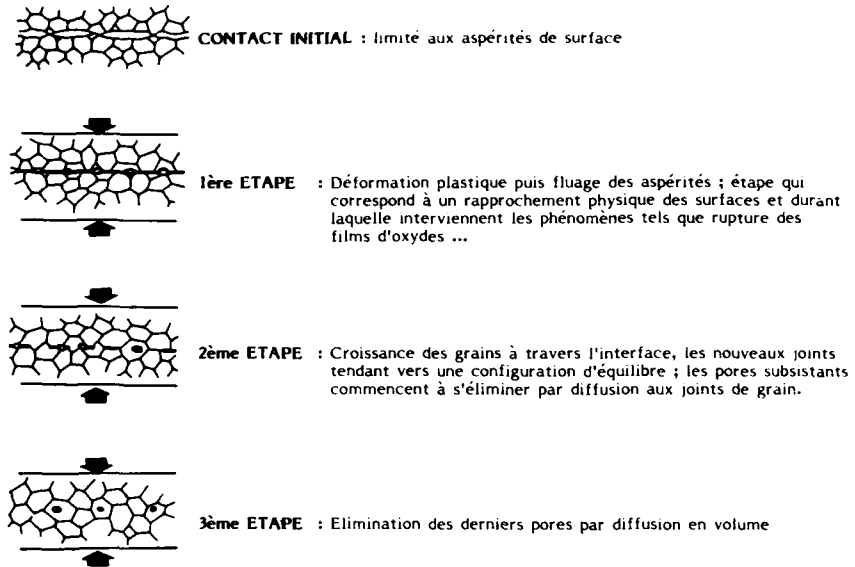


Figure 1 - Schématisation des trois étapes de soudage par diffusion

2.2 - Paramètres de soudage par diffusion

Le soudage par diffusion est essentiellement régi par les paramètres :

- . température
- . durée
- . pression

Température :

Le domaine de température préconisé se situe dans l'intervalle 900 à 950°C. La température retenue est de 925°C.

Durée - Pression :

A température de 925°C, les paramètres pression de soudage et durée de maintien à température sont précisés figure 2.

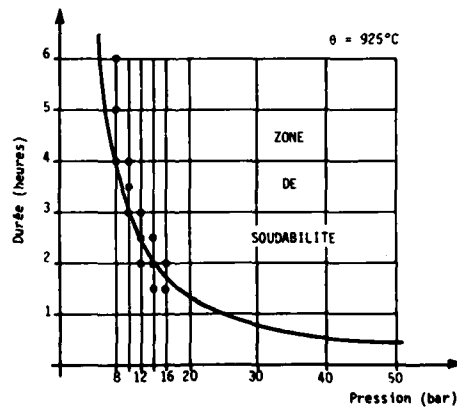


Figure 2

Par ailleurs, à cette température, le TA6V est relativement sensible à l'oxydation. L'utilisation du vide étant délicate et conduisant à des investissements importants, on a opté pour l'utilisation de gaz neutre (Argon) afin de réduire la pollution du matériau.

2.3 - Conditions opératoires retenues

Matériau : TA6V recuit

Préparation de surface :

Dégraissage alcalin

Décapage fluonitrique

Paramètres de soudage :

θ : 925°C

P : 8 bars

t : 5 heures

3. FORMAGE SUPERPLASTIQUE

3.1 - Définition

Un solide a un comportement superplastique lorsque dans certaines conditions de microstructure, de température et de vitesse de déformation, il est capable d'atteindre en traction des allongements à la rupture nettement supérieurs à ceux qu'il atteint dans les conditions habituelles.

(Le TA6V peut atteindre jusqu'à 800% d'allongement).

Le comportement superplastique est caractérisé par deux critères essentiels :

- il a lieu à haute température $\theta > 0,5 \theta_f$ (θ_f température de fusion du matériau)
- l'écoulement peut être décrit par une équation de la forme

$$\sigma = K \dot{\epsilon}^m$$

avec σ contrainte de déformation

$\dot{\epsilon}$ vitesse de déformation

m coefficient de sensibilité à la vitesse de déformation. Ce coefficient m détermine l'aptitude du matériau à la superplasticité. (m doit être supérieur à 0,3 pour observer le phénomène).

De plus, le grain du matériau doit être équiaxe, de taille faible (quelques microns) et stable à température élevée.

3.2 - Paramètres de formage superplastique

Température

Le choix de la température est conditionné par plusieurs facteurs :

- $\theta > 0,5 \theta_f$ pour se situer dans le domaine où le matériau a un comportement superplastique (pour le TA6V $\theta > 850^\circ\text{C}$).
- $\theta < \theta_\beta$ (θ_β : température du changement de phase $\alpha \rightarrow \beta$) pour éviter un grossissement important du grain et conserver un matériau biphasé (pour le TA6V $\theta < 950^\circ\text{C}$).
- θ compatible avec le soudage par diffusion du matériau. En effet, on associe fréquemment les deux phénomènes formage superplastique et soudage par diffusion en un seul et même procédé dit SPF/DB.

Pour respecter ces différentes considérations, la température de formage superplastique retenue est : $\theta = 925^\circ\text{C}$.

Vitesse de déformation - Contrainte de déformation ($\dot{\epsilon}$ et σ)

Ces paramètres sont choisis dans le but de favoriser le comportement superplastique du matériau représenté par le paramètre "m" : (Coefficient d'aptitude au formage superplastique).

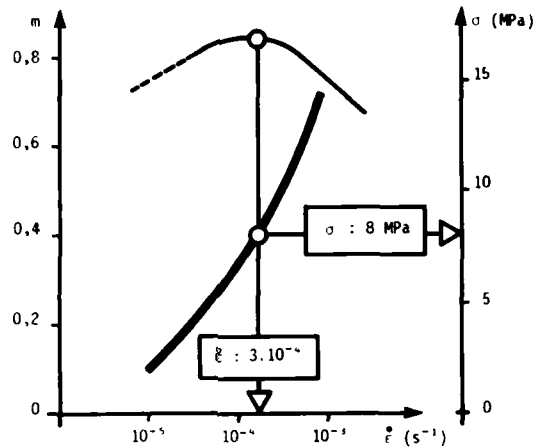


Figure 3 - Détermination des paramètres $\dot{\epsilon}$ et σ

3.3 - Conditions opératoires retenues

Matériau :

TA6V recuit (Taille de grain de l'ordre de 10 à 15 μm).

Paramètres :

Température : 925°C

Vitesse de déformation $\dot{\epsilon}$: $3 \cdot 10^{-4} \text{ s}^{-1}$

Contrainte de déformation σ : 8 MPa

Compte tenu de la température de réalisation et des contraintes faibles à appliquer, le moyen retenu pour réaliser le formage superplastique est un gonflage par gaz neutre (Argon).

Le respect des paramètres vitesse et contrainte de déformation, à la température définie, ne peut se faire que par l'application d'une loi de variation de pression pilotant ce gonflage en fonction du temps.

(Détermination de la loi de pression voir annexe 1).

4 - ASSOCIATION SOUDAGE PAR DIFFUSION ET FORMAGE SUPERPLASTIQUE

Les schémas ci-dessous illustrent les principales phases qui permettent d'associer les deux phénomènes pour aboutir à la réalisation d'une structure à partir de deux tôles.

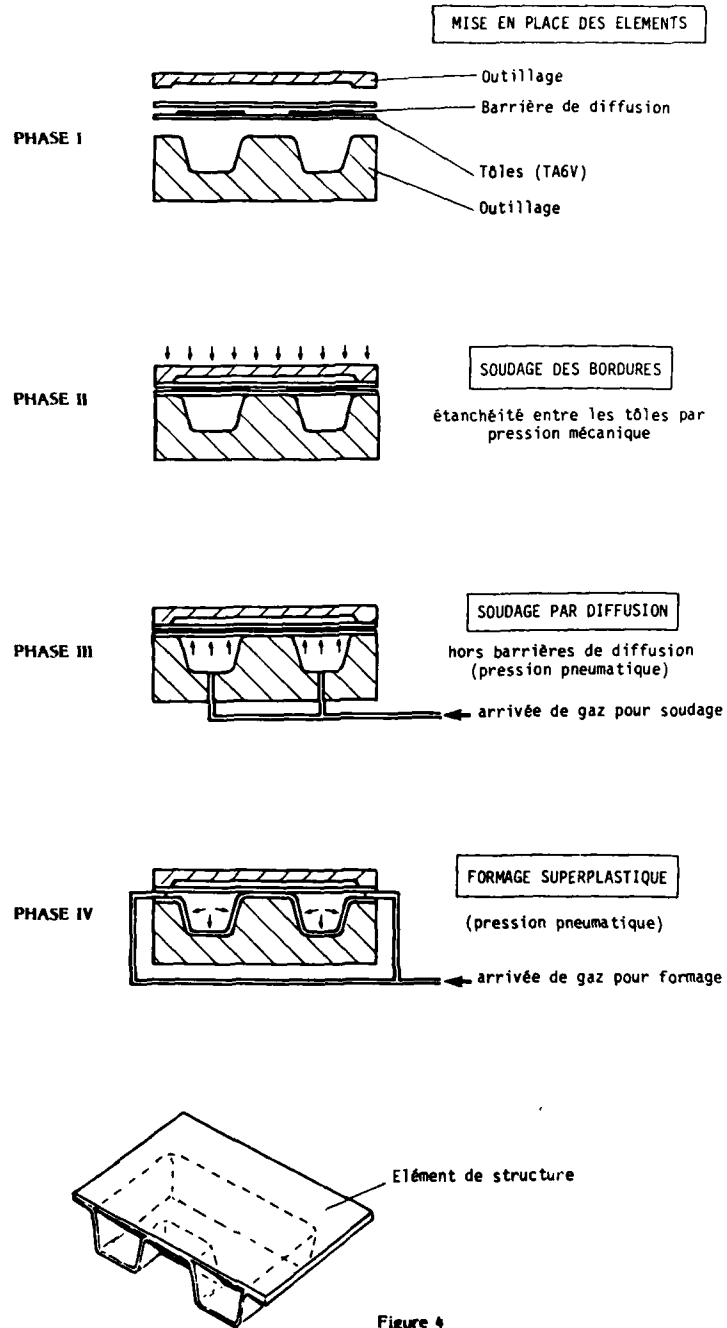


Figure 4

5. EXEMPLES DE REALISATION

5.1 - Définition des structures

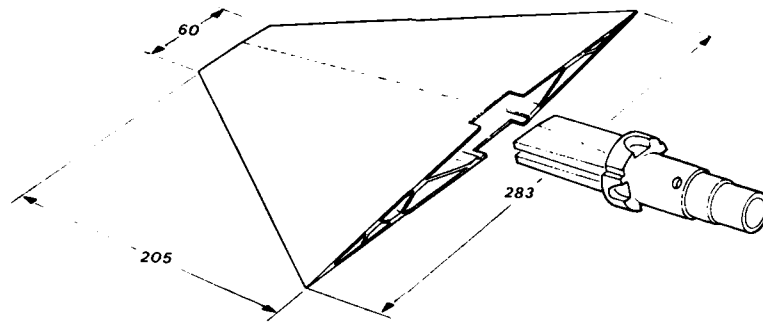
GOUVERNE D'ENGIN

Figure 5

Cette pièce se compose d'un caisson et d'une ferrure d'attache. Le caisson de profil aérodynamique est réalisé par SPF/DB, il est constitué de trois tôles, l'une d'entre elles assurant le raidissage interne. Le mât est rapporté ultérieurement par soudage.

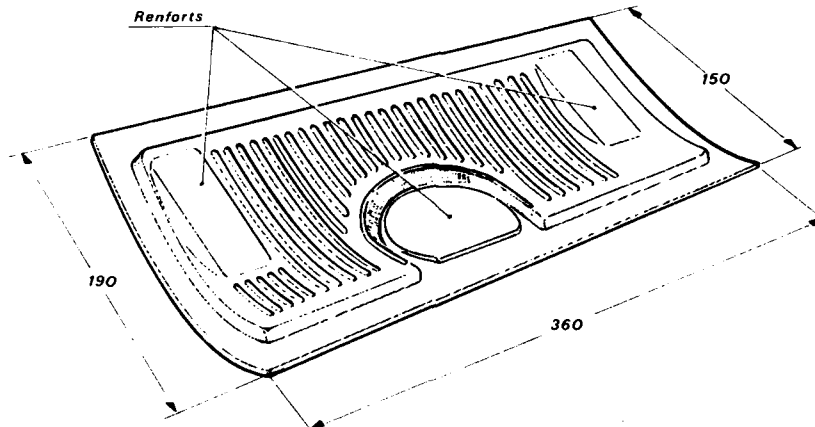
PORTE DE MAT REACTEUR

Figure 6

Cette porte est réalisée par SPF/DB. Elle est constituée de deux peaux dont l'une est formée au profil aérodynamique. Les renforts locaux, permettant sa fixation au reste de la structure, sont intégrés dans l'opération SPF/DB ce qui permet d'obtenir cette pièce en une seule phase.

5.2 - Gamme opératoire

La gamme de réalisation d'une pièce par SPF/DB comporte les principales phases suivantes :

Préparation des flans

- détournage à plat
- préparation de surface
 - . dégraissage alcalin
 - . décapage fluonitrique
- application des barrières de diffusion

Cycle SPF/DB

Nettoyage pièce

Contrôle

Détournage - finition

5.3 - Moyens

L'ensemble des moyens nécessaires à la réalisation des structures par SPF/DB est schématisé ci-après :

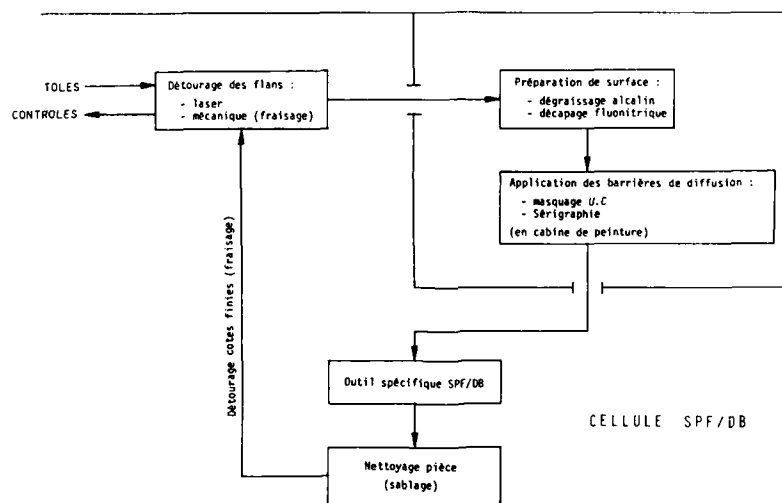


Figure 7

Les principales difficultés à résoudre en ce qui concerne la définition de ces moyens, portent sur ceux qui sont appelés à fonctionner à haute température, à savoir : les matrices et l'outil SPF/DB qui permet la mise en température, l'application des efforts mécaniques, l'introduction du gaz de gonflage et la reprise des efforts qui en résulte.

Le matériau utilisé pour la réalisation des matrices doit être dans le domaine 900 - 950°C :

- . dimensionnellement stable
- . résistant à l'oxydation
- . compatible avec le titane sur le plan dilatation

Par ailleurs, on doit également tenir compte de données économiques telles que le coût d'approvisionnement et la facilité d'obtention de formes complexes (usinabilité, moulabilité, ...) dans le choix du matériau.

Après une étude comparative des différents moyens industriels existants (fours, presses chauffantes) et, compte tenu des cycles de réalisation, nous avons opté pour l'étude et la réalisation d'un moyen autonome spécifique au procédé SPF/DB constitué d'une presse à plateaux chauffants dont les caractéristiques sont les suivantes :

- Température de fonctionnement en continu : 950°C
- Puissance électrique 50 KW
- Dimensions des plateaux chauffants 640 x 1100 mm
- 3 zones de régulation de température par plateau
- Reprise d'effort 40 Tonnes

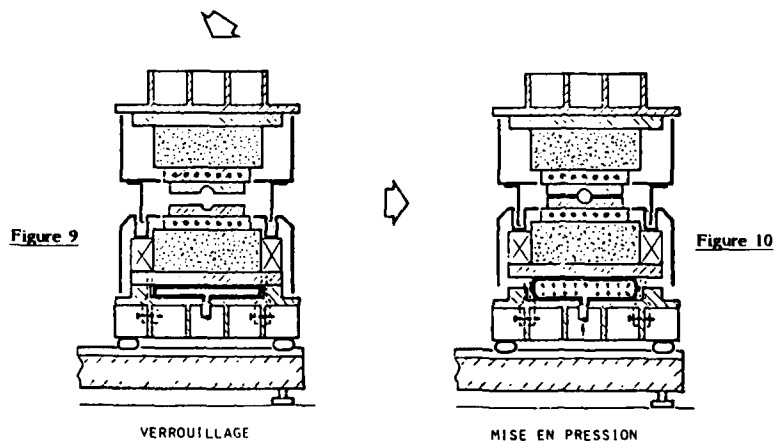
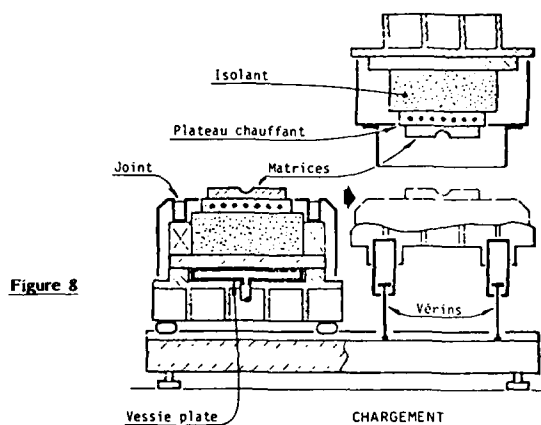
Cette presse est composée d'un bâti supérieur, reposant sur quatre vérins, l'animant d'un mouvement de translation vertical et d'un bâti inférieur animé d'un mouvement de translation horizontal (voir Fig. 8). Chaque bâti comporte une matrice et un plateau chauffant reposant sur un bloc d'isolant.

En position "ouverte", le dégagement du bâti inférieur permet une bonne accessibilité aux matrices, pour l'enfournement et le défournement des pièces.

En position "fermée", les efforts sont verrouillés entre les deux bâtis par l'intermédiaire de broches situées en zone froide (voir Fig. 9). Les matrices sont alors centrées l'une par rapport à l'autre.

L'effort nécessaire au soudage par diffusion, ainsi qu'à la reprise des efforts de gonflage, est appliqué par l'intermédiaire d'une vessie gonflable située sous le bâti inférieur (voir Fig. 10).

Par ailleurs, on sait que le procédé nécessite une atmosphère neutre. On réalise donc une étanchéité partielle, à l'aide d'une paroi solide du bâti supérieur, dont le bord plonge dans une rainure remplie de sable située sur le bâti inférieur. Cet ensemble forme une chambre de travail dans laquelle on peut introduire un gaz neutre.



L'ensemble de ce fonctionnement ainsi que la réalisation des cycles thermique et de pression sont entièrement automatisés (pilotage par microprocesseur - voir Fig. 11). La seule opération manuelle reste le chargement et le déchargement des pièces correspondant à quelques minutes sur un cycle SPF/DB d'une douzaine d'heures.

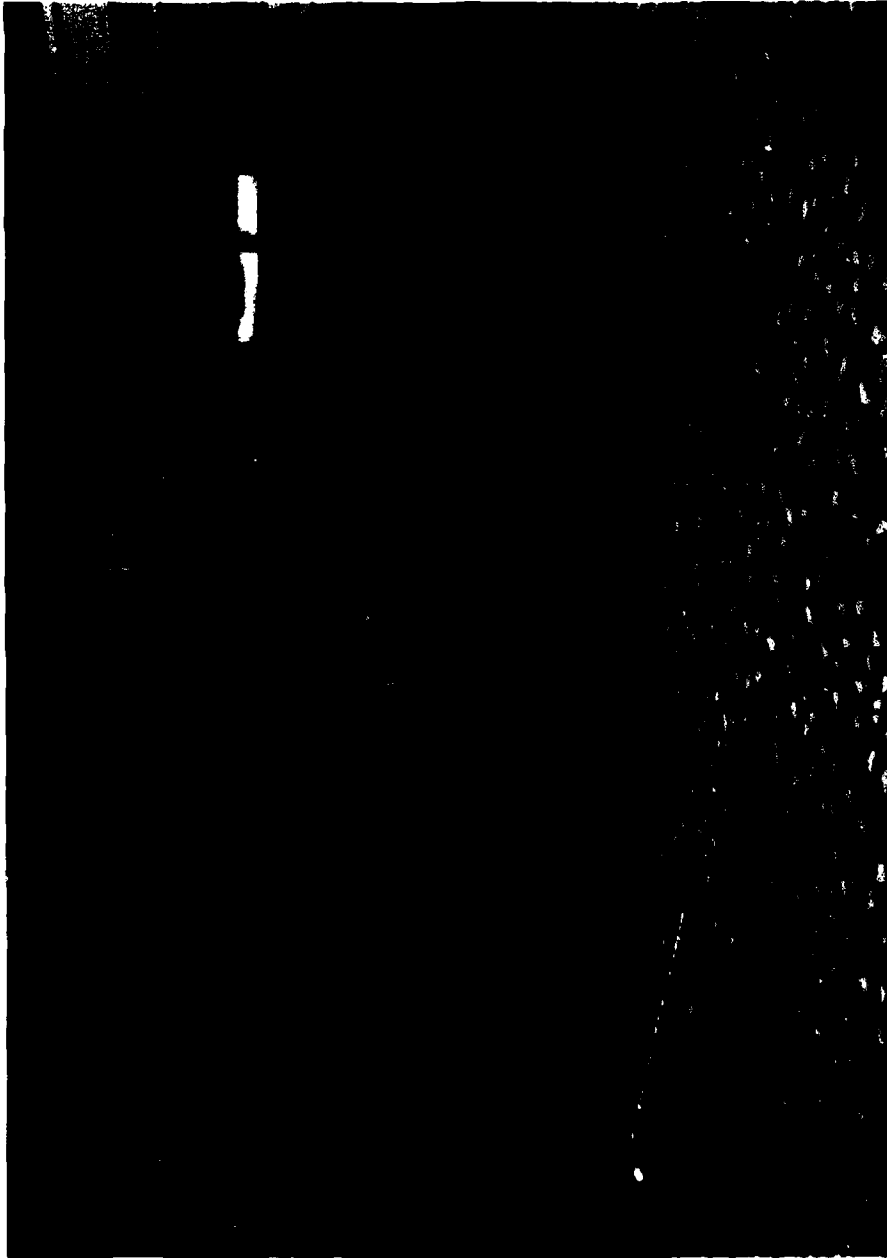


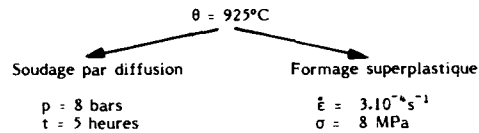
Figure 11

6. RESULTATS

La réalisation des structures définies précédemment permet de dresser un premier bilan de l'emploi de la technologie SPF/DB.

Sur le plan technique :

- les conditions opératoires ont été validées :



et le respect de ces conditions a conduit à l'obtention de résultats reproductibles.

- on a pu mettre en évidence, l'influence importante de la loi de pression associée au formage superplastique sur la qualité géométrique de l'élément à réaliser (forme, distribution des épaisseurs, etc ...).
- la faisabilité du contrôle par ultra-sons du soudage par diffusion a été évaluée, et l'on dispose ainsi d'une méthode fine d'appréciation des résultats qui contribue largement à la mise au point du procédé.
- l'influence du cycle thermique sur les caractéristiques mécaniques du matériau TA6V a été étudiée. Si son effet sur les propriétés statiques est faible, on observe des conséquences importantes sur les caractéristiques de fatigue (voir figure 12).

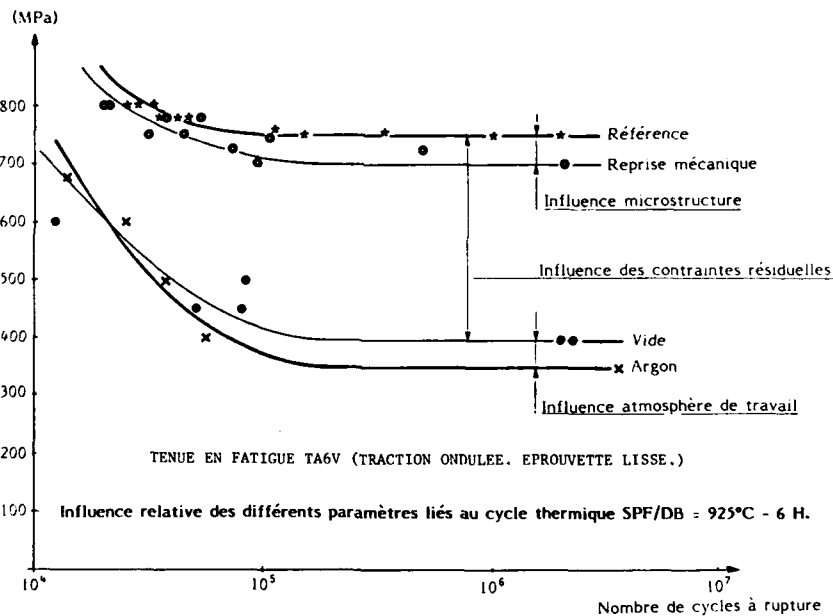


Figure 12

Cette chute de caractéristiques est attribuée essentiellement à trois causes :

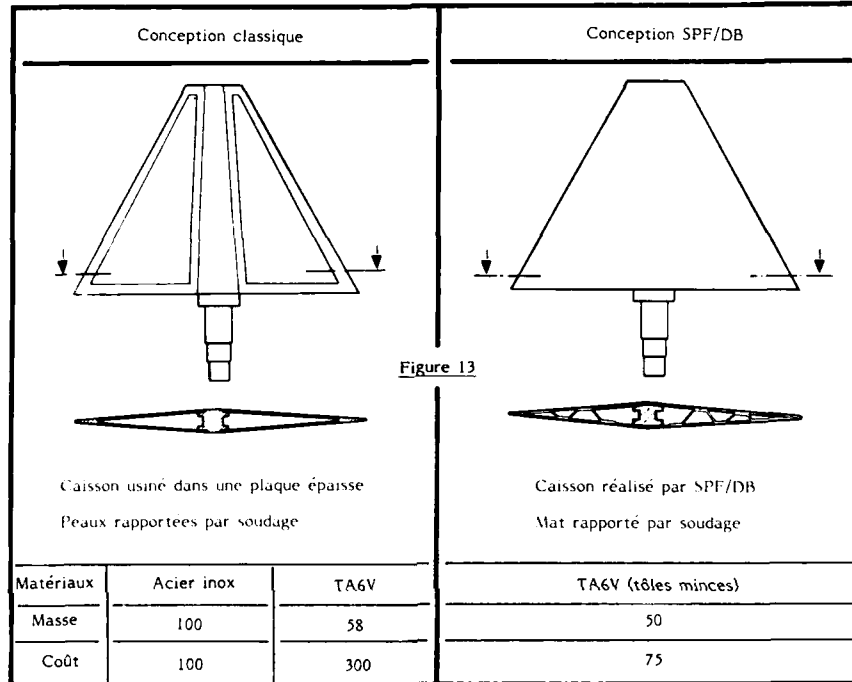
- . diminution des contraintes superficielles de compression induites par le laminage et/ou l'usage
- . pollution superficielle du matériau
- . modification de la microstructure

le premier de ces facteurs semblant prépondérant.

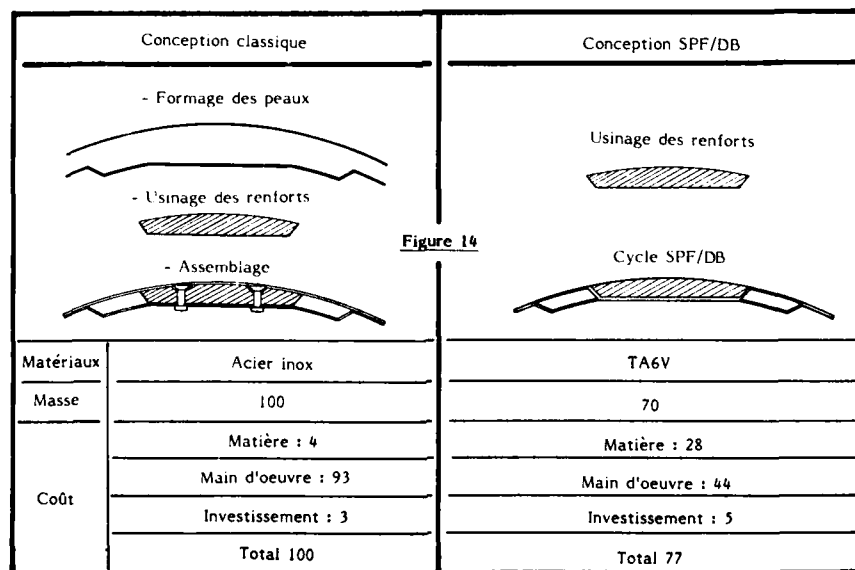
Sur le plan économique :

Pour les deux exemples de structures réalisés, le bilan économique est résumé dans les tableaux ci-dessous :
(Figures 13 et 14)

GOUVERNE D'ENGINE



PORTE DE MAT REACTEUR



On notera également, que la technologie SPF/DB permet une réduction sensible des en cours.

7. DEVELOPPEMENTS

Si l'utilisation du procédé SPF/DB pour la réalisation de structures aéronautiques en TA6V constitue une solution attrayante, de nombreux développements sont encore à conduire pour en déterminer précisément les possibilités et les intérêts.

A notre sens, ces développements concernent les principaux domaines suivants :

- la conception

- . développements de concepts plus performants (types de raidissages, intégration des reprises d'effort, etc ... voir figure 15),
- . mise au point de modèles mathématiques schématisant les grandes déformations et permettant d'optimiser les lois de mise en pression.

la connaissance des propriétés mécaniques des structures

- . influence des conditions opératoires sur les propriétés de base du matériau.
- . caractéristiques des joints soudés par diffusion.
- . comportement de structures réelles dans leur environnement de service (fatigue, vibrations, etc ...).

- l'industrialisation

Dans ce domaine, les efforts doivent essentiellement porter sur les points suivants :

- . coût matière (réduction des chutes),
- . coût outillage (nature des matériaux et méthodes d'obtention des formes),
- . philosophie et méthodes de contrôle car la méthode par ultra-sons ne peut pas être utilisée dans toutes les zones et son coût est élevé.

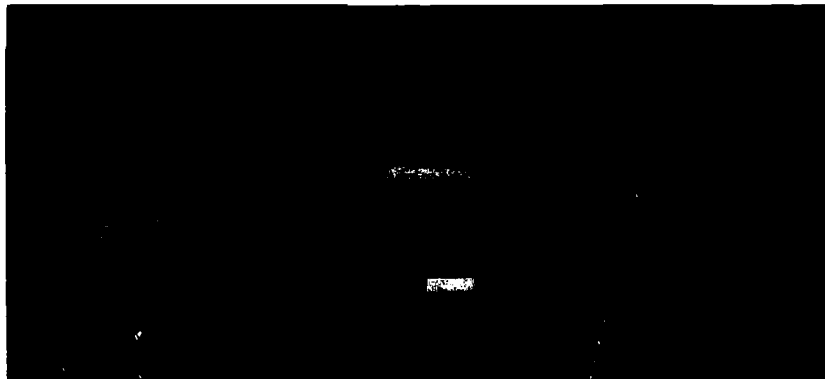


Figure 15

8. CONCLUSIONS

Les premières applications de la SPF/DB à la réalisation de structures en TA6V ont permis l'obtention de résultats positifs sur les plans faisabilité, qualité et coût. Elles ont également permis de mettre de évidence un certain nombre de problèmes : propriétés mécaniques du matériau, détermination des lois de pression, méthodes de contrôle, etc... qui définissent les principaux développements à entreprendre.

Cependant, un certain nombre de développements, de caractère plus général doivent être également entrepris pour mieux cerner les possibilités de cette technologie et pour en déterminer l'intérêt global (conception, coût).

Annexe

FORMAGE SUPERPLASTIQUE

1. DETERMINATION DE LA LOI DE VARIATION DE PRESSION

1.1 - Hypothèses

Sur le matériau : le matériau est isotrope
l'épaisseur est faible

Sur les déformations :

Hypothèse n° 1 (H_1) : le volume de matière reste constant

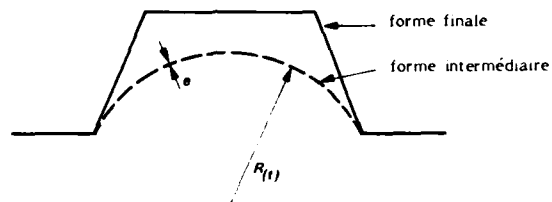
Hypothèse n° 2 (H_2) : la contrainte de déformation σ est constante durant le formage

Hypothèse n° 3 (H_3) : la vitesse de déformation $\dot{\epsilon}$ est constante durant le formage

Hypothèse n° 4 (H_4) : l'épaisseur faible des tôles permet l'application de la théorie sur la déformation des coques minces

1.2 - Remarques

La détermination des lois de pression ne s'applique que pour une déformation "style coque mince"



1.3 - Détermination de la loi de variation de pression

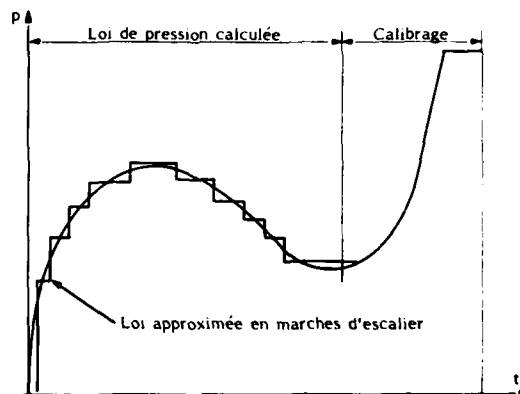
$H_4 \rightarrow P = f(\sigma, R_t, e)$

$H_2 \rightarrow \sigma = \text{cte d'où } P = g(R_t, e)$

$H_1 \rightarrow \dot{\epsilon} = \frac{K d (\log e)}{dt}$

$H_3 \rightarrow \dot{\epsilon} = \text{cte d'où } P = h(R_t, t) \text{ d'où } P = k(t)$

1.4 - Exemple type de cycle de formage



Annexe
(Suite)

2. PREDETERMINATION DE L'ÉPAISSEUR DE TOLE FORMEE

2.1 - Hypothèses

Hypothèse n° 5 (H_5) : l'épaisseur de tôle est constante sur une même déformée

Hypothèse n° 6 (H_6) : au contact avec le moule le frottement devient important : il n'y a plus de variation d'épaisseur de tôle

2.2 - Prédétermination

$H_1 \rightarrow e \, dS = e_0 \, dS_0$

$H_5 \rightarrow e$ au contact avec le moule en fonction de R_t et dS_0

$H_6 \rightarrow e$ finale

avec e_0 : épaisseur initiale de la tôle
 e : épaisseur au temps t
 dS_0 : élément de surface initial
 dS : élément de surface au temps t

RECORDER'S REPORT
SESSION III — INSPECTION METHODS, FLAWS AND NEW PROCESSES

by
P.R.Wedden
Westland plc
Helicopter Division
Yeovil, Somerset, BA20 2YB
England

In the absence of Dr P.Partridge, the recorder for Session III — "Inspection Methods, Flaws and New Processes", a brief statement was given by Mr P.R.Wedden, Chairman of Session III, which was directed toward the industry user viewpoint.

The first Session III paper — "Ultrasonic Testing Techniques for Diffusion Bonded Joints" evaluated the spectrum of parameters involved in ultrasonic testing and related these to the range of defects that arise in practice. There was concern for the inability to detect the smallest flaws that can occur in such joints and future research would need to be directed to this area.

The second paper, presented by Mr H.Craig, was "NDT of Electron Beam Welded Joints" with emphasis on micro-focus and real time x-ray. The advantages of micro-focus radiography were presented and demonstrated the ability to detect those defects that are of great concern to the user. The advantage of real time ability and the ultimate prospect of removing the subjective, human aspects of defect assessment was discussed, although no timescale could be given for the availability of this methodology to the aerospace industry.

The third paper — "Thermoelastic Testing of Stratified Materials" was extremely interesting and provided a new NDT technique to the problems of detecting flaws in laminated structures. *It is hoped that the technique, which has flexibility and wide ranging applicability, can be developed further and it was seen as an area to be pursued.*

Paper 15 — "The Influence of Welding Flaws on the Fatigue Strength of Electron Beam Welds in Ti 6—4" provided quantification of the effect on S—N performance, without apparent need for knowledge of crack growth rate, fracture toughness etc. Provided design fatigue allowables permitted the catastrophic effect of flaws on S—N fatigue resistance could be dealt with in a direct manner.

The fifth paper in this session was concerned with "A Real Time Vision System for Robotic Arc Welding". This showed the means of obtaining ultimate control by removing the human element and optimising the use of robots through feed back from process modelling of the weld parameters. It was considered that this approach would advance welding technology control.

The last paper in this session gave an account of the development and test background to the application of inertia welding for a critical helicopter component. The main points arising for this contribution — "Inertia Welding of Nitralloy "N" and 18% Nickel Marageing 250 Grade Steels for Utilization in the Main Rotor Drive Shaft for the AH-64 (Apache) Military Helicopter Program" was the freedom from weld defects and the overall weight saving achievable by a not particularly advanced technique when applied to dual materials.

ULTRASONIC TESTING TECHNIQUES
FOR DIFFUSION-BONDED TITANIUM COMPONENTS
by
Gustav Tober and Stefan Elze
MBB GmbH, Lemwerder, Dept. TE 347
D-2874 Lemwerder, Germany

SUMMARY

In the present ultrasonic investigations, diffusion-bonded titanium specimens with bonding defects were tested. In order to improve the defect detectability, high-frequency ultra sound was applied; the echo signals were analyzed in both the time and frequency domains.

1. INTRODUCTION

This paper describes ultrasonic (US) testing techniques for aerospace components manufactured by diffusion bonding (DB) in connection with superplastic forming (SPF). These techniques are very important for economic production of light structures made of expensive materials such as titanium alloy Ti6Al4V.

Owing to possible defects in the narrow DB zone, high demands are made on non-destructive US testing.

The limits of conventional US testing are shown and possible improvements by adequate signal evaluation mentioned.

2. DIFFUSION BONDING (DB) AND SUPERPLASTIC FORMING (SPF)

In the following, the DB and SPF techniques as well as combinations thereof are explained on the basis of examples. Depending on the design and manufacturing means, different types of DB/SPF components are produced:

- DB: The surfaces of two separate sheets are joined to one sheet by welding and by applying pressure and temperature (Fig. 1a top); it is also possible to butt-join two sections (Fig. 1a bottom).
- SPF: A sheet is formed to a special shape by applying pressure and temperature (Fig. 1b).
- DB/SPF: For a sandwich structure produced by this combined technique, for example, three sheets are first joined by diffusion bonding except in the areas provided with release agent. The component is then formed by introducing pressurized gas into the non-bonded areas (Fig. 1c).
- DB/SPF/DB: An example of this is the manufacture of a cooling outlet duct. First, two sheets are bonded at the edges and at a central strip and are then formed into a twin-duct. Finally, the two central walls are completely bonded together (Fig. 1d).

Fig. 2 shows two components manufactured according to the production processes illustrated in Figs. 1c and 1d. Other examples are engine bulkheads, fuselage frames, flap tracks, nacelle pylons.

3. DESCRIPTION OF DB DEFECTS

If the production parameters are not accurately observed, DB and SPF defects can occur.

The latter can appear as small surface cracks in heavily formed areas. They can be detected by means of dye penetrant or high-frequency eddy current tests.

Typical DB defects are bonding defects in the DB zone; their geometric properties are identified as follows (Fig. 3):

- gap with width $W \approx 0.5$ to $10 \mu\text{m}$
- known constant depth of defect
- size of single area about $15 \mu\text{m}$ or larger

These DB defects can involve different fillers:

- vacuum or voids (in the case of surface roughness or inadequate welding parameters pressure, temperature or time)
- thin oxide skin
- release agent used for DB/SPF (graphite, boronitride etc.)
- voids in combination with release agent or oxide skins.

Another feature of DB defects is the fact that the bond appears to be perfect although the bonding strength is very low. The static and dynamic strength values are then low, but not zero.

4. TEST SPECIMENS WITH DB DEFECTS

Approx. 15 different test specimens (1.5 to 5.5 mm thick) with incorporated defects were manufactured to examine US techniques with regard to their suitability for verification of DB defects.

- A groove pattern was milled into one of the sheets to be welded and release agent introduced into these grooves (Fig. 4b).
- Coarse- or fine-dispersive release agent was applied to the smooth surface of one of the sheets to be welded (Figs. 4a, b, c).
- No release agent was applied, but the welding parameter time was reduced to produce micro-defects (Fig. 4d).

In each case, a graphite solution was used as release agent. Fig. 4 shows examples of some specimens with artificially introduced defects and Fig. 5 shows metallographic microsections of selected areas.

5. US TESTING

5.1 PRELIMINARY CONSIDERATIONS ON US TESTING

Verification of defects by means of US waves is based on the following consideration:

If an otherwise homogeneous piece of material includes an area in which the sound velocity and/or density, i.e. the acoustic impedance, differ as compared to its environment, a US pulse is partly reflected at this spot.

The reflection behavior of such a defect depends on the acoustic impedance, the wavelength (or frequency) and the geometry of the defect. The ratio of defect to wavelength results in regular reflection or scatter.

The following should be noted in particular:

- Only probe/equipment combinations with US pulses shorter than the signal flying time in the material are suitable for testing of DB weldings (e.g. 1 mm + 1 mm). As the bonding defects are parallel to the surface, standard probes (perpendicular incidence, i.e. longitudinal waves) will be used. (In a 1 mm thick titanium sheet, the signal flying time from the surface to the backwall and back will be

$$\Delta t = 2 \text{ mm} / 6.24 \text{ kms}^{-1} = 0.32 \text{ } \mu\text{s}$$

- so that a test frequency of at least 10 MHz has to be selected).
- The reflectance, in particular of coarse-dispersive DB macro-defects, theoretically depends on their thickness and test frequency (e.g. an extensive, 1 μm thick graphite layer in titanium will reflect only approx. 0.5 % of the sound pressure at a test frequency of 1 MHz and approx. 5 % at 10 MHz) $1/2/3/$.
- For US verification of DB micro-defects with a diameter ϕ smaller than the US wavelength λ , the back-scatter is measured which increases super-proportionally with the ratio ϕ/λ . For a defect with $\phi \approx 50 \text{ } \mu\text{m}$ and a US wavelength $\lambda \approx 200 \text{ } \mu\text{m}$ ($\approx 30 \text{ MHz}$), for example, the amplitude of back-scatter will only be a fraction of the amplitude at regular reflection.

Thus, the use of high-frequency probe/equipment combinations should be preferred unless the associated effects such as increased sound absorption, structural scatter and surface scatter outweigh the advantages (4).

5.2 CONVENTIONAL AND HIGH-FREQUENCY US TECHNIQUES

Conventional US techniques, in this context, are techniques using probes of the usual frequency (1 MHz to 20 MHz) and involving echo height evaluation on the screen or by means of records.

Only equipment and probes permitting a clear distinction, as to time, between defect and backwall echoes were used. A 2 mm thick titanium sheet with a 0.3 x 0.3 mm groove was used to test the equipment. Only probe/equipment combinations permitting perfect distinction between the echo of the groove and the backwall echo were used for the investigations.

Based on the preliminary considerations, US test frequencies above 20 MHz were also tested.

Various US probes and equipment were used to measure the reflection behavior of a coarse-dispersive DB macro-defect in preliminary specimen 2 (Figs. 4a and 5a), as explained in Fig. 6, LH. Fig. 6a shows that the defect signal-to-noise ratio S/N (resulting from defect signal amplitude and noise amplitude) clearly increases with the test frequency. The defect signal-to-backwall signal ratio also increases with the test frequency as can be seen from the measuring points of Fig. 6b. Obviously, test frequencies below 10 MHz are not very suitable for verification of such DB defects. (This also

applied to measurements previously performed with the immersion through-transmission technique where practically only the milled defects in specimen 5 of Fig. 4b were resolved). The echo technique with frequencies higher than 30 MHz and using, in particular, shockwave probes V215BB (50 MHz) and V2049 (100 MHz) was the most suitable for resolving typical dispersive DB macro-defects.

The reflection behavior of fine-dispersive micro-defects in specimen 2.2 was examined in the same manner (refer to Fig. 7). Such defects could not be detected with non-focussing, low-frequency probes. Weak indications of these defects could only be achieved with non-focussing probes at frequencies higher than 30 MHz; a considerably improved resolution was achieved with a point-focussing probe having a working frequency of 40 MHz. One of the reasons is, no doubt, the reduced lateral volume from which the structural noise or the comparative backwall signal originates.

5.3 US SPECTROSCOPY

In the investigations described below efforts were made to establish signal features characteristic of DB defects. These signal features were to allow an evaluation even if a defect was no longer clearly identifiable in the time display /4/5/. For the investigations, certain parts of the HF time signal were gated and the frequency content determined by means of a spectrum analyzer (TR 4172).

Two different time domains (refer to Fig. 8) between surface and backwall echo (expected defect range) and the backwall echo were examined by using a 50 MHz probe. A faultless sheet shows the spectra illustrated in Figs. 8a and b. A dispersive DB macro-defect in a DB welding, as shown in Fig. 5a, results in the spectra shown in Figs. 8c or 8d. The frequency analysis of the expected defect range provides clearer indications than the analysis of the backwall echo. When comparing spectra 8b and 8d, it can be seen that the spectrum of the backwall echo lacks high frequency content if a defect occurs since this frequency content is preferably already reflected at the DB defect.

Fig. 9 shows the echo pattern of a small defect that can no longer be evaluated in the time range. However, the frequency spectrum of the expected defect range on Fig. 9, RH, shows a difference compared with the faultless sheet (Fig. 8a).

Investigations with regard to US spectroscopy also showed that defects can still be detected by means of frequency evaluation even when time evaluation can no longer be carried out.

5.5 AUTOMATION OF TESTING

Various types of sound coupling were also checked with regard to automatic testing of DB/SPF production parts:

- direct coupling with coupling paste
- immersion technique in water
- bubbler technique (using a local water delay path)

These types of coupling could also be used with high-frequency probes. Fig. 10 shows an example of a bubbler device that can also be controlled by a manipulator, with the help of a gimbal.

Automatic testing has commenced. In this case, the probe is controlled by means of a manipulator (X-Y shifting unit with stepping motor control) and DB defect signal amplitudes are further processed to amplitude plots or (color) C scans (refer to Fig. 11).

6. CONCLUSION

Various types of DB defects representing possible production-related types of defects for DB/SPF processes were introduced in numerous flat titanium specimens. These specimens were used to test US techniques with regard to defect resolution. Fig. 12 summarizes the results in a schematic form; according to these results, higher-frequency, focussing probes proved to be the most suitable probes. However, subsequent to completion of the measurements, the correlation between US indication and the size of the actual DB defect remains to be determined on the basis of a larger number of microsections and tensile tests.

7. REFERENCE DOCUMENTS

- /1/ J., H. Krautkrämer, Werkstoffprüfung mit Ultraschall, Springer-Verlag Berlin (1981), 22-27
- /2/ V.A. Sutilov, Physik des Ultraschalls, Springer-Verlag Wien (1984), 173-177
- /3/ G. Hübschen, F. Walte, R. Werneyer, Zur zerstörungsfreien Prüfung von Löt- und Schweißverbindungen, DVS-Berichte 69, 176-182
- /4/ H.-A. Crostack: Basic aspects of the application of frequency analysis, Ultrasonics (11/1977), 253-261
- /5/ R.S. Gilmore, M.L. Torreno, G.J. Czerw., L.B. Burnet, High-frequency ultrasonic testing of bonds: application to silicon power devices, Materials Evaluation (Jan. 1979), 85-72

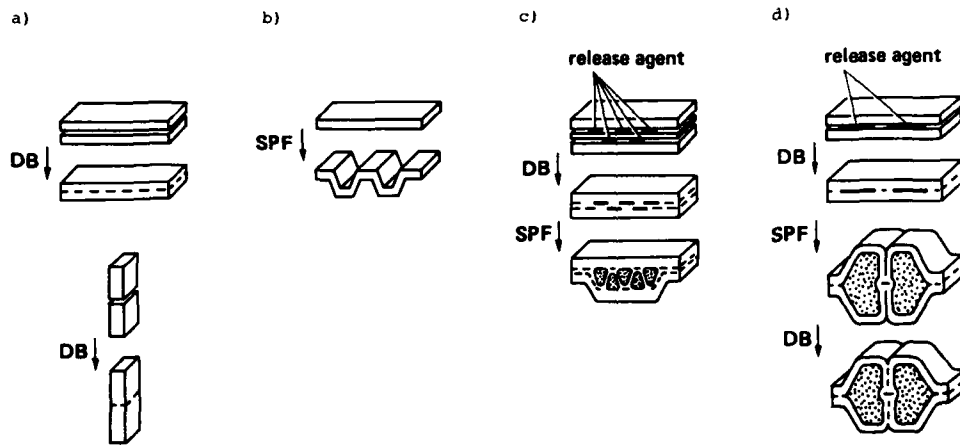


Fig. 1: Schematic diagramm of the manufacturing technique diffusion welding (DB) and superplastic forming (SPF)

- a) DB (areal and butt joints)
- b) SPF (corrugated sheet structure)
- c) DB/SPF (sandwich structure)
- d) DB/SPF/DB (special structure of a cooling outlet duct)

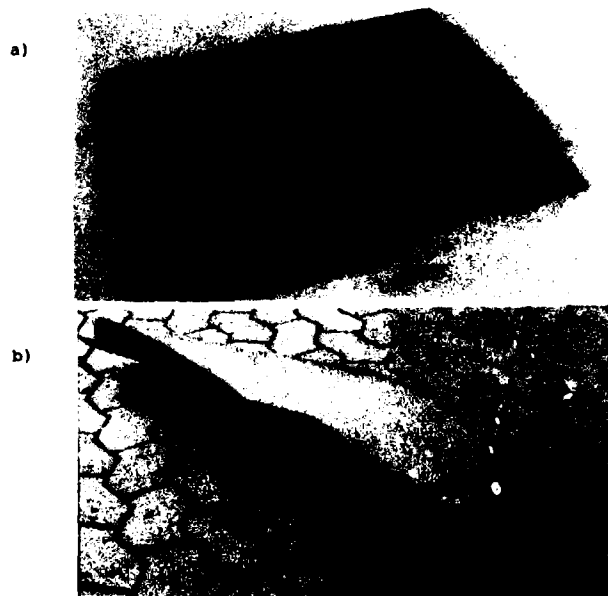


Fig. 2: Examples for DB/SPF-Components

- a) Sandwich structure
- b) Cooling outlet duct

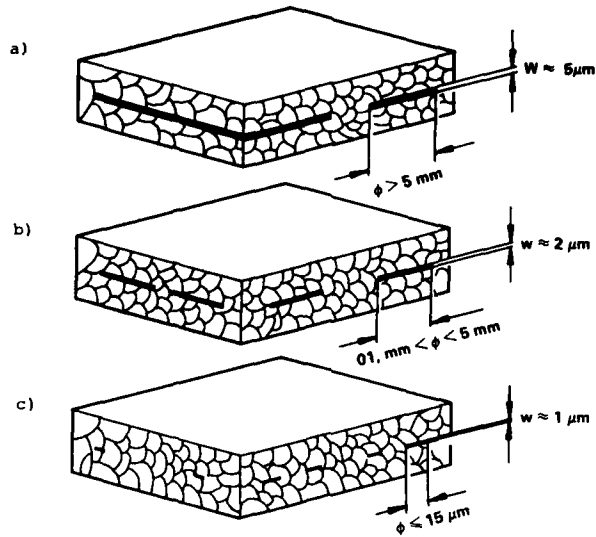


Fig. 3: Classification of DB-defects
 a) Coarse-dispersive macro defect
 b) Fine-dispersive macro defect
 c) Micro defect configuration

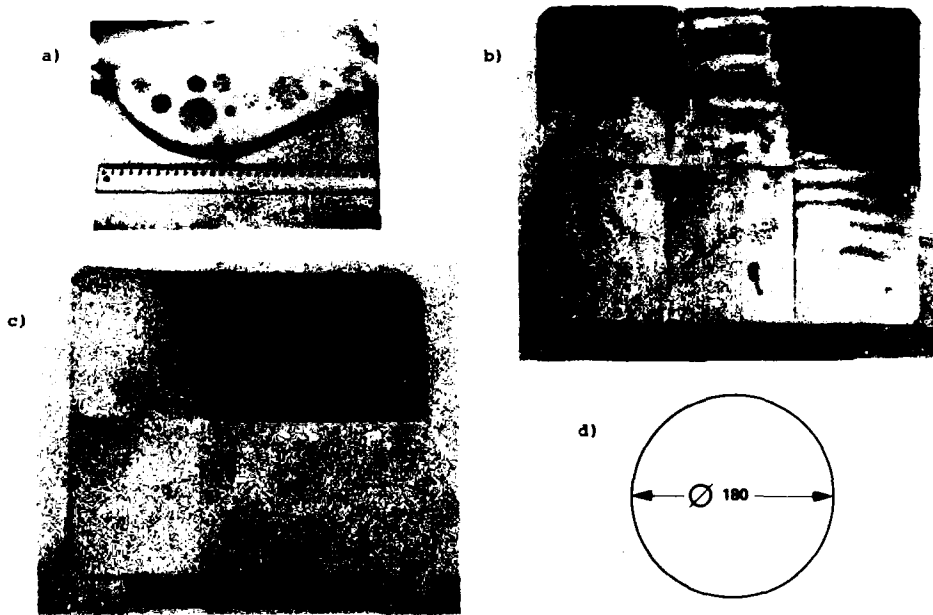


Fig. 4: Test specimen with different DB-defects (photograph before welding)
 a) Preliminary specimen 2 with dispersive defects
 b) Specimen 5 with milled and dispersive defects
 c) Specimen 4 with dispersive defects
 d) Specimen 2.2 (N21) with micro defects

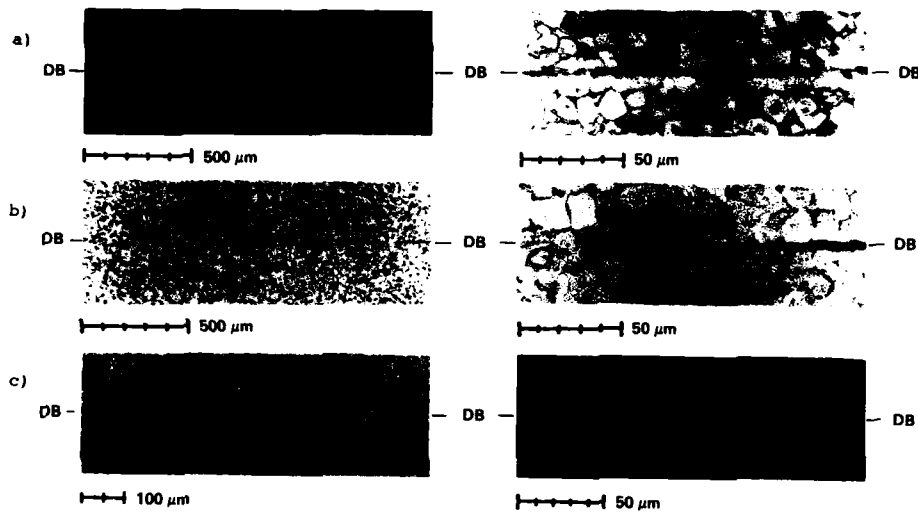
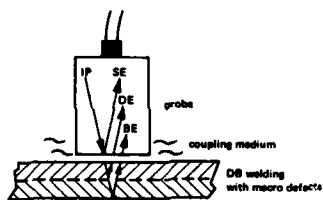


Fig. 5: Microsections with different DB-defects

- a) Course-dispersive macro defect in preliminary specimen 2
 b) Fine-dispersive macro defect in specimen 4 (right edge)
 c) Micro defect in specimen 2.2 (N22) (right edge)



IP = initial pulse
 SE = surface echo
 DE = defect echo
 BE = backwall echo
 N = noise

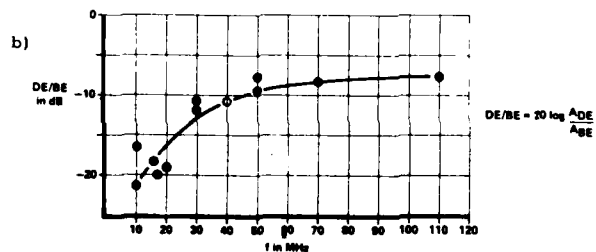
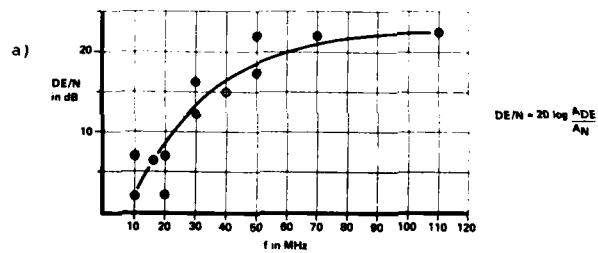
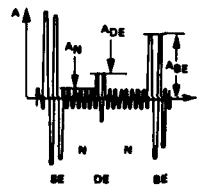


Fig. 6: Reflection behavior of a DB-macro defect versus US-frequency f

- a) Signal-to-noise ratio DE/N
 b) Defect signal-to-backwall signal ratio DE/BE
 (● non-focussing probe, ○ point-focussing probe)

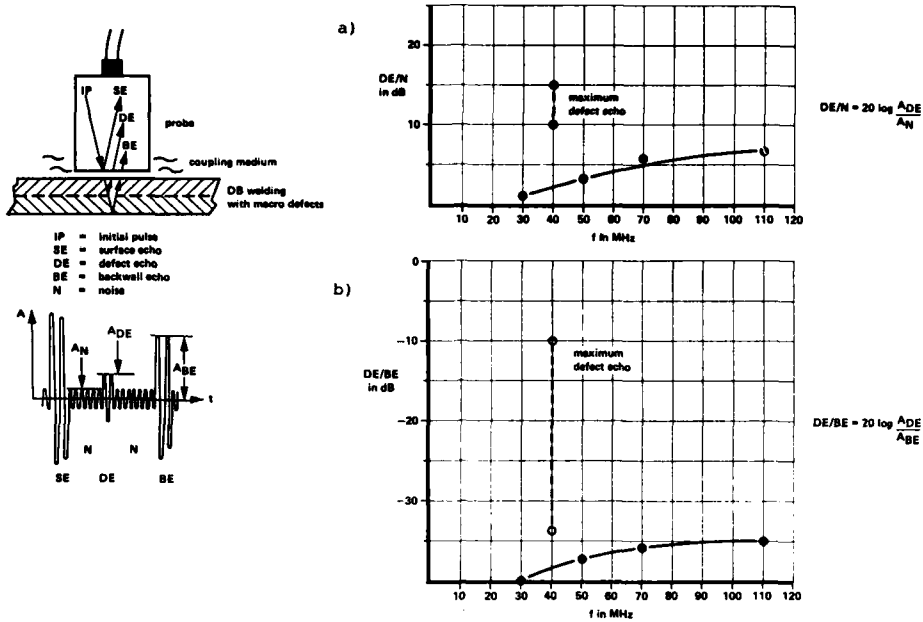


Fig. 7: Reflection behavior of a DB-micro defect versus US-frequency f

- a) Signal-to-noise ratio DE/N
- b) Defect signal-to-backwall signal ratio DE/BE
- (● non-focussing probe, ○ point-focussing probe)

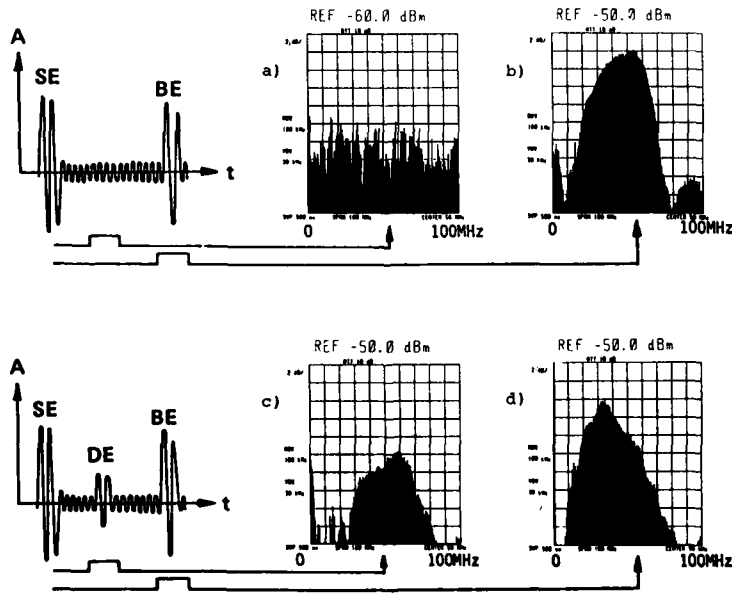


Fig. 8: Spectra of gated RF-signals (probe 50 MHz, non-focussing)

- a), b) Faultless sheet
- c), d) DB-specimen with macro defect (preliminary specimen 2)

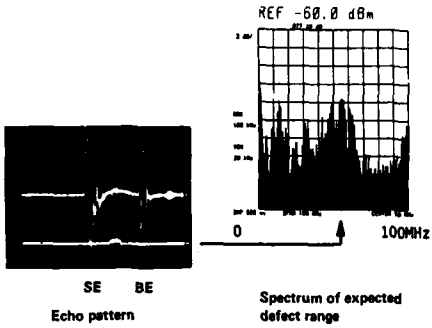


Fig. 9:
Evaluation of a small
DB macro defect (50 MHz,
non-focussing)

Fig. 10:
Probe V215
(50 MHz, non-focussing)
in bubbler technique

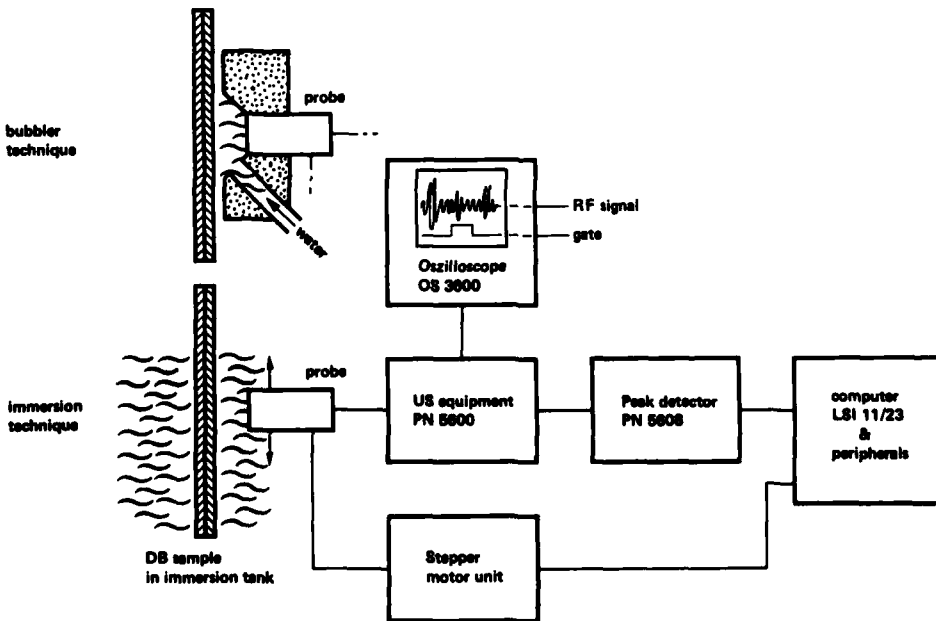
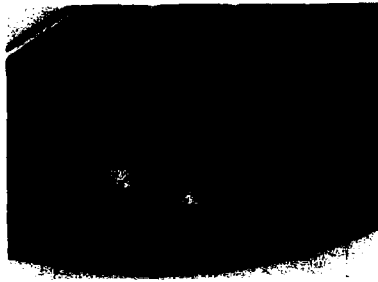


Fig. 11: Test equipment for pulse echo technique in bubbler or immersion technique

DB defects	US-method	Transmission focusing, non-focusing probes 5 and 10 MHz	Pulse/echo, non-focusing probes 10 up to 20 MHz	Pulse/echo non-focusing probes 30 up to 110 MHz	Pulse/echo point-focusing probes > 30 MHz
Course-dispersive macro defects (single defect size $w \approx 200 \mu\text{m}$; $\phi \approx 3 \text{ mm}$)	D	WD	WD	WD	WD
Course-dispersive macro defects (single defect size $w \approx 5 \mu\text{m}$; $\phi > 5 \text{ mm}$)	PD	D	WD	WD	WD
Fine-dispersive macro defects (single defect size $w \approx 3 \mu\text{m}$; $0,1 < \phi < 5 \text{ mm}$)	PD	PD	WD	WD	WD
Micro defect configurations (single defect size $w \approx 1 \mu\text{m}$; $\phi < 15 \mu\text{m}$)	ND	ND	PD	D	D

Fig. 12: Detectability of DB-defects with different US-methods

ND not detected
 PD partially detected
 D detected
 WD well detected

WELD QUALITY MONITOR AND CONTROL SYSTEM

F. Kearney and Dawn White
 U.S. Army Construction Engineering Research Lab.
 P.O. Box 4005, Champaign, IL 61820

William Ricci
 Process Research Div., Army Materials & Mechanics
 Research Center, Watertown, MA 02172

ABSTRACT

A non-contact Weld Quality Monitor (WQM) system is being developed to detect, identify, and correct for deviations from established welding procedures and conditions which lead to weld defects in real time. The WQM continually measures with conventional transducers all primary process parameters such as current, voltage, and travel speed, and computes weld quality parameters such as heat input and weld bead geometry. In addition, the WQM monitors the spectral signature of the welding arc by means of a high resolution microprocessor controlled spectrograph. Here, the presence of weld pool and arc atmosphere contaminants, flux and shield gas effectiveness, arc energy input, and penetration/dilution into the base material can be determined. The spectral response from the welding arc and measurements of process parameters are then normalized, compared to preset operating limits, and processed in real time. Necessary adjustments to primary process parameters will be made by automated compensation devices to eliminate weld defects in real time. When necessary, the specific location of discontinuities will be provided to facilitate further inspection.

INTRODUCTION

During the welding process, changes in parameters, consumables, and the weld arc atmosphere can occur without the operator's knowledge. These changes may result in thermal damage to the base materials and defects (e.g., hydrogen induced cracking, porosity, embrittlement, lack of fusion and penetration) which seriously reduce the strength and service life of the welded joint. The cost of locating and repairing these defects constitutes a significant portion of the total weld fabrication cost. Prior attempts have been made to develop techniques to quantitatively measure welding conditions. These methods, however, often require direct sensor-to-workpiece contact and are not considered suitable for production environments because of sensor temperature limitations, joint geometry limitations, and time lags which reduce the validity and reproducibility of the information obtained.

Process control techniques have advanced rapidly in the past decade, and as sensors, microprocessor technology, and artificial intelligence methods advance also, it can only be assumed that the rate of improvement in control technology will accelerate. The welding process is capital intensive, prone to quality control difficulties, and unpleasant for the human operator. Not surprisingly, a large effort is underway to automate welding and improve weld process control.

In a very simple welding controllers, an open loop exists, and the process is controlled, in essence, by turning a knob. This knob, which sets the "demand" signal, maintains the desired conditions (Figure 1). Most commercial welding power supplies, while greatly improved in the past few years, fall into this category. In a closed loop system (Figure 2), however, the controller utilizes feedback from sensors that measure the value of certain quantities of interest to improve process control. In the case of welding, it is the primary process parameters, arc current, voltage, and travel speed which are typically monitored. At CERL considerable attention has been given to developing sensors capable of measuring various welding parameters and resultant weld characteristics in real time. This development has progressed on two fronts.

First, a process data system (PDS) (Figure 3) [1] has been developed to measure arc current, voltage and travel speed. In the PDS, a Hall effect device is used to obtain arc current values, voltage is measured at the welding head, and one of a variety of methods (tachometer, shaft encoder, etc.) is used to measure travel speed. The analog output from these devices is digitized and the data used by a microprocessor to determine whether the process is being maintained within preset limits. Secondary information about the weld quality, such as heat input and nugget area may also be computed. The PDS generates this data in real time, and can be used to stop welding, or alert an operator when an out-of-limits event occurs; it can also be used to drive a feedback control system.

The second sensor system, which was developed in conjunction with the Radio Research Laboratory of the University of Illinois, is an optical data system (ODS) capable of detecting variations in weld arc chemistry. During welding, loss of shielding gas, contaminated electrodes, contaminated shielding gas, or any of a number of other difficulties which may be associated with welding consumables can cause defects in weldments ranging from porosity to cracking [2,3]. The detection of variations in weld arc chemistry which are the cause of such problems is not a simple matter. Because of the extremely high temperatures near the welding arc, a remote sensing method is required.

Remote arc sensing has been accomplished by the development of an opto-electronic method for observing the arc and noting variations in its composition. The high excitation energies in the arc plasma make spectroscopic analysis an attractive method of obtaining qualitative and quantitative information about events during welding. To this end, equipment capable of real-time evaluation of the spectral features of the welding arc was developed by the Construction Engineering Research Laboratory and the University of Illinois [4,6].

EXPERIMENTAL TECHNIQUES

The opto-electronic system consists of a high-resolution, microprocessor controlled spectrograph. A block diagram of the system is illustrated in Figure 4. The optical radiation emitted by the welding arc in the region from 300 to 1200 nanometers is collected by a fiber optic bundle. The bundle, which is designed to withstand the higher temperatures surrounding the welding arc, is terminated at the entrance slit of an Instruments SA HR-320 Spectrograph/Monochromator. The HR-320, used as a spectrograph, images a flat field spectrum onto a 1024 element linear diode array. The photodiode array can be moved through the spectrum to obtain samples with a band width of 60 nm. The resultant resolution of this system is on the order of 0.6 nm. The photodiode array is interfaced to a high-speed, analog-to-digital convertor and a LSI 11/23 microprocessor. The spectral data, along with measurements of the voltage, current and travel speed of the arc can be processed or stored on floppy disks for later analysis.

As seen in Figure 5, the emission lines characteristic of the various elements present in welding consumables (as well as contaminants) may be observed using the equipment just described. The intensity of an elemental emission line provides semiquantitative information concerning the concentration of that element in the welding arc. However, the welding arc is not a steady state system and emission line intensities are not independent of instabilities in the arc. But because so much iron and argon in the case of argon shielded processes is present in the arc relative iron and argon intensities and variations in the concentration of elements of interest can be observed independent of changes in weld process parameters. Accurate information about the concentration of these elements may be obtained [7].

To accomplish this, an emission line characteristic of the element of interest must be identified. A suitable line must then be chosen for normalizing purposes. Finally, a series of welds must be made, under closely controlled, varying conditions so that a relationship between relative emission line intensity and elemental concentration may be obtained.

The possibility of detecting hydrogen in a weld is of particular interest because the presence of diffusible hydrogen in a steel weld can cause hydrogen induced cracking (often referred to as cold or delayed cracking) or embrittlement of the joint. Either of these phenomena can severely impair the mechanical properties of the weldment and necessitate costly repairs. Because of its wide economic significance, detection of hydrogen is of interest as an example of how the ODS can be used to detect quality problems with welding consumable [8,9].

Tests were performed to determine whether it would be possible to develop techniques for the detection in real time of the arc hydrogen concentration capable of causing hydrogen cracking in armor steel (MIL A 12560) used in the production of the Abrams tank. Two series of tests were performed to achieve this goal. Initial experiments were performed to relate hydrogen emission line intensity with the amount of hydrogen present. The second group of experiments correlated hydrogen emission line intensity with the amount of diffusible hydrogen present in the weld metal and the occurrence of hydrogen induced cracking in test welds.

Because MIL A 12560 steel has a carbon equivalent of 0.8, it is quite susceptible to delayed cracking problems [10]. The manufacturer's studies have indicated that dissolved H levels of less than 2 ppm may cause cracking. In the experiment, low concentrations of hydrogen gas were introduced into the argon shielding gas of a GMA weld and test welds were made and observed by the opto-electronic system previously described.

At the request of the Abrams tank's manufacturer, cruciform tests were used to detect cracking. Silicone oil immersion tests were used to measure the quantity of H present in the completed welds [11].

RESULTS AND DISCUSSION

As in previous experiments [12], a linear relationship was found between the concentration of H gas in the weld shielding gas and hydrogen line intensity (Figure 6). Since hydrogen emission line intensity is sensitive to hydrogen from any source, this has applicability to such problems as organic contaminants and moisture. In addition, it was found that hydrogen emission line intensity could be related to the occurrence of cracking, and loosely, to the type and severity of cracking which occurred (Table 1). As seen in Figure 7, a correlation between hydrogen emission line intensity and the hydrogen content of the resulting weldment was developed. While these data are preliminary results, it is clear that it is feasible to use spectroscopic techniques to detect and measure hydrogen in the welding arc. Other consumables related welding difficulties which have proved to be measurable with this method include loss of flux in flux cored arc welding, and loss or reduction of shielding gas flow [12].

If improved sensors are to effectively enhance weld quality, better control is required. So, CERL's research efforts in this area have been directed towards adaptive feedback control, and a microprocessor based adaptive feedback controller has been developed for use with the PDS and ODS weld monitors. Adaptive feedback control differs from the control methods mentioned earlier in that it is capable of modifying the process to control function.

In control systems, the response to corrective control signals is described by transfer functions that are unique to a particular welding hardware configuration. Generally, these are complex functions of the form

$$K = A + iB$$

Each component in the control loop has a unique transfer function. For instance, in controlling wire feed speed, there would be two transfer functions: for the feed mechanism, a transfer function K_f , and for servoamplifier driving the motor, the function K_a . The transfer function describing this section of the control loop would be

$$K_{wf} = K_a \cdot K_f$$

The operation of conventional control systems requires that the transfer functions be invariant [14].

Adaptive control systems are distinguished by their ability to compensate automatically for changes in system parameters and signal inputs. The wire feed system mentioned will serve as an example. If slippage occurs in the wire feed rollers, the transfer function K could assume a value beyond the controller's compensation range. In adaptive control, the system dynamics or control algorithms could be modified automatically to accommodate to this slippage (Figure 8). Because CERL's sensor systems are advanced, this adaptive control of welding has greatly increased flexibility.

The current work in real time weld monitoring and adaptive control forms the basis for an intelligent machine/robot welder which is under development. In the new system, an expert data base using information acquired with the previously described sensor systems will make intelligent decisions concerning process control without human intervention (Figure 9). Work is underway on an expert system capable of driving an intelligent robot welder. Two major areas must be addressed. First, the ability to select the correct solution to a given welding problem must be developed. That is, the sensors must not only be able to detect an out of limits event; the expert system must also be able to diagnose the cause and correct the situation, or determine that a human operator must be alerted. Second, a fitness-for-purpose criterion must be included. Thus, when a potentially defective length of weld is formed, the significance of the defect may be assessed based on the ultimate service conditions, so that an appropriate reaction (continue welding, record defect location, stop welding, etc.) occurs.

The utilization of machine intelligence (expert system) is feasible because of the opto-electronic sensors which form a computer cognition system. The knowledge base for the system is being developed through the specialized welding research in progress at CERL. The inference machine used is a personal computer; presently both IBM and Apple products are being used. Parallel processing techniques will be used to couple the adaptive control and machine intelligence functions. The hierarchies for the state space search of the expert system are being developed to maximize response. Current techniques indicate the system will operate adequately for weld travel speeds of 20 inches per minute.

ARMY APPLICATIONS FOR THIS TECHNOLOGY

As previously mentioned, the WQM can be used to predict the occurrence of defects, such as hydrogen induced cracks, in armor steel weldments made with solid and flux cored electrodes. Similarly, the embrittlement of reactive metal weldments such as those based on Ti and Zr alloys can be predicted. Lack of penetration/fusion in dissimilar metal weldments can also be determined and adaptive control algorithms are presently being developed for the real time in-process correction of these defects. One prime application for this technology is in the joining of copper rotating bands to ferritic based artillery shell bodies.

The application of the WQM is not limited to joining processes. The WQM may also be used to control case depth and correct for surface melting in high energy beam surface modification processes such as the laser or electron beam heat treating, cladding or alloying of gear and bearing surfaces. WQM technologies can also be used to monitor self propagating high temperature synthesis reactions such as those used in the development of thermal batteries.

CONCLUSIONS

The results of ongoing welding research programs show that microprocessor based sensors of several kinds can be used to observe the welding process, and develop data concerning the weld as it is being produced. It is possible to correlate this data with the properties of the finished weld, making the use of microprocessor based control systems incorporating artificial intelligence a very attractive method of combined process and quality control; this is a result of the system's flexibility which offers a variety of responses (vary parameters, stop welding, note for later inspection) to the occurrence of an undesirable event. The effort to produce adaptive feedback control systems utilizing artificial intelligence should be pursued for welding since the process is very well suited to this type of control, both because of the cause and effect relationship between variation in process conditions and defects, and the human factors (operator, discomfort, etc.) involved. The rapidly advancing state-of-the-art in all facets of the hardware and software required for this type of monitoring and control should make an intelligent welding robot a reality in the very near future.

REFERENCES

1. Kearney, F. et al., "Nondestructive Testing for Field Welds: Real Time Weld Quality Monitor - Field Tests," CERL Technical Report M-295, June 1981.
2. Carbon, K. W., Lawrence, F. V., and Radzinski, J. B., "The Introduction of Discontinuities in High Strength Steel Weldments," CERL Preliminary Report M-27, December 1972.
3. Lundin, C. P., "The Significance of Weld Discontinuities - A Review of the Current Literature," WRC Bulletin 222, December 1976.
4. Norris, M. and Gardner, C. S., "Microprocessor Controlled Weld Arc Spectrum Analyzer," ERL Publication No. 512, Technical Report, October 1981.
5. Norris, M. E., "Microprocessor Controlled Weld Arc Spectrum Analyzer for Quality Control and Analysis," CERL Technical Manuscript M-317, June 1982.
6. Gardner, C. S. and Kearney, F., "Electro-Optic System for Non-Destructive Testing of Field Welds," Proc. Conference on Developments in Welding Processes and Consumables, to be published.
7. Blackmon, D. R. and Hock, V. F., "An Opto-Electronic Technique for Identifying Weld Defects in Real Time," Proceedings SAMPE annual meeting, October 1983, to be published.
8. Graville, B. A., The Principles of Cold Cracking Control in Welds, Dominion Bridge, Co., LTD, 1975.
9. Evans, G. M. and Wayland, F., "Diffusible Hydrogen as a Criterion of the Quality of Welding

- Additives," Deutch. Ver. fur Schweisstechnik, No. 50, p. 21-33, 1978.
10. Suzuki, H., "Cold Cracking and Its Prevention in Steel Welding," Trans. TWS, Vol. 1, No. 2, 1978.
 11. Bell, D. T., Gestal, W. J., and Hippen, E. F., "Determination of Diffusible Hydrogen in Weldments by the RPI Silicone Oil Method," Welding Journal, March 1981, 505-565.
 12. Blackman, D. R., Morris, M. E., et al., "Real Time Spectrographic Analysis of Hydrogen Concentrations in a Weld Arc," Proc. 1st International Conference on Solutions to Hydrogen Problems in Steels, ASM, 1982.



Fig.1 Open loop control system schematic

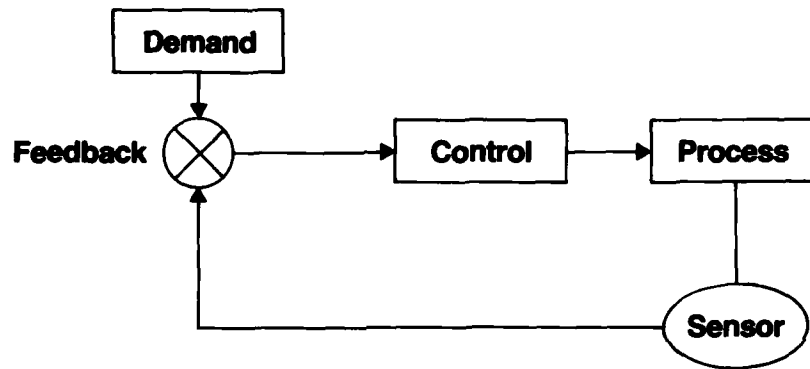


Fig.2 Schematic of closed loop control system

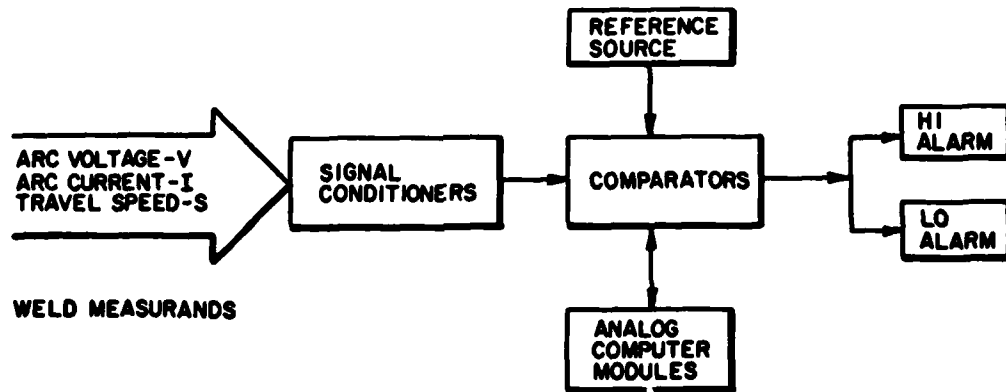


Fig.3 Schematic of process data system

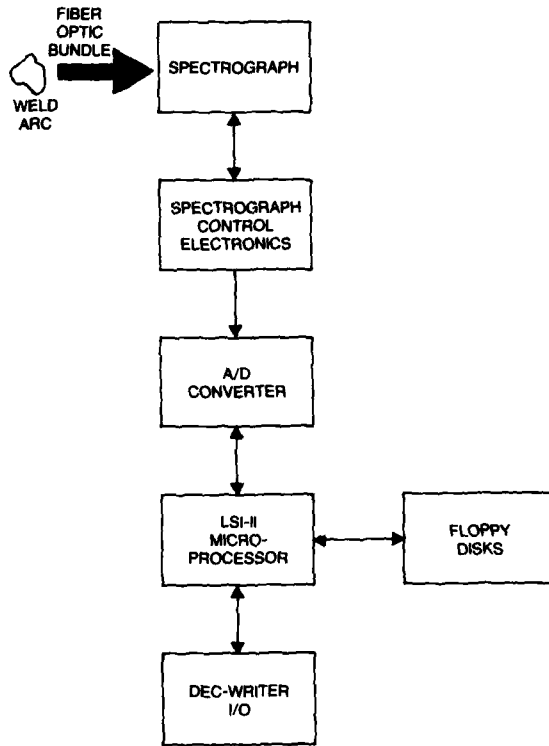
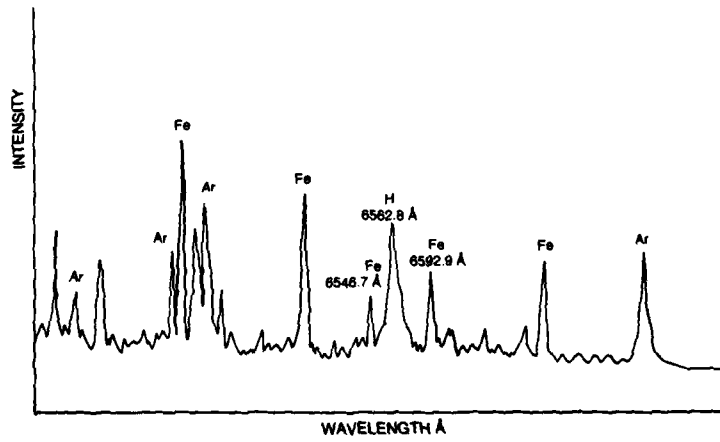


Fig.4 Schematic of optical data system



Low hydrogen concentration in weld arc

Fig.5 Typical welding arc spectrum, centered at 6562 Å

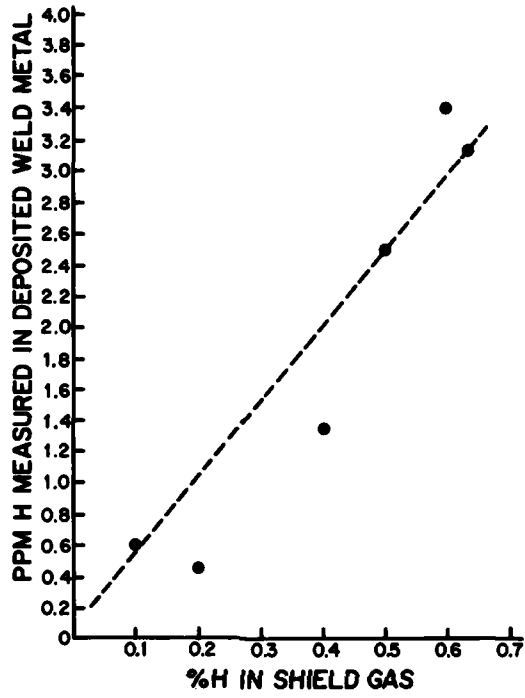


Fig.6 A linear relationship is found between relative hydrogen line intensity and hydrogen concentration in shielding gas

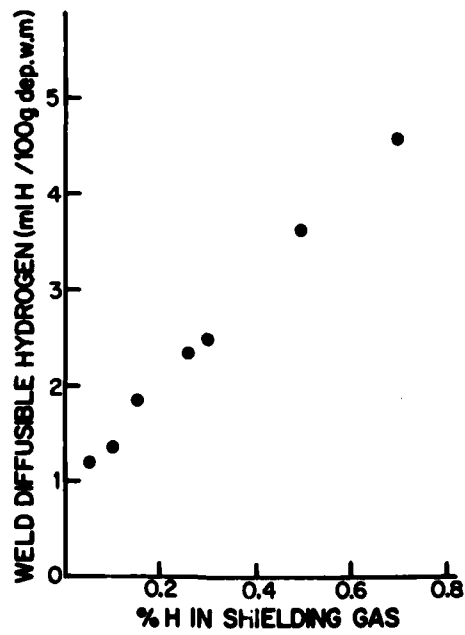


Fig.7 Hydrogen content of shield gas vs. hydrogen content measured in weldment

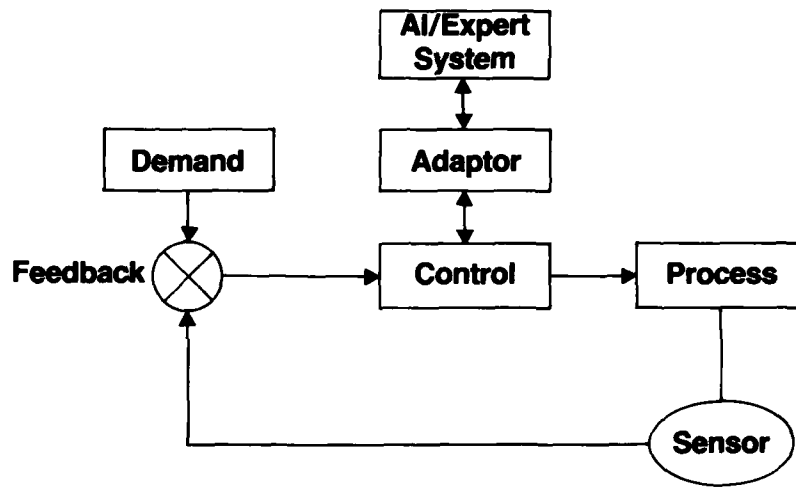


Fig.8 Schematic of intelligent welding robot

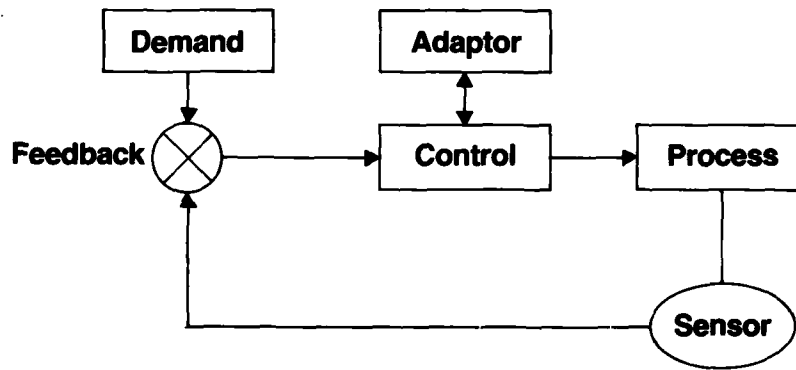


Fig.9 Schematic of adaptive feed back control system

TABLE 1

<u>Shield Gas Hydrogen Content</u>	<u>Type of Cracking</u>
.1%	none
.2%	mild weld metal cracking
.4%	severe weld metal cracking
.5%	weld metal and underbead cracking
.6%	weld metal and underbead cracking

NDT OF ELECTRON BEAM WELDED JOINTS(MICRO-FOCUS AND REAL TIME X-RAY)

R G Taylor
 Chief of NDT
 Rolls-Royce Limited
 Derby
 DE2 8BJ
 UK

1. INTRODUCTION

The introduction of Electron Beam Welding (EBW) into the aero engine industry in the early 1960's has presented many new problems for non-destructive testing. Highlighted among these are the following particular problems:-

- a) Accessibility - the use of EBW has resulted in the design of many "box-like" components which makes it difficult, or impossible, to apply conventional NDT methods satisfactorily.
- b) Centre-line defect orientation.
- c) Extremely narrow welds which makes the detection of defects by normal radiography very unreliable.

The traditional NDT methods such as conventional X-ray, fluorescent penetrant, magnetic particle, together with the occasional use of eddy current and, where accessibility permits, ultrasonics, have been extensively used for the inspection of EBW fabrications. However, the use of these methods has created considerable limitations in defect detection where extremely small defects (under 1mm (.040")) must be detected to guarantee a successful life cycle.

Initially, these limitations only applied to parts manufactured by EBW, but during recent years, EBW has been increasingly used during the repair and overhaul of aero engine components and the NDT limitations now extend into these areas.

Recently, significant developments have taken place which has enabled micro-focus X-ray techniques to be used in place of conventional X-ray on EBW and this has resulted in a considerable improvement in defect detection capabilities. An additional bonus has been the reduction in inspection costs and an improvement in productivity.

2. ACCESSIBILITY

The physics of electron beam welding makes it possible to weld pieces together which would be impossible with the more conventional welding methods such as Tungsten Inert Gas (TIG) commonly used in the industry. This in turn, has led to the design of welded components where accessibility is confined to the outside welded surface (Fig 1). This particular illustration is a titanium welded spool assembly on a helicopter engine and is a typical design of an EBW fabrication.

The main feature of these components, from an NDT point of view is the inability to see both sides of the weld for surface inspections and (with conventional X-ray and ultrasonics) the lack of access for X-ray film and sonic probes to examine the inside of the weld. In these particular cases the geometry completely eliminates the use of ultrasonics and conventional X-ray is limited to a double wall technique with its inherent lack of sensitivity.

In certain instances, the centre hole would allow the use of a standard rod anode unit and, by wrapping the X-ray film around the outside of the weld allow a single wall radiograph to be taken. This, however, is usually unacceptable because of the second problem associated with EBW that of centre line defect orientation.

3. CENTRE LINE DEFECT ORIENTATION

The preparation of a metal joint for EBW necessitates an extremely tight fit between the mating faces, usually created by "pressing" the faces together to obtain an "interference fit". Any subsequent lack of fusion which might result from a bad weld will also be extremely tight, and unlike lack of fusion in TIG welds, where the joint line is not tight, can only be detected by perfect X-ray beam orientation to the defect. (Fig 2).

Experiments have been carried out which shows that very severe lack of fusion can remain undetected with only a small deviation of X-ray beam to joint. In fact, a 40% lack of fusion in a 2mm (.080") thick weld was missed with the X-ray beam only 5° off the joint line.

Since standard rod anode units produce an X-ray beam with a back angle of approximately 70° (Fig 3) it follows that tight joint line defects cannot be detected using this type of equipment. Rolls-Royce and other Engine Companies require in their specifications for the X-ray of EBW, a maximum deviation of ± 2½° of beam to joint, and also require a proof of achieving this.

4. NARROW ELECTRON BEAM WELDS

Electron Beam Welds are normally very narrow (approximately 2mm (.080")) particularly for the material

thickness used in aero engine components. Conventional one to one (size) radiographs result in images which make it extremely difficult to interpret for defects within the weld bead. Typical EB defects, in addition to the lack of fusion, are very small cracks and porosity, with micro porosity being the most difficult to detect.

Many EB welds are on critical life components and it is therefore essential that all defects must be detected to guarantee a successful life cycle. Since the traditional DT methods all have limitations it was necessary to develop techniques to improve defect detection.

5. MICRO-FOCUS X-RAY

Although micro-focus X-ray has been used in Rolls-Royce since 1976 for the examination of cast turbine blades, the original equipment (Harwell E12) was not suitable for the X-ray of EB fabrications. This is largely due to the low energy of the E12 (90KV) and because it is a conventional window unit.

During the mid 1970's however two micro-focus units were developed which had the potential to X-ray EB welds:-

- a) TPD (Holland) 150KV rod anode
- b) Andrex (Denmark) 150KV rod anode

Both claiming focal spot sizes of less than 100 microns. They also had the ability to produce orthogonal radiation from a rod anode up to a metre long and 9mm diameter to allow insertion into small apertures.

The advantages of using this type of equipment are:-

- i) Access into the component to allow a circumferential weld to be exposed in one X-ray shot (Fig 4).
- ii) Correct (orthogonal) alignment of X-ray beam to joint line for the detection of lack of fusion (Fig 5).
- iii) Acceptable geometric unsharpness even with the short film to source distances and (Fig 6).
- iv) Geometric enlargement by moving the film away from the weld to overcome the narrow weld problem. (Fig 7)

Conventional single shot radiography require (on the helicopter spool) some 16 exposures, compared to the single exposure with micro-focus resulting in considerable saving in X-ray time. Similar savings can be achieved on other circumferentially welded components. More recently a number of rod anode micro-focus units with even smaller focal spots and higher energy have been marketed which considerably improves the results.

Notable amongst these are the Errington, Scanray and Ridge units with energies up to 160KV and focal spots in the region of 10 - 20 microns.

6. REAL TIME X-RAY

The development of high quality, high energy micro-focus X-ray equipment has allowed real time systems to be used for many applications.

In the past the real time system, together with conventional coarse focal spot X-ray units, were not capable of resolving small defects in dense metal welds but the use of micro-focus has now overcome many of the resolution problems. It is now possible to obtain X-ray sensitivities better than 1: (1:1) in aero engine materials and thicknesses of up to 5mm.

Our investigations have demonstrated that the type of defects present in EB welds can be detected by a combination of Real time and micro-focus and trials are now being carried out to determine the most suitable real time system to be used. A variety of real time systems are now available utilising either a range of image intensifiers or the phosphor screens used in our Lockheed RT System, together with computer aided image enhancement systems which will be necessary for the resolution requirements. A typical schematic arrangement is shown in Fig. 8 with the various alternatives which may be used for any given application.

The use of real time in this, and many other applications, will obviously result in cost savings by eliminating the need to use X-ray film but, equally attractive to an industry where reliability is vital, it will lead to improvements in this area, initially by making the task of image interpretation less hazardous and ultimately, by eliminating human error through the use of computerised pattern recognition methodology.

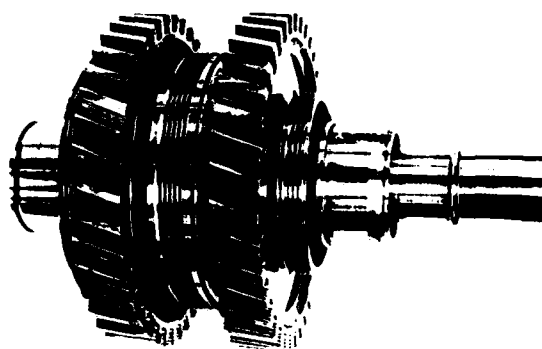
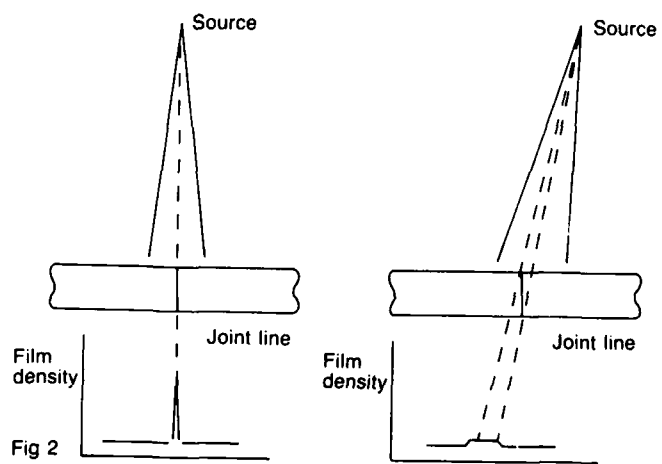


Fig.1



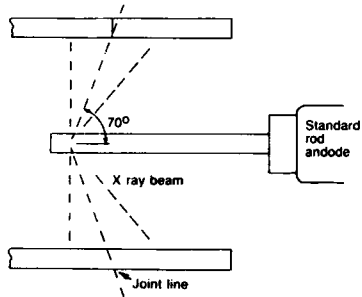


Fig 3

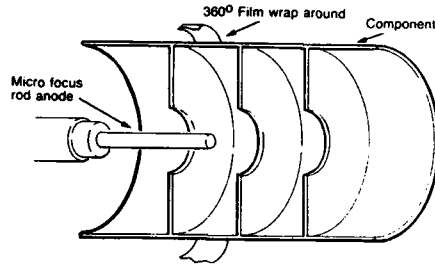


Fig 4

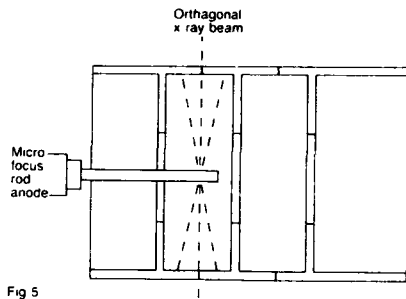


Fig 5

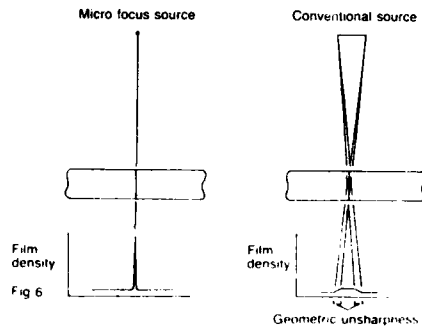


Fig 6

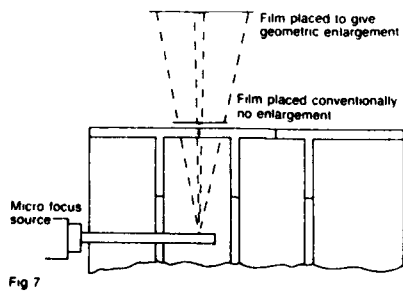


Fig 7

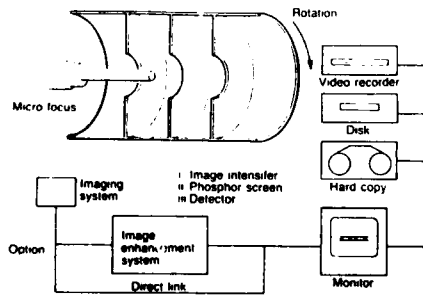


Fig 8

THERMOELASTIC TESTING OF STRATIFIED MATERIALS

PAOLO CIELO and MARC DUFOUR
National Research Council Canada
Industrial Materials Research Institute
Boucherville, Québec, Canada

Abstract A non-contact thermoelastic technique for the non-destructive testing of layered materials such as Aluminum-epoxy laminates or metallurgical coatings is described. A pulsed laser beam heats a small area on the surface of the layer to be tested, and the thermoelastic deformation of the layer is monitored by a sensitive optical probe. Unbonded areas can be recognized from the abnormally high deformation of the unbonded layer. Localized pulsed heating is shown to be far superior than the extended heating approach which is followed in holographic thermal stressing. The possibility to detect cohesive and adhesive defects by this technique is discussed. Two experimental configurations are described: in the first configuration the probing beam directly monitors the thermoelastic displacement of the heated area, while in the second a thermoelastically-generated annular stress wave converges towards the central probed point.

INTRODUCTION

Adhesively-bonded metal-to-metal or metal-to-core laminates are widely used as light-weight primary structures. Such materials require a careful inspection after being assembled to detect any extended bonding defect which would severely affect the structural resistance to transverse or shear loading. Typical defects to be detected in such structures are: 1) voids and delaminations, when an air gap exists at the bond interface; 2) reduced cohesive strength, when the shear and tensile modulus of the adhesive are reduced because of porosity in the glue line or inadequate temperature and pressure during curing which affect the shear and tensile modulus of the adhesive, and 3) adhesive unbonds, when the adherent and the adhesive are in physical contact (1-10 Å gap) with each other, but the interfacial bond is still zero. This is usually caused by a surface contamination of the adherends or by the inadequate storage of the resin film resulting in partial pre-cure. Similar defects are encountered in other stratified materials such as metallic or ceramic thermally-applied coatings⁴, which are increasingly used for corrosion or thermal protection of high-temperature surfaces such as fusion cells or turbine blades.

The NDT techniques which have reached the most advanced stage of development for the inspection of stratified materials are based on the ultrasonic and the radiographic approaches¹⁻³. Such techniques can detect most delamination and gross porosity defects, but they have very limited capabilities for the prediction of cohesive bond strength. As to the adhesive unbond defects, no technique is presently available for their detection^{4,5}. Indeed, air-filled gaps less than 100 Å thick are perfectly transparent to ultrasound^{6,7}, while such thicker gaps may be invisible if some liquid has infiltrated at the interface. Other limitations of the conventional techniques are, for radiography, the lack of visibility of any defect which does not produce a lack of material (such as gross porosity or resin filletting) and for ultrasound, the strong absorption by the adhesive film and the interference with material-boundary reflections (which makes, e.g., adhesive-to-core unbonds very difficult to be detected⁸). Finally, faster and less cumbersome techniques requiring no contact or water immersion of the piece and which can be applied where access is difficult or possible from one side only would be welcome, in particular for on-service inspections of the assembled structure.

A research technique which holds considerable potential for a more quantitative and noncontact inspection of layered materials is optical holography^{1-2,4,7-8}. In such a technique the inspected material is stressed either by an externally applied vacuum, by vibration or by thermal stress and the resultant surface deformation is observed with good accuracy (of the order of 1 μm) through a holographic interferogram. As the stiffness of the material is considerably reduced over an unbonded area, delaminations can be recognized from the abnormally high deformation of the unbonded layer. Such a technique measures directly the mechanical deformation under traction of the bonded structure, thus holding a potential for more quantitative evaluation of the glue-line stiffness and, under certain circumstances, of the adhesive strength.

Although holographic techniques have been successfully demonstrated for the inspection of metallic or composite laminates since several years⁹, they have found few applications out of the research laboratory. Part of the reasons for such an inertia are technical. In particular:

1) Because of the relatively long exposure time of the holographic plate, holography is highly sensitive to environmental disturbances such as low-frequency floor vibrations and ambient illumination. High-power pulsed lasers have been used in the past⁹ to avoid hologram blurring during the exposure time, but ambient vibrations during the heating period between the two exposures cannot be avoided. Consequently, the inspected object must usually be mounted on a cumbersome vibration-isolated table in a dark environment.

2) Of the different mechanical stressing techniques mentioned above, thermal stressing is by far the most practical, and the only one which is non-contact. The results obtained with thermal stressing are however less reliable than those obtained, e.g., by externally-applied vacuum

suction^{11,12}. Indeed, the thermoelastic deformation of the unbonded areas may arise from different mechanisms, such as a differential thermal expansion between the layer and the substrate (eventually producing thermal buckling, which is a second-order effect strongly dependent on the initial layer curvature¹⁰) or the establishment of longitudinal thermal gradients produced by the thermal-barrier effect of the unbonded interface (which is a weak effect and is related to the thermal resistance of the interface, rather than to the mechanical bond resistance as is the case for the applied-vacuum stressing technique). Extended-area thermal stressing thus appears very limited as to its capability to evaluate cohesive or adhesive strength properties.

3) Several practical problems have not yet been satisfactorily solved in holographic NDT. Some of these problems are: the presence of extended whole-body deformation producing a wide fringe pattern which is superposed to the disbond-related fringes; the lack of uniformity of extended heat sources used in surface thermal stressing; the difficulties encountered in automatic fringe interpretation; and finally the relatively low sensitivity which has stimulated the development of more elaborate techniques such as heterodyne holography¹³ (which can reach sensitivities of the order of 1/1000 of a wavelength at the expense of a more complex apparatus using two reference waves and a point-by-point scanning of the hologram).

In order to overcome such limitations, an interferometric point-by-point inspection technique has recently been developed at the Industrial Materials Research Institute^{10,14}. The next section presents an overview of the basic principle and of some typical experimental results using such a technique. A discussion of such results follows, with the aid of a finite-element thermo-elastic analysis. Finally, a non-contact ultrasonic impulse-loading technique for the dynamic analysis of the bonded structure is described.

PULSED THERMAL STRESSING OF THE PROBED SURFACE.

Two experimental techniques have been evaluated for the application of the mechanical stress on the interferometrically inspected material. In the first approach, which is described in this section, thermoelastic bending of the unbonded layer is produced by pulsed localized heating of the layer surface. In the second approach, vibrational stress is obtained at the point of convergence of a laser-generated surface acoustic wave. In both cases, the surface displacement is monitored by a focused interferometer, so that the technique is completely non-contact.

Description of the technique.

The basic principle of the dilatometric method is shown in fig. 1. A pulsed YAG laser is partially focused on the surface of the layered material, producing a transient thermoelastic bending moment which causes the layer to lift, if unbonded, while its position is monitored by a sensitive interferometer. The interferometer beam is focused on the surface, so that rough surfaces can be inspected by such a device with limited scattering losses. Interferometers of this kind are now commercially available which can detect displacements of the order of 0.01 μm on perfectly scattering surfaces, from any angle of incidence and at operating distances of the order of 10 meters¹⁵.

If the duration of the heating laser pulse is of the order of 1 ms or less, each point can be inspected during a time period which is much smaller than the typical ambient vibration period. Operation on the industrial floor is thus possible, while a large surface can be remotely scanned in a reasonably short time. Ambient illumination problems are avoided because of the high intensity of the focused probe beam. Surface displacements much smaller than half a wavelength can be monitored by the interferometer, so that a lower surface heating temperature is required compared to the holographic approach. Finally, the heat-source uniformity and fringe counting problems encountered with the holographic technique are eliminated.

An important experimental parameter is the ratio between the diameter of the heating beam and the diameter of the unbonded area. Previous experiments at our Institute used an extended heat source¹⁰. As shown in fig. 2, if an area much larger than the unbonded area is heated (fig. 2a, corresponding to the conventional configuration in thermal-stress holography) the layer is radially stressed, but no bending moment will develop, unless the layer is initially convex or exceeds the relatively high buckling threshold¹⁰. On the other hand, the pulsed focused heating configuration (fig. 2b) which has more recently been adopted at our Institute¹⁴ provides a much more efficient lifting moment. This was confirmed by a finite-element analysis using an axisymmetric model of the kind shown in fig. 3. The model represents a 750 μm -thick aluminum plate adhesively bonded to a massive aluminum substrate. A 3.5 mm-radius delamination is modelled by introducing some air elements as indicated in fig. 3. Laser surface heating over an area of variable radius is simulated by raising the temperature of some surface nodes (three nodes in fig. 3) to a temperature of 10°C. Fig. 3 shows (grossly exaggerated, for clarity) the deformation at equilibrium of the structure under such a thermal load. The vertical lift of the unbonded area, as obtained by such a model is plotted in fig. 4 as a function of the radius r of the heated area. As we can see, the lifting efficiency decreases abruptly when the radius of the heated area becomes similar or larger than the radius of the delaminated area, even if the total heating energy increases as r^2 .

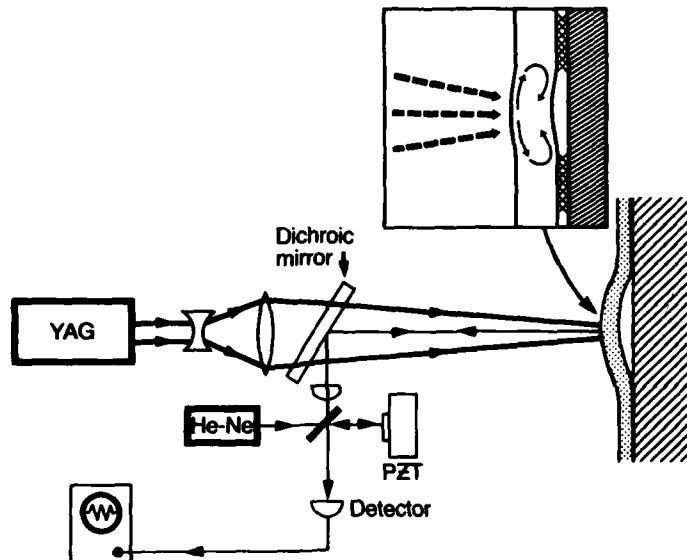


FIGURE 1: Experimental apparatus for the interferometric thermoelastic testing of a laminate. An unbonded layer bends when heated by a YAG pulse, while its displacement is monitored by a focused interferometer.

If a laser beam of fixed energy is used to heat the surface, maximum efficiency is obtained by focusing the beam as finely as possible on the probed surface, within the limits imposed by the thermal damage threshold. This was verified experimentally using the apparatus of fig. 1. Fig. 5 shows some experimental results obtained by focusing the constant-energy heating laser beam to different diameters in the center of the delaminated area. The sample was a 125 μm -thick Cu-Be plate epoxy-bonded to a Plexiglass substrate with the unbonded areas simulated by circular holes drilled through the substrate. Curve (a) was obtained with a 20 mm-diameter hole, while curve (b) was obtained over a 7 mm-diameter hole. We can see that the signal level increases monotonically with the reduction of the heating beam diameter, but that there is limited benefit to make the beam smaller than 10 or 20% of the unbond diameter. This point will be further discussed later.

Some real-unbond detection results are shown in figs. 6 and 7. The experimental curves were obtained by displacing the locally-unbonded sample under the well-centered heating and probing beams. Fig. 6 was obtained with a Cu-Be sheet epoxy-bonded to a solid Plexiglass plate, through some areas where the epoxy was missing. Curve 6(a) was obtained with a 2 J, 6 mm-diameter YAG laser pulse over a 10 mm x 30 mm missing-epoxy area, while curve (b) was obtained with 0.16 J, 0.7 mm-diameter pulses over a 3 mm-diameter air blister in the epoxy which was visible through the Plexiglass plate. The estimated surface temperature increase was 5°C and 35°C, respectively, for curves (a) and (b). The visibility of the unbonded regions, from the positions 2 mm to 12 mm on the abscissa for curve (a) and from 6 to 9 mm for curve (b), is quite satisfactory.

Fig. 7 shows some scanning curves obtained over a 20 mm-diameter delamination on the adhesive-to-core interface of an Al-epoxy honeycomb panel. The sandwich structure comprised two 0.3 mm-thick aluminum sheets bonded to a 3 mm cell-size aluminum honeycomb core, and the unbond was produced by inserting a 20 mm-diameter teflon disk between the epoxy film and the core prior to curing. The 0.75 J, 1 μs YAG pulses had a diameter of 1 mm for curve (a), 3 mm for curve (b) and 6 mm for curve (c). The unbonded area, from positions 4 mm to 24 mm is clearly visible, while the honeycomb-cell substructure is only visible when the heating beam is smaller than the cell size, curve (a), in agreement with the previous discussion. The relatively large displacement signals obtained in the well-bonded areas, particularly for curve (a), are believed to be caused, in part, by the linear thermal expansion of the Al-epoxy material, and in part by the relatively high compliance of the epoxy-to-core interface.

Fig. 8 shows a scan of the surface of a plasma-sprayed aluminum-on-steel corrosion-protective coating 250 μm thick. A 4 mm-wide adhesion defect was simulated by placing a Teflon strip on the substrate prior to the powder projection. The estimated surface temperature increase of the coating was 100°C, which explains the relatively large vertical displacement obtained on the well-bonded regions which is caused by the linear thermal expansion of the surface. As to the relatively small bending displacement of the unbonded region, it should be mentioned that the Teflon tape was probably melted by contact with the projected molten droplets during the spraying process, so that the artificial defect was probably one of cohesive weakness, rather than of complete lack of adherence.

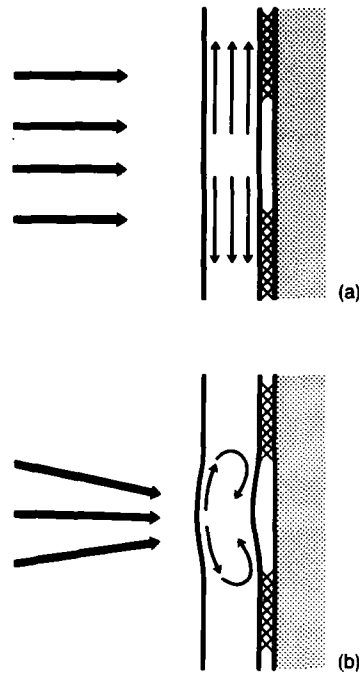


FIGURE 2:

Thermoelastic stress distribution
on a partially unbond layer under

- (a) continuous broad heating, and
(b) pulsed focused heating.

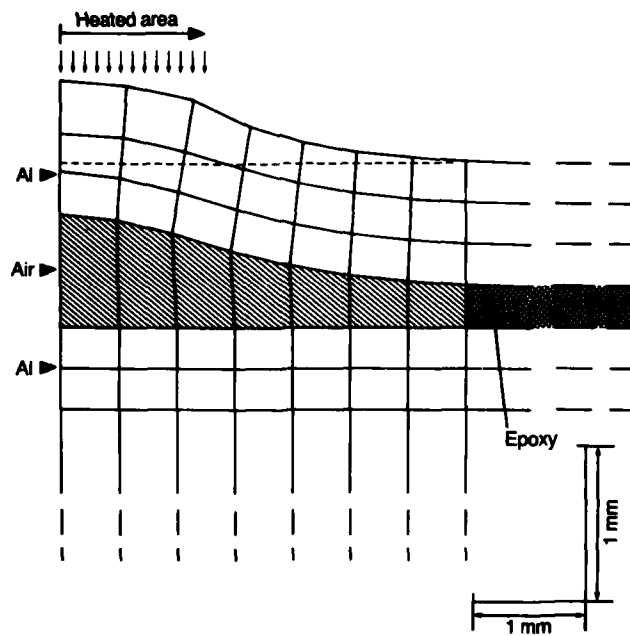


FIGURE 3: Axisymmetric plot of the thermoelastic deformation of an Al-epoxy-Al laminate, as obtained by a finite-element model (the deformation is grossly exaggerated).

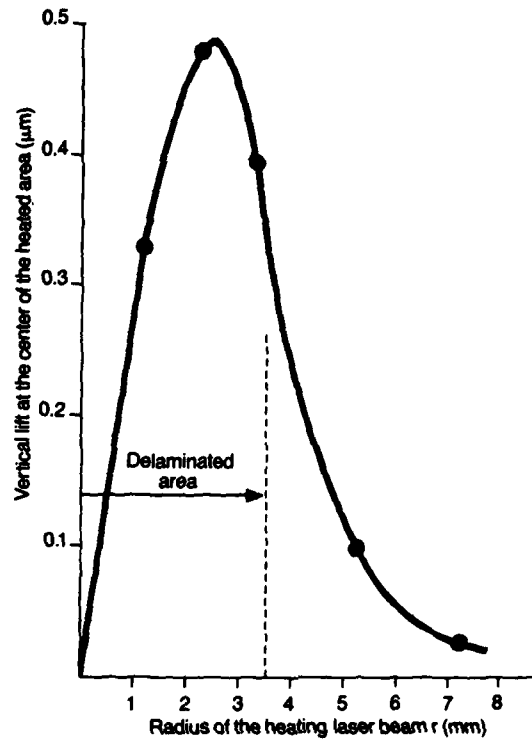


FIGURE 4: Results obtained with the finite-element model shown in fig. 3 as a function of the radius of the surface area constantly heated at 10°C .

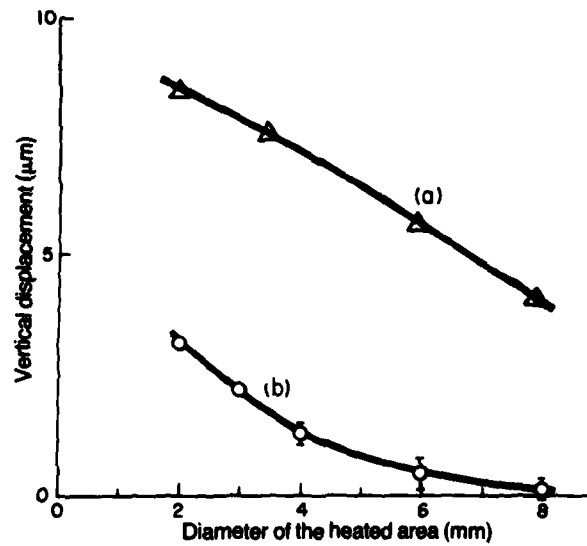


FIGURE 5: Experimental results obtained by focusing to a different diameter the constant-energy heating pulse on the top of a delaminated area of diameter (a) 20 mm and b) 7 mm.

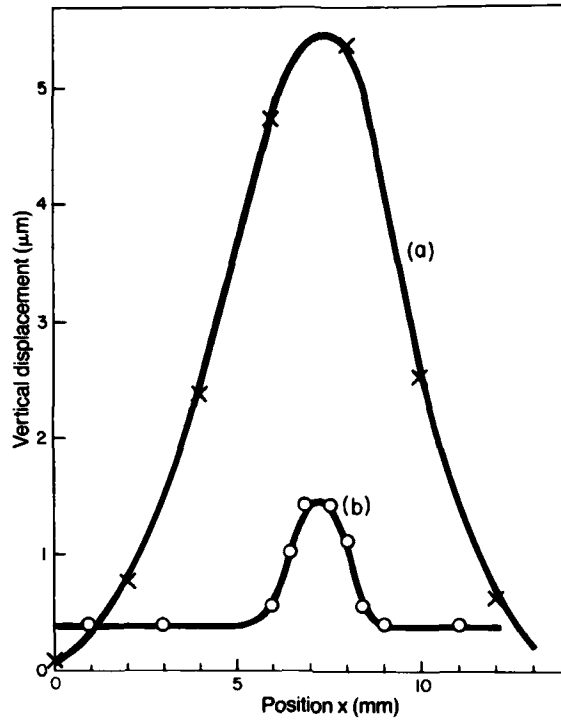


FIGURE 6: Spatial scanning of two unbond defects on an adhesively-bonded Cu-Be layer; (a) region unbonded between the positions $x=2$ to $x=12$ mm; (b) air blister on the 6 to 9 mm area.

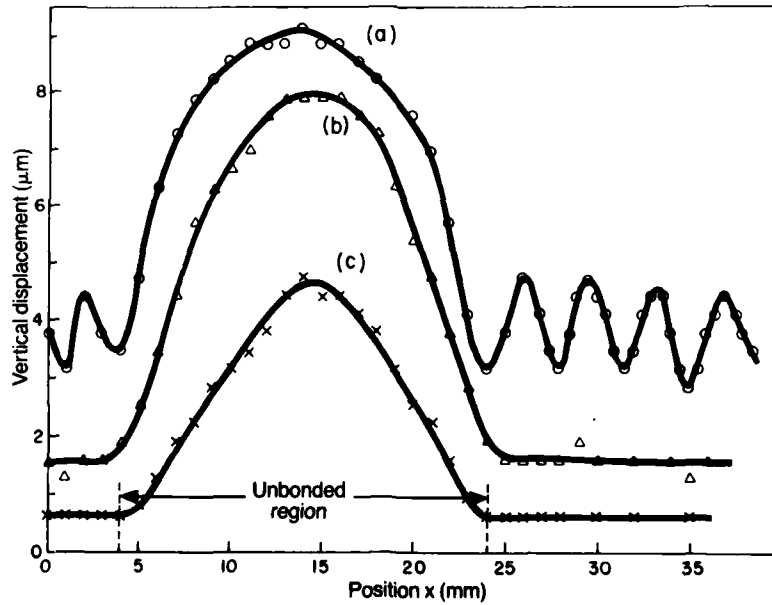


FIGURE 7: Scanning of a delaminated area on an Al-epoxy honeycomb panel, with a heating-beam diameter of (a) 1 mm, (b) 3 mm and (c) 6 mm.

Discussion

An additional diagnostic tool which has not yet been considered is the transient behaviour of the unbonded layer after the absorption of the heating pulse. For an opaque material, such a behaviour is determined by three parameters: 1) the heating pulse duration Δt ; 2) the thermal propagation time Δt_{th} :

$$\Delta t_{th} = l^2/4\alpha \quad (1)$$

across the thickness l of the unbonded layer, α being the thermal diffusivity of the layer material, and 3) the elastic response time Δt_{el} of the unbonded layer, which can be estimated from the frequency of the first harmonic f_1 of a circular plate with clamped edges¹¹:

$$\Delta t_{el} = \frac{1}{2f_1} = R^2/vl \quad (2)$$

where R is the radius of the delaminated area and v is the longitudinal sound velocity for a thin plate. In the experiments mentioned above, we had $\Delta t = \Delta t_{th} = 1 \mu s$, while Δt_{el} was much smaller.

The effect of the thermal propagation time can be understood with reference to fig. 9, which shows two time-resolved signals obtained with the plasma-sprayed coating on a position which is (a) well-bonded (point at $x = 2 \text{ mm}$ in fig. 8) and (b) unbonded (point at $x = 3 \text{ mm}$ in fig. 8). In both cases the linear thermal expansion of the heated material produced a surface displacement of nearly $1.2 \mu m$ which remains nearly constant after the absorption of the pulse if the heating beam diameter is large enough so that the radial thermal flow can be neglected¹⁰. The signal obtained on the unbonded area (curve b) shows an additional displacement caused by the bending mechanism illustrated in fig. 2b. Such a bending moment decays quickly when the thermal flow reaches the delaminated interface after a time of the order of the thermal propagation time $\Delta t_{th} = 1 \mu s$ across the layer thickness. A time-resolved analysis of such signals thus allows to separate the thermal-expansion component (which can be used to estimate the emissivity-dependent surface temperature increase) from the layer-lifting component.

As to the effect of the elastic rise time Δt_{el} , it could not be observed in our experiments because Δt was much larger than Δt_{el} , so that the layer displacement was quasi-stationary. A transient finite-element analysis was however carried out assuming a laser pulse duration Δt smaller than $5 \mu s$, which is much smaller than the elastic response time. The results of such an analysis are shown in fig. 10, where curve (a) refers to the vertical displacement of a $300 \mu m$ -thick aluminum layer over a 13 mm -radius unbonded area, while curve (b) refers to the same layer over a 4 mm -radius unbonded. In both cases, a heating temperature of $10^\circ C$ was assumed over a 3.5 mm -radius and a $50 \mu m$ -depth below the heated surface, which corresponds to the thermal propagation path in aluminum during the $5 \mu s$ pulse duration.

Fig. 10 shows that a measurement of the oscillation period of an impulse-loaded unbonded layer may be used to estimate the diameter of the unbonded area, in agreement with eq. 2. Other features of the finite-element curves shown in fig. 10, such as the relatively fast rise-time and slower decay of curve (a), can be understood from an inspection of the transient-displacement plots shown in figs. 11 and 12. As fig. 11 shows, the displacement of the 13 mm -radius delaminated layer is W-shaped after $10 \mu s$, while the rest of the unbonded area follows after $75 \mu s$. This provides a fast rise-time, which is determined by a higher-order-harmonic frequency, while the decay-time of the uniformly-oscillating plate is in better agreement with eq. 2. On the other hand, the 4 mm -radius unbonded is almost uniformly loaded, as fig. 12 shows, which explains the more regular shape of curve b in fig. 10. Fig. 12 also allows to estimate the thermoelastic strain of the epoxy layer which is of the order of 10^{-3} - 10^{-4} for a $10^\circ C$ heating, well below the non-linear range.

The finite-element model was also used to study the possibility to evaluate the cohesive toughness of the bond line by the thermoelastic technique. Fig. 13 shows the deformation of a well-bonded layer (Young's modulus $E = 3.4 \cdot 10^8 \text{ Pa}$ and Poisson's ratio $\nu = 0.4$ for the epoxy layer) under a $10^\circ C$ surface heating. The resulting vertical displacement in the center of the irradiated area was $0.08 \mu m$, to be compared with a displacement of $0.48 \mu m$ in similar conditions over a 3.5 mm -radius delamination (see fig. 4). Cohesive defects such as porosity or longitudinal cracks in the adhesive affect its tensile and shear properties. By assuming a weak epoxy layer ($E = 3.4 \cdot 10^8 \text{ Pa}$ and $\nu = 0.2$) the model gave a vertical displacement of $0.23 \mu m$. The evaluation of the elastic properties of the adhesive thus appears to be possible by this technique.

ULTRASONIC IMPULSE LOADING

As mentioned above, impulse loading of the unbonded layer would make possible a dynamic analysis of the elastic properties of the layer, which are related to the diameter of the unbonded area. The pulse duration of the YAG laser used in the experiments was either $1 \mu s$ (in the free-run mode), which is much larger than the elastic response time, or 10 ns (in the Q-switch mode), which is exceedingly short and produces a plasma breakdown of the surface if the beam is focused. An alternative technique was thus experimented for the impulse loading of the unbonded area.

The apparatus for such an experiment is shown in fig. 14. The system is similar to the dilatometric apparatus shown in fig. 1, but now the YAG laser is Q-switched and focused to an annular shape by a combination of a converging telescope and a refractive axicon (lens of conical cross-section)¹². The shape of the YAG-irradiated area is shown in the insert in fig. 14. As the finite-element model shown in fig. 15a shows, the thermoelastic expansion produced on the material

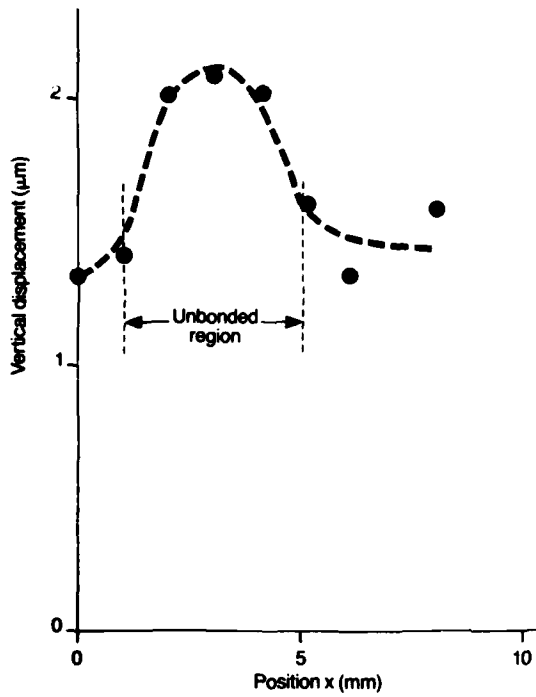


FIGURE 8:

Scanning across a 4 mm-wide delaminated region under a 250- μ m-thick plasma-sprayed aluminum-on-steel.

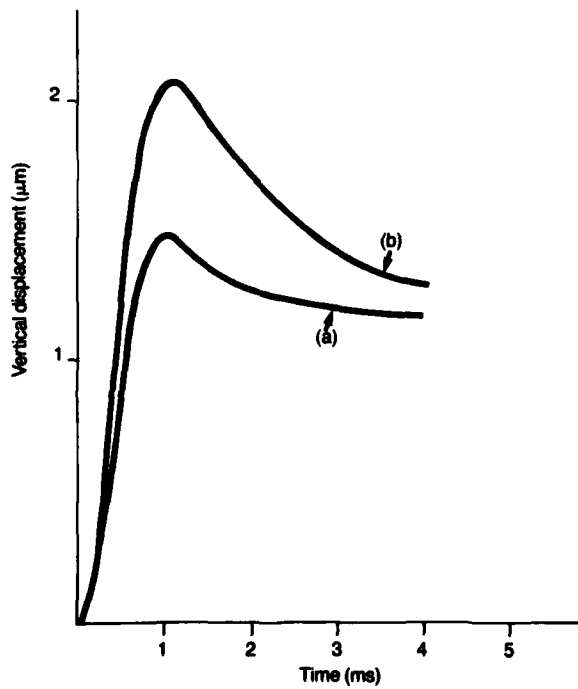


FIGURE 9:

Time-resolved signals obtained on the plasma-sprayed coating of fig. 8. Signal (a) was obtained on a well-bonded region, while signal (b) was obtained on a delaminated region.

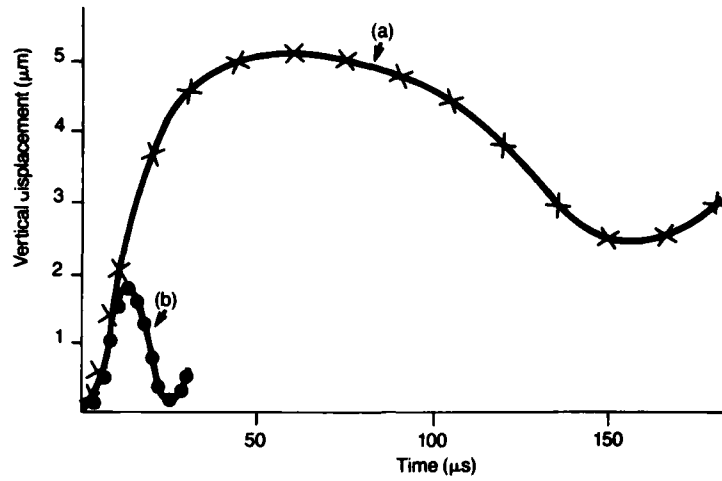


FIGURE 10: Computed elastic response of a 300 μm -thick aluminum layer to a short heating pulse over an unbonded area of (a) 13 mm and (b) 4 mm. A surface temperature of 10°C was assumed over a 3.5 mm-radius and a 50 μm -depth below the heated surface.

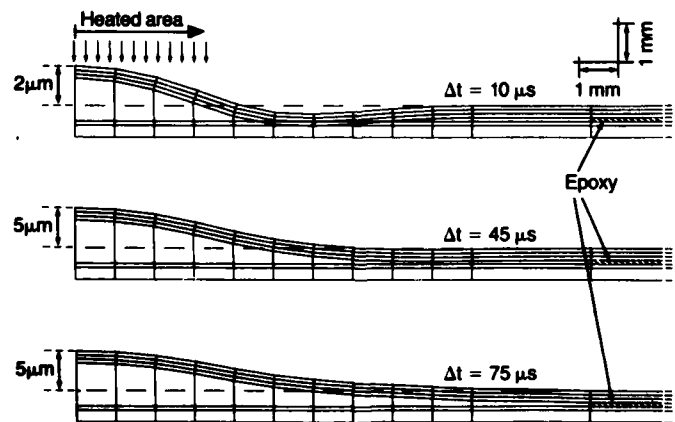


FIGURE 11: Plots of the finite-element model used to obtain curve (a) in fig. 10, after 10 μs , 45 μs and 75 μs , respectively, from the heating pulse. The maximum vertical displacement is normalized in the plots. Actual displacements are indicated in each plot.

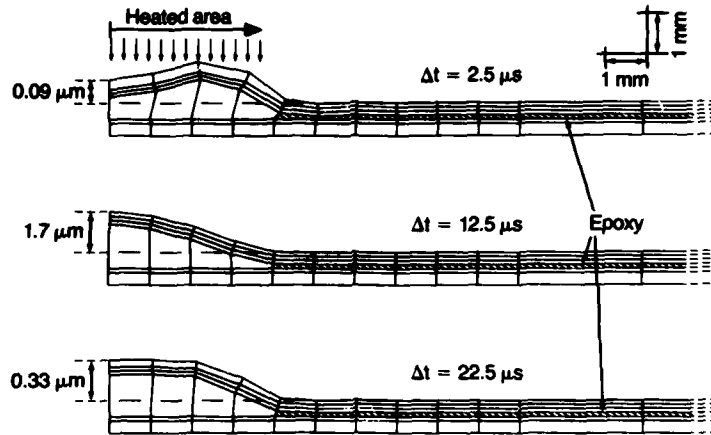


FIGURE 12: Plots of the finite-element model used to obtain curve (b) in fig. 10, respectively after 2.5 μ s, 12.5 μ s and 22.5 μ s after the heating pulse. The maximum vertical displacement is plot-normalized.

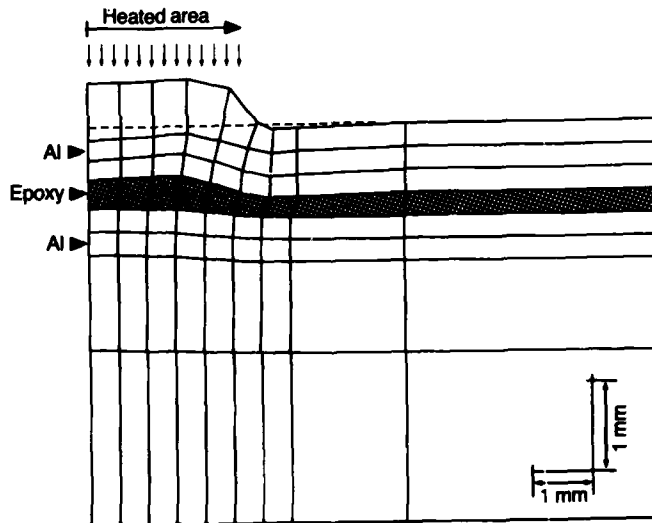


FIGURE 13: Thermal deformation of a 750 μ m-thick aluminum layer well-bonded to the substrate.

surface by the very short laser pulse generates an annular surface wave, which is seen as a negative pulse converging toward the He-Ne probed point in fig. 15a. The converging action of the surface wave produces an amplification of the ultrasonic pulse amplitude while it approaches the center of convergence. Amplification factors of the order of 20 have been observed on previous experiments performed on continuous materials¹⁸. Fig. 15b shows the surface displacement produced on the center of the annulus as monitored by the focused interferometer shown in fig. 14, with a solid-copper sample. The small P-wave arrival followed by the larger dipolar pulse corresponds to previous observations made with diverging surface waves¹⁹. The measurement of the surface-wave velocity obtained from the transit time of such a pulse has previously been used to characterize electroplated coatings of different thickness¹⁸.

Such an apparatus was used with layered samples in order to characterize the bond strength at the point of convergence of the annular wave. This approach provided a strong mechanical loading at the center of convergence while avoiding the thermal expansion component mentioned in the previous section. The larger surface of the annular area compared to the area of a center-focused spot allowed to finely focus the beam without experiencing surface-breakdown problems.

A first experiment was performed on a Cu-Be layer epoxy-bonded to a Flexiglass substrate. Fig. 16 shows the interferometrically-monitored surface displacement at the center of the heated annulus (a) on a well-bonded area and (b) at the center of a 5 cm-radius completely unbonded area. Although more work is required to interpret such curves in full detail, the following qualitative interpretation of such signals is proposed. The annular pulse converges towards the probed area, which is impulse-loaded after nearly 3 μ s. This value of the transit time, for a 7 mm-radius annulus, corresponds to the Rayleigh-wave velocity in this material. Little conversion of the surface-wave to Lamb modes thus appears to take place, probably because of the small width of the heated annulus compared to the layer thickness. The layer is set into oscillation at the arrival of the pulse, after which the converging pulse becomes a diverging annular pulse centered on the probed point. Such a diverging disturbance affects the motion of the loosely-bonded layer, which appears in fig. 20b as the vibration of an edge-excited membrane of increasing diameter. According to eq. 2, the resonance frequency of such a membrane decreases when its diameter increases, as observed in fig. 16b. The response of a well-bonded area, fig. 16a, is lower in amplitude and is more rapidly damped. Such a behaviour appears to be a direct consequence of the bonding action of the adhesive. An evaluation of the bonding strength may thus be made from a simple observation of the detected signal by this technique.

The observed amplitude of vibration is obviously smaller for thicker layers, such as the one shown in fig. 17. Such a laminate was composed by three adhesively-bonded aluminum plates of thickness 0.020", 0.020" and 0.016" respectively. An unbond defect was obtained by placing a 1 cm-diameter Teflon insert between the first plate and the epoxy film prior to bonding. Fig. 18 shows the response of such a sample (a) in the center of the unbonded area and (b) on a well-bonded area. The arrival of the P-wave after nearly 1.5 μ s and of the R-wave after 2.5 μ s are clearly visible. Fig. 18a shows the normal oscillation with a decreasing frequency after the converging-surface-wave arrival, with an amplitude which stops rising when the diverging-pulse diameter reaches the diameter of the unbonded area. A similar behaviour is observed for the well-bonded area, fig. 18b, but in this case a higher-frequency vibration component can be seen. Such a component is believed to be caused by the whole-body vibration of the three layers which are well-bonded in this case. A larger effective thickness corresponds to a larger vibration frequency, in agreement with eq. 2. A spectral analysis of the detected signal may thus provide an additional diagnostic tool for the inspection of sandwiched structures.

Finally, the aluminum-on-steel plasma-sprayed coating previously mentioned (see figs. 8 and 9) was inspected with the converging-wave technique. The 4 mm-wide unbonded area was analyzed using a heating YAG annulus of 8 mm in diameter. The results are shown in fig. 19. The obtained signals were more irregular than the ones previously obtained, probably because of the inhomogeneity of the porous coatings. Fig. 19a, obtained on the unbonded area, shows an oscillation which decays in a time which is of the order of the time required for the diverging pulse to reach the diameter of the delaminated area. Fig. 19b, obtained in a well-bonded area, shows a much larger vibration frequency as well as a much faster decay time, which may be related to small porosity within the coating.

Such results show that a dynamic analysis of impulse-loaded layers can provide a large amount of information on the cohesive and adhesive properties of the bonded layer. More work should be performed in order to determine which is the best experimental technique for impulse-loading, as well as to interpret the wide amount of information provided by such signals.

CONCLUSION

A novel thermoelastic technique has been developed for the inspection of layered materials. Similarly to the more conventional holographic interferometry approach, this technique is completely non-contact and directly measures the lift of the bonded layer under a mechanical load. Several practical problems of the holographic method, such as the sensitivity to ambient vibrations, heat-source uniformity and fringe-interpretation problems are avoided with the thermoelastic technique.

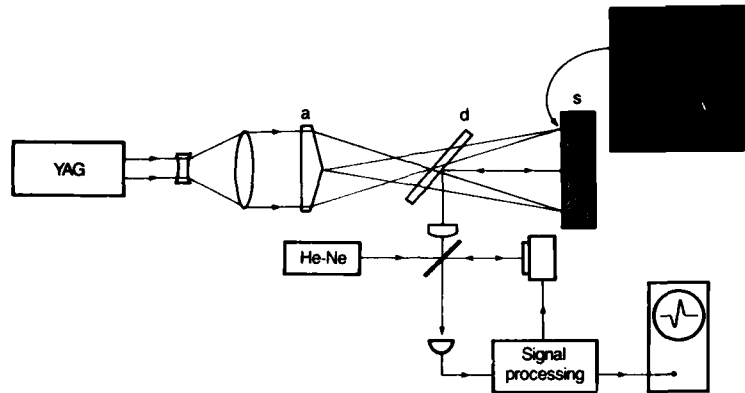


FIGURE 14: Experimental apparatus for the ultrasonic impulse loading of a layered material. An axicon-produced annular laser beam generates an ultrasonic surface pulse which converges toward the center of the annulus where a strong dipolar pulse is produced. The resulting surface displacement is monitored interferometrically.

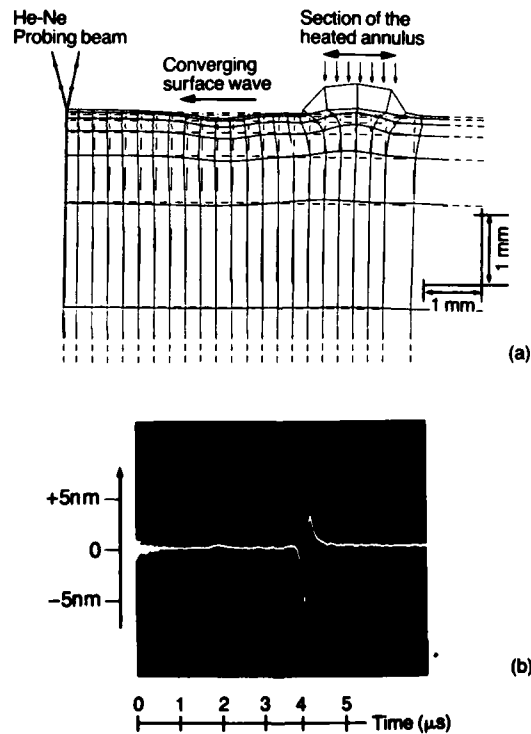


FIGURE 15: Generation of an ultrasonic convergent pulse on a homogeneous material; (a): section of an axisymmetric finite-element model showing the converging ultrasonic pulse after $0.8 \mu\text{s}$ from the heating laser pulse; (b) signal detected at the center of the annulus with the apparatus shown in fig. 14 versus time from the YAG pulse.

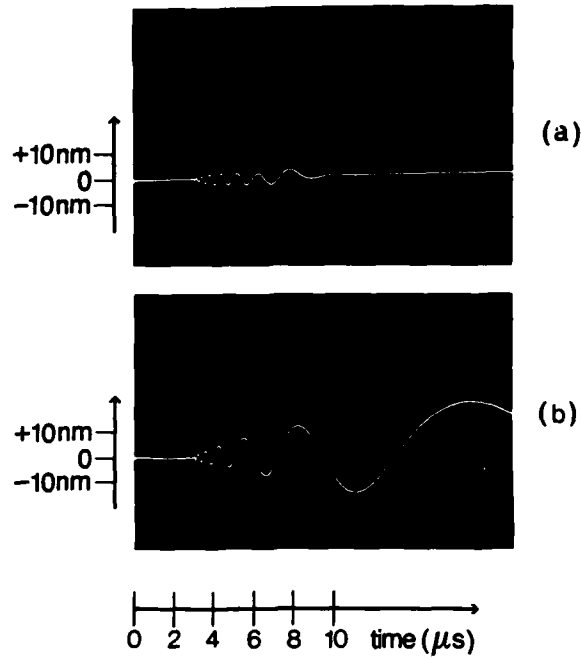


FIGURE 16: Response of a 0.125 mm-thick Cu-Be layer epoxy-bonded to a Flexiglass substrate to the ultrasonic pulse-loading technique; (a): well-bonded area; (b): unbonded area. The diameter of the annular heating beam was of 14 mm.

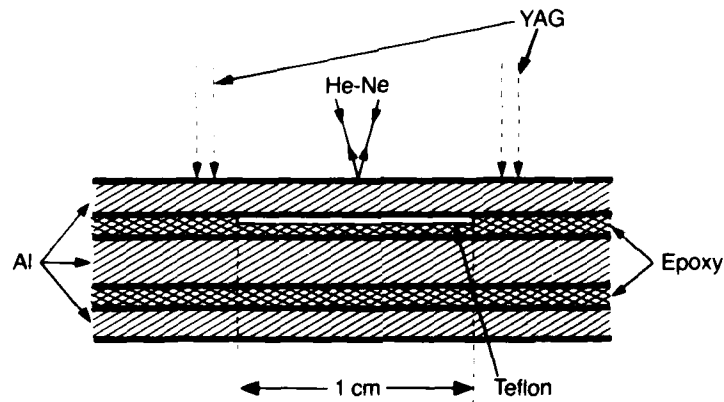


FIGURE 17: Schema of the artificial bonding defect produced on the 0.020" - 0.020" - 0.016" Al-epoxy laminate tested with the convergent-wave technique.

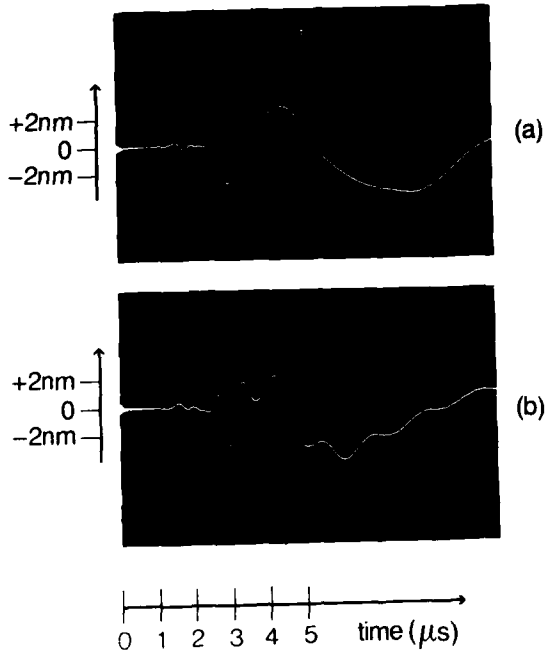


FIGURE 18: Response of the 0.020" - 0.020" - 0.016" Al-epoxy laminate shown in fig. 21 to the ultrasonic impulse-loading technique; (a): unbonded area; (b): well-bonded area. The diameter of the annular YAG beam was of 16 mm.

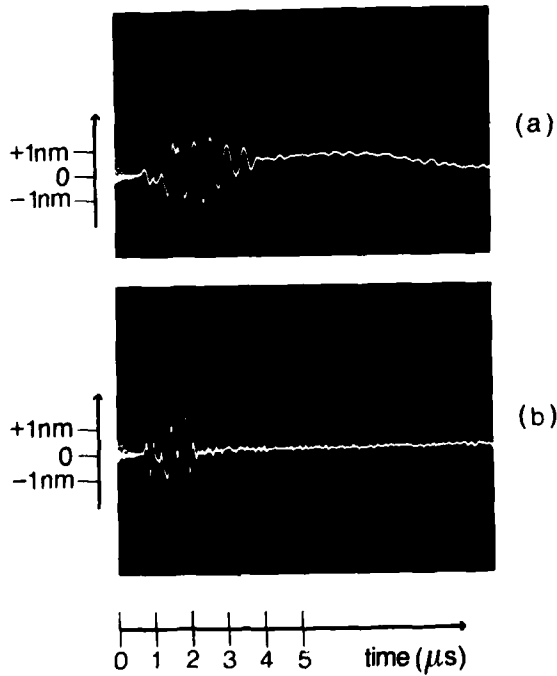


FIGURE 19: Response of a 250 μm-thick plasma-sprayed aluminum-on-steel coating to the ultrasonic converging-pulse technique; (a): unbonded area; (b): well-bonded area. The diameter of the annular YAG beam was 8 mm.

The essential feature of this technique is the possibility to thermally load a surface area smaller than the unbond diameter. This provides a lifting mechanism which could not be obtained with extended-thermal-stressing holographic techniques. Consequently, quantitative non-destructive evaluation of cohesive and adhesive properties of the bonded layer appear to be possible by the thermoelastic technique.

Finally, the pulsed nature of such a technique makes it an attractive tool for the dynamic analysis of the structure response to impulse loading. The thermoelastic technique is ideally suited for such an analysis because it is non-contact, so that the layer movement is not perturbed, it provides a strong lifting action, and it exactly measures the surface displacement with no distortion and with a wide and flat frequency response.

REFERENCES

1. E. Segal and J.L. Rose, NDT techniques for adhesive bond joints, in: Research techniques in NDT, edited by R.S. Sharpe (Academic Press, London, 1980), chapt. 8.
2. I.G. Scott and C.M. Scala, NDT Int., 15, 75 (1982).
3. N. Joiner, NDT-Austr., 17 (Apr. 1983).
4. H.D. Steffens and H.A. Crostack, Thin Solid Films, 83, 325 (1981).
5. J. Szilard, Ultrasound penetration through very thin gas layers embedded in solid bodies, Proc. 4th Int. Conf. on NDT, Sept. 9-13, 1963 (Butterworths, London).
6. H.H. Chaskelis and A.V. Clark, Mater. Eval., 38, 20 (1980).
7. L.A. Kersch, Laminate Inspection, in: Holographic NDT, edited by R. K. Erf (Ac. Press, New York, 1974).
8. G. Birnbaum and C.M. Vest, Int. Adv. in NDT, 9, 257 (1983).
9. R.M. Gagosz, Pulsed Holography, in: Holographic NDT, edited by R.K. Erf (Ac. Press, New York, 1974).
10. P. Cielo, G. Rousset and L. Bertrand, Optics and Lasers in Engineering, 1984 (to be published).
11. W.J. Harris and D.C. Woods, Mater. Eval., 32, 50 (1974).
12. T. Winkler, F. Erdmann-Jesnitzer and H. Haferkamp, Holographic evaluation of disbondings in sandwich plates, 36th Ann. Conf., Reinforced Plastics/Composites Inst., (Society of the Plastics Industry, 1981).
13. R. Dändliker, E. Maron and F.M. Mottier, J. Opt. Soc. Am. 66, 23 (1976).
14. P. Cielo, G. Rousset, L. Bertrand and E. P. Parkinson, Pulsed optothermal inspection of composite materials, 2nd Can. Symp. on Aerospace Structures and Materials, Ottawa, May 28-30, 1984.
15. V. Damm, D.I.S.A., Copenhagen, and F.A. Wedgwood, A.E.R.E. Harwell, England, private communications.
16. H.W. Carslaw and T.C. Jaeger, Conduction of heat in solids (Oxford University Press, Oxford, 1959).
17. J.W.S. Rayleigh, The theory of sound, chapt. 10 (Dover Publications, New York, 1945).
18. P. Cielo, F. Nadeau and M. Lamontagne, Ultrasonics, 1984 (to be published).
19. C.B. Scruby, R.J. Dewhurst, D.A. Hutchins and S.B. Palmer, Laser generation of ultrasound in metals, in: Research techniques in NDT, edited by R.S. Sharpe (Academic Press, London, 1982) chapt. 8.

INFLUENCE OF WELDING FLAWS ON THE FATIGUE STRENGTH OF ELECTRON
BEAM WELDMENTS IN Ti AL6 V4

by
Walter Schütz and Wolfram Oberparleiter
Industrieanlagen Betriebsgesellschaft mbH, D 8012 Ottobrunn,
Germany

SUMMARY

Electron beam welding is a well known joining method in aircraft construction. Although a lot of data is available on the fatigue behaviour of EB-welded Ti Al6 V4 alloy, only a few data on the effect of flaws in these weldments exist. Therefore artificial flaws of different size were produced in EB-weldments and the effect of these flaws on static strength, fatigue, fracture toughness and crack propagation was studied.

Experience has shown, that existing flaws may be not found or heavily underestimated by NDI. Also NDI cannot distinguish between sharp-edged flaws (which may behave like cracks) and spherical cavities. Only spherical cavities are allowable according to / 1 /; in the present investigation they reduced

the static strength	up to 35 %
the fatigue strength	up to 50 % (at N = 10 ⁵ cycles)
and the fracture toughness	up to 10 %

Such reductions therefore must be accounted for in the design phase of Ti Al6 V4 components containing EB-welds.

LIST OF SYMBOLS

a	mm	crack length
N	—	number of cycles
K _{1C}	MPa·√m	fracture toughness
S _m	MPa	mean stress
S _a	MPa	stress amplitude
R	—	stress ratio
S _u	MPa	ultimate tensile strength
s	mm	thickness of the specimens
w	mm	width of the specimens

1. INTRODUCTION

Electron-beam (EB-) welding has been used in a number of aircraft, among them the Tornado and the F 14, for titanium joints in fatigue loaded primary structure. There are data available for the fatigue strength, fracture toughness and static strength of (at least nominally) flawless electron-beam welded joints of titanium. However, to the authors' knowledge very little, if any, such data are available for EB-weldments containing flaws. It might be argued that electron beam welding usually will not produce flaws, but experience shows this to be too optimistic.

To obtain more information on the effect of flaws in EB-weldments, IABG carried out a test programme on intentionally flawed EB-welded specimens of Ti Al6 V4. As it is very difficult to obtain flaws of a certain size in a certain location in the specimens, these flaws were produced artificially. The specimens were nondestructively inspected and tested under static and fatigue loading. The results are described and discussed in this paper.

2. MATERIAL AND SPECIMEN GEOMETRY

The chemical composition and the mechanical properties of the Ti Al6 V4 alloy are shown in table 1. Fifteen plates (23 mm respectively 25 mm thick) of two different batches were available. These plates had been hot rolled, annealed and ultrasonically tested according to MIL - I - 8950 P class AA.

After EB-welding, including the artificial flaws where applicable, the specimens for the fracture toughness -, crack propagation, - fatigue - and static tensile tests were machined from these plates. The specimen geometries for the different tests can be seen from Fig. 1.

3. WELDING PROCEDURE, DEFINITION OF FLAW SIZE

As it is very difficult to obtain flaws in weldments when and specially where one wants them, artificial flaws were produced by making punch marks of different sizes in one of the butt faces. These punch marks were filled up with different amounts of vacuum grease before welding. This method was the only one suitable to obtain reproducible flaws.

AD-A173 979

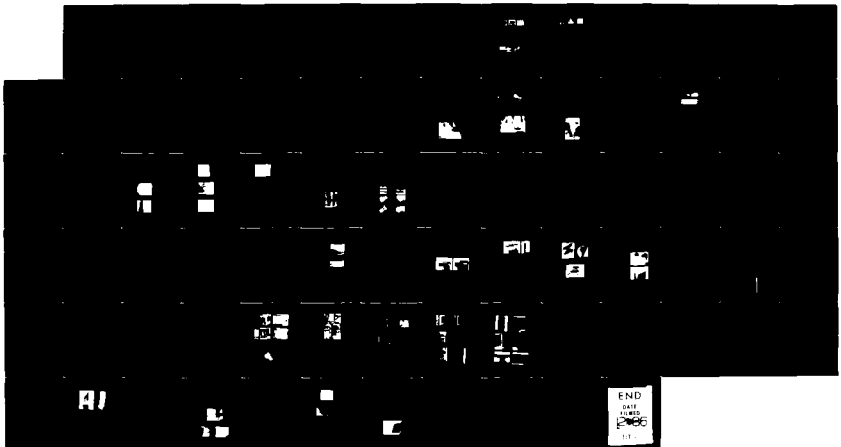
ADVANCED JOINING OF AEROSPACE METALLIC MATERIALS (U)
ADVISORY GROUP FOR AEROSPACE RESEARCH AND DEVELOPMENT
NEUILLY-SUR-SEINE (FRANCE) J GOLDAK ET AL. JUL 86
ACARD-CP-398

3/3

UNCLASSIFIED

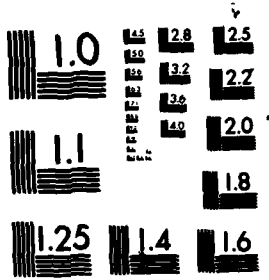
F/G 13/8

NL



AI

END
DATE
1986
11



MICROCOPY RESOLUTION TEST CHART
NATIONAL BUREAU OF STANDARDS-1963-A

EB-Welding of the Ti A16 V4 plates then was done in a Sciaky-Low Voltage equipment, type BE-44. According to the fabrication of the center wing box in question a weld thickness of 20 mm was defined, which mainly exists in that component. The pilot tests for the EB-welding were done using welding parameters identical to those used for the center wing box in production. However using these parameters, artificial flaws of the type required for the fatigue tests could not be obtained. Therefore the welding speed was increased from 20 mm/s to 25 mm/s. The welding parameters are shown in table 2.

Due to the higher welding speed it was possible to produce reproducible small, single flaws of the type wanted. Three different flaw sizes were defined for the fatigue and static tensile tests, Fig. 2:

definition	cavity (single or more flaws) mm	zone of high microporosity mm x mm
small flaws	< 0,4 \emptyset	< 1,0 x 1,5
medium size flaws	0,4 \emptyset to 1,2 \emptyset	1,0 x 1,5 to 1,5 x 5,0
large flaws	> 1,2 \emptyset	> 1,5 x 5,0

In most cases the surrounding of the cavities shows zones of high microporosity (probably caused by the vaporisation of the grease during welding) with coarse grain size. This formation of coarse grained structure in the vicinity of welding flaws (cavities) in EB-welded Ti A16 V4 can be seen from Fig. 3.

4. NONDESTRUCTIVE INSPECTION

After welding the specimens were nondestructively inspected by ultrasonic and X-ray, again according to the NDT-procedures of the aircraft in question and by the same inspectors.

The actual flaw sizes could be determined from the fracture surface of the broken specimens after the fatigue and static tensile tests. The actual flaw size then was compared to the ultrasonic and X-ray indications in order to check the reliability of both NDI-methods. According to the literature the limits of reliable indications of cavities or zones of high porosities are about 1,5 mm diameter / 2, 3 /. In the present investigation flaws were only reliably indicated by ultrasonic or X-ray if the diameter of the cavities was > 1,5 mm or zones of high porosity were larger than 2 mm.

According to the Grumman specification / 1 / sharp edged flaws are not allowable while single flaws without sharp edges are allowed up to 1,27 mm in a 12 mm thick plate and zones of high porosity up to 1,3 mm² in 20 mm thick plates.

In the LN 29 595 standard / 4 / the allowable size of a single flaw in class 1 Titanium components is 1,5 mm maximum.

5. RESULTS FROM THE STATIC TENSILE TESTS AND FATIGUE TESTS

5.1 FRACTURE TOUGHNESS

The fracture toughness tests were carried out according to the ASTM Standard E 399 using 3 point-bend specimens of 15 mm thickness and B/W = 0,5. In the specimens containing flaws only medium size flaws were present.

After an examination of the fracture surfaces the following 3 groups of K_{IC} values were obtained due to the position of the flaws in the specimens:

position of flaws, <u>Fig. 4</u>	number of specimens	\overline{K}_{IC} MPa \sqrt{m}
no flaws in the ligament	6	53
flaws in the ligament and near the crack front	9	54
flaws immediately at the crack front	3	48

The fracture toughness of EB-welded specimens of $\overline{K}_{IC} = 53 \text{ MPa } \sqrt{m}$ agrees quite well with fracture toughness obtained in prior IABG-investigations / 5 - 10 /.

Flaws in the ligament, but some distance away from the crack front, did not influence the fracture toughness ($\overline{K}_{IC} = 54 \text{ MPa } \sqrt{m}$) significant. If the flaw is located immediately at the crack front - a case which will not occur very often - fracture toughness only decreases by about 10 %. Therefore flaws in EB-welded components in general will have little effect on fracture toughness.

5.2 CRACK PROPAGATION

The specimen used in the crack propagation test is shown in Fig. 1. To study the effect of flaws

on the crack propagation behaviour artificial flaws were produced at equal distances of about 15 mm on both sides of the crack starter slot.

The crack propagation behaviour of EB-welded Ti Al6 V4 with flaws is shown in Fig. 5: The crack initiates at the crack starter slot and propagates first in the flawless weldment. When the crack reaches the flaw, crack retardation occurs, i.e. the crack propagation rate da/dN decreases.

This behaviour may be explained as follows: When the crack has reached the cavity a new crack has to be initiated at its rear. In addition, crack propagation rate is lower in the coarse grained structure around the cavity / 11 / than in the normal-grained structure away from the flaw. Both facts may cause retardation. If the crack has initiated again and grown to a length $>4 r$ it is no longer retarded / 17 /.

This positive effect of flaws on crack propagation behaviour, however, is more than balanced by the negative effect of a much larger scatter of crack propagation in the EB-welded specimens. This scatter is about twice that of the Ti Al6 V4 base material / 12 /.

5.3 RESIDUAL STATIC STRENGTH

To determine residual static strength of the EB-welded specimens the crack propagation tests were stopped at a certain crack length. The cracked specimens were then loaded to failure under a static load. Residual static strength then was calculated using the net section area taking into account the flaw area A and the existing crack a :

$$\sigma_{R,S} = \frac{F_{max}}{(W-A-a) \cdot s}$$

Fig. 6 shows the residual static strength plotted against the crack length a :

The residual static strength of EB-welded specimens containing flaws shows large scatter, especially, for large flaws. This may have been also caused by the different mechanical properties of the batches the specimens were machined from.

Generally the residual static strength of the EB-welded specimens is lower than the residual static strength of the base material / 6 /. Because there were no tests on EB-welded specimens without flaws it cannot be decided whether this decrease of residual static strength is caused by the EB-weld itself or by the flaws in the EB-weld. It is only known from prior work / 5 / that the residual static strength of EB-welded sheet material may be significantly lower than the residual static strength of the base material.

5.4 ULTIMATE TENSILE STRENGTH

The specimens for the static tensile tests either had no flaws or only medium size flaws. This enables a comparison of the ultimate tensile strength of

- the base material Ti Al6 V4
- EB-welded without flaws
- EB-welded containing flaws

Medium size flaws in EB-weldments reduce the ultimate tensile strength by about 35 % compared to the base material, even if the flaw area was accounted for. The position of the flaws in the fracture surface had no effect on the ultimate tensile strength.

The static tensile strength of EB-welded specimens without flaws was in the range of the static tensile strength of the base material.

5.5 FATIGUE

Fatigue life of EB-welded specimens was determined under constant amplitude loading at a stress ratio $R \approx 0$. After examination of the fracture surfaces of the specimens, the cycles to failure can be separated into 4 groups according to Fig. 2:

- | | |
|----------------------|---|
| Specimens containing | <ul style="list-style-type: none"> • large flaws • medium size flaws • small flaws • no flaws |
|----------------------|---|

The S-N-curves and the scatter bands of the individual groups are shown in Fig. 7. This figure shows two important facts:

- The fatigue strength (e.g. at 10^5 cycles) of weldments containing flaws is only 60 % of that of EB-weldments without flaws. In addition the flaw size can decrease fatigue strength by another 15 %.
- The scatter in fatigue life of EB-welded specimens with and without flaws may become very large (up to $T_N = 1:20$). It is much larger than the scatter usually expected for unwelded notched specimens of Ti Al6 V4 ($T_N \approx 1:1,5$). This high scatter may be caused by flaws which are situated in the fringe area of the fracture section, which usually lead to a shorter fatigue life. This result is

also confirmed by theoretical work in / 13 /. Lindh and Peshak calculated a 40 % decrease of the fatigue limit of EB-welded Ti Al6 V4 specimens with flaws in the fringe area compared to specimens with flaws near the center of the specimen.

Fig. 8 shows the mean S-N-curves of the EB-welded specimens with a notch without flaws compared to the S-N-curves of unwelded, notched Ti Al6 V4 specimens of different stress concentration factors K_t :

The mean S-N-curve of specimens without flaws is only slightly lower than the S-N-curve with $K_t=1,0$. So the EB-weld itself does not act as a sharp notch. The S-N-curve of specimens with large flaws, however, corresponds to the S-N-curve for the quite severe stress concentration factor $K_t \approx 5,0$. S-N-curves of specimens with small and medium size flaws correspond to $K_t=1,5$ to 3,6. This means flaws in the EB-weldment may act as very sharp notches depending on their size and must be accounted for in design.

Especially in the high cycle range the flaws act more severely than the corresponding notches: All S-N-curves of specimens with welding flaws are steeper than those of the notched specimens, Fig. 8. The reason for the shorter total life of EB-weldments containing flaws must be a reduction in the crack initiation phase because flaws in the EB-welds had a slightly favourable effect on the crack propagation phase.

From the literature / 13 - 16 / it is known that the stress concentration factor of single flaws (cavities) in an infinite elastic medium was found to be $K_t=2,04$. This factor increases if the flaw is situated in the fringe area of the cross section / 13, 16 /. Single flaws with cylindrical shape have a $K_t=3,0$.

The stress concentration factors of clusters or rectilinear flaws depend on the number, size and distance of the flaws to one another. K_t has to be estimated for the individual case, but normally a $K_t=3,5$ to 4.0 can be used / 14, 15 / for calculations.

5.6 NONDESTRUCTIVE INSPECTION

As discussed above, flaws in EB-weldments had a very significant effect on the fatigue life. Therefore an exact NDI is very important. Table 3 shows a comparison of the NDI indications with the real size of the defects in the fracture surface of the specimens after fatigue testing: X-ray or ultrasonic inspection using the Tornado equipment indicated less than 50 % of the flaws present in the specimens correctly. 11 of 93 flaws were not found in the ultrasonic inspection, 38 of 93 flaws were not found in the X-ray inspection. Further more, in a high percentage the size of the flaws was underestimated, see Table 3. Using both NDI methods together nearly 50 % of all flaws were indicated correctly but even 8 of 93 flaws were not found.

The flaws found in the fracture surface were sharp edged cavities surrounded by areas of microporosity. The cavities were indicated more exactly by both NDI methods but only if they are larger than 1,5mm in diameter.

6. CONCLUSIONS

- Even when X-ray and ultrasonic inspection are used together flaws may be not found in EB-welds or their size underestimated.
- Medium size flaws have no remarkable effect on the fracture toughness. Only flaws immediately at the crack front reduce K_{Ic} by about 10 %.
- EB-welds without flaws have no influence on the ultimate tensile strength. However, flaws in the weld reduce ultimate tensile strength by about 35 %, Fig. 9.
- Flaws have a favourable effect on crack propagation behaviour, but this effect is more than balanced by a large increase of the scatter.
- EB-welds reduce the fatigue strength of Ti Al6 V4 by about 20 %. If the weld additionally contains flaws a further reduction to less than 50 % of the fatigue strength of EB-welds occurs. The flaws behave like notches equivalent to $K_t \approx 2,5$ to 5,0. Furthermore EB-welded specimens with a notch without flaws show much larger scatter than unwelded notched specimens.

This large scatter of EB-welded specimens is very unfavourable for the application of EB-weldments, because it has consequences for the allowable stresses in the design of EB-welded components. Even if the mean values of welded and notched components are similar the allowable stresses of EB-welded components are much lower because of the higher safety factors due to the large scatter. Therefore in future it may be necessary to use higher safety factors for the design of highly loaded EB-welds than for the common notched components.

7. LITERATURE

- / 1 / Spezifikation GSS 6205 C der Grumman Aerospace Corporation "Electron Beam Welding of Titanium and Titanium Alloys"
- / 2 / Packmann, P.F., H.S. Pearson, J.S. Owens and G. Young: "Definition of Fatigue Cracks Through Non-destructive Testing". Journal of Materials 1969, Vol. 4, No. 3, pp. 666 ff.

- / 3 / Knorr, E.: "Reliability of the Detection of Flaws and the Determination of Flaw Size". AGARD-AG-176, 1974, pp. 196
- / 4 / LN 029 595. Entwurf vom Juli 1973. Schmelzgeschweißte, metallische Bauteile für Luft- und Raumfahrtgeräte
- / 5 / Mertens, D. und W. Schütz: Ermittlung von Werkstoffkennwerten an elektronenstrahlgeschweißten Ti-Legierungen. IABG-Versuchsbericht Nr. TF-273, Juni 1972
- / 6 / Oberparleiter, W. und W. Schütz: Ribfortschritt und Restfestigkeit an 6 mm dicken Titanplatten. IABG-Versuchsbericht Nr. TF-258, April 1972
- / 7 / Voigt, H. und H. Schult: Elektronenstrahl-schweißtechnik (EBW) - Luftfahrtwerkstoffe - Teil 1: EB-geschweißte Titanlegierungen. IABG-Versuchsbericht Nr. TF-383/1, Dezember 1973
- / 8 / Voigt, H. und H. Zocher: Arbeiten zur Elektronenstrahltechnologie in Zusammenarbeit mit der Fa. Steigerwald. IABG-Versuchsbericht Nr. TF-176, November 1970
- / 9 / Voigt, H. und H. Zocher: Abschlußbericht zur Studie 1970: Arbeiten auf dem Gebiet der Elektronenstrahl-Schweißtechnik, Teil I und II. IABG-Versuchsbericht Nr. TF-188, März 1971
- / 10 / Heidenreich, R. und W. Schütz: Bruchmechanikversuche an drei elektronenstrahlgeschweißten Luftfahrtwerkstoffen (X 2 Ni Co Mo 18/8/5, Ti A16 V4, Al Cu Mg). IABG-Versuchsbericht Nr. TF-364, Dezember 1973
- / 11 / Oberparleiter, W. and H. Zeitler: Correlation of Microstructure, Mechanical Properties and Fracture Toughness of Ti A16 V4. Fifth Intern. Conference on Titanium, Munich, 1984
- / 12 / Heidenreich, R. und W. Schütz: Untersuchung der Beta 1 - Schweißteile. IABG-Versuchsbericht Nr. TF-261, April 1972
- / 13 / Lindh, D.V. and G.M. Peshak: The Influence of Weld Defects on Performance. Welding Research Supplement, February 1969
- / 14 / Peterson, R.E.: The Interaction Effect of Neighbouring Holes or Cavities, with Particular Reference to Pressure Vessels and Rocket Cases. Journal of Basic Engineering, Transactions of ASME, December 1965, pp. 879-886
- / 15 / Wilhelm, D.P.: Fracture Mechanics Guidelines for Aircraft Structural Applications. Technical Report AFFDL-TR-III, Februar 1970
- / 16 / Boeing Report D6-24409 vom September 1969: The Influence of Weld Defects and Repair Welds on Performance
- / 17 / Bowie, O.L.: Analysis of an Infinite Plate Containing Radial Cracks Originating at the Boundary of an Internal Circular Hole. Journal of Math. & Physics Vol. XXXV Nr. 1, pp. 60-71

Batch	Plate No	Ultimate Tensile Strength R_m MPa	0,2 Percent Offset Yield Strength $R_{p0,2}$ MPa	Elongation A_5 %	Reduction of Area %
0270	1;2;3;4;5	986	977	15	42
0585	6; 7	965	930	11	36
0273	8;9;10	1056	1009	13	39
K-7733	11; 12	1096	1055	17	46
120	13; 14; 15	1110	1081	14	41

Chemical Composition (from material certificate)

Batch	Fe	C	O	N	H	Al	V	Cu	Ti
0270	0,07	0,025	0,12	0,005	0,0035	6,1	3,8		balance
0585	0,05	0,009	0,120	0,007	0,0022	5,8	3,8		"
0273	0,14	0,01	0,195	0,011	0,0029	6,4	4,0		"
K-7733	0,175	0,022	0,170	0,014	0,0073	6,2	4,0	0,005	"
120	0,14	0,018	0,180	0,010	0,0100	6,3	4,0		"

Table 1: Mechanical properties and chemical composition of the Ti Al6 V4 base material.

Welding speed	:	25 mm/sec
acceleration voltage	:	46 KV
beam current	:	300 mA
beam power	:	13,8 KW
focusing current	:	3.64 A
focusing	:	near surface
working procedure	:	continuous beam
beam direction	:	vertical
working distance	:	160 mm
pressure in the chamber	:	$< 10^{-4}$ Torr

Table 2: Parameters of the EB-welding procedure

NDI method	total number of specimens	NDI indication but no flaw existing	NDI indicat > real size	NDI indication = real size	NDI indication < real size		
					1 class	2 classes	flaw existing but not indicated by NDI
Ultra sonic Inspection	93	10	6	23	38	5	11
X-ray	93	--	2	44	8	1	38
Ultrasonic + X-ray	93	10	8	46	16	5	8

Table 3: Comparison of NDI-Results to real flaw size

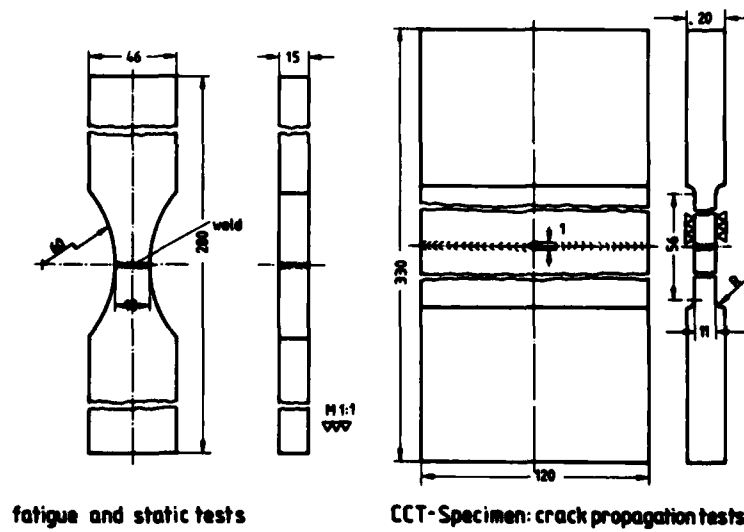


Fig. 1: Specimen geometry

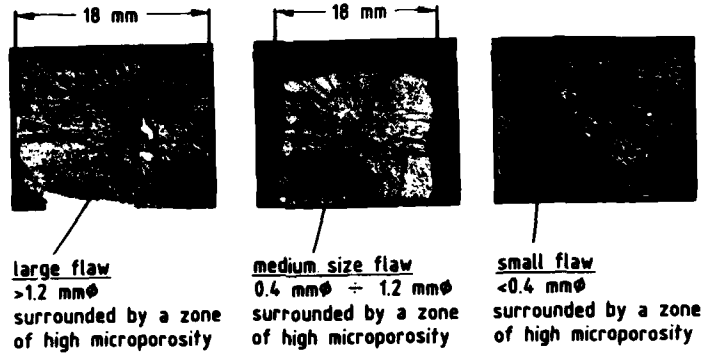


Fig. 2: Definition of the flaw sizes

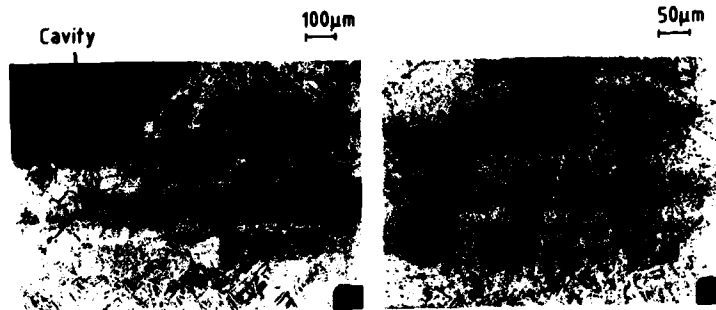


Fig. 3: Formation of coarse grained structure in the vicinity of welding flaws in EB-welded Ti A16 V4

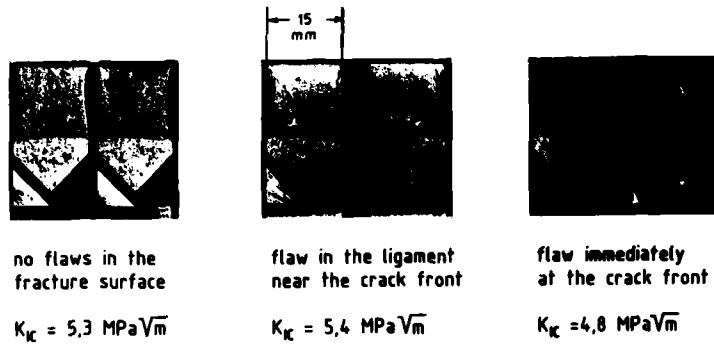


Fig. 4: Position of the flaws in the fracture toughness specimens

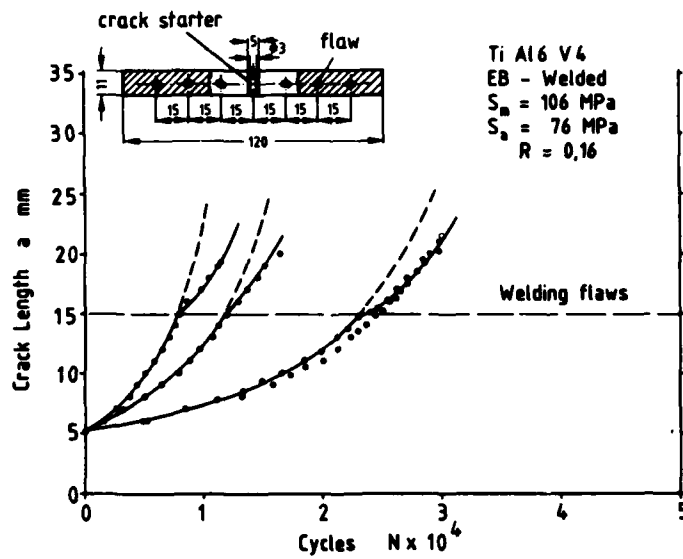


Fig. 5: Influence of flaws on the crack propagation behaviour in EB-welded Ti Al6 V4

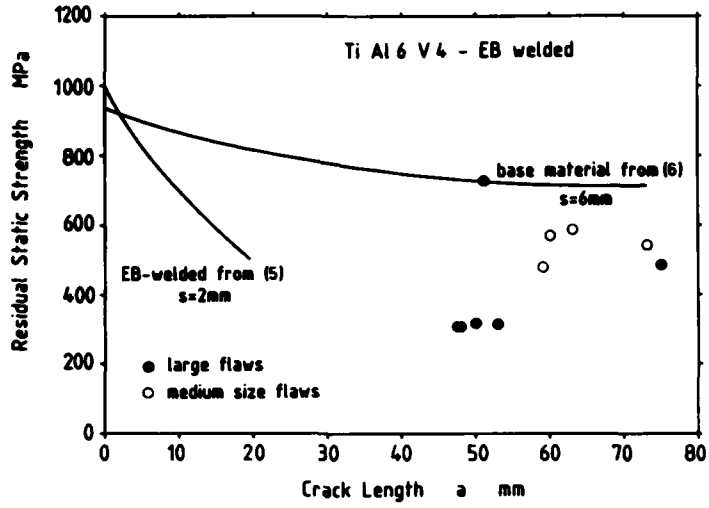


Fig. 6: Residual static strength of EB-welded Ti Al6 V4

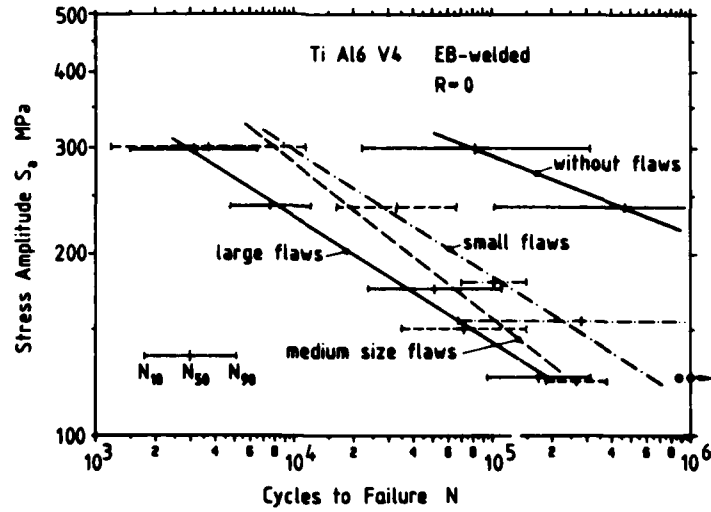


Fig. 7: Influence of flaw size on the fatigue life of EB-welded Ti Al6 V4

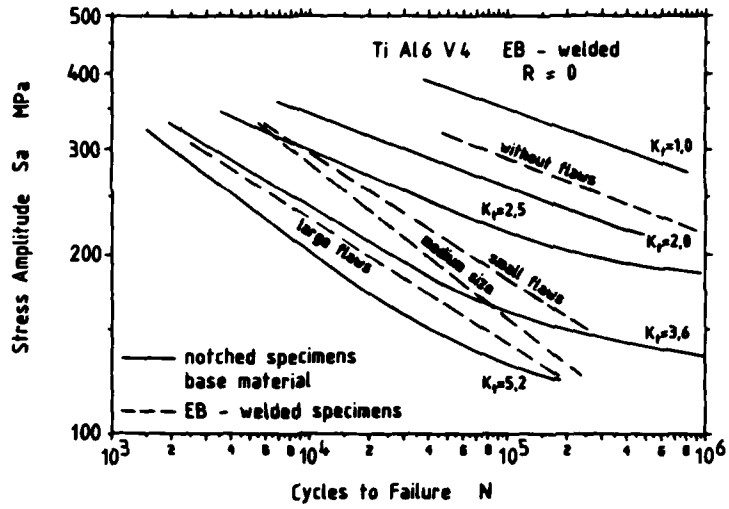


Fig. 8: Comparison of S-N-curves of EB-welded specimens and unwelded notched specimens with different K_t

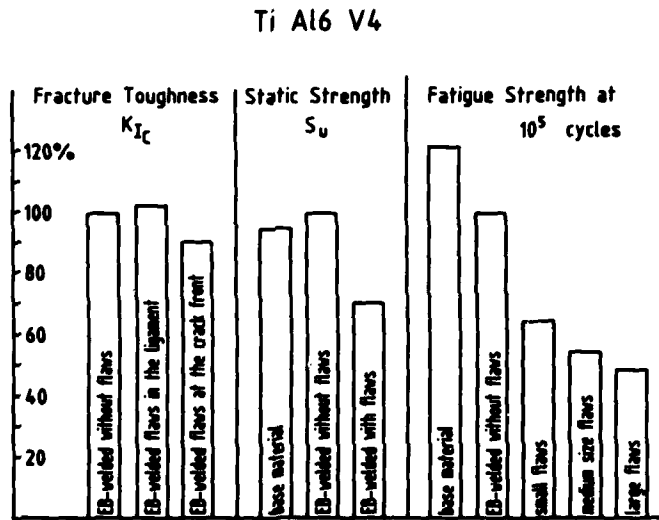


Fig. 9: Influence of flaws on the strength of Ti Al6 V4 - EB-weldments.

A REAL TIME VISION SYSTEM FOR ROBOTIC ARC WELDING

M. Dufour, P. Cielo, F. Nadeau

Industrial Material Research Institute (IMRI)
National Research Council Canada
75, de Mortagne
Boucherville (Québec)
Canada J4B 6Y4

ABSTRACT

Fast real-time vision systems for robotic arc welding have been developed and successfully implemented for seam tracking and adaptive welding functions (mass and heat balance). Typical seam tracking errors of 0.3 mm were achieved for single pass type joints (lap, butt, fillet).

In one system the weld preparation profile is first enhanced by a projected laser target formed by a line and dots. A standard TV camera is used to observe the target image at an angle. The rapid pre-processor developed by NRCC and Leigh Instruments Inc as part of the visual aid system of the space shuttle arm is then used to analyse the video signal in real time.

Another active vision system was developed in order to process more complex types of joints. It is based on laser flying spot scanning with a mechanically synchronized scanning system for projection and range finding.

With a passive system the weld preparation temperature is mapped in front of the arc using a fiber optic bundle. The temperature profile of the joint is then analysed by a micro-computer.

Because no single sensor is universal, the combination of active and passive systems on the same robot arm allows the arc welding robot to perform complex tasks.

Furthermore, the use of an off-line programming system greatly simplifies the programming task of an arc welding robotic workcell equipped with vision sensors.

1- An integrated robotic arc welding work cell

The arc welding automation problem for small to medium batch applications could only be solved by the development of adequate real time adaptive welding techniques and of adequate off-line task planning techniques to form an integrated arc welding system.

Adaptive welding is a combination of two interrelated functions. The first one is seam tracking. Without it, automation could not go further than the blind repetition of preprogrammed actions. The torch-to-joint relative position uncertainties caused by the workpiece manufacturing, the jiggling and positioning operations and the robot repeatability are large enough to cause an unacceptably high proportion of bad welds even if the selected welding parameters are appropriate to the type of joint.

The second adaptive welding function concerns the heat and mass balance of the process achieved through the real time control of the welding parameters, mainly arc voltage and current, wire feed speed and the travel speed. Optimal values of those parameters are strongly related to the joint geometry variation and also to the thermal characteristics of the workpiece along the joint. Additional complications arise from the close interaction that exists between these parameters. A parameter cannot be adjusted alone. Instead, a reliable and realistic model of the welding process in use is required and all adjustments should conform to this model. The main difficulty is caused by the absence of practical sensors which are able to measure directly and in real time some critical characteristics of the weld like the depth of penetration or the weld bead metallurgical characteristics. The parameter control relies instead on indirect measurements like the joint geometry in front of the torch or the joint side temperature. This in fact is an open loop control system as shown in figure 1.

Off-line task planning is a combination of several interrelated functions. The first function usually associated with it is trajectory planning. In general this means finding an acceptable path to welds while avoiding collision and respecting the robot and positioner work envelope. For arc welding applications, an acceptable path is also one that will keep a given weld surface-gravity relative orientation. The weld sequence should also be organized to minimize the workpiece thermal distortion and residual stress. The cycle time should be kept as short as possible to improve productivity.

The second function to be executed off-line is the gathering of the information required by the robot to perform the adaptive welding. The torch-to-joint relative position and the target welding parameters need to be defined.

It is then essential that a counter-reaction strategy be defined. At this stage of development of the technology it is utopic to think that the robot could incorporate an adequate counter-reaction strategy for every type of joints and situations and also be able to decide by itself which one is to be applied. Instead, we need to execute that function off-line.

What we propose is a combination of those important functions. With our approach the robot is specialized for welding, not for learning. This is advantageous in cases of diversified production in small-batch production, where learn runs on a robotic station may occupy a significant portion of the working hours. For this purpose, an off-line task planning system integrating state-of-the-art CAD/CAM technology is well adapted for such task optimization. A block diagram of such a system is given in figure 2.

2. Vision applied to welding

2.1 Generalities

In order to incorporate real time modifications to the program fed into an automated welding station (trajectory and process parameters), real time sensing of the relevant weld area characteristics has to be achieved. In simplified terms, these characteristics are joint axis coordinates, joint profile characteristics (Ex: gap size for butt welds), pool geometry, and pool location with respect to the joint axis. Since these characteristics are rather simple geometrical features whose space coordinates become of relevant significance to improve the welding operation, artificial vision appears to be an essential tool for adaptive welding.

In addition, the effects of the accumulation of heat in the workpiece during the process, as well as those of heat sinks or any sources that may change the heat dissipation regimes are not always properly taken care of in the program. Small adjustments in the setting of the welding parameters are thus required to assure a sound weld.

These characteristics of the welding process naturally direct us to the development of two main kinds of vision systems that complement each other.

2.2 Active vision

2.2.1 NRCC Camera using a projected light stripe

The analysis of the image made by the intersection of a laminar light beam with the workpiece surface as shown in figure 3 has been the basic approach for seam location and recognition. Adaptive functions such as seam tracking have been achieved through this scheme¹⁻².

In order to cope with the processing time requirements imposed by the welding technology the first approach used at NRCC (IMRI)⁴ has been to reduce the number of relevant features in the image from which significant and sufficient information can be obtained and used to perform the welding adaptive functions. A modular pre-processor whereby each module is dedicated to a given feature has thus been used to incorporate vision to welding systems.

The pre-processor is based on a joint development made by the National Aeronautical Establishment of the NRCC and Leigh Instruments Corporation. It works with a standard NTSC camera and was first aimed at being a visual aid to the Canadarm manipulation from the NASA Space Shuttle⁵. Each pre-processor module functions are as follows: a) the obtention of a binary image, using a preselected threshold contained within a dynamically programmable rectangular window covering a small portion of the field of view, and b) the determination of the area and of the first moment of the white level feature within the window. Image coordinates, and through simple triangulation, space coordinates of a selected feature within the field of view, are thus obtained at a rate of 30 Hz. By cleverly selecting a number of relevant features in the image, and by properly treating the expected relationships between these features, adaptive functions such as seam tracking of a variety of weld geometries including butt, lap and fillet joints can be performed. It is in this modular approach that lies the interest of the vision system for welding developed at NRCC (IMRI). It can cope with welding travelling speed requirement trends by using rather simple and proven technology.

Figure 4 shows the block diagram of the vision system developed at IMRI. As most systems, the projection unit uses a laser source and the receiver unit uses an adapted narrow band filter to eliminate the intense light noise created by the arc. The optical axes of both units are at an angle so that triangulation can be performed.

At IMRI, we have chosen to put the projection unit near the torch where it is much less affected by heat and spatters. The camera is directly subjected to the hard welding environment. However, the optical components which are directly exposed to the hostile welding environment are particularly rugged. As it is shown in figure 5, only the small aperture of the iris is exposed. An internal gaseous pressure or a small exchangeable window prevents surface contamination by fumes and spatters. This configuration is appropriate to maximize the projected light intensity from the laser source while a lot of attention of the image is required for the camera.

The laboratory prototype of the vision head is shown in figure 6. It could be much further reduced in size by repackaging the camera unit.

The camera image is fed into the pre-processor modules that provide area and first moments of individually selected features of the image. The microprocessor carries out logical and mathematical operations to drive the torch coordinates, change the welding parameters, and window locations in the field of view. The window locks on the selected feature, with an imposed relationship between its center and the centroid of the feature.

As an example, figure 7 shows the image sensed by the camera for a fillet joint. The windows from the four modules are superposed. The cross-hair is a representation of the computer solution. Each module gives the precise coordinates in the image plane of the surface center of a short section from one of the two lines representing the joint profile. The line equations are computed from the result of two modules. The joint position and its orientation are computed from the intersection of the two lines.

Figure 8 shows a 6 axis robot welding a fillet joint (GMAW) whose trajectory (height and lateral position) is corrected by the vision system. Typical accuracy of 0.3 mm was achieved for the lateral position of the joint.

2.2.2 NRCC - SRI Camera using a flying spot scanner with synchronized detection.

The first moment method described in the last section is not adequate to deal with the rather complex joint profile geometry that characterizes multipass types of joints. It would certainly give part of the answer but the detailed measurement of the joint profile is still required for further analysis. The extraction of the joint profile from the camera image is a possible solution¹. However, the use of a moving projected dot with synchronized detection^{2,6,7} instead of a projected light stripe is more promising for the time being because it needs less processing power and because a much better image contrast can be obtained with the same laser light power.

Figure 9 shows the typical configuration of a geometrically synchronized scanner. It is a prototype developed by Servo-Robot Inc. (SRI)⁷ in collaboration with NRCC. This principle is different from other moving dot sensors⁸ in that the linear detector output is almost constant for a flat surface for a very wide field of view. It simplifies greatly the sensor output processing because the distance information is available directly. Once calibrated, the camera gives very precise results. Appendix 1 gives the specifications of the SATURN camera manufactured by SRI.

The first design step is to define a reference plane for which the detector output will be "zero". As it is shown in figure 10, any object surface not aligned with the reference plane will produce a linear detector output with the following relation if θ is small:

$$p = K \Delta x_0 = Z\theta$$

where

- p detector output
- K constant
- Z position of the object surface from the reference plane
- θ angle of the intersection of the source and detector axis at the reference plane. It is desirable to keep it small for a compact camera.

Figure 11 shows the SATURN camera mounted on a six axis robot and using a seventh axis to align the camera-torch relative position along the seam.

2.2.3 Discussion

To select a seam tracker from a moving dot or a laminar light beam type of active vision systems one has to make several considerations.

The most obvious advantage of moving dot systems is that the laser light power is more concentrated (20mw over 1mm^2 instead of $1\text{mm} \times 30\text{mm}$). Thus, for the same laser source power they provide a much better image contrast of the structured light pattern over the low frequency component of the light noise generated by the arc. For arc welding processes involving high arc power and for processes such as pulsed or spray GMAW for which splatters are inexistant, the light noise low frequency component is the main source of perturbation experienced. For laminar light beam systems, this problem could be overcome by using a much higher total laser source power or by using a better image

analysis algorithms. The cost of such high power laser source is actually prohibitive. However the semiconductor laser technology is evolving very fast and low cost lasers should be available within a few years. On the other hand, the image from a laminar light beam system is integrated for a much longer time (33 msec at 30Hz instead of typically 130 usec for the same scanning rate) thus reducing high frequency light noise as the one created by particle-projection, fine surface irregularities (ex. grinded surfaces) or speckle.

The second main advantage associated with moving dot with synchronised scanning systems is that the detector signal requires much less processing power. This is highly desirable even if the technology trends are for a tremendous and accelerated increase in computing power at a low cost and for the development of highly sophisticated and powerful algorithms usefull for laminar light beam systems.

A laminar light beam system requires no moving parts and allows more rugged optical configuration to be used in the hostile welding environment. Using a telecentric configuration with a small aperture iris the light beam crossing the interference filter will be parallel for both types of system. However, because of the much longer exposure time of each detecting element of the camera compared with the focused-spot detector, the aperture of the diaphragm is much smaller in the laminar-beam approach than in the moving-dot approach. This results in a larger depth of field and increased particle-projection protection (see figure 5) for the laminar-beam techniques. Viewing distances used in welding are short so a laminar light beam system requires less space. Synchronised scanning moving dot systems lose their advantage over short distance because of the mechanical size of components.

It is thought that active and passive vision systems should be combined on the same automatic welding system. The same processor used in laminar light beam active vision systems could then be used in a visible band passive vision system to measure weld puddle characteristics.

Some more advanced projected light pattern such as the projection of isolated dots obtained by a fiber-optic array³ could also easily be added to a laminar light beam system.

2.3 Passive vision

2.3.1 Generalities

Passive systems can be divided into reflective or emissive systems, depending on whether the observed visual pattern is produced by reflection of the ambient light from the inspected object, or whether it is produced by direct thermal emission from the hot surface. Passive optical sensors have been used to view directly the thermal emission from the surface being welded¹⁰⁻¹¹. The possibility to inspect in real-time the temperature of the welded materials is very attractive, because the temperature distribution around the welding pool provides an important information on the welding status. Measurable variables such as the pool shape, absolute temperature and symmetry of the temperature distribution are directly related to several welding process parameters such as joint mismatch, gap and plate thickness fluctuations, arc blow or the visco-dynamic and thermal conductivity properties of the plates. However, optical inspection by a video camera or a photodiode array operating in the 0.4 to 1.0 μm spectral range is limited to the welding pool and the surface immediately adjacent, because thermal emission in this spectral range falls abruptly at temperatures lower than 1000K. Moreover, arc-shielding is a problem in this spectral range. Operation in the longer wavelength spectral region is thus preferable in order to increase the signal-over-arc-background ratio³. Long-wavelength thermographic inspection during welding has recently been proposed for the thermal characterisation of the welding process¹²⁻¹⁵. At IMRI, with the collaboration of the Welding Institute of Canada (WIC), a specially designed vision system has been designed from that principle¹⁶. Figure 12 gives a schematic view of the system.

2.3.2 Passive I.R. vision applied to GMAW.

By mapping the surface temperature of a butt joint in front of the welding torch and by adequate signal analysis, precise seam tracking was performed. As it was plotted from a computer simulation (finite element modelling), the diagram at figure 14a shows that highly visible temperature discontinuities characterise the position of the joint. Figure 14b is the typical output from the I.R. line sensors focused along the line AA of figure 14a. The distance between the two peaks is related to the gap size. The minimum corresponds to the center of the joint. By moving the lateral torch position slightly in order to keep the two peaks at the same level, the system could equilibrate the heat input to the two plates. Using this sensor, joints as the one shown in figure 15 are easily welded.

2.3.3 Passive I.R. vision applied to PAW.

Plasma arc welding is more and more in use by the industry. It produces a very controllable arc and is particularly useful for very thin sheet welding (1mm) and for thick sheet welding (10mm) using the keyhole method. However, the parameter adjustment required to keep the process in the "keyhole" state is very difficult to perform and prevents the use of that process in fully automatic welding systems.

I.R. vision constitutes an elegant solution to that problem. By focussing the I.R. line sensor on the joint surface from the center of the arc to the outside of the weld puddle it is possible to detect the keyhole condition as the speed changes. Figure 16 shows typical measurements made from an aluminium surface which is particularly difficult to be seen by a welder.

There is a clear signal shape difference between a melt-in condition and a "keyhole" condition. This phenomenon is explained by the fact that the gap column inside the keyhole is more emissive than the solid or liquid metal surface. The reverse situation appears for steel.

The control strategy in this case could be to use the fastest speed possible in order to keep the "keyhole" condition.

2.4 Discussion

The main interest of the passive IR approach as compared to active light-projection systems lies in the capability of the former to directly sense the temperature distribution around the welding pool. Parameters such as the pool width and cooling rate, or the overheating of one side of the workpiece produced by heat-sink or arc-blowing effects could not be monitored by active sensors which supply only morphological information.

Seam-tracking capabilities of passive thermal-imaging systems appear however to be limited to butt-welding at low speeds because of the reduced thermal-propagation rate in front of the welding pool. The integration of the thermal-monitoring capabilities of such sensors with the morphological information from an incorporated light-projection or reflective sensor would thus appear to be most convenient at the present state of the technology.

The use of the information provided by the vision systems is not a trivial problem. As it was stated earlier, there is no direct information available about the characteristics that need to be controlled like the depth of penetration or the metallurgical properties. Instead, an open loop control strategy has to be defined. Since no working theoretical model exists for most welding processes, real-time control strategies have to rely on empirical ones. Because of the large number of variables to deal with, a systematic test procedure to be executed off-line needs to be designed.

3. Off-line welding parameter planning

3.1 Generalities

Welding parameter planning is as important for the weld quality as could be trajectory planning for the robot productivity. It should then be considered as such while developing an off-line task planning system for robotic arc welding applications.

Current practice in the industry doesn't include any structured method to define welding parameters. Most of the time, parameter selection is based on the welder experience or on some documentation available within the company or from standard tables. Successive trials may be performed in some cases to adjust the parameter values. Usually one parameter is varied alone for a given test sequence.

Several drawbacks characterize this approach. First it is human competence dependent. Second, it gives very little information about the process compared to the work it requires. For example it doesn't provide information about parameter tolerances or about quality variation related to parameter variations. Thirdly, the resulting solution may be acceptable but probably not optimised. Finally, it certainly gives no information about what kind of welding parameter variations should be performed for some conceivable joint characteristics variations.

The method proposed by Galopin and Boridy under a joint IMRI-ETS program looks promising¹⁷. It is a computer assisted experimentation approach based on statistical analysis of the experimental results with appropriate selection of experiment characteristics. It is a systematic approach in that all aspects of the experiments are considered: geometry variation of the joint, welding parameter variations, material property variations and also all the quality criteria.

3.2 A systematic method for welding parameter selection.

3.2.1 Experiments characteristics definition

Even with simple types of joints many variables have to be considered if usable results are to be obtained. One may have to make a selection in order to keep the complexity of the analysis within some reasonable figures. For example, a butt joint from thin metal sheets with shear cutted sides experiment should consider the following variables:

- 1- gap size
- 2- alignment errors
- 3- voltage variation (GMAW)
- 4- wire feed speed
- 5- advance speed

It is then desirable to restrict possible variations of these parameters to some probable values. Variation margins should however be wide enough to include even some unacceptable quality results in order to give an operational knowledge of the process dynamics. For example, the gap size variation limits for a butt joint may be computed from the workpiece tolerances and other associated dimensional uncertainties and the voltage variation limits may be based on standard tables.

Using the computer, it will then be possible to define the characteristics of the experiments by randomly combining the selected welding parameters. This is the only way to produce workable results from a limited number of tests when there are many variables. Obviously, the greater the number of experiments the better will be the reliability and the better will be the resolution of the empirical model that will be obtained from the analysis.

3.2.2 Experiment results analysis

Some quantifiable quality criteria first need to be defined. For the first welding pass for example, the depth of penetration should certainly be considered. One may also be interested by the size or the number of inclusions.

A statistical analysis of the results may then be performed. Polynomial regression curves are computed to relate the quality with the welding parameters. Depending on the number of experiments and on the number of variables, regression factors of the first, second or third degree will be available.

Using these multidimensional curves, it will then be possible to determine if some variables are uncorrelated to the weld quality. It will be possible to find maxima from the multidimensional field or to determine what new experiments to perform in order to find a "quality" maximum.

The results from the analysis are of great value for a real time adaptive welding system. From the statistical analysis, a multidimensional volume in which the weld quality is found acceptable can be selected thus providing the welding system with a reliable counter-reaction model instead of only some target welding parameter values.

CONCLUSION

There is no single sensor that could provide all the information required for adaptive welding. A possible solution is to combine active and passive sensors within the same vision system.

It has been demonstrated that the vision head of an active vision system based on the projection of a laminar light beam can be packed in a small volume while being particularly well adapted to the welding environment. For simple types of joints (laps, butt and fillets), image analysis using a simple and fast algorithm is possible.

For the time being, moving-dot active systems are more advantageous because they need less processing power and a smaller laser source. This contributes to produce a lower cost system. A state-of-the-art commercial product has been built using such a method.

With the recent introduction on the market of long wavelength (5µm) optic fibers it is now possible to monitor the temperature down to about 200°C inside and surrounding the welding pool. A rugged industrial prototype has been built at IMRI and successfully used for seam-tracking butt joints and to measure weld puddle size and position for GMAW and GTAW, and to detect "keyhole" state for PAW.

We have proposed a practical solution for the selection of welding parameters. The method gives high level information which would enable efficient real time adaptive arc welding.

REFERENCES

1. Morgan C.G., Bromley J.S.E., Davey P.G., Vidler, A.R., "Visual Guidance Techniques for Robot Arc-Welding", Third Int. Conf. on Robot Vision and Sensory Controls, SPIE Vol 449, Cambridge Nov. 7-10, 1983.
2. Oomen G.L., Verbeek W.J.P.A., "A Real-time Profile Sensor for Robot Arc Welding", Third Int. Conf. on Robot Vision and Sensory Controls, SPIE Vol 449, Cambridge Nov. 7-10, 1983.
3. G. Rider, "Control of Weldpool Size and Position for Automatic and Robotic Welding", Third Int. Conf. on Robot Vision and Sensory Controls, SPIE Vol 449, Cambridge Nov. 7-10, 1983.
4. Dufour M., Bégin G., "Adaptive Robotic Welding Using a Rapid Image Pre-Processor", Third Int. Conf. on Robot Vision and Sensory Controls, SPIE Vol 449, Cambridge Nov. 7-10, 1983.
5. Pinkney H.F.L., "Theory and Development of an On-Line 30Hz Video Photogrammetry System for Real-Time 3-Dimensional Control", Symposium of Commission V, Photogrammetry for Industry, Stockholm, August 14-17, 1978.
6. Rioux M., "Laser Range Finder Based on synchronized Scanners", Applied Optics, Vol. 23, n. 21, Nov. 1, 1984.
7. Bégin G., Boillot J.P., Michel C., Teubel G., "Third Generation Adaptive Arc Welding Unit", Conf. int. sur l'automatisation et la robotisation en soudage et technique connexes, Strasbourg, sept. 2-3, 1985.
8. Bamba T., Muruyama H., Kodaira N., Tada E., "A Visual Seam Tracking System for Arc-Welding Robots", 7th Int. Conf. on Industrial Robot Technology, Gothenburg, Oct. 2-4, 1984.
9. Dufour M., Cielo P., "Optical inspection for adaptive welding", Applied Optics, Vol. 23, number 8, April 15, 1984.
10. Rider G., "Measurement of Weld Pool Size by Self Scanned Photodiode Arrays", Proc Int. Conf. on Low Light and Thermal Imaging Systems, IEE, London, 1975.
11. Shende V.A., "Linear Regression Modelling of GTAW for Developing a real-time Feedback Control", CWR Technical Report 529501/-82-4, Ohio State University, 1982.
12. Alexandrov N., Boillot J.P., Villemure D., "Régulation en temps réel du sondage à l'arc électrique", Report ISC-RC-88, The Welding Institute of Canada, July 1982.
13. Lukens W.E., Morris R.A., "Infrared temperature sensing of Cooling Rates for Arc Welding Control", Welding Journal, Vol 61 (1), pp. 27-33, 1982.
14. Chin B.A., Goodling J.S., Madsen N.H., "Infrared Thermography Shows Promise for Sensors in Robotic Welding", Robotics Today, Vol. 5, pp. 85-87, 1983.
15. Boillot J.P., Cielo P., Bégin G., Michel C., Lessard M., Fafard P., Villemure D., "Adaptive Welding by Fiber-Optic Thermographic Sensing: An Analysis of Thermal and Instrumental Considerations", accepted for publication in the Welding Journal in 1985.
16. Bégin G., Boillot J.P., "Welding Adaptive Functions Performed through Infrared (IR) Simplified Vision Schemes", Third Int. Conf. on Robot Vision and Sensory Controls, SPIE Vol 449, Cambridge Nov. 7-10, 1983.
17. Galopin M., Boridy E., "Experimentation assistée par ordinateur dans la recherche et le développement en soudage", CAD/CAM and Robotics 1984, Montréal, nov. 1984.

APPENDIX 1 - CHARACTERISTICS OF SRI SATURN CAMERA

Operating wavelength	830 nm
Field of view	10 mm x 10 mm
Depth of field	100 mm
Scanning frequency range	10 to 100 Hz
Laser power	20 mW
Maximum welding current tolerance	500 A
X and Y precision (at a range of 150 mm)	± 0,2 mm
Overall dimensions	100 x 60 x 60 mm
Overall weight	800 Gr

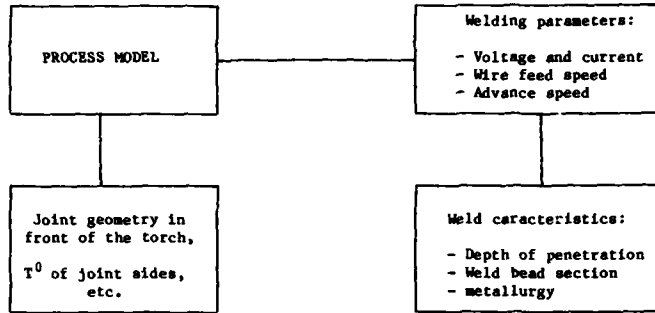


FIGURE 1 - Adaptive welding using an open loop strategy

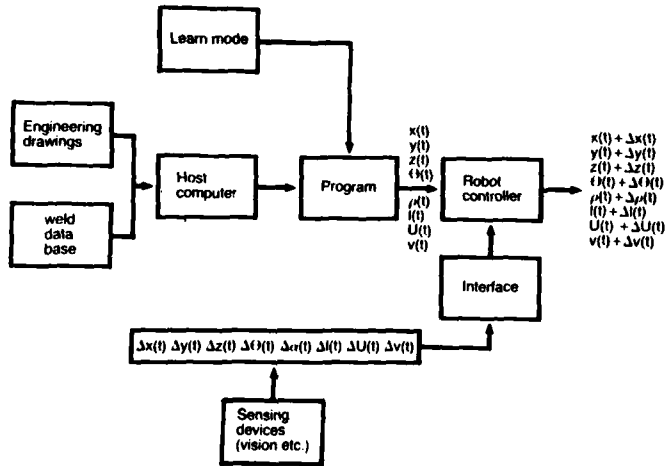


FIGURE 2 - Block diagram showing an ideal integrated automatic welding system.

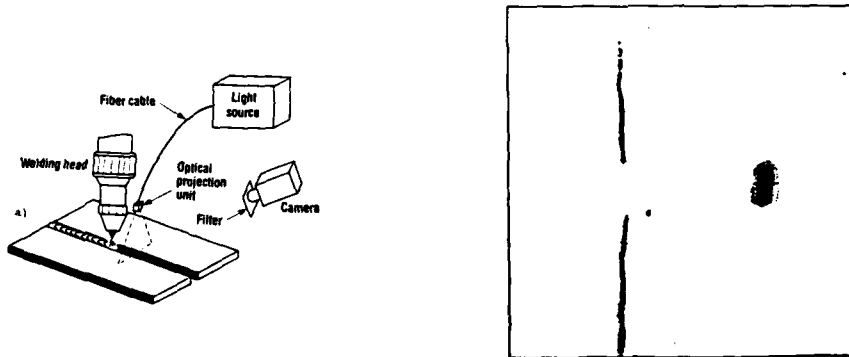
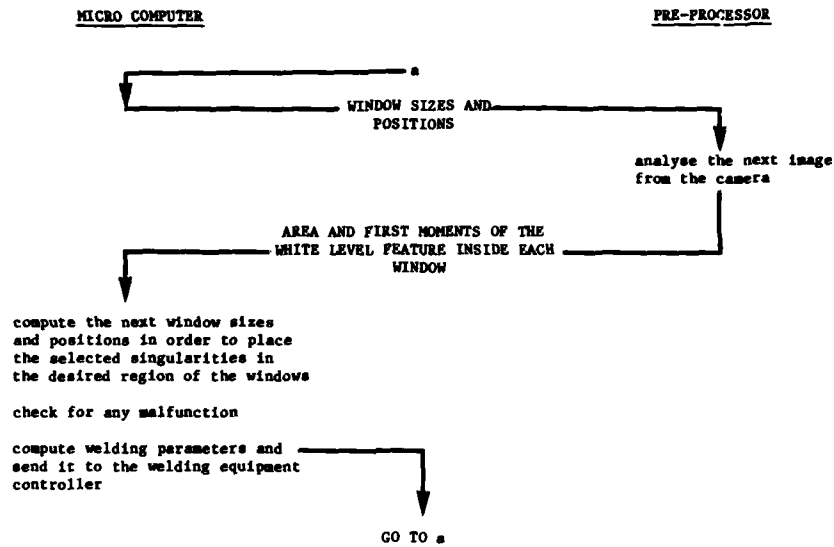


FIGURE 3 - Intersection of a laminar light beam with the spaced plates to be welded (a) and its image viewed from the camera displayed on a monitor (b)

COMPUTER AND PRE-PROCESSOR COMMUNICATION

BLOCK DIAGRAM



HARDWARE BLOCK DIAGRAM

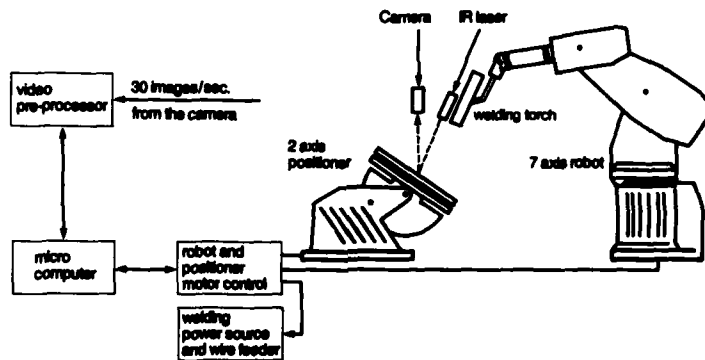


FIGURE 4 - Vision system based on the first moment technique.

- a Detector
- b Interference filter
- c Spherical lens
- d Small aperture in the plastic covered aluminum shield
- e Gaz flow direction
- f Aligned optic fibers
- g Cylindrical lens

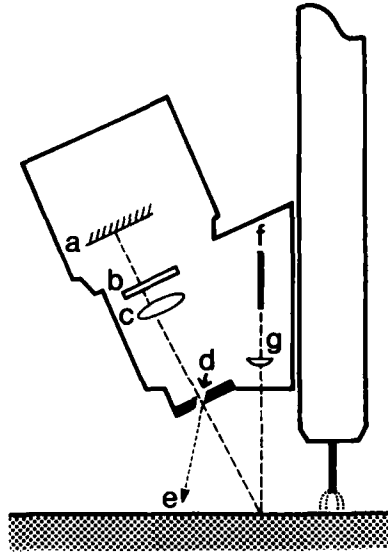


FIGURE 5 - Optic configuration of the vision system based on the first moment technique

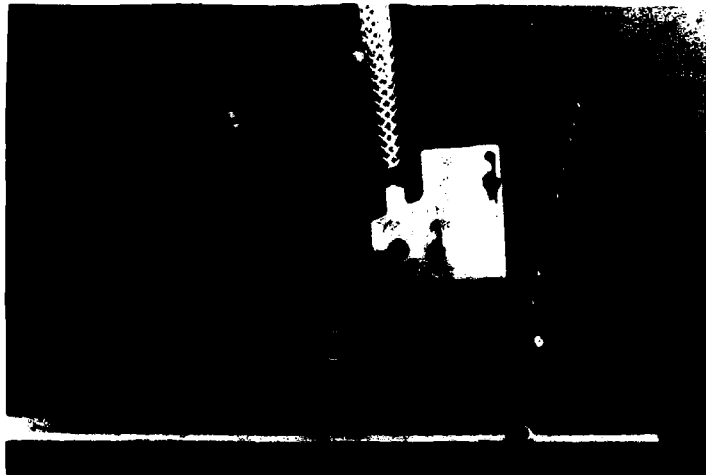


FIGURE 6 - Vision Head prototype of the system based on the first moment technique.

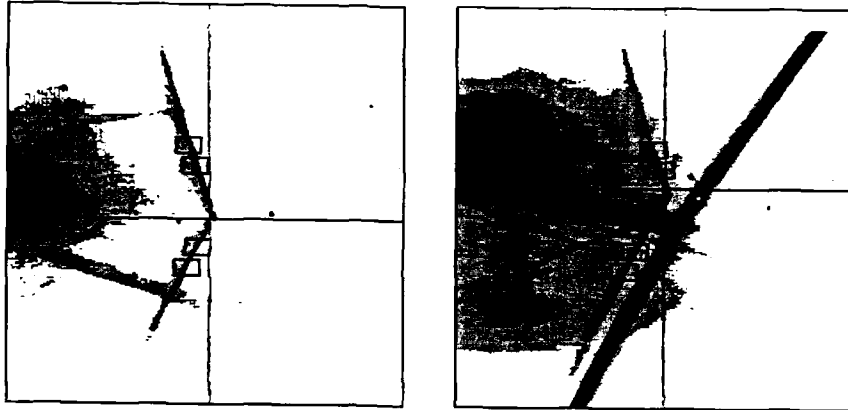


FIGURE 7 - Camera image of the intersection of the laminar light beam with the fillet joint. The rectangular window and the crossed hairs are superposed by the computer.

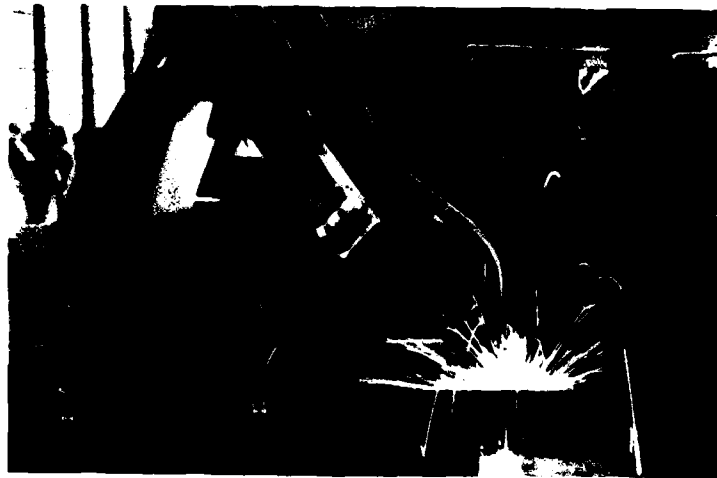


FIGURE 8 - The trajectory of a six axis robot is corrected (height and lateral position) while welding (GMAW) of fillet joint using the first moment vision system.

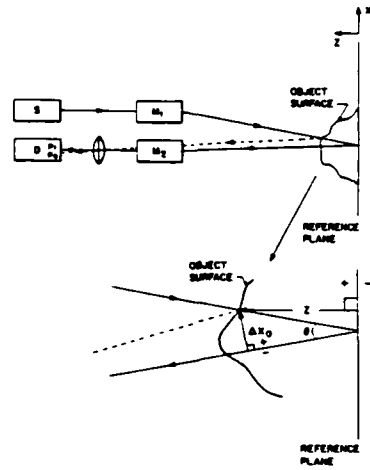
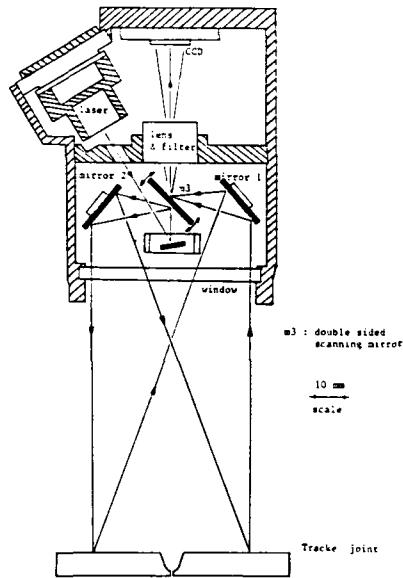


FIGURE 9 - Saturn Vision head from Servo-Robot Inc. is an example of geometrically synchronized scanner.

FIGURE 10 - Synchronized Geometry



FIGURE 11 - The Saturn camera is mounted on a six axis robot using a seventh axis to enable its rotation around the torch.

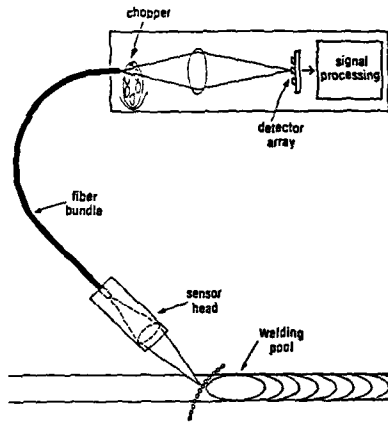


FIGURE 12 - Schematic view of the linear-array fiber-optic thermographic sensor.

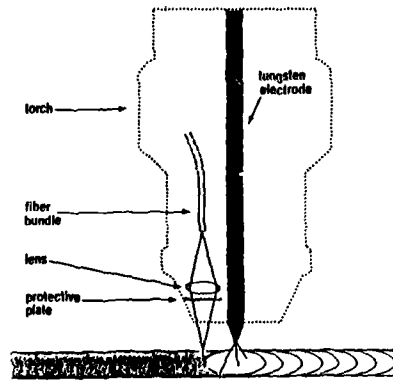


FIGURE 13 - Detail of the sensor head mounted inside the welding torch.

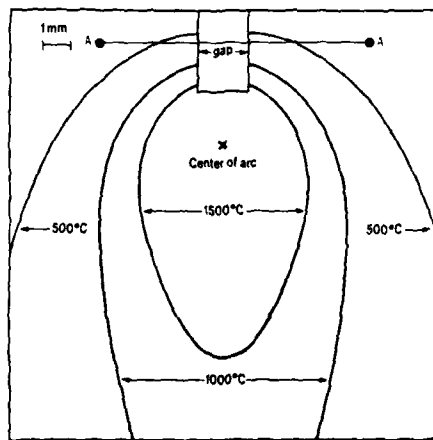


FIGURE 14a - Thermal distribution at the surface of the weld area as obtained from the numerical model (carbon steel, weld speed 2.6 mm/s).

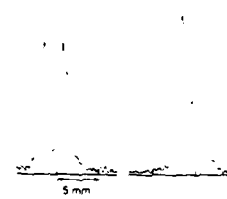


FIGURE 14b - Record of the emission profile during scanning ahead of the pool during a welding operation.



FIGURE 15 - Example of an irregular welding path followed by a GMAW head guided by a fiber-optic thermographic sensor, before and after welding.

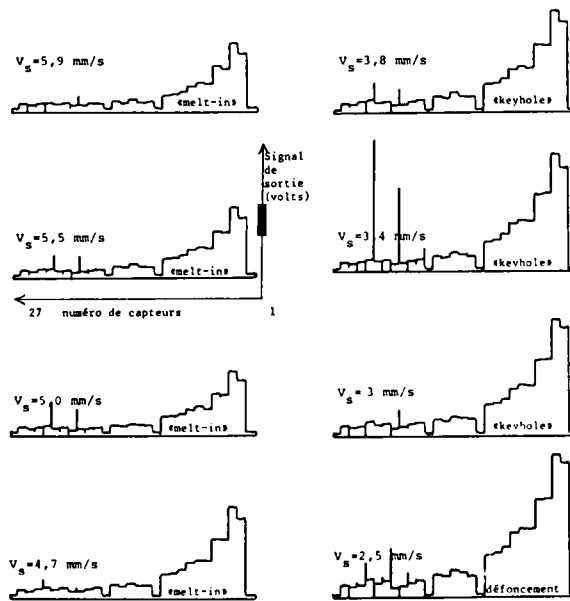


FIGURE 16 - Emission profile taken from far outside the weld pool created by a PAW torch up to the center. Material is Aluminum 6061-T 6.

INERTIA WELDING OF NITRALLOY "N" AND 18 NICKEL
MARAGING 250 GRADE STEELS FOR UTILIZATION IN
THE MAIN ROTOR DRIVE SHAFT FOR THE AH-64
MILITARY HELICOPTER PROGRAM

by

A.G. Hirko
Manager

Materials, Processes and Standards Department
and

L.L. Soffa

Metals Section Manager

Materials, Processes and Standards Department
Hughes Helicopters, Inc.

A Subsidiary of McDonnell Douglas

Centinela and Teale Streets

Culver City, California 90230

U.S.A.

SUMMARY

The study program conducted and presented in this technical publication was performed at the testing laboratories of Hughes Helicopters, Inc., Culver City, California. Preproduction feasibility studies were performed on laboratory type inertia welded specimens of Nitralloy "N" and 18 Nickel Maraging 250 Grade Steel prior to a full-scale engineering development program. The full-scale program consisted of producing scaled down drive shaft components to produce engineering test parts and to develop process control parameters for guide lines in the production program. Initial studies consisted of a metallurgical development program to arrive at a satisfactory post aging cycle for the composite or dual alloy drive shaft. In addition, metallurgical and static and dynamic tests were made from coupons excised from inertia-welded assemblies to establish structural behavior. Several sub-scale inertia-welded test specimens were tested in torsion loading to develop flight structural performance. Torsion tests on sub-scale inertia-welded components showed the inertia weld exhibited strength characteristics equal or better than the parent metal for the Nitralloy "N" alloy component. The improved two-alloy, inertia-welded components shows an approximate weight saving of 10 to 15 pounds over a drive shaft produced from Nitralloy "N". This is due to a higher strength/weight ratio of 18 Nickel Maraging 250 Grade Steel as compared to Nitralloy "N".

INTRODUCTION

Strength/weight improvement and enhanced performance characteristics are critical challenges to aerospace engineers in the rotary wing industry. Improvements can be in the form of using metallic or combinations of metallic materials or a substitution of composite (nonmetallic) materials and metallic alloys. Resulting weight reduction can provide improved payloads and efficiency.

The AH-64 military helicopter is a high technology, rotary wing aircraft whose mission provides:

- Day, night and adverse weather operations
- Multiple firepower options, long range target acquisition detection and destruction
- Precise navigation
- Improved combat survivability
- High reliability

The AH-64 has advanced state-of-the-art materials built into its systems and structures, including:

- High purity, high strength aluminum alloys (structural applications)
- Electroslag-refined, low alloy, high strength steels for ballistic and structural applications
- High performance with improved fracture toughness titanium alloys
- High strength, precision-rolled, corrosion-resistant alloys for rotor blade and special design structures

This presentation will review the engineering and manufacturing studies and the development program which preceded the implementation of the inertia welding of the three-piece drive shaft for the AH-64 production program. The early development program and the prototype aircraft, of which approximately seven aircraft were produced, had a

one-piece drive shaft. This component was produced from a forged billet approximately 7 inches in diameter by 60 inches in length. The alloy used is known as Nitralloy "N". This alloy contains aluminum and nickel in sufficient quantities to provide it with secondary hardening characteristics. One of its advantages over other nitriding grades of steel is its ability to minimize distortion during the nitriding cycle. The nitrided surface provides for excellent wear on the teeth and the pitch line of the gears.

Although nitriding is employed to produce a hard case on the teeth of the drive shaft, one of the most serious deficiencies that occurs during the nitriding process is a thin layer of nitride needles (white in color) that appear on the surface with sharp spikes. These spikes act as stress raisers. This white layer must be removed to preclude early failures of the teeth in service. The white layer is usually removed by machining or grinding methods.

OBJECTIVE

The purpose of this engineering test program was to develop metallurgical and fatigue data for inertia-welded Nitralloy "N" to 18 Nickel Maraging 250 Grade Steel, and to develop acceptable weld procedures for production of a higher strength, lower weight, main rotor drive shaft.

CONCLUSION

The results of this investigation are as follows:

1. Feasibility trials on miniature specimens for inertia welding the two alloys were successful.
2. A post-aging cycle was developed for the dual-alloy material that yielded excellent static and fatigue properties which could be used for a production hardware program.
3. Fatigue specimens excised from scaled-up inertia-welded test components produced excellent test results.
4. Full-section test specimens which simulated the production main rotor drive shaft were tested in torsion and exhibited excellent flight structural performance characteristics.
5. The inertia-welded, dual-alloy, torsion test specimens exhibited structural capability equal to or better than the parent metal for the Nitralloy "N" one-piece drive shaft.
6. Metallurgical examination of the inertia-welded material showed an excellent martensite conducive to good fatigue behavior after welding, with the supplemental heat treatment.
7. Microhardness tests performed on metallurgical specimens of the inertia-welded dual alloy material indicate good hardness recovery after the post welding aging cycle.
8. The inertia-welded main rotor drive shaft has been established as a reliable production process.
9. The three-piece drive shaft results in a weight savings that is critical to improved performance of the helicopter.

TEST PROCEDURE

The materials utilized for this experimental test program are as follows:

1. Nitralloy "N" procured to Specification HMS 6-1133.
- (a) Chemical composition:

Element	Minimum	Maximum
Carbon	0.21	0.26
Manganese	0.50	0.70
Silicon	0.20	0.40
Phosphorus		0.025
Sulfur		0.025
Chromium	1.00	1.25
Nickel	3.25	3.75
Molybdenum	0.20	0.30
Aluminum	1.10	1.40
Copper		0.35
Iron	Remainder	Remainder

(b) Chemistry of material:

C	Mn	P	S	Si	Ni	Cr	Mo	Cu	Al
0.25	0.61	0.010	0.002	0.39	3.29	1.19	0.26	0.05	1.12

(c) Room temperature static mechanical properties after aging (reference Table II HMS 6-1133):

P/N 7-113100094 Coupling, Drive Shaft Lower P/N 7-113100096 Coupling, Drive Shaft Upper	
Ultimate Tensile Strength Minimum	180,000 psi (1241 MPa)
Tensile Yield Strength Minimum	170,000 psi (1172 MPa)
Elongation 2 in. (51 mm) Percent Minimum	10
Reduction of Area Percent Minimum	40

(d) Static mechanical properties after full heat treatment including aging:

Ultimate Tensile Strength psi	192,000 193,500
Tensile Yield Strength psi	181,000 184,300
Elongation, Percent in 2 inches	16.1 15.3
Percent Reduction of Area	49.9 50.4

2. 18 Nickel Maraging 250 Grade Steel procured to Specification HMS 6-1080 (test material for center section, three-piece drive shaft).

(a) Chemical composition:

Element	Minimum	Maximum
Carbon		0.03
Nickel	17.0	19.0
Cobalt	7.0	8.50
Molybdenum	4.6	5.20
Titanium	0.30	0.50
Aluminum	0.05	0.15
Copper		0.50
Chromium		0.50
Manganese		0.10
Silicon		0.10
Phosphorus		0.010
Sulfur		0.010

(b) Chemical analysis:

C	Si	Mn	S	P	W	Cr	V	Mo	Co	Ni
0.014	0.04	0.05	0.009	0.007		0.21		4.83	8.28	18.38

Al	Ti	Cu	B	Zr	Ca	Ta	Nb	O ₂	N ₂	H ₂	Ppm
0.11	0.48	0.10	0.003	0.011	0.05 (Added)						

- (c) Mechanical properties after aging in accordance with HMS 6-1080 (4.0 to 10.0 in. (102.0 to 254.0 mm) in diameter):

Property	Long.	Trans.
Ultimate Tensile Strength ksi (MPa)	245 (1724)	245 (1724)
Ultimate Yield Strength ksi (MPa)	240 (1655)	240 (1655)
Elongation, Percent, 2 in. (51 mm) 4D	5.0	3.0
Percent Reduction in Area	30.0	20.0

- (d) Room temperature static mechanical properties:

Ultimate Tensile Strength	254,100 psi
Ultimate Yield Strength	247,400 psi
Elongation	6.0%
Reduction of Area	30.0%

PRELIMINARY INERTIA WELD TEST SPECIMENS

Six pre-trial inertia weld test specimens, one inch in diameter by four inches in length, were fabricated from Nitralloy "N" and heat treated to their full strength level.

Six additional specimens of the same configuration but made from 18 Nickel Maraging 250 Grade Steel were heat treated to their full strength level.

One each of the Nitralloy "N" fatigue specimens and one each of the 18 Nickel Maraging 250 Grade Steel test specimens were joined by inertia welding to evaluate the weld zone and to determine the static mechanical properties of the weld after post-aging at 975°F to restore the static strength after welding.

The results of static mechanical property tests that were excised from the inertia weld test specimens are shown below.

Specimen Number	Ultimate Tensile Strength	Tensile Yield Strength	Elongation, Percentage in 2 in.	Percent Reduction of Area
1	188,000	178,000	13.0	50
2	189,000	181,000	13.0	53
3	188,000	180,000	13.0	53

Microscopic examination and microhardness tests of the inertia-welded materials are shown in Figures 1 through 6.

Figure 1 shows the macrostructure of the inertia-welded test specimen.

Figure 2 shows the weld interface between the maraging steel and the Nitralloy "N". The dark etching zone is the Nitralloy "N" alloy. The lighter etching zones are areas that appear to have been less affected by heat from the weld process.

Figure 3 depicts the weld interface of the two alloys.

Figure 4 shows the heat affected zone of the Nitralloy "N".

Figure 5 shows the typical microstructure of Nitralloy "N" material. This alloy exhibits excellent martensite formation after the secondary aging or tempering operation.

Figure 6 shows the microstructure of the 18 Nickel Maraging 250 Grade Steel after aging to full strength.

SUMMARY OF METALLURGICAL EXAMINATION

1. No evidence of weld defects were observed in the cross section of the maraging steel/Nitralloy "N" inertia weld examined.
2. The Nitralloy "N" revealed a rehardened zone immediately adjacent to the weld interface and an overaged zone at the edge of the heat affected zone.
3. The heat affected zone on the maraging steel side was approximately twice as wide as the size of the heat affected zone on the Nitralloy "N" side.

Figure 7 illustrates the hardness traverse across the inertia weld. The hardness of the heat affected zone is indicated in addition to the parent metal hardness.

COUPON FATIGUE TESTS

Tubular material approximately three and one half inches in diameter with one quarter to three eighths of an inch in wall thickness and six to eight inches in length, of which one side was fabricated from Nitralloy "N" and heat treated to full strength and the opposite side was produced from 18 Nickel Maraging 250 Grade Steel that was aged to full strength, was inertially welded. Following the weld process, a post-aging cycle was employed, at two different temperatures, 925°F and 950°F.

Figure 8 illustrates the specimen geometry from a side view of the torsional load fatigue test. These tubular specimens were used to excise coupons for fatigue tests. Figure 9 illustrates the configuration of the fatigue specimen excised from inertia-welded torsional fatigue specimen. Figure 10 illustrates the test setup used to perform the fatigue tests on the inertia-welded test specimens. Figure 11 describes the results of the axial load fatigue tests as plotted in the form of an S/N curve (Stress/Life Diagram). This data is generated from specimens that were aged at two different temperatures, 925°F and 950°F. Figure 12 illustrates the weld trial specimen for establishment of the proper weld parameters. Figure 13 illustrates the inertia-welded, three-piece, main rotor drive shaft.

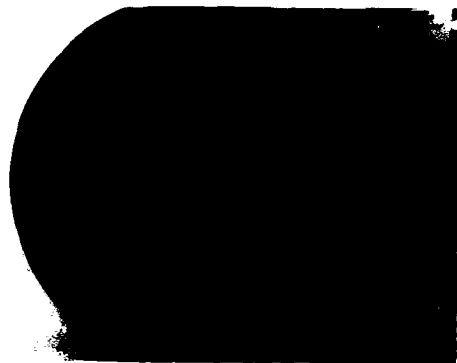


Figure 1. Inertia Weld. Macrophotograph of the weld between 18 Nickel Maraging 250 Grade Steel (right) and Nitralloy "N" (left). 2.9X, Nital Etch

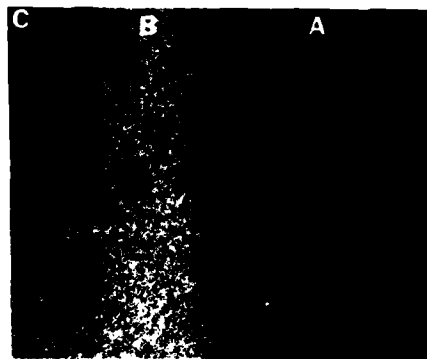


Figure 2. Weld Interface. Arrow indicates the weld interface between the maraging steel (right) and Nitralloy "N" (left). The Nitralloy "N" revealed a dark etching zone (A), a light etching zone (B), and an intermediate etching zone (C). 50X, Nital Etch



Figure 3. Weld Interface. "Fingers" of weld penetration between the Nitralloy "N" (left) and the maraging steel (right) were displayed. 1000X, Nital Etch

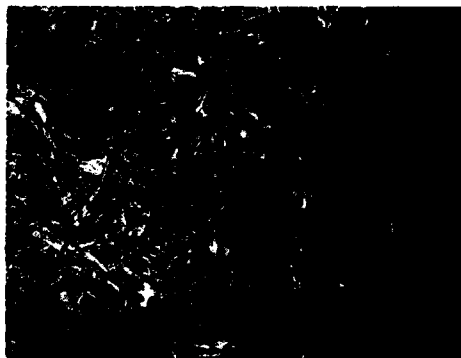


Figure 4. Nitralloy "N" Heat Affected Zone. Photomicrograph showing the microstructural differences between the dark and light etching zones of the heat affected zones of the Nitralloy "N" alloy. 400X, Nital Etch



Figure 5. Nitralloy "N". Typical microstructure of the Nitralloy "N" base metal. 400X, Nital Etch



Figure 6. Maraging Steel. Typical microstructure of the 18 Nickel Maraging Grade 250 Steel base metal. 400X, Nital Etch

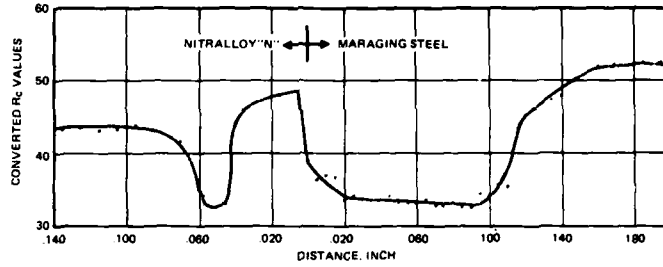
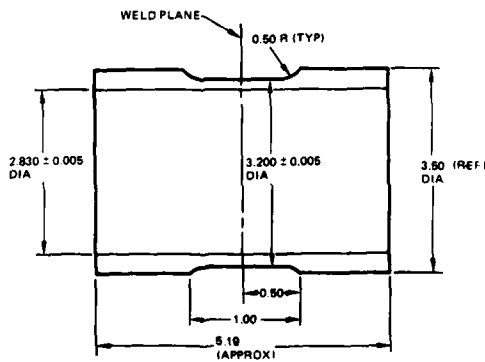


Figure 7. Plot of the Hardness Traverse Across the Inertia Weld Specimen Geometry



Weld Parameters

	3.50 inch dia.	5.250 inch dia.
Thrust	90,000 lbs	148,000 lbs
1st Stage Speed	1950 rpm	1300-1400 rpm
WK ²	418.5 lb-ft ²	1225 lb-ft ²
Upset after Weld	0.424 ± 0.020 inch	0.405

Figure 8. Torsional Load Fatigue Tests

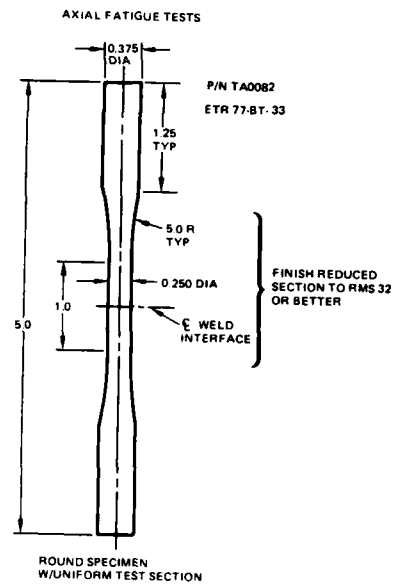


Figure 9. Fatigue Test Specimen (Axial Fatigue Tests)

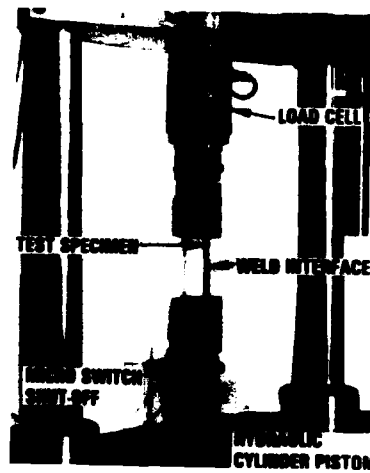


Figure 10. Test Specimen Installation, Inertia Weld Fatigue Test

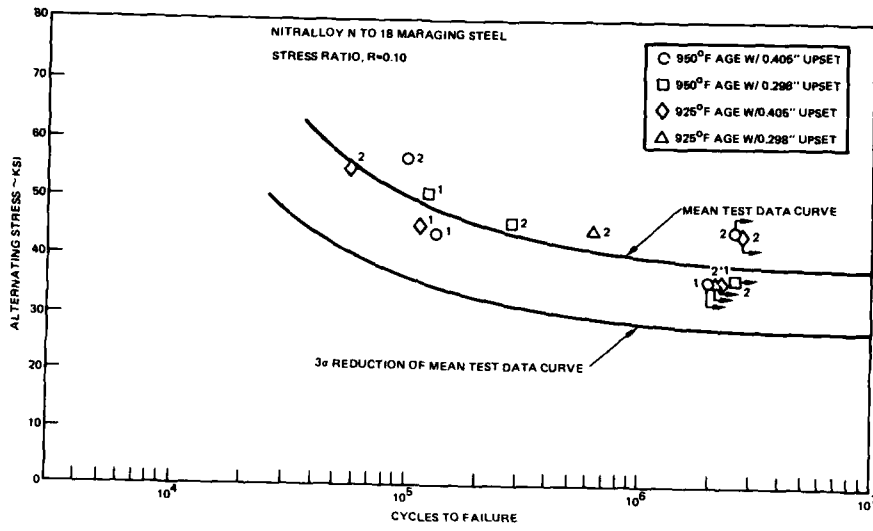


Figure 11. Fatigue Test Results for Round Test Specimens Excised from Inertia-Welded Tube Sections

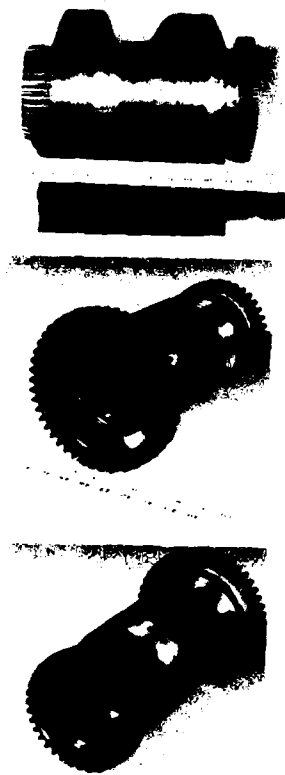


Figure 12. Weld Trial Specimen (Inertia-Welded, Main Rotor Three-Piece Drive Shaft)

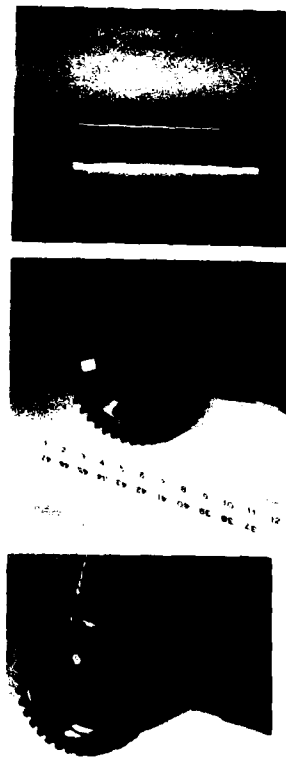


Figure 13. Inertia-Welded, Main Rotor Three-Piece Drive Shaft

DISCUSSION SUMMARY
SESSION IV REPAIR TECHNIQUES
BY
MARKO YANISHEVSKY
QUALITY ENGINEERING TEST ESTABLISHMENT
DEPARTMENT OF NATIONAL DEFENCE
OTTAWA, ONTARIO, CANADA
K1A 0K2

The objective of the fourth session of the Advanced Joining of Materials Specialist Meeting II was to examine state of the art repair techniques. Four papers were presented describing improved methods of joining metallic materials, measures for correcting inherent manufacturing defects, and techniques for repairing metallic material which has seen service-induced deterioration. Regrettably, the paper on "Healing of Fatigue Cracks in the Aircraft Steel 1.7734 by Repair Welding" was removed from the programme.

The first paper described a TIG Plasma Keyhole welding technique, for joining cast aluminum materials, being employed at Swiss Aluminum Ltd. To date this technique has exhibited particular effectiveness in eliminating cracking at the weld bead/parent metal interface in high copper content aluminum castings, which currently present formidable joining difficulties. With further development of TIG Plasma Keyhole welding, cast aluminum materials may foreseeably find use in high stress applications.

The remaining three papers addressed advanced repair techniques for damaged aircraft engine components. The described techniques themselves were all substantially different; however, they all shared a common concern which requires further development - effective cleaning of the surfaces to be joined.

The paper presented by J. Lesgourgues from SNECMA on "The Application of the Rechargement - Brasage - Diffusion (RBD) Process to the Deposition of Anti-Wear Alloys" was of particular interest. RBD is a novel process which allows repair of worn and damaged superalloy parts through the application of new surfaces via diffusion brazing. The procedure is simple in principle. Selected powders are blended together, and following chemical and thermochemical cleaning of the part in a fluoride atmosphere, these are applied to components in the form of powder transfer tape or via self-reservoir preforms. Several hundred of these preparations are then simultaneously put through a short thermal cycle in a vacuum furnace to complete the repair.

The discussion which followed the presentation addressed specific details about the powder blends used in the RBD process. The powders utilized in the RBD process can be modified for each application. They consist of a base metal, filler and special additives. The base metal is typically superalloy, though the exact chemical composition may be very different from the parent material. The filler metal used is typically nickel, silicon and boron, or nickel, chromium and boron. (Titanium, aluminum and tungsten affect the brazing stage and should be avoided). Specific additives are used to improve the chemical composition of the powder and to enhance melting at specific temperatures. Since elements that lower the melting point of the powder diffuse out during the thermal cycle, it is possible to use repaired components at temperatures higher than that required for the original melt. Through proper preform preparation, extensive extra machining can be avoided, adding to the simplicity and apparent economy of the process. In the discussion, HIPing was suggested as an added step to the process. SNECMA did not consider HIPing due to it being relatively expensive; moreover the RBD procedure as described appeared to adequately repair cast engine parts. The RBD process is available and is currently being employed by some repair firms.

A second technique that has shown promise for the repair of turbine engine materials is the Diffusion Densification Healing (DDH), presented by A.J.A. Mom from NLR. In this work both welding and DDH were evaluated for the repair of F100 turbine vanes. Conventional welding of the vanes was first attempted; however, it caused excessive microcracking in the heat affected zone and many convex cooling holes were being plugged with weld material. Of 157 weld-repaired vanes, 56 had to be scrapped. DDH was developed by Chromalloy Corporation to overcome this problem. During the discussion questions were posed addressing details of material preparation for DDH and the HIPing requirement. Preparation for DDH involves the removal of the vane coating (de-aluminization) gaseous fluoride cleaning for oxide removal, welding of large cracks, bonding of the remaining cracks with a superalloy bonding mixture, typically consisting of Inconel 6-2-5 base material with a filler, HIPing of the repaired part and finally recoating of the vane. HIPing was found to be particularly necessary to prevent coating delamination. The repaired vanes were tested under an elaborate simulation of service conditions in which the DDH repaired vanes performed substantially better than the conventionally weld repaired vanes.

The last paper of the session dealt with the repair of gas turbine compressor blades. Paul Lowden of Liburdi Engineering described a series of welding, diffusion brazing and vacuum plasma spraying techniques. Microcracking in the heat affected zone was prevalent in all of the techniques. To overcome some of these problems, it was recognized that the filler material must be properly matched with the parent metal and both pre and post weld treatments would be required to improve the performance of the parts.

From the presentations, it was evident that many problems remain unsolved. Discussions after the presentations centered on cleaning techniques, metal fillers and qualification of the repair techniques. Proper component preparation and cleaning were recognized as the key steps determining the effectiveness of a repair technique. Much more consideration is still necessary to improve this step in most repair processes. The preparation of metal fillers is also of great importance, since improper selection may render a given technique useless in specific applications. Some opinions were expressed on the use of HIPing to enhance already developed techniques. Finally, it was recognized that to fully qualify a technique, much more extensive testing under service type conditions must be performed to ensure the performance of the repaired components.

R4-2

Future AGARD Specialist Meetings on Advanced Joining of Materials could consider addressing the joining/fastening of hybrid materials i.e. metallic to composite and composite to composite. As well, the repair of composite materials is a rapidly growing area where much research and development efforts are being concentrated worldwide. All these subject areas could be reviewed in terms of available state-of-the-art processes, methods of inspection and necessary qualification techniques.

WELDING OF ALUMINIUM CASTINGS

by
 Dr. J. Leupp, Dr. A. Maitland and K. Schellenberg
 Materials Technology Department
 Swiss Aluminium Ltd. R+D
 CH-8212 Neuhausen am Rheinfall
 Switzerland

SUMMARY

Developments in the field of electronics have recently made available new methods and power sources which enable even the most difficult aluminium casting alloys to be welded economically. Each method has specific applications where it is optimally employed. The best results in fabrication welding are obtained with the TIG-PLASMA-KEYHOLE process. With this method the normal classification of casting alloys into those which weld easily and those which weld badly no longer applies. Excellent welds can be obtained for example with the high strength AlCu alloys. The flawless, fine grained weld bead provides mechanical properties equivalent to those of the parent metal - both under static and fatigue loading conditions.

The best results in finish and repair welding have been obtained using TIG welding with variable polarity. If due care is taken, this method also enables excellent results to be achieved under all types of loading conditions.

Examples where the described methods are successfully employed include not only aircraft constructions but also parts for railway vehicles and electrical switch-gear.

INTRODUCTION

Welded structures incorporating high strength aluminium casting alloys and having a favourable cost/property ratio would have excellent opportunities in the transportation field. The use of the correct welding technique to meet the high standards required there is, however, an important prerequisite for penetrating that market.

Two of the properties which diminish the weldability of aluminium in general are its high thermal conductivity and strong tendency to oxidise. Additional problems, due to the special characteristics of cast material are, however, encountered when welding castings. Solving these problems calls for considerable effort and expense - the magnitude of which depends of course on the demands to be made of the joint. If the castings only have to hold together then all casting alloys can be rated "easily weldable". If the requirements are higher than this e.g. specific mechanical properties, air tightness or surface finish, then the number of alloys that can be easily welded is reduced to only a few. The reasons for this are as follows:

1. No casting can ever be considered quite perfect and any imperfections at that stage can of course interfere considerably with the quality of the weld. Microporosity and occluded oxide for example can lead to pores, stringers and inclusions etc. in the weld bead.
2. Local differences in structure arise during the solidification of the casting with the result that low melting point constituents form in the interdendritic regions. Under the influence of the heat of welding these remelt and open up as cracks immediately next to the weld bead.
3. Very large temperature gradients exist during welding. Together with the shrinkage that occurs on solidification of the weld pool, these steep thermal gradients produce internal stresses immediately next to and in the weld bead. In some cases such stresses can exceed the tensile strength of the material; the result can then be thermal cracking and hot tearing of the weld bead due to the lack of metal feed to compensate for shrinkage.

High grade welds can be expected therefore only from a process which takes these problems into account.

TERMINOLOGY

The welding of casting alloys can be usefully divided into three groups:

Fabrication Welding

Welding together two castings which are integral parts of the final assembly.

Finish Welding (Repair Welding)

Eliminating flaws which have arisen during the production of a component (e.g. casting flaws, flaws produced during machining etc. of the component). In English speaking countries this is also known as repair welding. The nature of the flaw is,

however, usually quite different from the types of flaw arising in service (fracture, fatigue cracks). Also, the circumstances under which the flaw can be detected and the repair carried out are usually more favourable than those prevailing in service (familiarity with the part and alloy design criteria, expertise and equipment available) so that it seems appropriate to distinguish between production "corrections" and the higher-risk in-service repairs.

Repair Welding

Restoring a part which has been damaged in service so that it is again operational. This aspect is not dealt with in the present work.

Aluminium casting alloys for all three groups have come to be broadly subdivided - in terms of weldability - so that Si-containing alloys are considered readily weldable while Cu-containing alloys have only limited weldability. Of course this classification depends very much on the welding method used, and on the workpiece in question.

FABRICATION WELDING

If all the welding methods available today are compared for their technical and economic suitability for joining aluminium castings, then TIG-Plasma-Keyhole welding scores best. The joints made by this method are excellent in every respect viz.,

- largely free of pores and shrinkage cavities
- fine structure
- no adverse effects on the adjacent parent metal due to crack formation
- excellent mechanical properties under static and fatigue loading.

These characteristics are dealt with in greater detail below in connection with specific examples.

STRUCTURE

Plasma-Keyhole welding [1,2] is in principle controlled plasma cutting - with the difference that, instead of leaving a gap, a weld seam is formed. The plasma stream that penetrates the material creates an approx. 4 mm diameter hole which is present throughout the whole of the welding operation i.e. moving at a speed of about 15 cm/min. through the material. Behind the hole the molten filler metal flows into the gap under the forces of gravity, surface tension and the pressure of the inert gas. The result is a weld seam that exhibits excellent properties. The special way of creating the weld bead means that as a rule it is only possible to operate with the welding gun horizontal and the workpiece vertical.

The geometry of the resultant weld bead has a low notch profile i.e. the kind of notch effect caused by excessive filler material at the crown and root of the weld. The structure of the weld bead is very fine compared with that of the parent cast metal [3]. There is no porosity or shrinkage voids, and the transition from the parent metal to the weld bead - always a critical region - is also uniform and free of flaws.

MECHANICAL PROPERTIES

Static Loading

The high quality of the weld structure is reflected in the good values obtained by uniaxial tensile testing: test pieces stressed perpendicular to the direction of welding fractured far from the weld bead. By providing notches in the weld bead it was possible to induce fracture there. In that case e.g. with welded KO1 (G-AlCu4MgAgTi) artificially age hardened after welding (T6), a tensile strength of 515 MPa was obtained compared with 430 MPa in the parent metal. The fracture surface lay at 45° to the direction of loading, which indicates good ductility in the material. This combination of good ductility and high strength also results in an approx. 25 % improvement in fracture toughness at the middle of the weld seam compared with that of the parent metal (fig. 1). This means that the weld bead is able to arrest or at least slow-up cracks growing into it from the parent metal.

Fatigue Loading

When determining fatigue strength it is advisable not to use test pieces from very short welded lengths. The cooling conditions at such welds are not comparable with those in real structures, and the different internal stresses created could lead to wrong conclusions. For this reason a cast pipe-shaped component was designed to provide suitable test pieces [3]. The overall dimensions of that component were 1200x150x100 mm with a wall thickness of 8 mm. For fatigue testing this was divided longitudinally or transversely and then welded together again. After heat treatment the component was fatigue tested as whole on a 3 point bend type testing rig. The result is a very close simulation of practical conditions.

The purpose of these trials was to obtain for design purposes concrete information about the load-bearing capacity of the welded joint under fluctuating load conditions. As some dependence on alloy type was to be expected, three different, but typical alloys were welded (for mechanical properties see [4]).

Alloy B3 is in fact an experimental alloy containing about 4.5 % Cu and exhibiting good strength, ductility and toughness. The most striking result with that material was that the longitudinally welded pipes were able to withstand a higher load for the same number of cycles than the non-welded pipes (fig. 2). Pipes with transverse welds suffered no loss in performance. Similar results were obtained with the AlSi7Mg alloy A 356.

The performance of the well known, high strength alloy K01 (A 201, G-AlCu4MgAgTi) containing silver varied somewhat. The fatigue properties of the longitudinally welded pipe were the same as those of the non-welded pipe. Transversely welded lengths supported slightly lower loads, especially in the high load / low cycle range (fig. 3). K01 is not as tough as B3 therefore the notch effect of the transverse weld has a negative effect on the load bearing capacity of the former.

FABRICATION WELDING - CONCLUSIONS

The results obtained here show that TIG-Plasma-Keyhole welding yields excellent mechanical properties with high strength casting alloys. It is therefore conceivable that welded castings could be employed in highly stressed systems. The comparative ease of producing smaller individual parts means that such welded structures would offer significant cost savings over a much more complicated single casting.

It would be possible e.g. with alloy K01 which is difficult to cast, to manufacture assemblies which would be impossible to cast (or if so then only at the expense of a high reject rate). Furthermore, these results and experience from practical welding indicate that the original classification of alloys with respect to weldability is no longer valid. The Cu-containing alloys in general, and K01 in particular, are readily weldable, without problem. With the Si-containing casting alloys weld bead porosity can be a problem if optimum welding conditions are not observed exactly. In spite of that, these alloys can also be classified as readily weldable.

FINISH WELDING

This form of welding is most important in relation to difficult-to-cast parts. The difficulty in casting can be due to the alloy or to the size and shape of the part in question. The Cu-containing K01 alloy is an example of the first of these categories, SF-6 housings (which can be up to 2 m in height) an example of the second. Both categories have in common a large financial penalty if the part has to be scrapped because of relatively small flaws. In the extreme this could even determine whether a part can continue to be produced by the foundry. Only a widely accepted method for finish welding can be of help in such cases. At present finish welding is in fact an art which depends on the experience of the individual welder. Consequently each welding job is highly specific and does not easily fall into a series of categories or classification.

The most important parameters affecting finish welding are:

- Alloy composition
- Casting geometry (shape, wall thickness, stiffness)
- Condition (heat treatment)
- Requirements of the part and place to be corrected (air tightness, mechanical properties, surface finish)

Giving due regard to these aspects, the following parameters then have to be determined:

- Preheat temperature
- Filler metal
- Welding method

CRACK SUSCEPTIBILITY

In the following an attempt has been made to chart out the problem and an approach to solving it using a simple model for this purpose. Consider a model workpiece (fig. 4) featuring three different classes of crack susceptibility.

Class 1 means "highly susceptible to cracking", and applies to places where there are large differences in wall thickness and geometrically stiffened zones.

Class 2 (susceptible to cracking) refers mainly to flaws in the middle of a free surface.

Class 3 (less susceptible to cracking) applies to all edges.

The correct welding parameters can then be obtained from a set of tables. This is demonstrated by way of example for the alloy K01. Table 1a lists the preheating temperatures for the various crack susceptibility ratings and welding methods.

Examples

In practice this takes the following form. A component exhibited fine cracks in the K01 casting which had to be repaired. According to the model these belonged to crack susceptibility class 1. The table indicates that using the TIG square wave technique the part has to be preheated to at least 250°C. The welds made under these conditions were perfect in every respect and pass all relevant tests.

A second example involves a large housing made of the Si-rich alloy A 356 (G-AlSi7Mg) [5]. By error a threaded hole was made in the wrong place. The location of the flaw indicated a crack susceptibility of about class 2. This meant that the part could be put in order by using TIG DCSP He welding without any preheating (Tab. 1b).

FATIGUE LOADING CAPACITY

In the transportation field where the part has to withstand fluctuating loads the question quickly arises as to what loads such welds are capable of supporting. Only on the basis of this data and the distribution of the stresses in the part in service is it at all possible to judge whether finish welding is in fact permissible.

This point will receive increasingly more attention in our laboratories. Some initial results, however, are already available. The cast tube described above lends itself well for this purpose as flaws can be simulated in various places from the lowest stressed to the highest stressed regions. This enables a series of Wöhler curves to be obtained (fig. 5) or a particular type of repair weld and with that a good indication of the load bearing capacity of the repaired part under specific conditions.

FINISH WELDING - CONCLUSIONS

In conclusion it should be emphasised that establishing these fatigue strength values is an important aspect of a further reaching aim viz., to make finish welding a generally accepted method in product manufacture. To achieve that aim, it is most important that such investigations help establish suitable, systematic welding methods and procedures of the form mentioned at the start.

REFERENCES

- [1] M. Tomsic and S. Barhorst, "Keyhole Plasma Arc Welding of Aluminium with Variable Polarity Power", *Welding Journal*, Feb. 1984, p. 25-32.
- [2] A.C. Nunes, Jr., et.al., "The Variable Polarity Plasma Arc Welding Process: Its Application to the Space Shuttle External Tank", NASA Technical Memorandum 82532, June 1983.
- [3] J. Leupp: "Hochwertige Gusschweissungen mit dem TIG-Plasma-Stichlochverfahren", *Schweizer Aluminium Rundschau* 6 (1984), p. 6-10.
- [4] J. Leupp: "Das Bruchverhalten von Aluminium-Gusslegierungen", *Z. Material + Technik* 11 (1983) 1, p. 5-10.
- [5] J. Leupp: "Fertigungsschweissen von Werkstücken aus Aluminium-Gusslegierungen", *Schweizer Aluminium Rundschau* 2 (1985), p. 18-23.

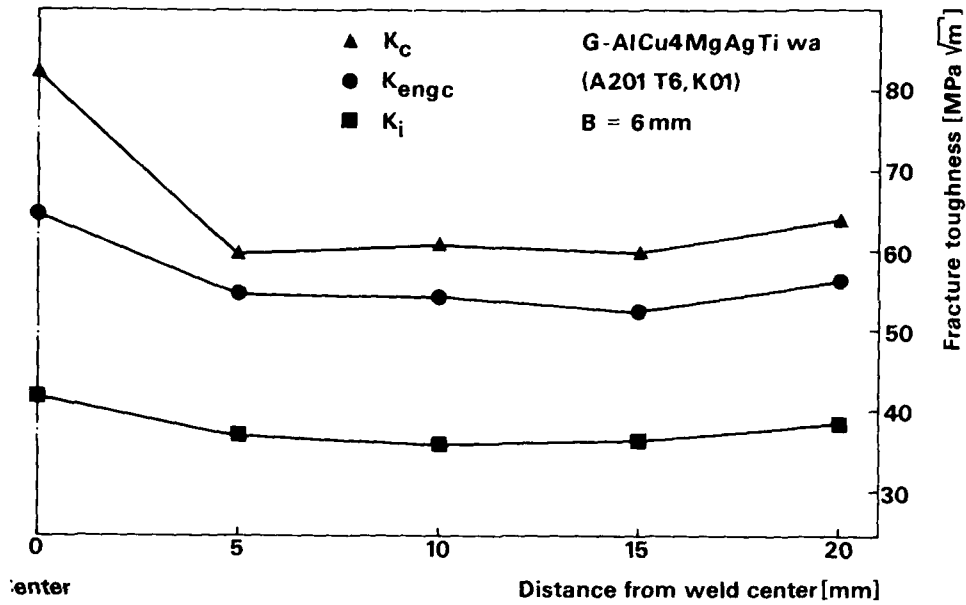


Fig. 1 Fracture toughness of a weld seam (K_C evaluated using maximum load P_{max} and actual crack length, K_{engc} : P_{max} and initial crack length, K_i with potential drop method)

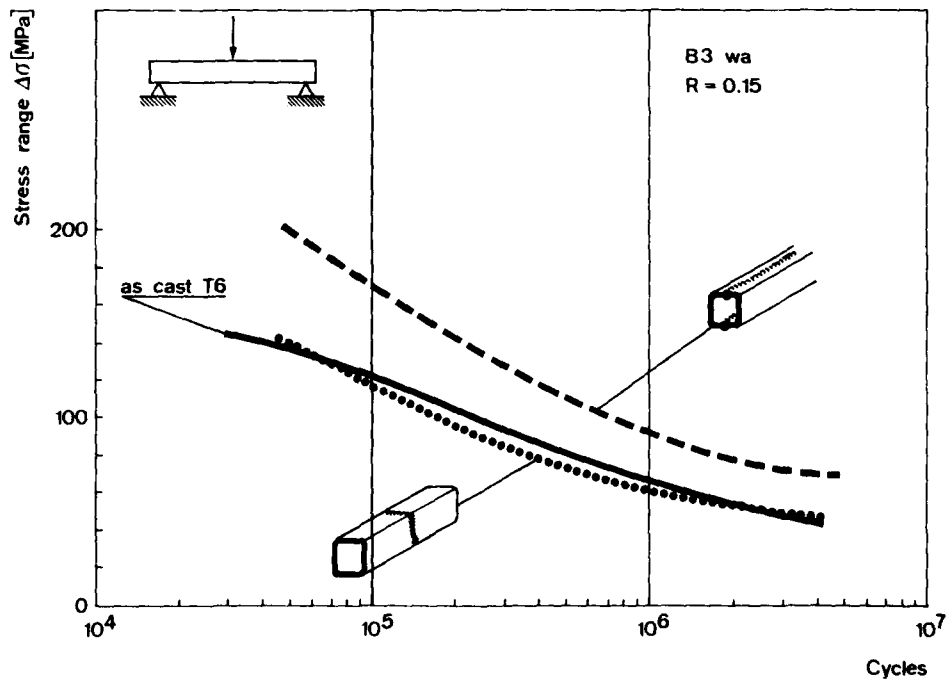


Fig. 2 S-N-curves for welded and unwelded tubes (alloy B3 T6)

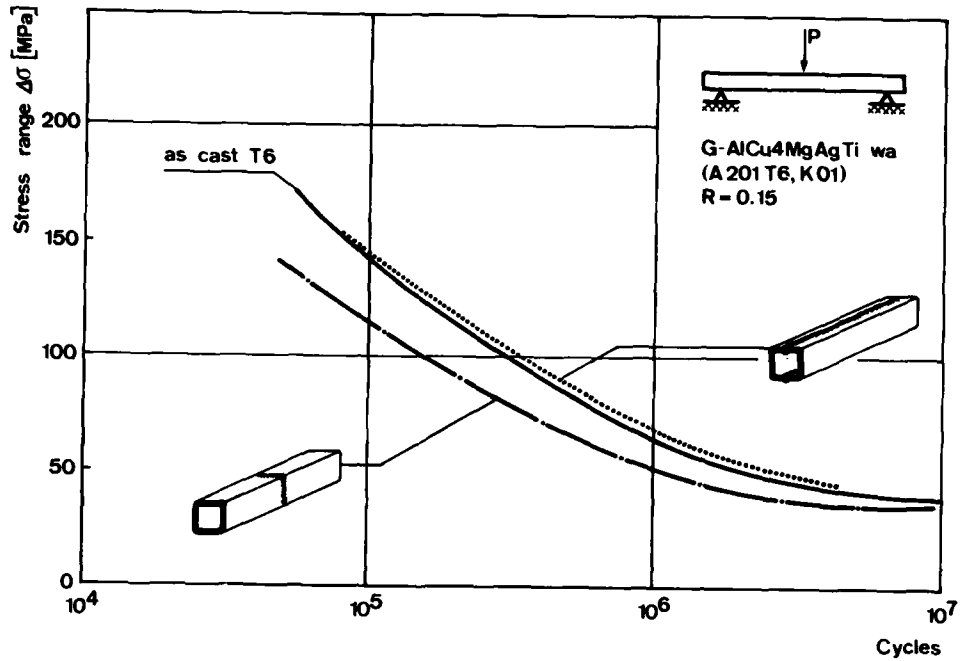


Fig. 3 S-N-curves for welded and unwelded tubes (alloy K01 T6)

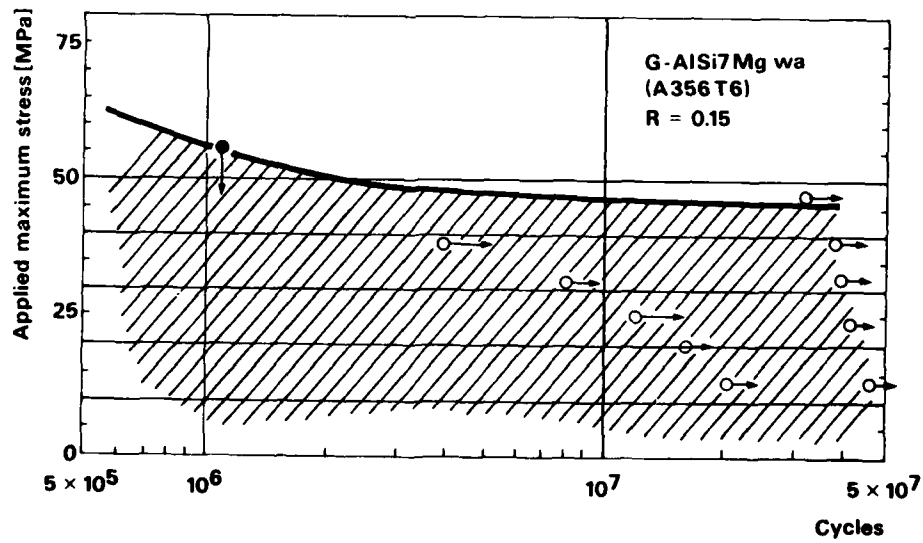
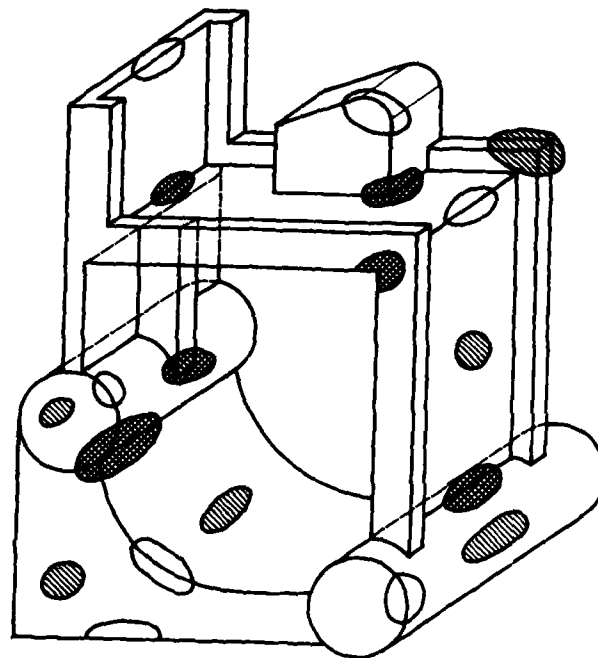


Fig. 5 Permissible maximum stresses as a function of lifetime for finish welded zones of crack susceptibility class 2 (A 356 T6, filler metal 4043)



-  **Class 1 : High susceptibility to cracking**
-  **Class 2 : Moderate susceptibility to cracking**
-  **Class 3 : Low susceptibility to cracking**

Fig. 4 Model component with zones for varying crack susceptibility

Alloy : G-AlCu4MgAgTi			
Welding method Susceptibility to cracking class	TIG DCSP	TIG Square wave	TIG
1	RT - 80 °C	250 °C	> 250 °C
2	RT - 50 °C	100 °C	> 100 °C
3	RT	RT - 50 °C	> 100 °C

Alloy : G-AlSi			
Welding method Susceptibility to cracking class	TIG DCSP	TIG Square wave	TIG
1	RT - 80 °C	100 °C	> 100 °C
2	RT	50 °C	> 50 °C
3	RT	RT	RT - 80 °C

Alloy : G-AlCu			
Welding method Susceptibility to cracking class	TIG DCSP	TIG Square wave	TIG
1	RT - 80 °C	100-200 °C	> 200 °C
2	RT - 50 °C	100 °C	> 100 °C
3	RT	RT	RT - 100 °C

Table 1a - c

Preheating temperatures for various crack susceptibility classes, welding processes and alloys (1a: K01 T6; 1b: AlSi-type; 1c: AlCu-type).

THE APPLICATION OF THE "RBD" PROCESS
TO THE DEPOSITION OF ANTI-WEAR ALLOYS

Par/by

J. LESGOURGUES

Laboratoire assemblages métallurgiques

SOCIÉTÉ NATIONALE D'ÉTUDES ET DE CONSTRUCTION DE MOTEURS D'AVIATION

2, Boulevard Victor - 75724 PARIS CEDEX 15

SUMMARY

Initially, the "Rechargement-Brasage-Diffusion" (RBD) * was developed by SNECMA to solve problems occurring during assembly and repair of cast superalloys turbine parts. Beyond the metallurgical possibilities it offers, this process has proved to be economical. Subsequent developments in this field have shown it was possible to apply alloys with specific characteristics, e.g. antiwear properties. This paper presents various applications of the RBD process, mainly in the field of wear protection.

1. INTRODUCTION

One of the purposes of metallurgy in the field of turbine engines is to develop and use more and more resistant materials at increasing temperatures. Unfortunately, although quite logically, the improvements made in the field of metallic alloys are bound with increasing difficulties in applying metallurgical assembly techniques.

This problem is particularly critical with cast superalloys :

- brazing, resulting in an heterogeneous bonding, does not provide satisfactory mechanical characteristics in most applications,
- fusion welding locally produces very high stress levels which the limited ductility of materials does not balance. A frequent and direct consequence is hot cracking.

This shortcoming of traditional techniques has been partially solved by the development of diffusion bonding processes, especially diffusion-brazing combining brazing technological simplicity with a good bonding quality.

To extend the limits of the first DFB processes (1) (2), a new category of techniques has been developed consisting in using prealloyed powders as filler metal.

The RBD process developed by SNECMA belongs to this category. Used alone or combined with DFB, RBD solved many problems of assembly or repair on superalloy turbine parts (3). Its economical interest gave the impulse to new studies to extend its use to coating and surfacing concurrently with traditional processes : TIG welding, plasma spraying or more recent techniques such as laser beam coating.

This work has shown that this process could solve various specific problems through the determination of the nature of prealloyed powders and of the thermal cycle. For instance, large size and accurate features can be produced or surfacing can be provided with specific properties such as antiwear resistance (4).

The purpose of this paper is to describe the RBD characteristics and applications, more particularly in relation to antiwear protection.

* "Rechargement-Brasage-Diffusion" (RBD) stands for coating or surfacing by diffusion-brazing.

2. RBD PRINCIPLE AND PROPERTIES

The principle of RBD consists in determining the nature and proportions of a prealloyed powder mixture capable of being sintered and brazed by applying a thermal cycle.

The RBD specificity lies in the determination of the mixture constituents including :

- a) a base powder which does not melt during the thermal cycle. It is chosen from well known superalloy grades (nickel or cobalt base). This powder, whose proportion in the mixture usually varies from 75 to 85 %, is the main element giving its final properties to the applied RBD material.
- b) a filler metal used to diffusion-braze the grains of the base powder and of the shape created on the part. Generally an alloy with a simple constitution is chosen. For instance, the simultaneous presence of Si-B and Cr, W, Mo (etc) elements is rejected in order to obtain satisfactory physical properties (capillarity, wettability, etc). Consequently the filler metal proportion in the mixture may be rather small ; it seldom exceeds 25 %. So the final proportion of Si and/or B in the applied metal is very low, which provides the following advantages :
 - . good ductility in the deposit
 - . limitation of the chemically affected area in the part metal, hence the possibility to multiply the number of interventions.
- c) specific additives, also in the form of powders, to adjust the chemical composition, if necessary, or give the alloy special properties.

Unlike other processes of the same category, the overall composition of the applied RBD material may be very different from the composition of the parts. This composition is always determined according to its own properties with regard to the intended application. Naturally it must be checked that there is no incompatibility.

Once the mixture is determined, a pre-operation is required in order to apply the material at the right place on the part. Generally, this operation consists in preparing a paste, a tape, a preform, etc.

The explanations given hereafter provide a good example of the possible preparations.

In general, the thermal cycle necessary for sintering and diffusion-brazing takes place in a vacuum furnace. The diffusion phase of the cycle does not change with the deposit shape or thickness ; it only depends on the grain size of the base powder.

For the commonly used superalloys, the temperature is comprised between 1100 and 1200°C with holding time of 15 minutes to several hours according to :

- a) the nature of the mixture constituents
- b) the properties required.

Moreover, the thermal cycle is determined in order to correspond to the heat treatments applied to the parts.

Through its flexibility, the RBD process offers the following advantages :

- a) varied and accurate geometry shapes can be produced :

Figure 1 illustrates the production of a boss on a part in Rene 77 ; figure 2 shows how a hole can be filled with a few tenths of a millimeter thick RBD skin.

- b) deposits with a thickness of one tenth of a millimeter to several centimeters can be obtained, with a hardness which may vary from HV 200 to nearly HV 1000,
- c) for some grades intended for this purpose, mechanical properties equivalent to those of many cast superalloys (3) can be achieved,
- d) hard facing coatings capable of receiving a thermochemical protection, such as the SNECMA APVS process (5), can be deposited,
- e) good antiwear properties : it has been shown (4) that results equivalent to those of some cobalt base superalloys can be obtained in the field of dry wear for temperatures ranging from 250 to more than 750°C.

FIG 1 : Production of a boss on a superalloy cast part.

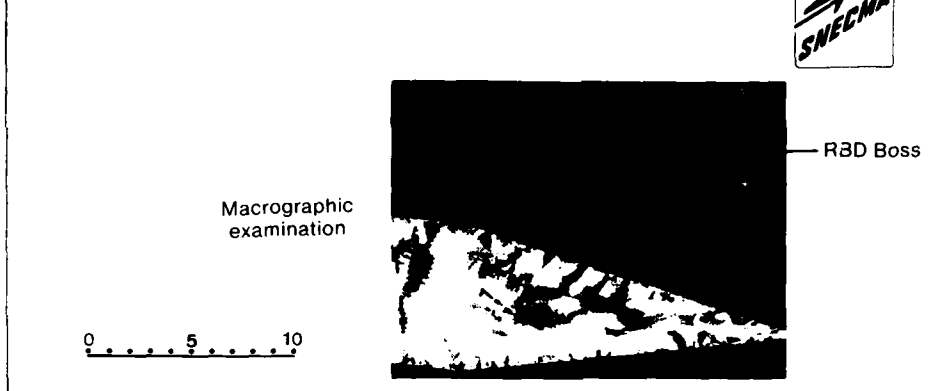
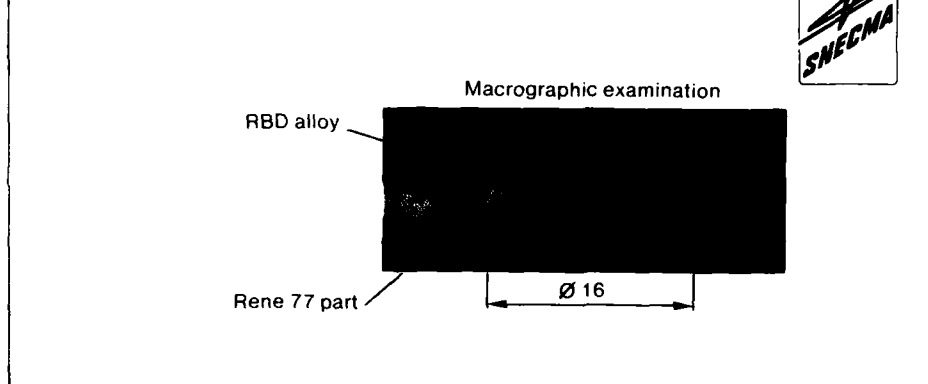
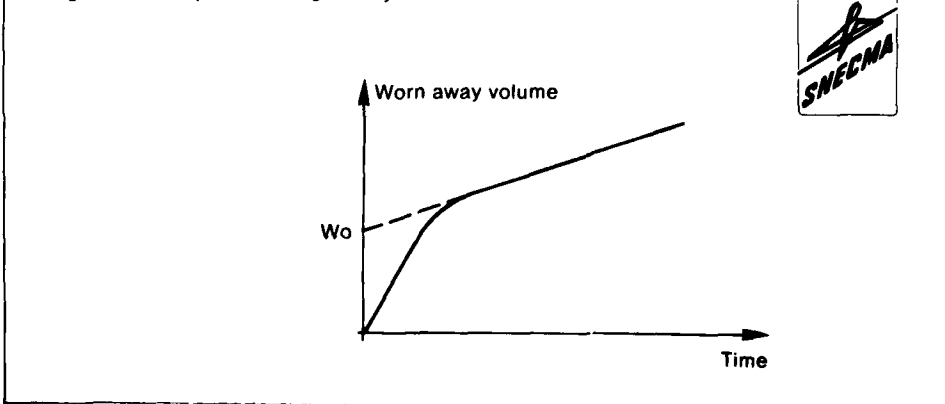


FIG 2 : Filling a hole.



The test carried out by SNECMA (4) (6) to evaluate the antiwear properties of a material consists in rubbing two samples one against the other in specific load, amplitude and temperature conditions. The volume of material worn away during the test is plotted versus time (see fig. 3). Since the parts in an engine are subjected to an extended range of temperatures at each cycle, a significant parameter to evaluate the quality of an alloy is the extrapolated initial wear value (W_0) against temperature.

Fig. 3 : Values plotted during the dry wear test.



The table below (Fig. 4) gives the W_0 value computed for some well known Co base alloys and, for comparison, the results with an RBD grade.

FIG 4 : Wear results.

. Initial wear W_0 in $\text{mm}^3 \times 10^{-3}$
 . Load 8 daN
 . Amplitude 2 mm.

Alloy *(deposited by TiC welding)	TEST TEMPERATURE - °C			
	20	250	400	750
HS 31 *	80	480	120	12
CM 64 *	110	500	2250	4
T 800 *	20	20	280	20
RBD 191 A	400	250	40	10



The values given in this table reveal differing characteristics :

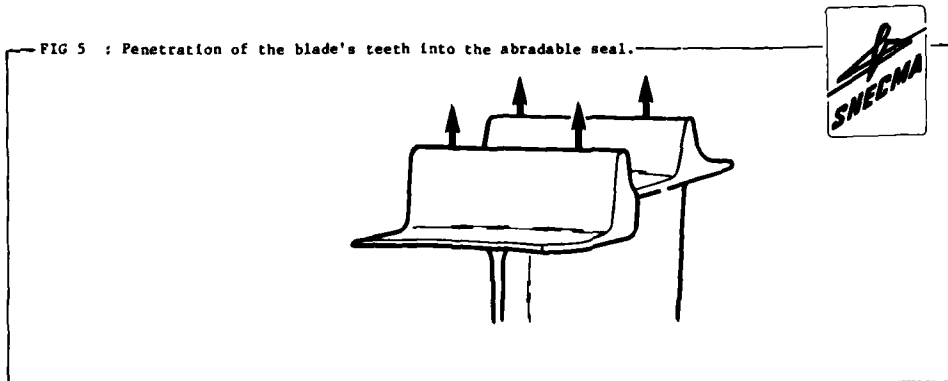
- CM 64 has a poor resistance at medium temperatures, but its behaviour is excellent at high temperatures,
- T800 is relatively good at all levels, particularly at low temperatures when compared with other materials,
- HS31 and RBD 191 A have a relatively poor resistance in cold conditions but are good at medium temperatures and very good at high temperatures.

The last characteristic is particularly interesting as far as parts in the engine are subjected to low temperatures for a very short time only. They normally operate at temperatures ranging from 350 to 900°C approximately.

3. RBD APPLIED TO SURFACING

3.1. TURBINE BLADE TEETH REPAIR

Turbine blade teeth wear is due to penetration in the abradable seal used to assure flowpath tightness (see Fig. 5).

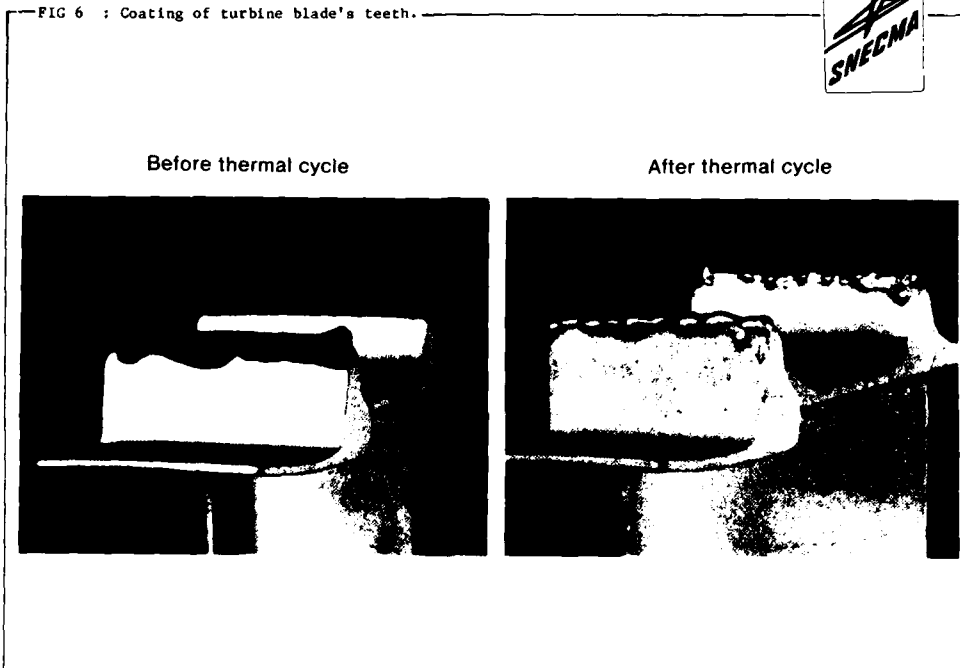


The currently applied repair process consists in carrying out a TIG welding on the tooth tips. This manual operation is rather expensive. Moreover, it is difficult to perform due to the poor weldability of the alloys.

The RBD application has been considered under the following sequence :

- chemical pickling of parts,
- RBD mixture application in the form of a paste with a syringe ; fig. 6 shows that three layers are enough to apply one millimeter approximately,
- thermal cycle corresponding to the solution heat treatment applicable to the alloy from which the parts are made,
- tooth machining.

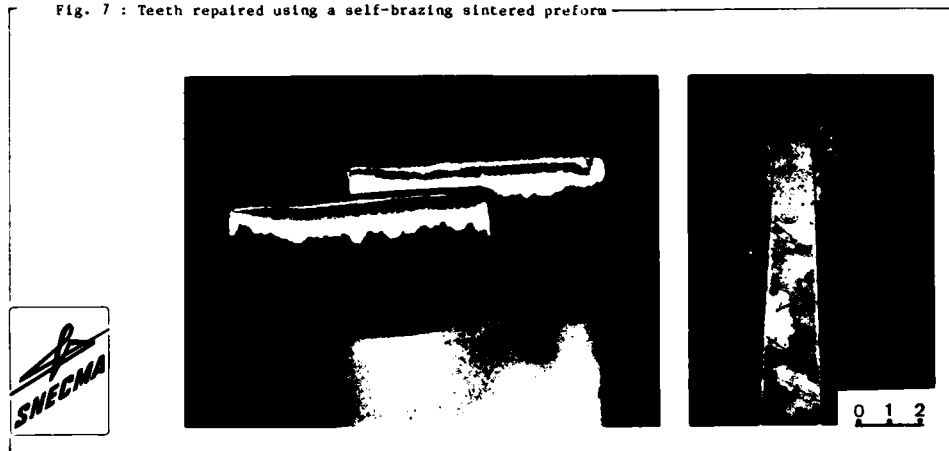
FIG 6 : Coating of turbine blade's teeth.



The nature of the alloy applied by the RBD process makes it possible to obtain characteristics in operation at least as good as with a new part or a TIG repaired part ; however the main advantage of this solution is its production cost. Since 600 parts may be processed simultaneously, the time required is less than one minute per part. The gain for the whole surfacing operation is more than 50 % of the cost of the process presently applied.

This process may also be applied using a sintered preform, more expensive than the application with a syringe but easier to introduce in production. The results obtained with a preform are illustrated in Fig. 7.

Fig. 7 : Teeth repaired using a self-brazing sintered preform



3.2. HARDENING OF BLADE SHROUD CONTACT SURFACES

This operation, extensively described in ref. (4) consists in applying an alloy withstanding dry wear on blade shroud contact surfaces.

The application of the technique used today, i.e. manual TIG welding, is very difficult and expensive. As a matter of fact, a cobalt-base alloy must be applied, whose melting temperature is higher than that of the nickel-base alloy from which the parts are made (NKLSCADT), without melting the surface of the part to avoid hot cracking and dilution of the hardening alloy, while nevertheless assuring a sufficient bonding on a surface of a few square millimeters.

The other methods considered to replace TIG welding include plasma spraying, laser beam deposition and RBD.

Plasma spraying is badly adapted to this application. The small surface and the arrangement of the area to be faced cause a loss more than 90 % of the sprayed powder, the benefit of the full automatization being completely lost.

Laser beam surfacing brings a substantial gain through a total automatization, a less important quantity of material to be applied and less machining after coating (5). However :

- the implementation is difficult, particularly the feed of filler metal.
- The investment is important, approximately five to six million francs per unit. The fact that a large-scale production may require the acquisition of several machines has an aggravating effect. For instance, with 1 min 30 per blade, the production of 200 000 parts per year represents 5 000 hours of machine use.

RBD may be applied in two different ways depending on how the mixture is applied :

- a) application of a tape (Fig. 8), an economical solution but a thick deposit cannot be obtained,
- b) resistance welding of a sintered RBD preform (Fig. 9).

FIG 8 : Thin coating obtained by means of a tape.

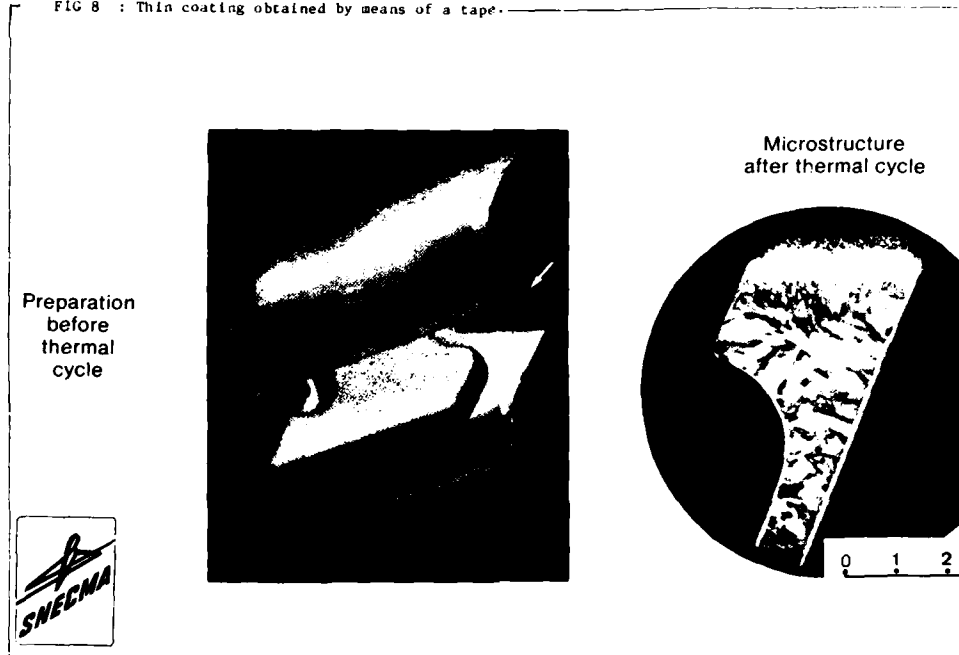
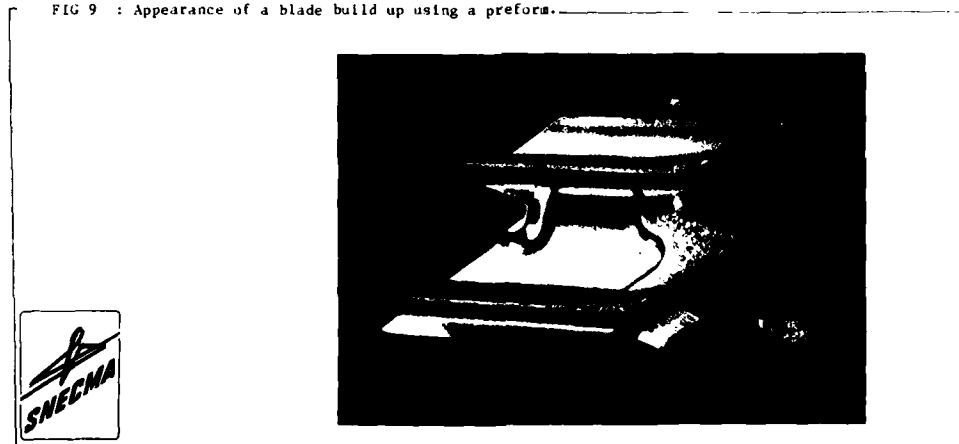


FIG 9 : Appearance of a blade build up using a preforma.



In both cases :

- 1) the RBD thermal cycle exactly corresponds to the part final heat treatment, i.e. coating is carried out at no additional cost at the same time as the heat treatment,
- 2) deposits are almost to finished dimensions, which eliminates the need for expensive machining operations after coating.

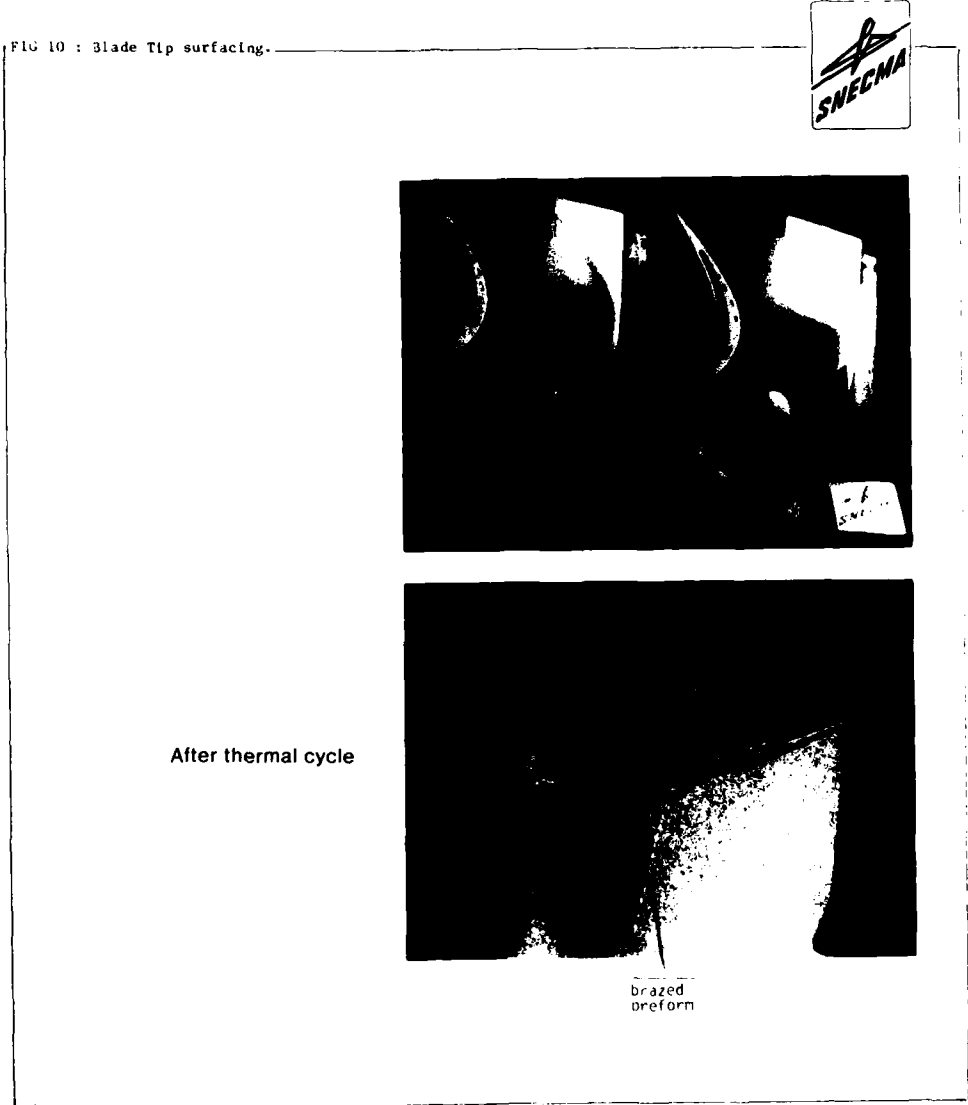
With regard to the required equipment, and using the same example as previously :

- a) the investment is the same as for a conventional vacuum furnace, approximately three million francs,
- b) the production of 200 000 parts by batches of 600 parts requires about 3 500 hours of machine operation.

It should also be noted that this process may be applied on new parts as well as at the repair stage.

3.3. BLADE TIP HARD FACING

Surfacing of blade tips worn in operation is identical to tooth hard facing (para. 3.1.). However the implementation is more difficult due to a more complex geometry and thinner walls. Photographs of Fig. 10 show a hard faced test piece.



3.4. HOLE SALVAGING

Surfacing of hole internal surface may be necessary :

- on a new part, in case of machining errors,
- on a part worn in operation.

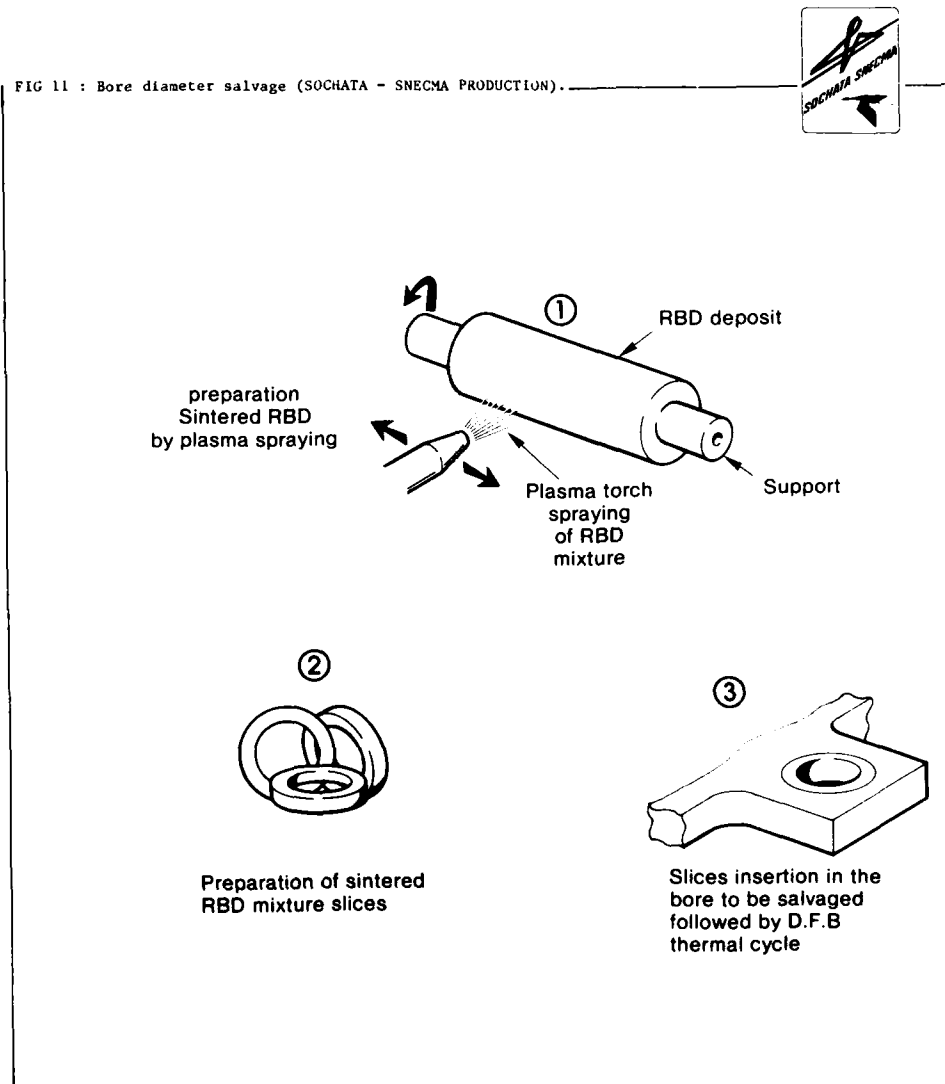
An operating procedure has been developed which consists in manufacturing a self-brazing ring in sintered RBD mixture, inserting it in the hole to be salvaged and then applying the diffusion-brazing thermal cycle.

The specificity of this technique illustrated by Fig. 11 lies in the production of the sintered ring.

The constituents of the RBD mixture are plasma-sprayed on a support until the deposit is 1 mm thick.

The outer part of the rod obtained is ground, still using the support, to the dimension required to allow insertion in the hole. Slices are then cut from the rod, and the support is subsequently eliminated by a chemical process.

FIG 11 : Bore diameter salvage (SOCHATA - SNECMA PRODUCTION).



3.5. CASE REPAIR AND SURFACING

This application is not relevant to antiwear problems. However it has been chosen to illustrate the possibility of surfacing large-size, thin sheet metal parts at the repair stage.

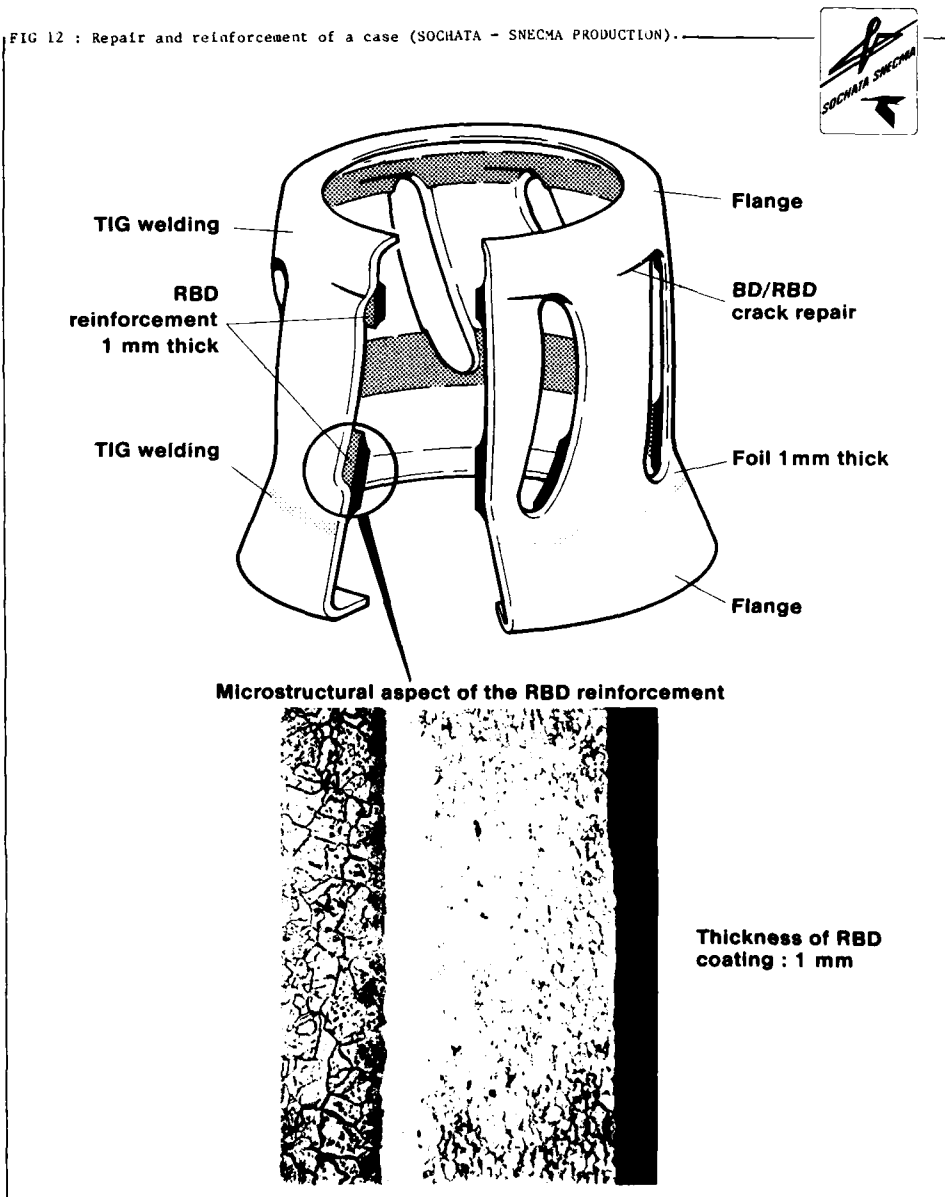
The casing (see Fig. 12) whose central section consists in a 1 mm thick metal sheet presented a local weakness resulting in fatigue cracks during service.

The operation, therefore, consisted in repairing the existing cracks and locally doubling the metal sheet thickness to strengthen the part. This was nearly impossible to perform by welding due to the tight tolerances, especially on the coupling flanges.

In addition to the now conventional repair by the DFB/RBD process (see examples in ref. (3)) it was possible to apply an alloy ring more resistant than the alloy of the casing using the RBD process. To obtain a deposit with a uniform geometry, the powder mixture was plasma sprayed before the diffusion-brazing cycle (see Fig. 12).

Various RBD material grades may be used to carry out this type of surfacing on parts and surfaces of all dimensions.

FIG 12 : Repair and reinforcement of a case (SOCHATA - SNECMA PRODUCTION).



4. CONCLUSION

The purpose of this paper was to explain the possibilities of the RBD process in the field of surfacing, more particularly with regard to antiwear protection.

The few examples given have illustrated the wide range of possible applications, from hole filling with a few tenths of a millimeter thick skin to the surfacing of a sheet metal casing, with, in all cases, the possibility to provide the surfacing material with specific characteristics.

In the field of antiwear protection, the main advantage of the RBD process is its economical aspect due to the fact that the coating operation and the part heat treatments may be performed simultaneously and a great number of parts may be processed simultaneously.

Finally, it should be noted that the RBD industrial application does not give rise to major problems, as some other new techniques would have. This mainly comes from the fact that we benefit from a long experience in the field of vacuum brazing.

5. REMERCIEMENTS

L'auteur tient à adresser ses plus vifs remerciements à tous les membres des services qui l'ont aidé dans la réalisation des travaux de cette présentation et tout particulièrement à la Sochata-SNECMA pour leur contribution, notamment dans le domaine de la projection par plasma.

6. REFERENCES

- (1) GS HOPPIN III, TF BERRY, Activated Diffusion Bonding WELDING JOURNAL, II, November 1970, pp 505a - 509a.
- (2) DS DUVALL, W.A. OWCZARSKI, T.L.P.R Bonding, WELDING JOURNAL, 4, April 1974, pp 203 - 214.
- (3) Y. HONNORAT - J. LESGOURGUES, Turbine Stator Parts Repair by Diffusion Brazing.
AGARD Specialist Meeting, Maintenance in Service of High Temperature Parts, CP n° 317, pp 9-1 - 9-12.
- (4) J. LESGOURGES, Deposition of anti-wear alloys on turbomachine parts by the RBD process, First International Conference on Surface Engineering (SES - WI), Brighton England, 25 - 28 June 85, pp 39-1 - 39-21.
- (5) G. GAUJE, R. MORBIOLI, Vapor Phase Aluminizing to protect Turbine Airfoils, 1983 Annual Meeting of the Metallurgical Society of AIME, Conference Proceedings SUBHASH C. SINGHAL, pp 13 - 26.
- (6) J. THIERRY - R. SPINAT, Comment réduire l'usure des pièces non lubrifiées dans les turbomachines. AGARD Specialist Meeting, Fretting in Aircraft Systems CP n° 161.

EVALUATION OF DDH AND WELD REPAIRED F100
TURBINE VANES UNDER SIMULATED SERVICE CONDITIONS

A.J.A. Mom¹⁾, N.M. Madhava²⁾, G.A. Kool¹⁾ and M. Dean³⁾

- 1) National Aerospace Laboratory NLR
Anthony Fokkerweg 2, 1059 CM Amsterdam
The Netherlands
- 2) Chromalloy Division Oklahoma,
1720 National Boulevard, Mid West City, Oklahoma
USA
- 3) Turbine Support Europa
Siriusstraat 55, Tilburg
The Netherlands

SUMMARY

Cost and delivery times of high technology turbine components are a strong impetus for the development of advanced repair processes with the ability of complete restoration of unserviceable components. One of such advanced processes, diffusion densification healing (DDH), was applied for repair of cracked and unserviceable F100 turbine vanes. The DDH process was evaluated under simulated service test conditions with respect to the conventional weld/patch coat repair procedure.

The evaluation shows that the DDH process is a remarkably effective restoration process, resulting in strongly improved test behaviour in relation to the original weld/patch coat procedure.

Additional advantages are that scrap rates during repair are likely to be considerably reduced and that for the future some relaxation of current repair limits might even be considered.

1. INTRODUCTION

The advanced jet engine component designs and materials that were introduced in the mid-sixties provided the impetus for new and demanding challenges for the coating and repair of engine components. Present engine components are extremely expensive and replacement delivery times may also be very long. In this respect it is not unusual that repair processes are developed which are able to refurbish unserviceable parts at moderate cost and within acceptable time limits. One of those new repair processes is diffusion densification healing (DDH), a process which was developed by the Chromalloy Corporation. This paper describes the application of this process on a number of unserviceable F100 first stage turbine vanes, delivered by the Royal Netherlands Air Force, and the subsequent evaluation of the repair process by simulated service testing at the NLR facilities. The DDH repair process was compared with the original weld repair process.

2. BACKGROUND OF THE F100 VANE REPAIR

The F100 first stage vane, which comprises two integrally cast airfoils, is a complex cored configuration, cast from PWA 1422 (DS Mar-M 200 + HF), a high strength, directionally solidified (DS) nickel-base superalloy. The earliest attempts (late 70's/early 80's) to repair the vane involved totally removing both vanes from the doublet and bonding new DS vanes to the inner and outer buttresses using the transient liquid phase (TLP) bonding process [1]. However, the high cost and complexity of this repair, combined with poor engine test results, initiated a search for a higher integrity, lower cost repair. The first approach (currently the only PWA/USAF approved repair) involved welding of cracks with MERL 72 (a cobalt-base alloy) and patch coating with Sermaloy J. The weld/patch coat approach, however, suffers from many process limitations and technical problems. These process/problem areas include:

1. To effectively weld PWA 1422 a pre-weld high temperature heat treatment is required and must be combined with HIP to inhibit coating degradation and/or delamination. If delamination does occur the part is scrap.
2. Welding of advanced superalloy materials such as PWA 1422 with a weld material such as MERL 72 is extremely difficult. Excessive heat input and thermal cycling frequently result in heat affected zone cracking, micro-cracking and distortion.
3. Welding of the row of cooling holes on the convex vane surface (required as part of the repair and modification process) frequently results in limited penetration and cracking along the DS grain boundaries.
4. After the weld repair numerous small and even some large cracks remain and are not repaired. These cracks lead to both coating and substrate degradation and can result in premature vane failure during engine service.
5. The patch coating on the cobalt base MERL 72, weld-repaired areas and on the engine-run coating on the remainder of the vane is not as environmentally resistant as freshly applied PWA 73 coating.
6. Because of the inherent technical problems and process limitations the yield of the weld/patch coat repair is low in terms of parts actually salvaged.

The latter point is illustrated in table 1 which shows for a random batch of vanes a high rejection rate which can be attributed to the weld repair process. It was expected that application of the DDH process could greatly reduce the scrap rate by reduction or elimination of welding and hence reducing heat affected zone cracking and part distortion. In the following the background of the DDH process and its application on F100 vanes is presented.

3. DIFFUSION DENSIFICATION HEALING (DDH)

3.1. The DDH process comprises the following steps

1. Component (and cracks) cleaning: all cracks are cleaned using a gaseous fluoride reducing atmosphere to remove service induced oxides.
2. Crack bonding: large cracks (i.e. in excess of 0.25 mm wide) are welded with a base alloy compatible weld material. All other cracks and cracks emanating from the welds are bonded and/or sealed using specially designed bonding material mixtures. At the bonding temperature the bonding mixture melts, diffuses and resolidifies, filling or sealing the cracks and repaired regions with a cast superalloy type composition.
3. Hot isostatic pressing (HIP): HIP densifies and further homogenizes the repaired areas.

The process results in a dense, high integrity repaired region with physical and metallurgical properties approaching those of the base alloy. The process has been developed for a variety of hot section components consisting of various superalloys like B-1900, IN 738, IN 713, René 80, X-40, Mar-M 509 and, now, PWA 1422.

3.2. DDH application on F100 turbine vanes

The DDH process has now been applied to the repair and modification of F100 first stage turbine vanes. DDH bonding alloys and process parameters for PWA 1422 were developed and procedures for the repair and modification were defined.

It turned out that by using the DDH process the problems encountered with the weld/patch coat process could be greatly eliminated. No coating degradation occurs because all relevant high temperature heat treatments, including HIP, are carried out on a dealuminized component and the coating is reapplied after full restoration of the vane. With the DDH process all cracks are thoroughly healed and bonded. Welding is conducted with Ni-base welding wire which is compatible with the base material and the coating. The row of cooling holes on the convex airfoil surface, which have to be closed as part of the modification, are bonded instead of plug welded, thereby eliminating cracking and assuring adequate penetration. In addition, the entire component is hot isostatically pressed to fully densify and homogenize both the welded and bonded regions. This is unlike the weld repair process, for which the HIP treatment is done before welding and repair. Lastly, the yield of the DDH process is significantly improved with respect to the weld/patch coat repair process.

Figure 1 shows several stages of the DDH repair process as conducted on an F100 first stage vane.

4. THE EVALUATION TESTING PROGRAMME

Because of the apparent advantages of the DDH process over the weld repair process the Royal Netherlands Air Force decided to perform an evaluation of weld and DDH repaired vanes under simulated service conditions and to compare the results with new vanes tested under the same conditions. The testing and evaluation was performed at the NLR laboratory.

A schematic view of the NLR high velocity burner rig facility is given in figure 2. Air with a total pressure up to 1.45 bar is delivered by three series-connected centrifugal compressors to the cold and hot stream sections. In the hot stream section the air is heated by two conventional kerosene burners. The resulting combustion gases are mixed in a chamber containing baffle plates in order to obtain homogeneous flow. At this stage pollutants are injected if and as required.

The gas stream can be controlled to any temperature between 600 °C and 1075 °C with a Mach number up to 0.75. At 1000 °C the temperature variation across the nozzle exit plane is ± 5 °C.

During testing the vanes or blades can be provided with cooling air from a heat exchanger which is connected with a by-pass of the hot gas stream exhaust nozzle. Downstream of the rectangular nozzle are provisions for non-rotating blade and vane cascade configurations.

Temperature variations representative of flight-by-flight conditions are obtained and monitored with the aid of an HP 2100 process computer which controls the fuel flow, motion of the cascade support between hot and cold nozzles and to intermediate positions, and pollutant injection. Figure 3 shows a cascade of F100 first stage vanes including the equipment for internal cooling.

The test conditions were chosen to simulate service within a desired life time of about 1800 cycles. This was accomplished by a stepwise increase in test condition severity owing to the injection of pollutants and the reduction of cooling effectivity. In total the vanes were subjected to 1900 start-stop cycles according to the temperature profiles shown in figure 4. The figure also shows the heating and cooling rates, maximum test temperature, cycle duration and pollutant conditions. The data reflect the temperature condition at the airfoil leading edge.

5. RESULTS

A representative view of the condition of the vanes before and after testing is shown in figures 5 and 6. As can be seen from figure 5 it is clear that the DDH repair results in a more complete restoration of the vane than the weld repair. Both airfoils of the weld repaired vane still showed cracking and crazing affected areas.

After the test (Fig. 6) the weld repaired vanes showed extensive cracking, severe degradation of the areas already affected by craze cracking, and corrosion attack. The DDH repaired vanes showed slightly more pronounced cracking than as-new vanes, occurring mainly in the repaired areas and some coating flaking. However, their condition was clearly superior to that of the weld repaired vanes, see table 2.

Cross-sections at representative airfoil locations support the above findings (see Tab. 3 and Fig. 7). Cross-sections of the DDH repaired vane before testing show the excellent ability of the process to repair through the thickness cracks and crazing cracks. Only occasionally were tips of craze cracks still present owing to incomplete oxide removal. The weld repaired vane, however, still showed extensive crazing and through the thickness cracks.

Cross-sections prepared after testing showed DDH repaired areas to be very resistant to cracking with only incidental wall thickness penetration at repairs. Porosity was noted in repaired areas but this did not seem to seriously affect crack behaviour (Fig. 7). The weld repaired vanes, however, showed severe wall thickness penetration at or near repaired areas and severe craze cracking and base metal attack at those areas which were originally already affected by craze cracking. This additionally shows the advantage of the DDH repair over the weld repair because craze cracking cannot be repaired by welding.

6. DISCUSSION

The condition of the as-delivered repair welded vanes indicate that this approved repair procedure did not result in complete rejuvenation of the vanes. Apparently not all cracks may or can be repaired by welding and new cracks develop as a result of the welding procedure. Additionally, crazing type of cracking cannot be repaired in this way, as was clearly shown in figures 5 and 7. On the other hand the DDH repair resulted in an uncracked, smooth vane surface and the elimination of crazing affected areas.

After the simulated service tests the weld repaired vanes showed the worst condition, caused on the one hand by growth and widening of already existing cracks and the development of new cracks, and on the other hand by severe degradation of unrepaired areas affected by crazing. The DDH repaired vanes showed a better condition after testing. This was considered to be due to the absence of initial cracks, to complete or nearly complete restoration of crazing affected areas, and to the fact that the diffusion braze repaired areas seemed to be less sensitive to cracking than weld repaired areas. The DDH repaired vanes behaved less favourably than new ones because of a slight preference for cracking at repaired areas. However, the success of this repair process is still remarkable.

7. CONCLUSION

Advanced repair techniques, such as the DDH repair, offer considerable advantage over conventional weld repair techniques for rejuvenation of high technology turbine components. The current investigation shows that DDH repair results in a nearly complete restoration of F100 turbine vanes. This is due to a combination of factors:

a very effective oxide removal procedure, also for fine craze cracks; a complete or nearly complete bonding alloy penetration in through the thickness cracks but also in craze cracks; a HIP treatment for additional densification; and finally the application of a new coating to restore surface finish and corrosion protection.

Another economically interesting aspect of the DDH process is that scrap rates during repair very probably can be strongly reduced. In the future one might even consider some relaxation of current repair limits so that a still higher repair yield could be obtained.

8. REFERENCE

1. Duvall, D.S., Owczarski W.A. and Paulonis, D.F.: TLP bonding: a new method for joining heat resistant alloys; presented at the AWS annual meeting, Chicago, April 1973; Welding Journal, Vol. 53, 1974, pp. 203-214

TABLE 1
Scrap and salvage rates during weld repair of F100 turbine vanes

Total number of vanes available for repair	208
Not repairable	51
Scrapped in process (43 due to cracking resulting from convex cooling hole weld plugging)	56
Repaired and serviceable	101

TABLE 2
Macroscopic classification of cracking and corrosion attack
before, during and after testing

vane type	condition		
	Before testing	After 1300 cycles	After 1900 cycles
as new		o	oo
DDH repaired		o	oo
weld repaired	ooo o	ooo oo	ooo oo

o number of cracks < 10; maximum crack length 10 mm
 oo number of cracks 10 - 20 and/or maximum crack length 10 - 20 mm
 ooo number of cracks > 20 and/or maximum crack length > 20 mm
 o porosity and/or crazing
 oo severe crazing

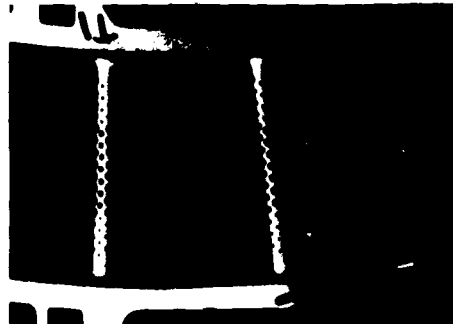
closed symbols indicate that cracks opened due to corrosion attack.

TABLE 3
Classification of cracking and corrosion attack after testing
based on cross-sectional microscopic condition

vane type	condition after 1900 cycles
as new	coating attack
DDH repaired	coating attack + porosity in repaired areas + incidental wall thickness penetration along repairs
weld repaired	severe coating attack + base metal attack + severe wall thickness penetration



AS RECEIVED DISTRESSED VANE



CLEANED AND PARTIALLY WELDED CRACKS



BOND ALLOY APPLICATION PRIOR TO VACUUM BOND



DDH REPAIRED VANE

Fig. 1 F100 1st stage vane. DDH repair sequence on vane used for rig test (except photograph left below - representative condition on different vane)

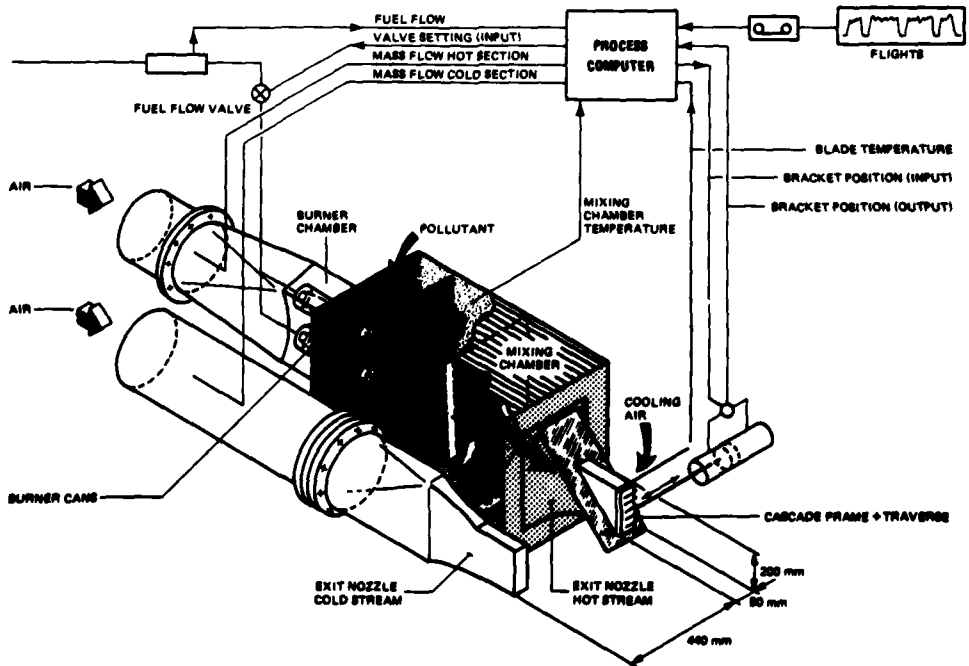


Fig. 2 Test rig used for the evaluation of turbine vane repairs



Fig. 3 First stage F100 turbine vane cascade including the air cooling connections

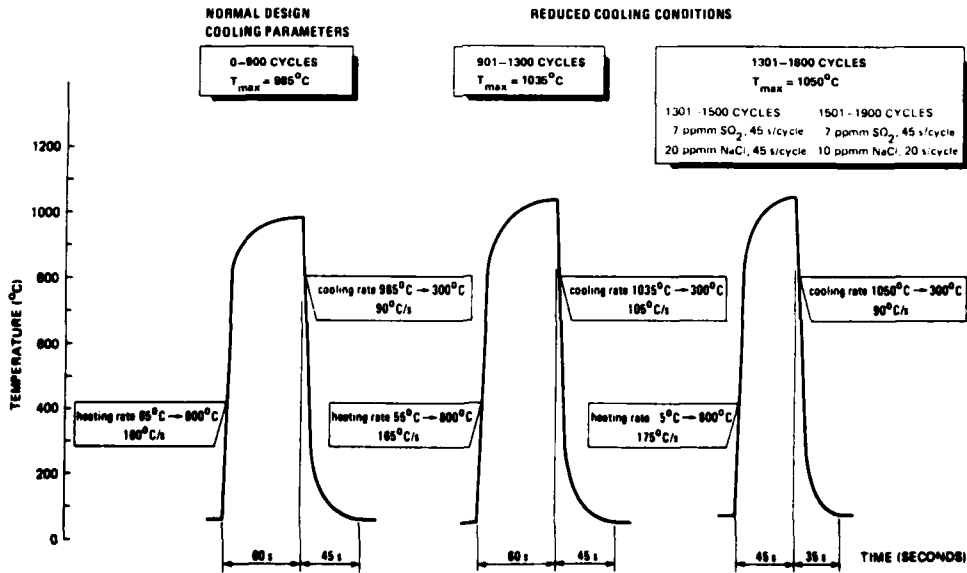


Fig. 4 Temperature profiles and pollutant conditions during the test

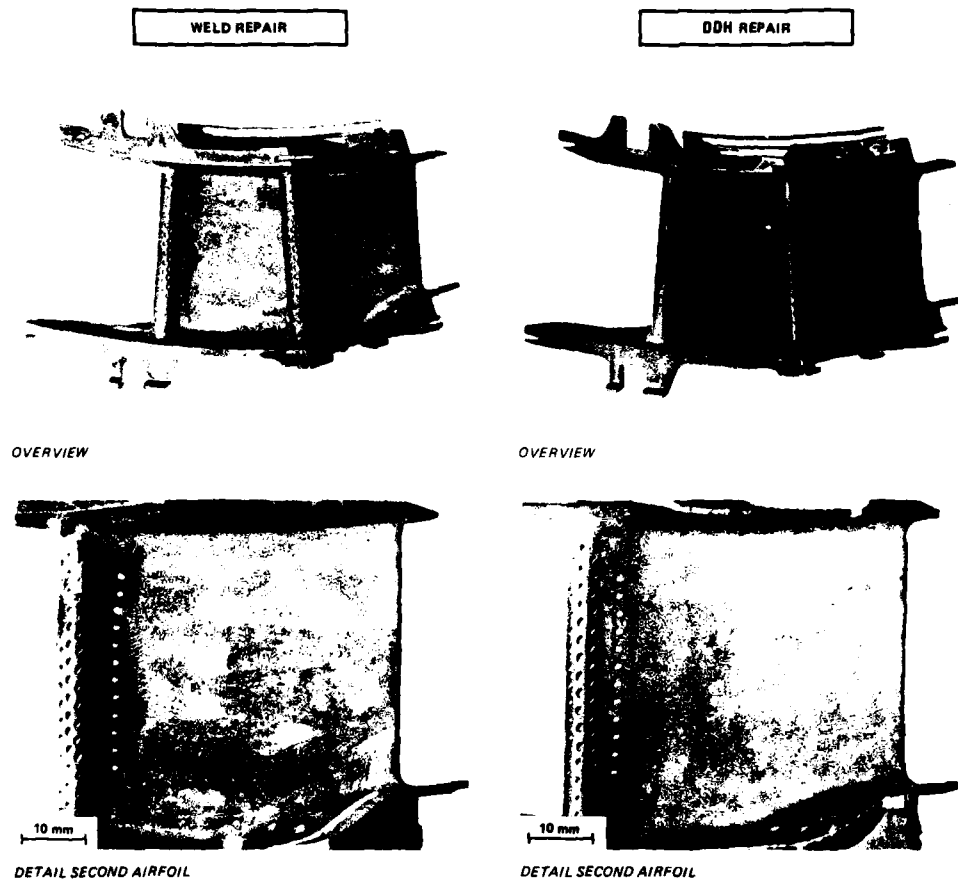


Fig. 5 Representative conditions of weld and DDH repairs before testing.
(Note blend repair at trailing edge of forward airfoil of DDH repaired vane)



Fig. 6 Representative conditions of weld and DDH repairs after the test

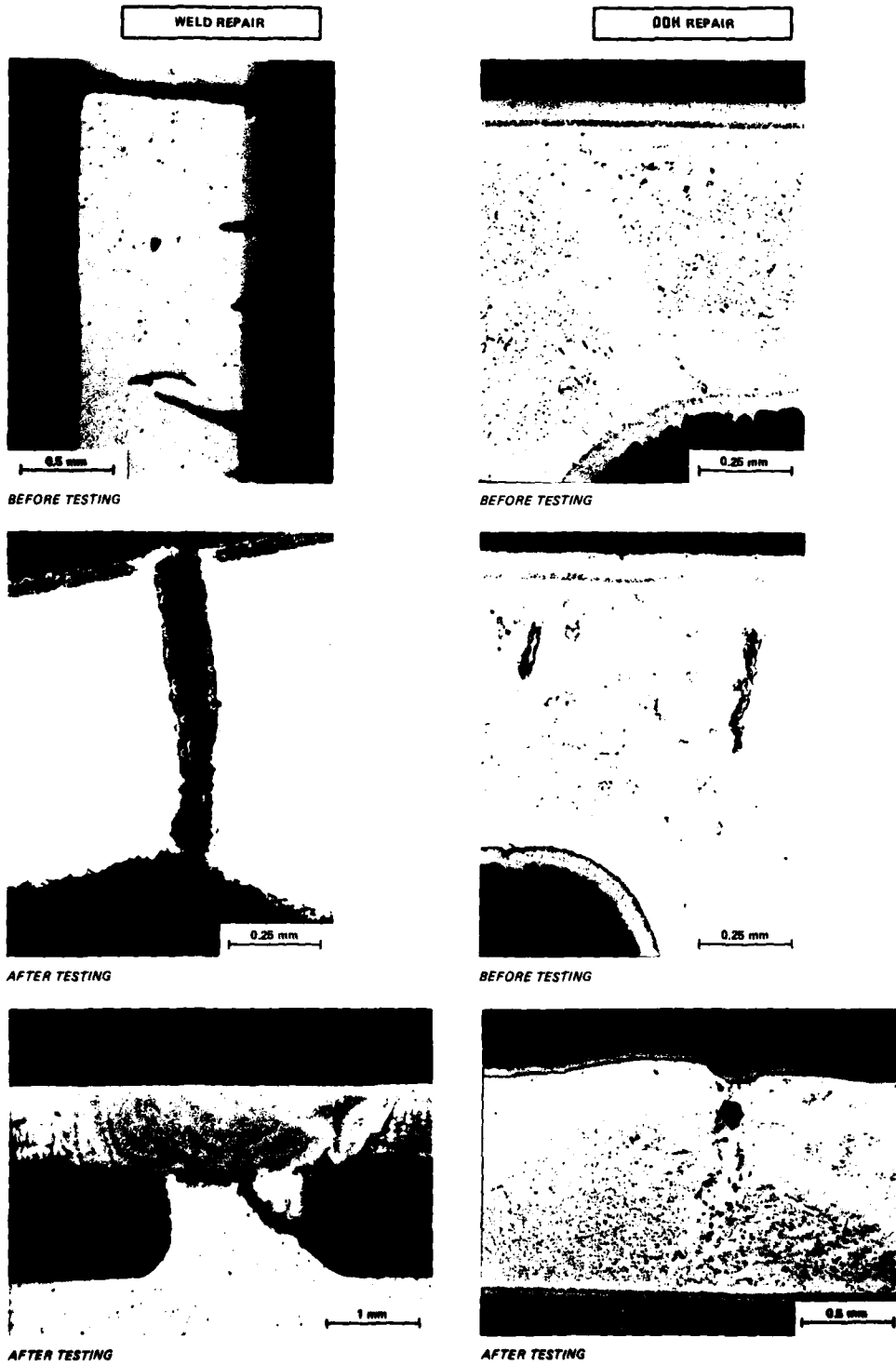


Fig. 7 Representative cross sections of weld and DDH repaired vanes before and after testing

REPAIR TECHNIQUES FOR GAS TURBINE COMPONENTS

J. Liburdi, President
 P. Lowden, Metallurgical Engineer
 Liburdi Engineering Limited
 3334 Mainway,
 Burlington, Ontario.
 L7M 1A7

ABSTRACT

In this paper, areas in which the state of the art in gas turbine repair technology needs to be advanced will be discussed.

A large part of the discussion deals with current inadequacies of weld repair techniques for high strength superalloys and with possible areas for improvement. In particular, the problems of poor weldability and the low strength of conventional weld repairs are examined, with emphasis on areas for further development including; welding with matching filler metals, pre-weld heat treatment and preparation, modification of welding techniques and post-weld HIPing and heat treatment.

Another area of discussion is the need for improved techniques for resurfacing and repair of airfoil damage. Two techniques appear to be promising for this application; diffusion brazing and vacuum plasma spraying.

The importance of NDT limitations and mechanical analysis with regard to the development and implementation of novel repair techniques is emphasized. Disregard of these factors can lead to repairs which are substantially cosmetic in nature.

INTRODUCTION

Ten years ago, most hot section turbine components which exhibited physical damage resulting from corrosion, impact and rubs, would have been scrapped and replaced. But recently, due to the high price of replacement turbine parts and the potential shortage of critical alloys, welding techniques for the repair of service damage have been developed and have been increasingly accepted as economical alternatives to component replacement. Unfortunately, the scope of the repairs has often been limited by the low strength of the repaired area and the poor weldability of the nickel base superalloys used in high performance gas turbines.

The purpose of this paper is to identify the shortcomings of conventional repair procedures and to examine several new techniques which may extend the current limits to repairs. Also, the requirements for qualifying new repair techniques and identifying their limits will be discussed.

CONVENTIONAL REPAIR TECHNIQUES

The conventional repair of service damage to turbine parts typically involves the removal of the damaged area by grinding or cutting followed by the restoration of the missing metal by Gas Tungsten Arc (GTA) welding. The excess weld metal is then dressed off to restore the original airfoil shape. A typical repair of a turbine blade is shown in Figure 1.

Such procedures can be used to repair virtually all types of damage in the solution strengthened nickel and cobalt alloys found in stationary components due to their relatively good weldability. In contrast, the precipitation-hardened superalloys used for rotating turbine blades are difficult to weld and repairs are therefore generally performed using lower strength filler alloys and as such, are limited to the less critical blade tip area.

Weld Metal Cracking

One of the major welding problems associated with the higher strength nickel base alloys is their tendency to form cracks in the weld metal when they are used as filler metals. These cracks occur as the result of several factors during or after the solidification of the weld pool.

For example, segregation can be a problem in highly alloyed materials. The rejection of alloying metals and impurities can result in the formation of thin liquid films between grains which, under the action of welding stresses, can initiate cracks in the solidifying weld metal. Cracking by this mechanism has been referred to as "solidification cracking".⁽¹⁾

Another mechanism by which weld metal cracking can occur is known as "subsolidus" or "ductility dip" cracking.⁽²⁾ Such cracking is not associated with segregation; rather it appears to be due to the poor ductility of high strength superalloys at approximately 800°C. Cracking in the HAZ can occur by a similar mechanism.

Strain is a major factor in weld metal cracking. In addition to the normal thermal contraction strains resulting from welding, volume changes associated with the precipitation of gamma prime particles in the solidified metal result in more shrinkage strains. Due to the poor ductility of the higher strength alloys, these strains cannot be adequately accommodated, particularly in restrained weld configurations. The level of residual stress can be high enough to propagate a crack which initiated as a solidification or ductility dip crack through several tiers of weld metal.

To avoid the problem of weld metal cracking, repairs are generally made with solution strengthened alloys such as Inconel 625. Due to the high ductility and absence of second phase precipitation during solidification, the stresses developed during welding are much lower. However, as shown in Figure 2, the strength of Inconel 625 is substantially lower than that of the alloys it is commonly used to repair. Therefore, repair limits outlining when the weaker alloys can be safely used must be established.

Repair Limits

Consider, for example, an unshrouded turbine blade. As shown in Figure 3, the average centrifugal stress decreases from a maximum at the hub to zero at the tip, while the temperature is highest at mid-airfoil. The blade alloy and the temperature profile determine the allowable stress for a reasonable life expectancy at various blade heights. Near the blade tip there is a greater margin between the allowable and actual stresses which permits the use of a lower strength filler metal. It is important to note that lower in the airfoil such weaker alloys may not be used since the applied stress exceeds their allowable stress.

In a typical shrouded blade, the margin between applied and allowable stresses remains small even under the shroud, as seen in Figure 4. Therefore, repairs with weaker filler metals are limited to damage on the shroud and cannot be used in the airfoil.

Another factor which must be considered when welding with dissimilar metals is the effect of differences in the thermal expansion coefficient between the filler metal and the base alloy. In a notch type repair, for example, if the filler metal has a lower coefficient of expansion than the surrounding base metal, the welded area will be subjected to a tensile stress during operation. In combination with steady state or cyclic loading, such thermal stresses could cause premature failure of the repaired area even when the net section stress is within the allowable limits. Further details on the effect of dissimilar metals and joint geometry are contained in a previous paper.⁽³⁾

Heat Affected Zone Cracking

The second major weldability problem with higher strength nickel base superalloys is the formation of HAZ cracks during welding by mechanisms referred to as "liquation cracking".⁽¹⁾ Cracking by liquation occurs as a result of the local melting of the base metal along the grain boundaries in the HAZ. Due to welding strains, the liquated boundaries adjacent to the fusion line are pulled apart to form microcracks.

The localized melting which causes HAZ microcracking occurs as a result of variations in composition which cause the material adjacent to the boundaries to melt at a lower temperature than the surrounding material. Two distinct mechanisms have been identified by which such variations in composition can occur. In the first mechanism, solute segregation at the grain boundaries exists prior to welding and locally depresses the melting point. A second mechanism, which is referred to as "constitutional liquation", involves a change of the local composition during welding due to the rapid decomposition of carbides along the grain boundaries. In particular, MC type carbides have been identified as releasing boron and carbon during welding of Udimet 700, resulting in liquation cracking in this alloy.⁽⁴⁾ However, the same effect could also be expected from the decomposition of M₂₃C₆ type carbides, particularly since they precipitate preferentially at grain boundaries.

In our program, the alloy IN738LC was studied in detail and was found to exhibit microcracking in the heat affected zone typical of higher strength nickel base superalloys.

Samples for the investigation were removed from service-exposed industrial turbine blades and given the following heat treatments; solution treated, solution treated + aged, solution treated + overaged. The samples were then GTA welded in a low restraint edge type configuration using both matching IN738LC and Inconel 625 filler metals.

The welded samples were examined non-destructively by fluorescent penetrant inspection and longitudinally profiled by optical metallography as shown in Figure 5. The profiling technique was found to be necessary since examination of single sections often failed to locate the defects due to their relatively small size and low density. Selected samples were also examined by scanning and transmission electron microscopy.

None of the samples prepared exhibited cracking when examined non-destructively. However, metallographic examination revealed that all of the samples had HAZ cracking of similar appearance, size and distribution. As shown in Figure 6, the cracks form in the region adjacent to the weld fusion line and extend 50 - 400 μ m into the base metal. It was observed that the cracks tended to be longer in the center of the weld than at the edge.

To determine the mechanism by which cracking occurred, the nature of the grain boundaries in the heat affected zone was examined by electron microscopy. An area adjacent to the grain boundary appeared to have been affected by the welding cycle to a depth approximately corresponding to that of the HAZ microcracks. The grain boundary carbide layer had dissolved and in a thin region (approximately 3 μ m) adjacent to the boundary, the gamma prime appears to be absent as shown in Figure 7. Closer examination of this region revealed that the primary gamma prime particles had dissolved and re-precipitated as fine particles. In some instances, the gamma prime had reformed in a eutectic morphology, as shown in Figure 8, suggesting that liquation of the grain boundary had occurred. Energy dispersive spectroscopy (EDS) of the region adjacent to the boundary indicated that it had been enriched in chromium and tantalum which are major metallic elements in $M_{23}C_6$ and MC carbides respectively.

Based on these observations, it was concluded that the HAZ microcracking mechanism in IN738 was constitutional liquation. The decomposition of grain boundary carbides appears to have resulted in the formation of an enriched layer adjacent to the grain boundary. Presumably this layer was also enriched in carbon and boron which could not be detected by EDS analysis. This resulted in the lowering of the melting point at the grain boundary and the associated formation of a liquated layer which was pulled apart by welding stresses.

Unlike weld metal cracking which can be controlled by altering the properties of the filler wire, no adequate means have previously been developed for prevention of HAZ cracking. Good welding practice which reduces the heat input and restraint can reduce the severity of cracking and eliminate it in less crack sensitive alloys. However, some cracking appears to be unavoidable in higher strength alloys unless modifications can be made to the base metal. For example, grain boundary liquation caused by solute segregation can be lessened by the use of homogenization treatments. Other factors such as the grain size and composition of the base metal, which have been shown to influence HAZ cracking,⁽²⁾ cannot readily be modified except during the manufacture of the component. It has also been shown that the use of filler metals with lower solidus temperatures lessen the HAZ crack sensitivity of Inconel 713c.⁽⁵⁾ However, in the current investigation of IN738LC, no difference in the HAZ microcracking as a function of filler alloy was found.

REPAIR PROCESSES

In order to extend the application of repairs beyond their current limits, a number of new techniques have been or are currently being developed. These techniques include improvements of conventional GTA weld repairs to overcome the problems of low weld metal strength and HAZ cracking as well as alternative techniques for resurfacing and repair of airfoil damage.

Matching Filler Metals

One approach to extending the limits of the conventional GTA weld repairs is to use higher strength filler metals. Ideally, the weld metal used should have the same composition as the base metal so that their thermal expansion and creep properties will match as closely as possible. This would allow extension of the repairs into more highly stressed regions of the airfoil without causing a reduction of component life due to creep or thermal fatigue.

In the case of the intermediate strength alloys, it is possible to prepare welds using matching composition filler wires by controlling the stresses generated during welding. This is accomplished by using low restraint weld configurations and minimizing weld heat input. Using these techniques, matching filler repairs have been performed on A286, Inconel X750, Inconel 700 and Udimet 500 alloy components with samples prepared as shown in Figure 9. As shown in Figure 10, after hot isostatic pressing and heat treatment, these repairs result in strengths which are somewhat below parent metal properties but far superior to conventional welding alloys such as Inconel 625. The slightly lower properties are likely due to a combination of factors such as microsegregation in the weld and grain size differences between the weld and the base metal.

In higher strength alloys, modifications to welding procedures to reduce thermal strains are, in general, insufficient to prevent weld metal cracking because the high Al and Ti contents result in substantial shrinkage strains from the precipitation of gamma prime. Welds prepared using IN738LC filler wire were found to crack through the weld metal after the deposition of 2 - 3 tiers of weld metal despite precautions to minimize restraint and heat input. In order to minimize the shrinkage strains resulting from gamma prime precipitation, a modified welding wire was prepared in which niobium had been added in place of some of the aluminum and titanium content to slow the aging response. Welds prepared in a similar manner exhibited markedly improved crack resistance with no cracking occurring until 7 - 8 tiers of weld metal had been deposited. It is hoped that further refinements of the composition of the modified filler wire will result in the elimination of the weld metal cracking while maintaining most of the normal base metal properties.

In order to procure the custom filler alloys in wire form, it was necessary to first develop a technique for manufacturing wire using a powder metallurgy approach. As shown in Figure 11, the process yields 100% dense wire without the surface contamination normally present in conventionally drawn wire. Since the technique uses powders, it is suitable for the preparation of any alloy which is available in powder form, and by mixing

various pre-alloyed powders, it can also be used to create a range of modified alloys.

Pre-Weld Treatment

To prevent HAZ cracking, it is often necessary to modify the condition of the base metal prior to welding. Service exposure can result in structures which severely lower the weldability of an alloy such as brittle topologically close packed phases and continuous grain boundary carbide films. These structures increase the severity of liquation cracking or ductility dip cracking by decreasing the ductility of the alloy and its ability to accommodate welding strains. Fortunately, these structures can be easily eliminated by a solutioning treatment. Depending on the alloy, the treatment may include solution treatment only or solution treatment and aging or overaging cycles.

Although such simple thermal treatments are adequate to eliminate cracking in less crack sensitive alloys, they do not alter the conditions which cause constitutional liquation cracking and are therefore ineffective in alloys such as IN738 as was demonstrated in our initial investigation of the crack mechanism. However, subsequent investigations have identified non-standard treatments which alter the nature of the grain boundaries and effectively reduce the crack sensitivity. Using such treatments, it has proven possible to repeatedly produce defect-free welds on IN738 base material, provided precautions are taken to minimize heat input and weld restraint.

Post-Weld Treatment

Hot Isostatic Pressing (HIP) is a proven technology for the manufacture of superalloy components. In addition to being used to consolidate powder metallurgy preforms, it has been applied to the elimination of porosity in superalloy castings, the healing of creep cavities in service exposed turbine blades,⁽⁶⁾ as well as the closing of minor weld defects.

HIP has been successfully applied to the elimination of weld porosity and micro-porosity, resulting in improved strength and ductility in weld repaired regions; however, HIP was not as effective in closing cracks in the heat affected zone of the base material.

Preliminary results from our investigation on the effects of HIP on HAZ cracks in IN738 suggest that this approach should be used with caution.

IN738 samples were welded in the fully heat treated condition using Inconel 625 filler wire and were examined in the as-welded and HIP'd conditions. In both cases, the samples were found to exhibit HAZ cracking. However, it was noted that the density of cracks had decreased in the HIP'd condition suggesting that the HIP treatment had been effective in healing some of the cracking. The cracks which did not heal were thought to have been open to the surface during HIPing so that they were not pressed. Any application of HIPing to healing HAZ cracking would therefore need to incorporate some means of sealing surface cracks to be effective in healing all of the damage present.

ALTERNATIVE NON-FUSION PROCESSES

Recently, several technologies have emerged as alternatives to the conventional weld repair techniques. In particular, two techniques which are well-suited to the repair of general airfoil damage are vacuum plasma spraying and diffusion brazing.

Vacuum Plasma Spraying

It has been reported that it is possible to deposit fully dense layers of nickel base superalloys with tensile and thermal fatigue properties superior to the cast base alloys by vacuum plasma spraying.⁽⁸⁾ This technique is already being used to apply uniform corrosion coatings on the blade airfoils. If the thickness and location of the sprayed deposit could be controlled, repaired parts could be built up without the use of fusion processes such as welding.

In order to evaluate the potential for applying the technique to components such as blades, where creep is an important consideration, samples were prepared by vacuum plasma spraying IN738 powder onto an IN738 substrate. As shown in Figure 12, a fully dense structure was obtained with no evidence of interfacial oxidation. The deposit was hot isostatic pressed to eliminate any residual porosity and mechanical test bars were removed through the deposit substrate interface for stress rupture and tensile tests.

The results of the stress rupture and tensile testing are shown in Figures 13 and 14. Although both the creep and tensile properties are below the normal cast IN738 properties, the results are encouraging. The failures in the creep bars were found to occur in the plasma deposit rather than at the interface as shown in Figure 15, while the failures in the tensile bars occurred either in the plasma deposit or at the interface.

Although the results of the initial investigation of vacuum plasma spraying as a repair technique are promising, several major obstacles may limit its continued development. These include the inability to localize the build-up without significant over-spraying and the line-of-sight nature of the spraying process.

Diffusion Brazing

A number of techniques based on the use of a low melting filler alloy which is inter-diffused with the base metal have recently been developed. The filler metal is applied as a powder mixture of low melting and regular alloys using standard brazing practice. However, unlike conventional brazing, the melting point depressant is diffused into the base metal to prevent the formation of brittle phases. Strengths approaching 100% of the parent metal have reportedly been achieved by this technique.^(9,10) Like plasma spraying, this technique is well-suited to repair of airfoil damage, since it can be applied in controlled thicknesses.

The application of these techniques has primarily been limited to stationary components. However, if filler alloys based on the higher strength nickel base alloys can be developed, it should be possible to extend its application to higher stressed components.

QUALIFICATION OF NEW REPAIR TECHNIQUES

Before new repair procedures can safely be applied to components which are to be returned to service, it is necessary that they be subjected to a thorough qualification procedure. This procedure includes the determination of the mechanical properties including creep, tensile, fatigue and thermal expansion characteristics; as well as mechanical stress analysis to determine the safe limits for the application of the repair.

It is also important that the types of defects likely to be encountered during application of the repair be characterized during the qualification procedure. The inspection techniques currently used for conventional weld repair are likely to prove inadequate to detect the defects in new repair procedures, particularly those which do not involve welding. For example, with the standard techniques of fluorescent penetrant and x-ray inspection it is difficult to detect HAZ microcracking which is likely to be encountered during high strength weld repair or delamination which may occur with overlay techniques. The identification of defect types during the qualification stage allows the implementation of either proper process controls to prevent the defect or inspection procedures to detect it.

CONCLUSIONS

The use of conventional weld repair processes using weaker filler metals will severely restrict the refurbishment of the higher strength alloys used in more advanced jet engine designs. In order to extend the repair limits in higher strength superalloys, it is necessary to both overcome the cracking tendency exhibited by these highly alloyed materials, as well as develop matching filler alloys for the repair buildup.

Several new techniques for extending the current limits appear to be promising. These include modifications to the welding technique and base metal treatment capable of producing defect-free repairs in high strength alloys such as IN738, as well as techniques for applying surface overlays by vacuum plasma spraying and diffusion brazing. These non-fusion processes have potential for development as alternatives to welding on high strength components and by using a combination of these techniques, it should be possible to extend repairs to higher stressed areas.

However, all of these processes must be properly qualified to ensure they are not applied in areas where their strength is inadequate and also that suitable inspection techniques and process control are applied. In most cases, conventional x-ray and penetrant inspection will not be adequate and must be augmented by detailed metallography to detect microcracking or lack of fusion.

REFERENCES

1. B.G. Baker, Phil. Trans. R.Soc., 1976, A282, 207.
2. R. Thamburaj; et al., Int. Met. Rev., 1983, 28 (1), 1.
3. J. Liburdi, J. Wilson, Proc. 12th Turbomachinery Symposium, College Station, Texas, Nov. 1983, 21.
4. W.A. Owczarski; et al., Weld. J., 1966, 45 (4), 1455.
5. W.H. King; et al., "Superalloy Filler Metal Optimization", Technical Rept. AFML-TR-78-177, December, 1978.
6. J. Liburdi, J. Wilson, Cdn. Aero. Space J., 1981, 27 (4), 363.
7. W. Elsner, Prakt. Met. 1982, 19, 199.
8. M.R. Jackson; et al., "Production of Metallurgical Structures by Rapid Solidification Plasma Deposition", GF Rept. 81CRD201, August, 1981.

22-6

9. R.S. Duvall, J.R. Doyle, "Repair of Turbine Blades and Vanes", ASME paper 73-GT-44, January, 1973.
10. Y. Honnorat, J. Lesoburge, in Maintenance in Service of High Temperature Parts, AGARD CP 317, Noordwijkenhout, Holland, 1981, paper 9.

ACKNOWLEDGEMENTS

The authors are grateful for the support of the National Research Council of Canada in the development of high strength repairs for superalloys.

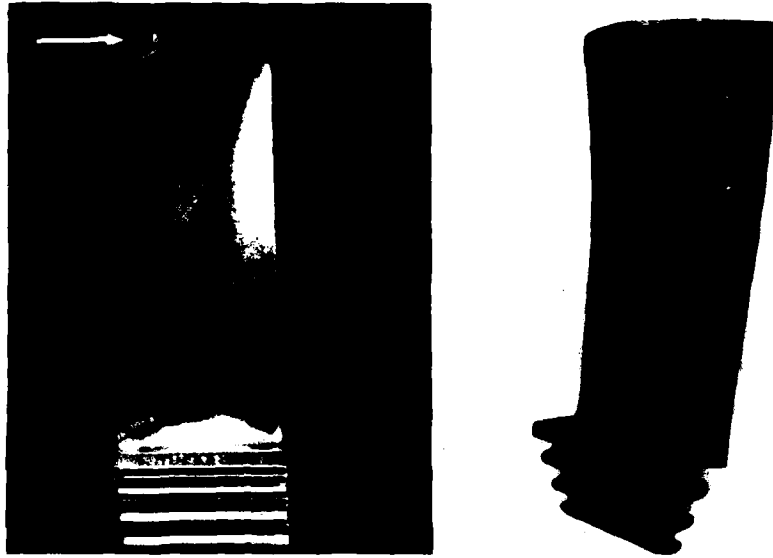


Figure 1 - Typical repair of impact damage and rubbing.

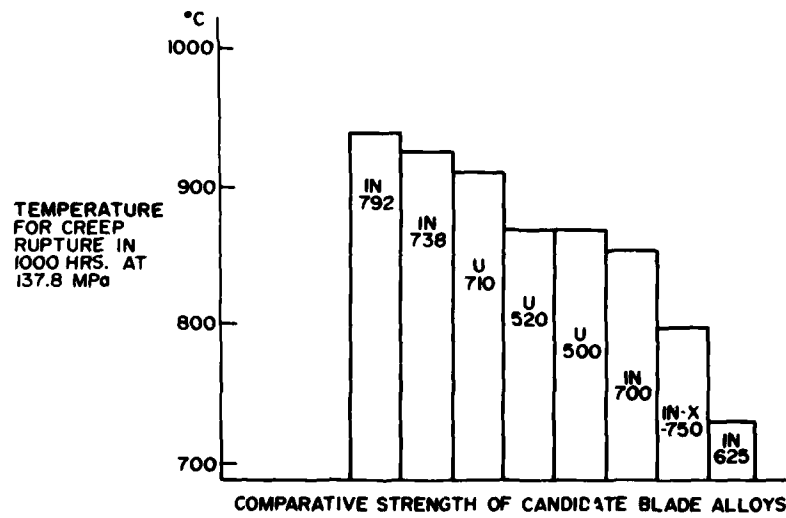


Figure 2 - Comparative creep strength of common blade alloys.

FIGURE 3 TYPICAL TEMPERATURES AND STEADY STRESSES
FOR A FREE STANDING BLADE

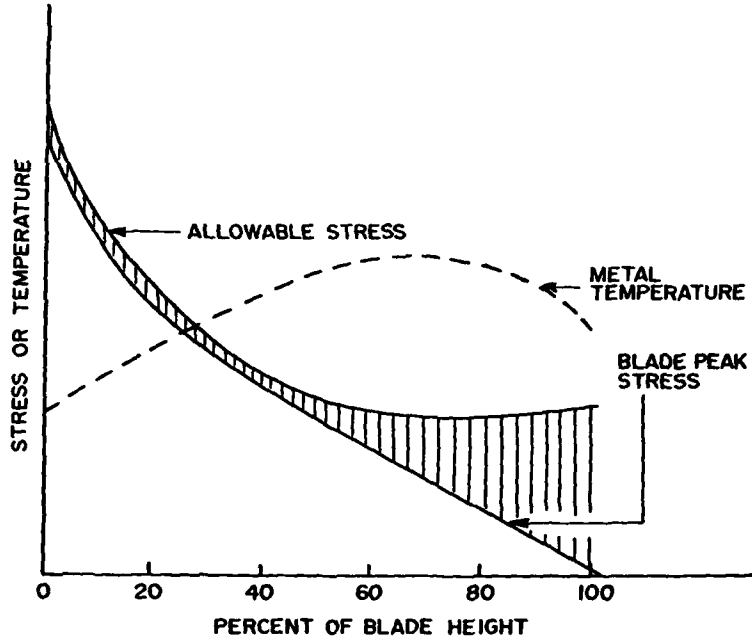
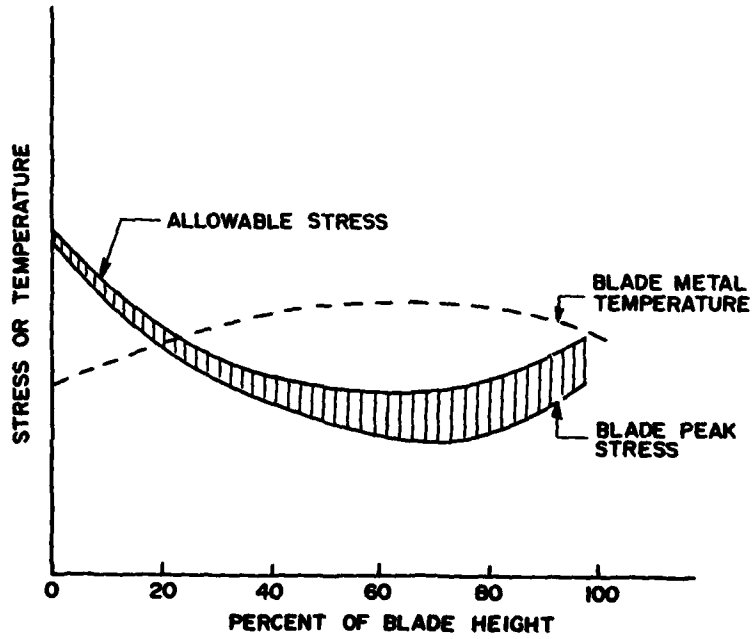
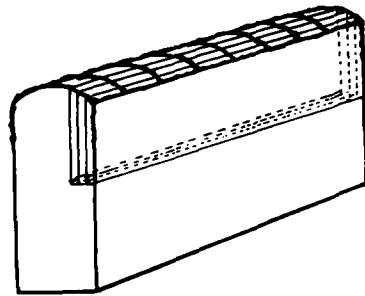


FIGURE 4 TYPICAL TEMPERATURES AND STEADY STRESSES
FOR A SHROUDED BLADE





Weld Profiling Technique

Figure 5 - Samples were profiled by examining a series of parallel sections through the weld by optical metallography.

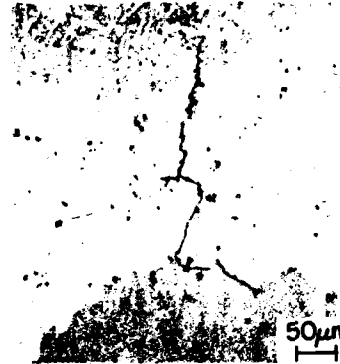


Figure 6 - Photomicrograph of a typical HAZ microcrack in an IN738 weld.



Figure 7 - SEM photomicrograph showing an affected grain boundary in a region of IN738 base metal adjacent to the weld pool.

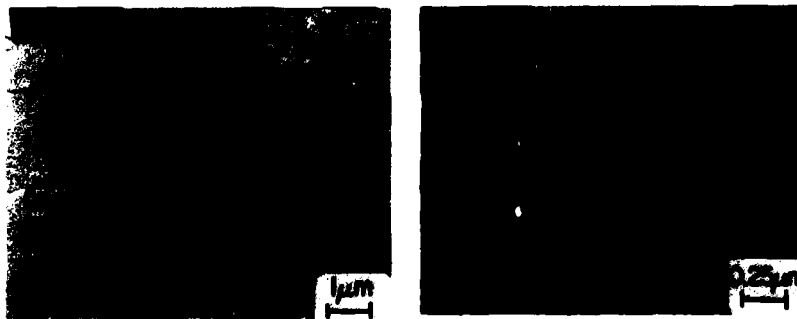
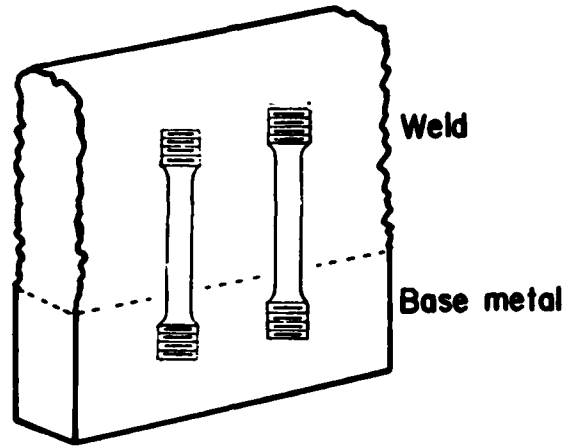


Figure 8 - TEM replica of IN738 grain boundary structure in the altered region adjacent to the weld pool.



Mechanical Testing Samples

Figure 9 - Sketch of sample used to prepare mechanical test bars.

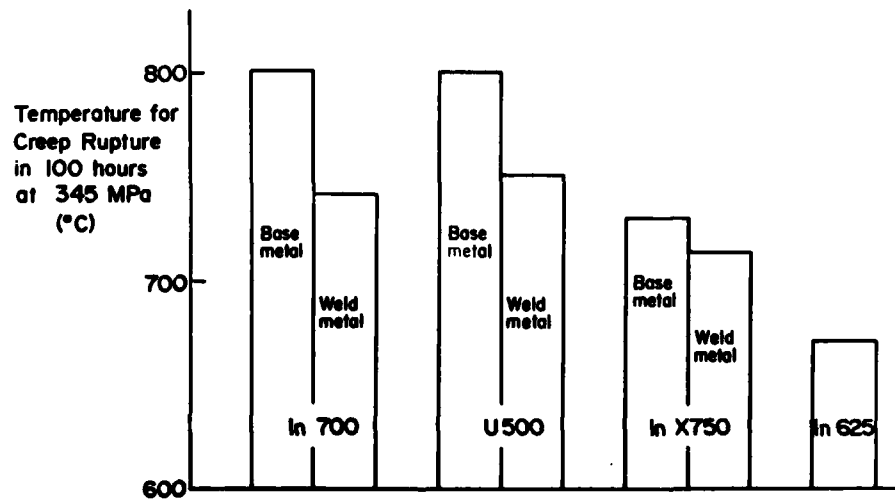


FIGURE 10 Comparative Strengths of Weld Repairs

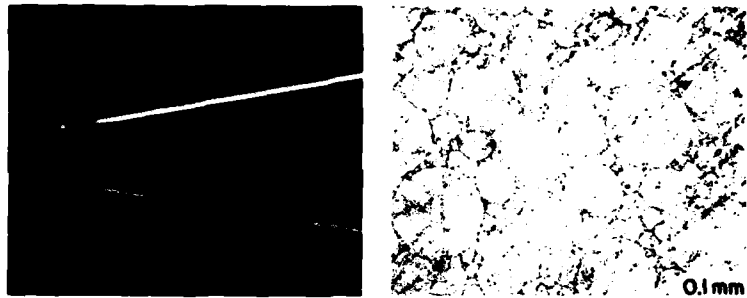


Figure 11 - Photographs of powder metallurgy wire used to prepare high strength weld samples.



Figure 12 - Vacuum plasma sprayed deposit of IN738 powder on IN738 substrate.

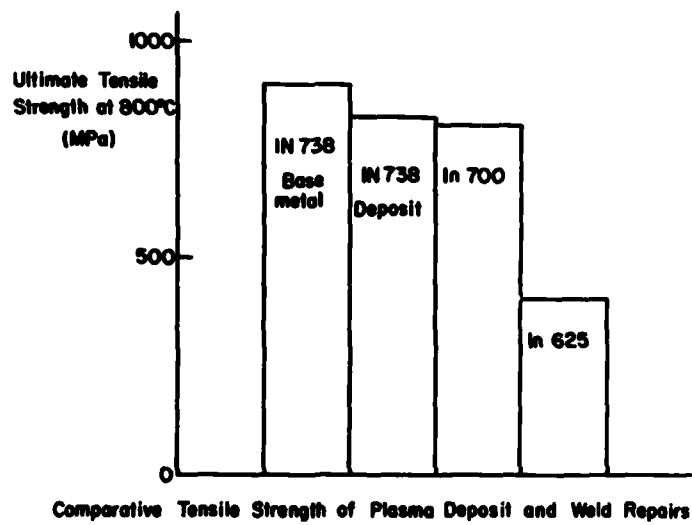


Figure 13 - Tensile strength of vacuum plasma sprayed IN738 deposit.

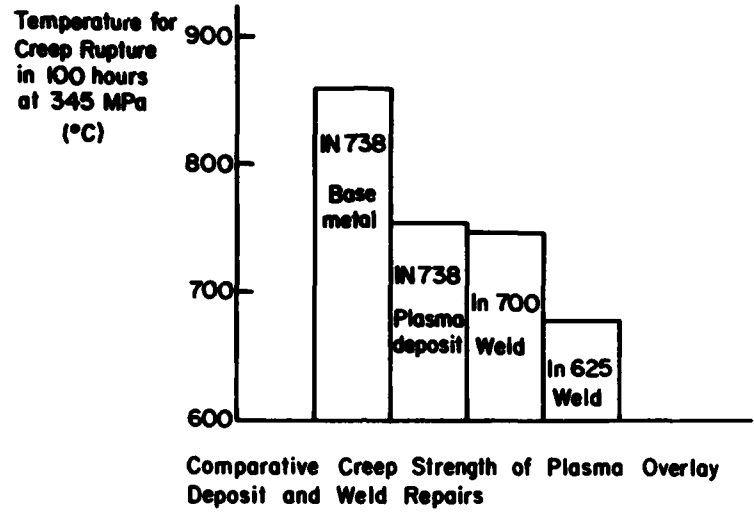


Figure 14 - Stress Rupture Strength of vacuum plasma sprayed IN738 deposit.

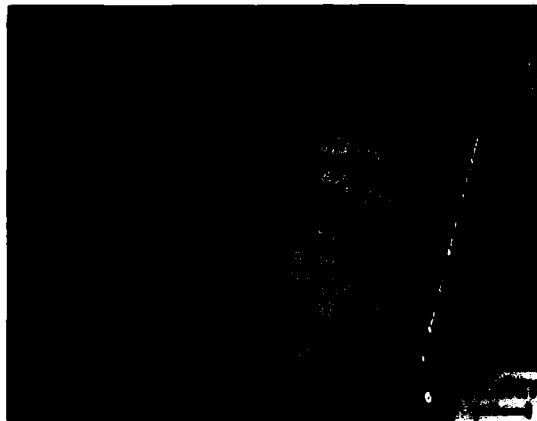


Figure 15 - Photograph showing the failure of a plasma sprayed test bar in the IN738 deposit, away from the interface.

REPORT DOCUMENTATION PAGE

1. Recipient's Reference	2. Originator's Reference	3. Further Reference	4. Security Classification of Document						
	AGARD-CP-398	ISBN 92-835-0397-X	UNCLASSIFIED						
5. Originator	Advisory Group for Aerospace Research and Development North Atlantic Treaty Organization 7 rue Ancelle, 92200 Neuilly sur Seine, France								
6. Title	ADVANCED JOINING OF AEROSPACE METALLIC MATERIALS								
7. Presented at	the 61st Meeting of the Structures and Materials Panel of AGARD in Oberammergau, Germany, 11-13 September 1985.								
8. Author(s)/Editor(s)	Various		9. Date July 1986						
10. Author's/Editor's Address	Various		11. Pages 280						
12. Distribution Statement	This document is distributed in accordance with AGARD policies and regulations, which are outlined on the Outside Back Covers of all AGARD publications.								
13. Keywords/Descriptors	<table border="0"> <tr> <td>Alloys</td> <td>Structural engineering</td> </tr> <tr> <td>Metal working</td> <td>Joining</td> </tr> <tr> <td>Aerospace engineering</td> <td></td> </tr> </table>			Alloys	Structural engineering	Metal working	Joining	Aerospace engineering	
Alloys	Structural engineering								
Metal working	Joining								
Aerospace engineering									
14. Abstract	<p><i>These papers</i></p> <p>The papers contained in this report were presented at the 61st Meeting of the Structures and Materials Panel. They provide a review of the "state of the art" of advanced techniques of joining which are currently available to manufacturers; they also make known newly-emerged joining techniques, and spotlight outstanding problems which call for further research and development.</p> <p>In these and other aspects the papers reflect the opportunity offered by the Meeting for an exchange of information between the various sectors of the engineering industry.</p> <p align="center"><i>Agard CP-398</i></p>								

<p>AGARD Conference Proceedings No.398 Advisory Group for Aerospace Research and Development, NATO ADVANCED JOINING OF AEROSPACE METALLIC MATERIALS Published July 1986 280 pages</p> <p>The papers contained in this report were presented at the 61st Meeting of the Structures and Materials Panel. They provide a review of the "state of the art" of advanced techniques of joining which are currently available to manufacturers; they also make known newly-emerged joining techniques, and spotlight outstanding problems which call for further research and development.</p> <p>P.T.O.</p>	<p>AGARD-CP-398</p> <p>Alloys Metal working Aerospace engineering Structural engineering Joining</p>	<p>AGARD Conference Proceedings No.398 Advisory Group for Aerospace Research and Development, NATO ADVANCED JOINING OF AEROSPACE METALLIC MATERIALS Published July 1986 280 pages</p> <p>The papers contained in this report were presented at the 61st Meeting of the Structures and Materials Panel. They provide a review of the "state of the art" of advanced techniques of joining which are currently available to manufacturers; they also make known newly-emerged joining techniques, and spotlight outstanding problems which call for further research and development.</p> <p>P.T.O.</p>	<p>AGARD-CP-398</p> <p>Alloys Metal working Aerospace engineering Structural engineering Joining</p>
<p>AGARD Conference Proceedings No.398 Advisory Group for Aerospace Research and Development, NATO ADVANCED JOINING OF AEROSPACE METALLIC MATERIALS Published July 1986 280 pages</p> <p>The papers contained in this report were presented at the 61st Meeting of the Structures and Materials Panel. They provide a review of the "state of the art" of advanced techniques of joining which are currently available to manufacturers; they also make known newly-emerged joining techniques, and spotlight outstanding problems which call for further research and development.</p> <p>P.T.O.</p>	<p>AGARD-CP-398</p> <p>Alloys Metal working Aerospace engineering Structural engineering Joining</p>	<p>AGARD Conference Proceedings No.398 Advisory Group for Aerospace Research and Development, NATO ADVANCED JOINING OF AEROSPACE METALLIC MATERIALS Published July 1986 280 pages</p> <p>The papers contained in this report were presented at the 61st Meeting of the Structures and Materials Panel. They provide a review of the "state of the art" of advanced techniques of joining which are currently available to manufacturers; they also make known newly-emerged joining techniques, and spotlight outstanding problems which call for further research and development.</p> <p>P.T.O.</p>	<p>AGARD-CP-398</p> <p>Alloys Metal working Aerospace engineering Structural engineering Joining</p>

In these and other aspects the papers reflect the opportunity offered by the Meeting for an exchange of information between the various sectors of the engineering industry.

ISBN 92-835-0397-X

In these and other aspects the papers reflect the opportunity offered by the Meeting for an exchange of information between the various sectors of the engineering industry.

ISBN 92-835-0397-X

In these and other aspects the papers reflect the opportunity offered by the Meeting for an exchange of information between the various sectors of the engineering industry.

ISBN 92-835-0397-X

In these and other aspects the papers reflect the opportunity offered by the Meeting for an exchange of information between the various sectors of the engineering industry.

ISBN 92-835-0397-X

END

DATE
FILMED

12-86